SEARCHING FOR KINETIC CONTROL OF EXCITED-STATE EVOLUTION IN FE(II) POLYPYRIDYL CHROMOPHORES

By

Sara Linnae Adelman

A DISSERTATION

Submitted to
Michigan State University
in partial fulfillment of the requirements
for the degree of

Chemistry–Doctor of Philosophy

2020

ABSTRACT

SEARCHING FOR KINETIC CONTROL OF EXCITED-STATE EVOLUTION IN FE(II) POLYPYRIDYL CHROMOPHORES

By

Sara Linnae Adelman

Iron(II) polypyridyl chromophores represent an earth-abundant alternative to ruthenium-based complexes in photo-induced electron transfer applications, yet the sub-150 fs metal-to-ligand charge transfer (MLCT) excited-state lifetime endemic to low-spin Fe(II) polypyridyls has hampered their widespread use. One promising avenue towards achieving a longer-lived MLCT excited-state lifetime is through the exertion of kinetic control, made possible through the identification and subsequent disruption of the nuclear coordinate of excited-state deactivation. With this aim, a series of structurally similar iron(II) polypyridyl complexes spanning from low-spin to high-spin, including a spin crossover complex, were synthesized, which allowed for the determination of reorganization energy from the lowest-energy excited state ($^5T_2$) to the ground state ($^1A_1$) through a combination of variable temperature transient absorption and magnetic susceptibility measurements. In addition to experimentally determining the reorganization energy and electronic coupling constant associated with this conversion, we will deduce the kinetically competent degree of freedom associated with this transition through a convergence of analyses from semi-classical to fully quantum mechanical non-radiative decay theories. A ruthenium(II)-based analog of the spin crossover complex provided insight into the geometric distortions coupled to the deactivation of the MLCT excited states. Coupled together, these results offered new guidelines for ligand design, inspiring the synthesis of new iron(II) complexes with unique photophysical dynamics and establishing new roadmaps towards controlling excited-state dynamics in this class of compounds.

Dedicated to all those in my life whose focus, determination, and achievement inspire mine.

ACKNOWLEDGEMENTS

Thank you to my advisor, Jim, for supporting me over these last six years, giving me a project that I've enjoyed exploring, and encouraging me to seek out opportunities that have enriched by grad school experience. I'd also like to thank my committee for the guidance they've provided, helping me get through tough synthetic (Aaron and Babak) and theoretical (Rémi) problems. Dr. Richard Staples has not only solved way too many disordered crystal structures for me, but also never failed to remind me to keep my eye on the prize. Thank you to Dr. Dan Holmes and Professor Gary Blanchard for helping me collect some of the data that made this dissertation possible. Thanks Bob Rasico. your creative problem solving abilities helped me set up many experiments.

I wouldn't have learned as much as I did without the McCusker group members, Chris, Dani, Jennie, Monica, Selene, and Drew who took the time to train me and passed down so much amassed knowledge: thank you! I appreciate Hayden, Karl, Matt and Jon for proofreading my dissertation. Thank you, Bryan, for collecting ultrafast TA on the cages, doing so many calculations, and always being willing to be a scientific sounding board. Thank you all for being wonderful labmates.

Thank you to everyone at the dojo for reminding me that friendship, learning, and cooperation is always the better route.

Finally, I'd like to thank my family for their unwavering support, none of this would have been possible, or hold the same significance, without you.

TABLE OF CONTENTS

LIST OF TABLES

LIST OF FIGURES

KEY TO ABBREVIATIONS

2-Cl-phen: 2-chloro-1,10-phenanthroline

2-Me-phen: 2-methyl-1,0-phenanthroline

2-OMe-phen: 2-methoxy-1,10-phenanthroline

2-pycarb: 2-pyridinecarboxaldehyde

6-Me-2-pycarb: 6-methyl-2-pyridinecarboxaldehyde

A: frequency factor

AgOTf: silver triflate

Bpy: 2,2'-bipyridine

CCDC: Cambridge Crystallographic Data Centre

$CHCl_3$: chloroform

$Cr(acac)_3$: tris(acetylacetonate)chromium(III)

DC: direct current

DCM: dichloromethane

DFT: density functional theory

DMF: dimethylformamide

DSSC: dye-sensitized solar cell

E_a: activation energy

E_{ox}: electrochemical oxidation potential

eq.: equation

Et_2O: diethyl ether

EtOAc: ethyl acetate

EtOH: ethanol

FC: Franck-Condon factor

Fc/Fc^{+}: ferrocene/ferrocenium couple

FFT: fast Fourier transform

GS: ground-state

GSR: ground-state recovery

$\hbar\omega$: oscillation frequency

H_{ab}: electronic coupling constant

HOMO: highest-occupied molecular orbital

HS: high-spin

IRF: instrument response function

ISC: inter-system crossing

k_B: Boltzmann constant

K_{eq}: equilibrium constant

K_{HL}: equilibrium constant describing the high- to low-spin conversion

k_{HL}: rate constant for the high- to low-spin conversion

K_{LH}: equilibrium constant describing the low- to high-spin conversion

k_{LH}: rate constant for the low- to high-spin conversion

k_{nr}: rate of nonradiative decay

k_{obs}: observed rate constant

k_r: rate of radiative decay

LF: ligand field

LMCT: ligand-to-metal charge transfer

LPSVD: linear predictive singular value decomposition

LS: low-spin

MeCN: acetonitrile

MeOH: methanol

MLCT: metal-to-ligand charge transfer

NH_4OH: ammonium hydroxide

OLED: organic light-emitting diode

Phen: 1,10-phenanthroline

Ppy: 2-phenylpyridine

SCO: spin-crossover

S_M: Huang-Rhys factor

T: temperature

$T_{1/2}$: temperature at which the concentration of high- and low-spin population is equal

Terpy: 2,2':6,2"-terpyridine

THF: tetrahydrofuran

TPAA: tris[N-(2-pyridylmethyl)-2-aminoethyl]amine

Tren: tris(2-aminoethyl)amine

$Tren(py)_3$: tris(2-tris(2-pyridin-2-ylmethylene)amino)ethyl)amine

VT: variable temperature

VT-TA: variable-temperature transient absorption

γ_{HS}: mole fraction of high-spin population

γ_{LS}: mole fraction of low-spin population

ΔA: change in absorbance

$\Delta G°$: change in free energy

ΔH: change in enthalpy

Δ_O: ligand-field splitting parameter

ΔQ: geometric displacement along a nuclear coordinate

$\Delta Q_{LF/GS}$: geometric displacement between the $^5T_2$ ligand-field excited state and $^1A_1$ ground state

$\Delta Q_{MLCT/GS}$: geometric displacement between the ^{3}MLCT and $^1A_1$ ground state

$\Delta Q_{MLCT/LF}$: geometric displacement between the ^{3}MLCT and $^5T_2$ excited state

ΔS: change in entropy

$\Delta\Delta G°$: change in free energy differences

λ: reorganization energy

λ_i: innter-sphere reorganization energy

λ_o: outer-sphere reorganization energy

λ_{probe}: probe wavelength

λ_{pump}: pump wavelength

μ_{eff}: effective magnetic moment

Φ_r: radiative quantum yield

χT: magnetic susceptibility

χT_{HS}: magnetic susceptibility of a spin-crossover complex with 100% high-spin population

χT_{LS}: magnetic susceptibility of a spin-crossover complex with 100% low-spin population

CHAPTER 1. CHALLENGES TO USING EARTH-ABUNDANT FE(II) CHROMOPHORES IN LIGHT-INDUCED ELECTRON TRANSFER TRANSFORMATIONS

1.1. Introduction

Sunlight is an abundant and inexhaustible energy resource. In two hours, the amount of energy that strikes the Earth in the form of sunlight is greater than the total amount of energy consumed worldwide in 2017, and the sun will persist for another 4 billion years.[1–3] Facing overwhelming evidence that carbon dioxide emissions from the combustion of fossil fuels are raising the global average temperatures,[4] the need has never been greater to convert sunlight into useable and carbon neutral energy.[5] One of the most inspiring chemical models for transforming sunlight into energy is found in Nature: photosynthesis. In this process, the absorption of photons is crucial to generating a transmembrane potential gradient that ultimately harnesses the sun's radiant energy in the form of chemical bonds.[6] Compelled by these fundamental features of photosynthesis, chemists have long sought to exploit the photo-induced charge-separated excited states of molecular chromophores to drive energetically uphill transformations.

Transition metal chromophores have proven to be excellent platforms to explore the prospects of charge-separated excited states. Under certain conditions molecules of this class are

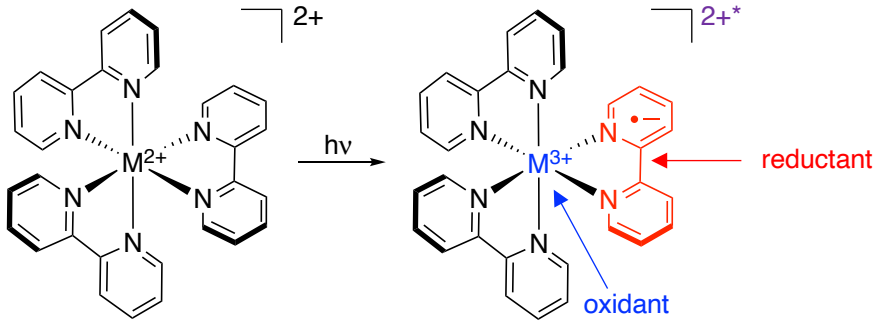

Figure 1.1. Scheme showing a metal-to-ligand charge transfer (MLCT) excited state in a theoretical transition metal polypyridyl chromophore.

capable of strongly absorbing visible light to generate ligand-to-metal and metal-to-ligand charge transfer (LMCT and MLCT) excited states. A general transition metal chromophore with π-accepting ligands is drawn in Figure 1.1. Upon absorption of a photon, this theoretical molecule populates a MLCT excited state, in which the metal center is formally oxidized and the ligand is reduced. From this charge-separated excited state, the complex can act either as an oxidant (from the metal center) or a reductant (from the reduced ligand), allowing for the possibility of electron-transfer reactivity that was not feasible in the ground state. The optical and redox properties of the ground and excited states can be tuned through synthetic modification of the ligands, providing the option of tailoring to meet the demands of specific applications.

The original workhorses that proved the utility of MLCT excited states are ruthenium(II) and iridium(III) polypyridyl chromophores. Coordination compounds of these d^6 transition metals with strong-field π-accepting ligands tend to absorb visible light to populate long-lived and emissive ^{3}MLCT excited states.[7,8] Two representative chromophores, $[Ru(bpy)_3]^{2+}$ and $Ir(ppy)_3$ are shown in Figure 1.2. As second- and third-row transition metals, the ligand-field (LF) strengths of Ru and Ir are relatively high, destabilizing metal-centered LF excited states to make them energetically inaccessible during excited-state evolution. Accordingly, in both $[Ru(bpy)_3]^{2+}$ and $Ir(ppy)_3$ the lowest-energy excited states are predominantly ^{3}MLCT in character and typically exhibit excited-state lifetimes on the order of microseconds, as summarized in the Jablonski diagrams in Figure 1.2.[9,10] Coupled with the ability to modify ground- and excited-state properties via ligand design, this excited-state behavior has encouraged the use of Ru(II)- and Ir(III)-based chromophores in an expansive array of light-induced electron transfer applications, including solar energy conversion,[11–13] solar fuel generation,[3,14] and photoredox catalysis for the synthesis of organic building blocks.[15,16] It should be noted that there are some organic chromophores that have

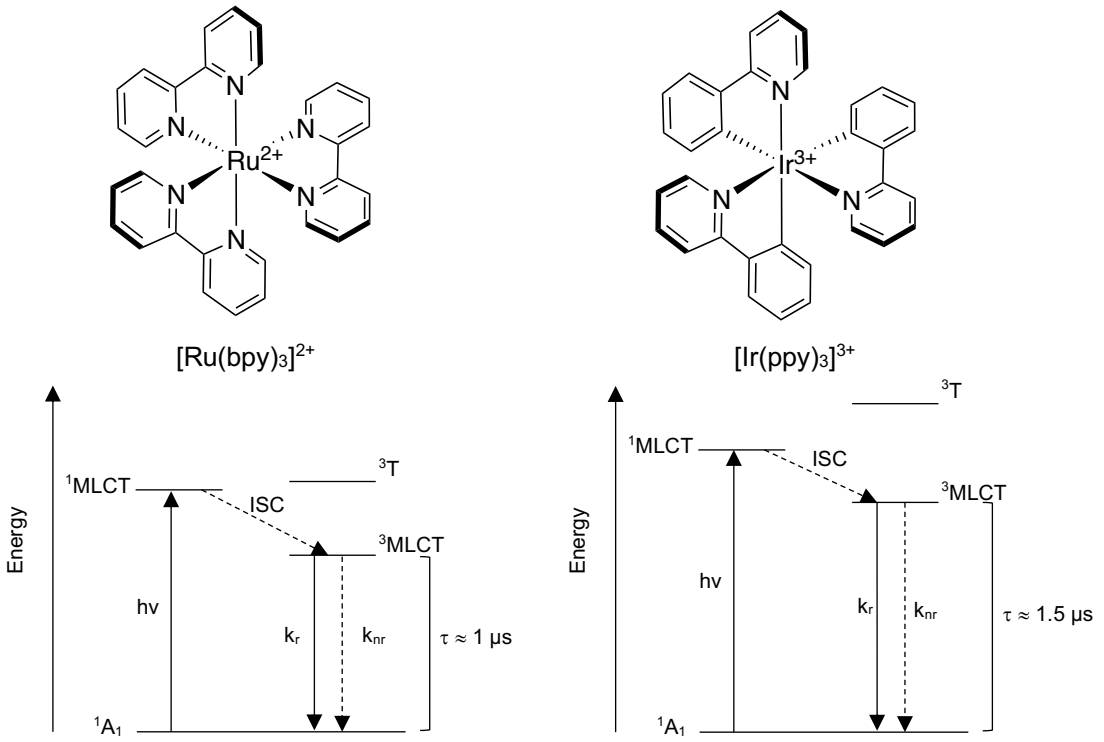

Figure 1.2. Drawings of two of the most well-studied transition metal chromophores, $[Ru(bpy)_3]^{2+}$ and $[Ir(ppy)_3]^{3+}$, along with their general Jablonski diagrams, where ISC = intersystem crossing, k_r and k_{nr} are radiative and nonradiative rates, respectively. Note: these drawings are not to scale and the given excited-state lifetimes are approximately average values found in the literature for the complexes in solution at room temperature.

been used in solar harvesting and photoredox catalysis, but transition metal chromophores tend to be more stable and have access to more synthetically-tunable photophysics.[3]

One glaring issue with the extensive use of Ru(II) and Ir(III), however, is the fact that these elements are some of the rarest on Earth (Figure 1.3).[17] For light-induced electron transfer applications that are material-intensive, the low abundance of these elements raises a major obstacle to their widespread scalability. On the other hand, first-row transition metals are orders of magnitude more plentiful than their second- and third-row congeners. As such, the last decade has witnessed a surge in investigations into the capability of first-row transition metals to replace these exotic elements.[18]

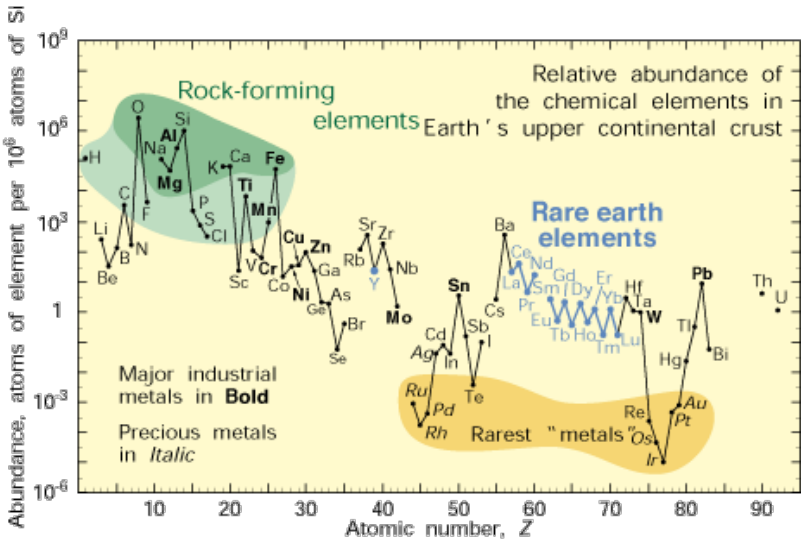

Figure 1.3. Abundance (atom fraction) of the chemical elements in Earth's upper continental crust as a function of atomic number. From reference 17.

Unfortunately, there is a fundamental barrier to using earth-abundant transition metals in applications which require long-lived charge-transfer excited-state lifetimes. Due to the primogenic effect,[19,20] the radial extension of the *d*-orbitals in first-row transition metals is contracted compared to the later series transition metals. This attenuates the metal-ligand orbital overlap in complexes with first-row versus second- and third-row transition metals, decreasing the effective LF strength.[21] As a result, metal-centered LF excited states are stabilized, and in contrast to what is observed in Ru(II) and Ir(III) chromophores (Figure 1.2), the lowest-energy excited states in first-row transition metal complexes tend to be LF in nature. These metal-centered states provide a deactivation pathway for the highly-desirable charge-transfer excited states, shortening their lifetimes and severely hampering the use of first-row transition metal complexes in photo-induced electron transfer reactions.

Nonetheless, there are some promising results using first-row transition metals in photoredox applications. By far, the most successful endeavors have employed Cu(I), as its d^{10} electron count eliminates the possibility of LF excited states. Correspondingly, Cu(I) polypyridyl complexes can have long-lived and emissive ^{3}MLCT excited-states, which have been exploited in

dye-sensitized solar cells, OLEDs, and photoredox catalysis.[22–26] Encouraging results are emerging from the use of chelating isocyanide ligands with Mo(0) and Cr(0). These $3d^6$ complexes have relatively long-lived (~1 μs and 2 ns, respectively) and room-temperature emissive ^{3}MLCT excited-states,[27] and the Mo(0) complexes have catalyzed base-promoted homolytic aromatic substitution reactions.[28] Work is also underway to tap into light-induced reactivity from LF excited-states,[29] yet formidable hurdles remain due to their metal-localized nature and impediments towards energetic tuning.[30]

Iron is an attractive alternative to rare second- and third-row transition metals, as it is highly abundant (Figure 1.3) and when sufficiently strong-field ligands are employed, Fe(II) adopts a low-spin d^6 configuration ($^1A_1$), isoelectronic to its group eight congener, Ru(II).[31] Despite the similarities in ground-state electronics, it has long been recognized that the excited-state dynamics of $[Fe(bpy)_3]^{2+}$ and $[Ru(bpy)_3]^{2+}$ are very different. In 1980, Creutz et al. monitored the transient absorption spectra of the two complexes in solution following visible excitation.[32] They observed that, while the excited state of $[Ru(bpy)_3]^{2+}$ absorbed visible light, the transient absorption spectrum of $[Fe(bpy)_3]^{2+}$ only exhibited ground-state bleaching (negative ΔA) over the entire visible region. Combined with the fact that no luminescence was observed in $[Fe(bpy)_3]^{2+}$, these results prompted the authors to assign the excited state populated at timescales longer than 10 ps as LF in nature. Since this first report, the photophysical decay cascade of low-spin Fe(II) polypyridyl chromophores has been delineated through a variety of time-resolved spectroscopic techniques and computational studies, which will be briefly summarized here.

Like $[Ru(bpy)_3]^{2+}$, $[Fe(bpy)_3]^{2+}$ absorbs visible light to populate a ^{1}MLCT excited state that rapidly (<30 fs) undergoes intersystem crossing to the ^{3}MLCT.[33,34] Unlike $[Ru(bpy)_3]^{2+}$, however, the LF strength in $[Fe(bpy)_3]^{2+}$ is weak enough that a high density of LF states are lower in energy

than the ^{1,3}MLCT excited-state manifold (Figure 1.4).[35–37] As a result, deactivation from the ^{3}MLCT to the lowest-energy excited state, the $^{5}T_2$, occurs within 150 fs,[34,38] and samples a ^{3}T intermediate.[39] No significant changes in ^{3}MLCT lifetimes of low-spin complexes have been imparted through synthetic modification of polypyridyl ligands; attempts to do so include changing ligand denticity, appending sterically bulky substituents, and imposing a near-perfect octahedral coordination environment.[40–47] Once the $^{5}T_2$ excited-state is populated, vibrational cooling occurs in ~1-10 ps.[38,40,48] Ground-state recovery occurs from this high-spin LF state on the order of nanoseconds.[49,50] The observed $^{5}T_2$ lifetimes are quite dependent on the nature of the ligands and can range from ~200 ps – 60 ns.[44,51,52]

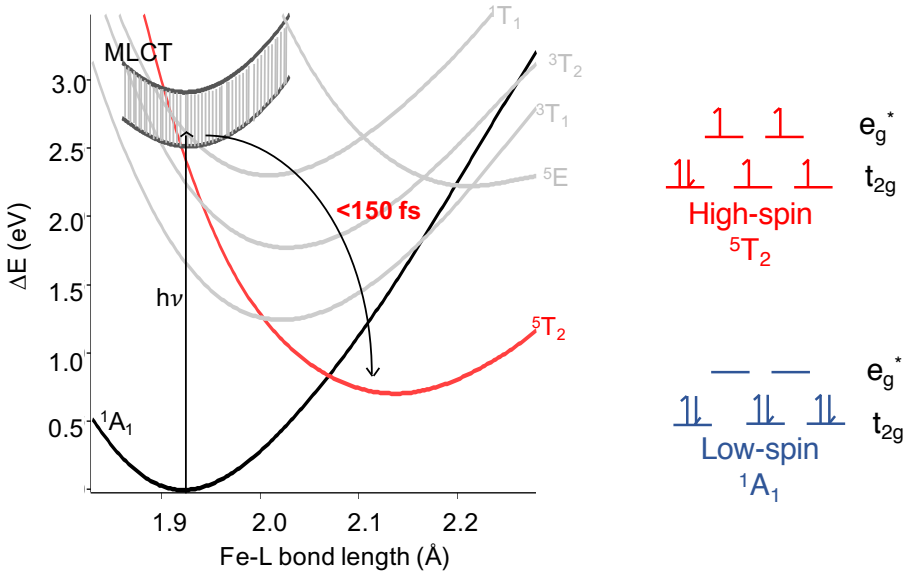

Figure 1.4. Calculated potential energy surfaces of the electronic states in $[Fe(bpy)_3]^{2+}$, reproduced from reference 35, and the occupancy of the ligand-field split *d* orbitals in high- and low-spin states.

The ultrafast ^{3}MLCT decay has been extremely prohibitive to the use of iron-based chromophores in the same types of photoinduced electron transfer applications that their Ru(II) analogs excel in, as the timescales for processes such as injection of an electron into a semi-conductor (several picoseconds) or diffusion in solution (tens of nanoseconds) for biomolecular

reactions require MLCT excited-state lifetimes orders of magnitude longer than those found in low-spin Fe(II) polypyridyl chromophores.[7,53] In spite of this handicap, Fe(II) polypyridyl-based can generate electrical current when sensitized to a semi-conductor in DSSCs.[54] These assemblies suffer from very poor power conversion efficiency (0.35 %), even under optimized conditions, a fact that has primarily been blamed on the very short lifetime of the ^{3}MLCT excited state.[55] Photoredox catalysis may be possible from the $^5T_2$ LF excited state in low-spin Fe(II) polypyridyl chromophores,[56,57] but undoubtedly attempts to extend these preliminary results will be plagued by the relatively weak photoreductant abilities, metal-centered nature, and difficult-to-tune energetics of the $^5T_2$ excited state.[58] These underwhelming examples make it clear that in order to access efficient light-induced electron transfer with Fe(II) polypyridyl chromophores, the lifetime of the ^{3}MLCT excited state must be prolonged.

Research is well underway to tackle this challenge. Work so far has largely focused on employing very strong-field ligands to destabilize metal-centered excited states and achieve low-spin Fe(II) chromophores with ^{3}MLCT lowest-energy excited-states. To date, the culmination of this work is an Fe(II) carbene complex prepared by Wärnmark and coworkers (Figure 1.5a), which exhibits a ^{3}MLCT excited-state lifetime of 528 ps with no indication of LF excited-state

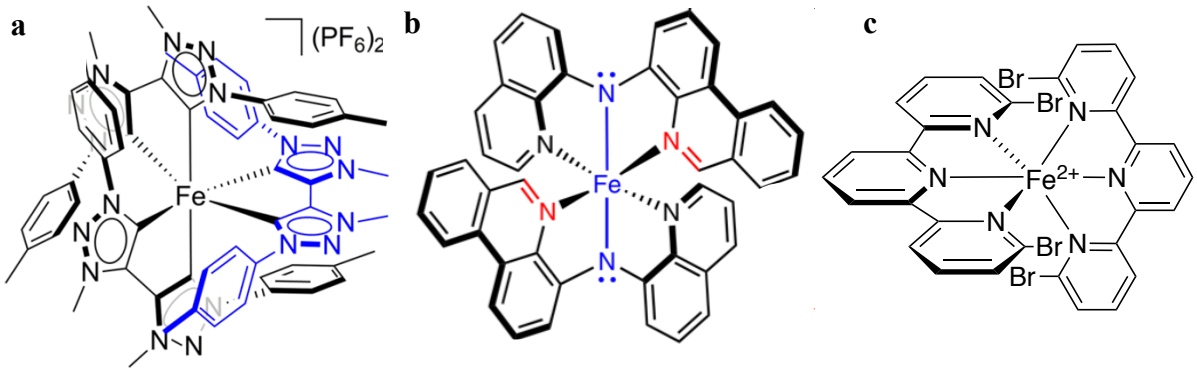

Figure 1.5. Drawings of (a) Wärnmark and coworkers' Fe(II) carbene complex (b) The Herbert group's Fe(II) complex with a mixed benzannulated phenanthridine, quinoline, and amido ligands, and (c) The Damrauer group's high-spin $[Fe(6,6''\text{-dbterpy})_2]^{2+}$ complex.

population.[59] The same group demonstrated that carbene ligands can also appreciably stabilize LMCT excited-states in Fe(III).[60] Very recently, Braun *et al* employed an elegant ligand design strategy to invert the nature of the highest-occupied molecular orbital (HOMO) of an octahedral Fe(II) complex from the metal-centered nonbonding t_{2g} orbitals to antibonding (π^*) ligand-centered orbitals. The resulting chromophore (Figure 1.5b) had a record-breaking nanosecond charge-transfer excited-state lifetime.[61] Taking a different route, the Damrauer group designed 6,6"-halogenated terpyridine ligands that stabilized the high-spin $^5T_2$ configuration as the ground electronic state. Upon the absorption of visible light, $[Fe(6,6"\text{-dbterpy})_2]^{2+}$ (Figure 1.5c) populated a ^{5,7}MLCT excited state, which exhibited a 17 ps lifetime.[62]

Unquestionably, recent strides towards achieving longer-lived ^{3}MLCT excited states in Fe(II) chromophores has made the replacement of Ru(II) and Ir(III) with earth-abundant first-row counterparts much more feasible now than a decade ago. This progress is thanks mostly to the strategy of changing the energetic landscape of Fe(II) excited states to make them more closely resemble that of Ru(II). However, one tactic to manipulate the photophysical properties of Fe(II) polypyridyl chromophores has been relatively unexplored: hindering the geometric changes (vibrational modes) coupled to MLCT deactivation into lower-lying LF excited states. In essence, this is a kinetic, rather than energetic, approach to this problem.

There is precedence that targeting kinetically relevant vibrational modes through ligand design can favorably impact the photophysics of first-row transition metal chromophores. For instance, a slew of time-resolved spectroscopic techniques revealed that tetrahedral Cu(I) polypyridyl complexes undergo a dynamic Jahn-Teller flattening distortion to a pseudo-square planar geometry in their ^{1}MLCT excited-states, essentially wasting potential energy due to this large structural reorganization.[22] To eliminate this problem, researchers installed bulky

substituents onto the polypyridyl ligands to disrupt this problematic flattening distortion. The result was a new generation of Cu(I) chromophores with long-lived, highly-emissive ^{3}MLCT excited-state lifetimes and greatly decreased excited-state reorganization.[26,63] In addition, it was shown decades ago that trigonal distortions are likely kinetically relevant to the $^2E \rightarrow {}^4A$ ground-state recovery process of Cr(III) chromophores.[64] Looking to extend ^{2}E excited-state lifetimes, Heinze and coworkers designed chelating ligands that were expected to hinder these trigonal distortions, and the resulting Cr(III) complex exhibited a remarkably long ^{2}E excited-state lifetime and an increased emission quantum yield compared to unhindered complexes.[65]

The first step to obtaining similarly productive results in low-spin Fe(II) systems is identifying the modes that compose the nuclear coordinate of the $^3\text{MLCT} \rightarrow {}^5T_2$ intersystem crossing. This is not straightforward, as all known Fe(II) complexes[i] are non-emissive, voiding the use of the information-rich experiment that is steady-state emission.[66] In addition, the sub-150 fs ^{3}MLCT decay kinetics require observation with very short time resolution which tends to complicate experimental setups and data interpretation.[67] Auböck and Chergui used ultrafast visible and UV transient absorption spectroscopy with ~70 fs time resolution on $[Fe(bpy)_3]^{2+}$ and observed vibronic coherences that correspond to a symmetric Fe-N breathing mode in the $^5T_2$ state.[68] These findings were corroborated by Lemke *et al*, who used ultrafast optical pump/x-ray absorption probe studies on the same molecule and observed that a similar mode was coherently active during $^3\text{MLCT} \rightarrow$ LF conversion[ii] in the same molecule.[38] They proposed that low-symmetry Fe-N bond deformation modes aided the dephasing of this symmetric Fe-N breathing mode. Computational studies have also indicated that torsional modes should be considered when

[i] There has been an example of emission from a LMCT excited-state on a Fe(III) chromophore

[ii] In this study sampling of a ^{3}T ligand-field state during ^{3}MLCT decay was observed. However, the lifetime of this intermediate is so short (<70 fs) that it is not considered to be significant to the coherently observed vibrational modes past the fact that it indicates that population of the e_g^* orbitals occurs within 120 fs following excitation.

describing the ^{3}MLCT deactivation nuclear coordinate of $[Fe(bpy)_3]^{2+}$.[69] Taken together, these studies suggest that both Fe-N breathing and bending modes are kinetically significant to the $^3MLCT \rightarrow {}^5T_2$ ISC.

In contrast to the Cu(I) and Cr(III) examples, no attempts have been made to manipulate the photophysical dynamics of Fe(II) chromophores via disruption of supposedly relevant modes. Therefore, in this dissertation indirect steps will be taken to identify the vibrational modes coupled to the $^3MLCT \rightarrow {}^5T_2$ excited-state decay in Fe(II) polypyridyl chromophores and provide complimentary evidence to the results found with ultrafast studies. Once we have a firm definition of the nuclear coordinate, the identified modes will be targeted synthetically. The resulting new Fe(II) chromophores will be fully characterized to determine whether or not we were successful in our goal of disrupting the vibrational modes driving the $^3MLCT \rightarrow {}^5T_2$ conversion.

1.2. Contents of Dissertation

Chapter 2 first summarizes the findings of our 2019 *Chemical Science* report[50] on using variable-temperature ultrafast time-resolved absorption spectroscopy to gain insight on the nature of the nuclear coordinate coupled to the $^5T_2 \rightarrow {}^1A_1$ ground-state recovery process in a series of low-spin Fe(II) polypyridyl chromophores. Then, these results are confirmed and expanded upon by investigating the ground-state recovery dynamics in a polypyridyl Fe(II) spin-crossover complex. This same spin-crossover complex is the main focus of Chapter 3, in which two nonradiative decay theories are used to determine the average frequency of the vibrational mode(s) coupled to the $^5T_2 \rightarrow {}^1A_1$ conversion. Additionally, a ruthenium(II) analog of the spin-crossover complex is used to approximate the geometic distortions associated with formation of the ^{3}MLCT excited state. These two analyses will serve as the basis of computational work to determine how these two nuclear coordinates intersect. Chapter 4 explains how the findings of

the previous chapters inspired the exploration of Fe(II) chromophores with sterically hindered polypyridyl ligand frameworks. This chapter describes the synthesis and photophysical characterization of a new class of iron(II) chromophores with macrocyclic ligands. Finally, Chapter 5 discusses the future directions spawned by the research presented in this dissertation.

REFERENCES

REFERENCES

1. Tsao, J.; Lewis, N.; Crabtree, G. Solar FAQs; 2006.

2. BP Statistical Review of World Energy; 2018.

3. Armaroli, N.; Balzani, V. Solar Electricity and Solar Fuels: Status and Perspectives in the Context of the Energy Transition. *Chem. Eur. J.* **2016**, *22*, 32–57. https://doi.org/10.1002/chem.201503580.

4. Intergovernmental Panel on Climate Change (IPCC). Climate Change 2014: Synthesis Report. Contribution of Working Groups I, II and III to the Fifth Assessment Report of the Intergovernmental Panel on Climate Change; Geneva, Switzerland, 2014.

5. Lewis, N. S. Aspects of Science and Technology in Support of Legal and Policy Frameworks Associated with a Global Carbon Emissions-Control Regime. *Energy Environ. Sci*. **2016**, *9*, 2172–2176. https://doi.org/10.1039/c6ee00272b.

6. Dogutan, D. K.; Nocera, D. G. Artificial Photosynthesis at Efficiencies Greatly Exceeding That of Natural Photosynthesis. *Acc. Chem. Res.* **2019**, *52*, 3143–3148. https://doi.org/10.1021/acs.accounts.9b00380.

7. Juris, A.; Balzani, V.; Barigelletti, F.; Campagna, S.; Belser, P.; Von Zelewsky, A. Ru(II) Polypyridine Complexes: Photophysics, Photochemistry, Electrochemistry, and Chemiluminescence. *Coord. Chem. Rev*. **1988**, *84,* 85–277.

8. Deaton, J. C.; Castellano, F. N. Archetypal Iridium(III) Compounds for Optoelectronic and Photonic Applications. In *Iridium(III) in Optoelectronic and Photonics Applications*; Zysman-Colman, E., Ed.; John Wiley & Sons, 2017; pp 1–69. https://doi.org/10.1002/9781119007166.ch1.

9. McCusker, C. E.; McCusker, J. K. Synthesis and Spectroscopic Characterization of CN-Substituted Bipyridyl Complexes of Ru(II). *Inorg. Chem*. **2011**, *50*, 1656–1669. https://doi.org/10.1021/ic102085b.

10. Finkenzeller, W. J.; Yersin, H. Emission of $Ir(Ppy)_3$. Temperature Dependence, Decay Dynamics, and Magnetic Field Properties. *Chem. Phys. Lett*. **2003**, *377*, 299–305. https://doi.org/10.1016/S0009-2614(03)01142-4.

11. O'Regan, B.; Grätzel, M. A Low-Cost, High-Efficiency Solar Cell Based on Dye-Sensitized Collodial TiO_2 Films. *Nature* **1991**, *353*, 737–740. https://doi.org/10.1016/0146-5724(84)90144-4.

12. Vougioukalakis, G. C.; Philippopoulos, A. I.; Stergiopoulos, T.; Falaras, P. Contributions to the Development of Ruthenium-Based Sensitizers for Dye-Sensitized Solar Cells. *Coord. Chem. Rev.* **2011**, *255*, 2602–2621. https://doi.org/10.1016/j.ccr.2010.11.006.

13. Baranoff, E.; Kumar, P. Iridium Complexes as Photoactive Center for Light Harvesting and Solar Cell Applications. In *Iridium(III) in Optoelectronic and Photonics Applications*; Zysman-Colman, E., Ed.; John Wiley & Sons, 2017; pp 655–681. https://doi.org/10.1002/9781119007166.ch14.

14. Kagalwala, H. N.; Chirdon, D. N.; Bernhard, S. Solar Fuel Generation: Structural and Functional Evolution of Iridium Photosensitizers. In *Iridium(III) in Optoelectronic and Photonics Applications*; Zysman-Colman, E., Ed.; John Wiley & Sons, 2017; pp 583–615. https://doi.org/10.1002/9781119007166.ch12.

15. Twilton, J.; Le, C. C.; Zhang, P.; Shaw, M. H.; Evans, R. W.; MacMillan, D. W. C. The Merger of Transition Metal and Photocatalysis. *Nat. Rev. Chem*. **2017**. https://doi.org/10.1038/s41570-017-0052.

16. Mills, I. N.; Porras, J. A.; Bernhard, S. Judicious Design of Cationic, Cyclometalated Ir(III) Complexes for Photochemical Energy Conversion and Optoelectronics. *Acc. Chem. Res.* **2018**, *51*, 352–364. https://doi.org/10.1021/acs.accounts.7b00375.

17. Geological Survey, U. Rare earth elements - critical resources for high technology https://pubs.usgs.gov/fs/2002/fs087-02/ (accessed Jan 22, 2020).

18. Wenger, O. S. Photoactive Complexes with Earth-Abundant Metals. *J. Am. Chem. Soc.* **2018**, *140*, 13522–13533. https://doi.org/10.1021/jacs.8b08822.

19. Pyykkö, P. Relativistic Effects in Structural Chemistry. *Chem. Rev*. **1988**, *88*, 563–594. https://doi.org/10.1021/cr00085a006.

20. Kaupp, M. The Role of Radial Nodes of Atomic Orbitals for Chemical Bonding and the Periodic Table. *J. Comput. Chem.* **2007**, *28*, 320–325. https://doi.org/10.1002/jcc.20522.

21. McCusker, J. K. Electronic Structure in the Transition Metal Block and Its Implications for Light Harvesting. *Science* **2019**, *363*, 484–488. https://doi.org/10.1126/science.aav9104.

22. Iwamura, M.; Takeuchi, S.; Tahara, T. Ultrafast Excited-State Dynamics of Copper(I) Complexes. *Acc. Chem. Res*. **2015**, *48*, 782–791. https://doi.org/10.1021/ar500353h.

23. Housecroft, C. E.; Constable, E. C. The Emergence of Copper(I)-Based Dye Sensitized Solar Cells. *Chem. Soc. Rev.* **2015**, *44*, 8386–8398. https://doi.org/10.1039/c5cs00215j.

24. Lazorski, M. S.; Castellano, F. N. Advances in the Light Conversion Properties of Cu(I)-Based Photosensitizers. *Polyhedron* **2014**, *82*, 57–70. https://doi.org/10.1016/j.poly.2014.04.060.

25. Czerwieniec, R.; Leitl, M. J.; Homeier, H. H. H.; Yersin, H. Cu(I) Complexes – Thermally Activated Delayed Fluorescence. Photophysical Approach and Material Design. *Coord. Chem. Rev*. **2016**, *325*, 2–28. https://doi.org/10.1016/j.ccr.2016.06.016.

26. Hossain, A.; Bhattacharyya, A.; Reiser, O. Copper's Rapid Ascent in Visible-Light Photoredox Catalysis. *Science* **2019**, *364*, 450–461. https://doi.org/10.1126/science.aav9713.

27. Büldt, L. A.; Wenger, O. S. Chromium(0), Molybdenum(0), and Tungsten(0) Isocyanide Complexes as Luminophores and Photosensitizers with Long-Lived Excited States. *Angew. Chemie Int. Ed*. **2017**, *56*, 5676–5682. https://doi.org/10.1002/anie.201701210.

28. Herr, P.; Glaser, F.; Büldt, L. A.; Larsen, C. B.; Wenger, O. S. Long-Lived, Strongly Emissive, and Highly Reducing Excited States in Mo(0) Complexes with Chelating Isocyanides. *J. Am. Chem. Soc.* **2019**, *141*, 14394–14402. https://doi.org/10.1021/jacs.9b07373.

29. Glaser, F.; Wenger, O. S. Recent Progress in the Development of Transition-Metal Based Photoredox Catalysts. *Coord. Chem. Rev*. **2020**, *405*, 213129. https://doi.org/10.1016/j.ccr.2019.213129.

30. Juban, E. A.; Smeigh, A. L.; Monat, J. E.; McCusker, J. K. Ultrafast Dynamics of Ligand-Field Excited States. *Coord. Chem. Rev*. **2006**, *250* (13–14), 1783–1791. https://doi.org/10.1016/j.ccr.2006.02.010.

31. Wenger, O. S. Is Iron the New Ruthenium? *Chem. Eur. J*. **2019**, *25* (24), 6043–6052. https://doi.org/10.1002/chem.201806148.

32. Creutz, C.; Chou, M.; Netzel, T. L.; Okumura, M.; Sutin, N. Lifetimes, Spectra, and Quenching of the Excited States of Polypyridine Complexes of Iron(II), Ruthenium(II), and Osmium(II). *J. Am. Chem. Soc.* **1980**, *102*, 1309–1319. https://doi.org/10.1021/ja00524a014.

33. Cannizzo, A.; Van Mourik, F.; Gawelda, W.; Zgrablic, G.; Bressler, C.; Chergui, M. Broadband Femtosecond Fluorescence Spectroscopy of $[Ru(bpy)_3]^{2+}$. *Angew. Chemie - Int. Ed.* **2006**, *45* (19), 3174–3176. https://doi.org/10.1002/anie.200600125.

34. Gawelda, W.; Cannizzo, A.; Pham, V.-T.; van Mourik, F.; Bressler, C.; Chergui, M.; Mourik, F. Van; Bressler, C.; Chergui, M. Ultrafast Nonadiabatic Dynamics of $[Fe^{II}(bpy)_3)]^{2+}$ in Solution. *J. Am. Chem. Soc.* **2007**, *129* (26), 8199–8206. https://doi.org/10.1021/ja070454x.

35. De Graaf, C.; Sousa, C. Study of the Light-Induced Spin Crossover Process of the $[Fe^{II}(Bpy)_3]^{2+}$ Complex. *Chem. Eur. J.* **2010**, *16* (15), 4550–4556. https://doi.org/10.1002/chem.200903423.

36. Pàpai, M.; Vankó, G.; Graaf, C. De; Rozgonyi, T. Theoretical Investigation of the Electronic Structure of Fe(II) Complexes at Spin-State Transitions. *J. Chem. Theory Comput*. **2013**, *9*, 509–519. https://doi.org/10.1021/ct300932n.

37. Sousa, C.; De Graaf, C.; Rudavskyi, A.; Broer, R.; Tatchen, J.; Etinski, M.; Marian, C. M. Ultrafast Deactivation Mechanism of the Excited Singlet in the Light-Induced Spin Crossover of $[Fe(2,2\text{-Bipyridine})_3]^{2+}$. *Chem. Eur. J.* **2013,** *19* (51), 17541–17551. https://doi.org/10.1002/chem.201302992.

38. Lemke, H. T.; Kjær, K. S.; Hartsock, R.; van Driel, T. B.; Chollet, M.; Glownia, J. M.; Song, S.; Zhu, D.; Pace, E.; Matar, S. F.; et al. Coherent Structural Trapping through Wave Packet Dispersion during Photoinduced Spin State Switching. *Nat. Commun*. **2017**, *8*, 15342.

39. Zhang, W.; Alonso-Mori, R.; Bergmann, U.; Bressler, C.; Chollet, M.; Galler, A.; Gawelda, W.; Hadt, R. G.; Hartsock, R. W.; Kroll, T.; et al. Tracking Excited-State Charge and Spin Dynamics in Iron Coordination Complexes. *Nature* **2014**, *509* (7500), 345–348. https://doi.org/10.1038/nature13252.

40. Monat, J. E.; McCusker, J. K. Femtosecond Excited-State Dynamics of an Iron(II) Polypyridyl Solar Cell Sensitizer Model. *J. Am. Chem. Soc*. **2000**, *122* (17), 4092–4097. https://doi.org/10.1021/ja992436o.

41. Smeigh, A. L. Ultrafast Dynamics Associated with Transition Metal-Based Sensitizers for Titanium Dioxide Based Solar Cells, PhD Dissertation, Michigan State University, East Lansing, MI, 2007.

42. Jamula, L. L. Design and Synthesis of Iron(II) Terpyridyl Complexes for Application in Dye-Sensitized Solar Cells, Master's Thesis, Michigan State University, East Lansing, MI, 2010.

43. Brown, A. M. Excited-State Dynamics of Iron(II)-Based Charge Transfer Chromophores, PhD Dissertation, Michigan State University, East Lansing, MI, 2011.

44. Jamula, L. L.; Brown, A. M.; Guo, D.; McCusker, J. K. Synthesis and Characterization of a High-Symmetry Ferrous Polypyridyl Complex: Approaching the $^5T_2/^3T_1$ Crossing Point for Fe^{II}. *Inorg. Chem*. **2014***, 53*, 15–17. https://doi.org/10.1021/ic402407k.

45. Miller, J. N. Ultrafast Dynamics of Iron(II)-Based Complexes in Solution and Semiconductor-Chromophore Assemblies, PhD Dissertation, Michigan State University, East Lansing, MI, 2018.

46. Carey, M. C. Achieving a Long-Lived Charge-Separated Fe(II) Chromophore: Insights into the Role of Reorganization Energy on the Ultrafast Photophysical Processes of d^6 Polypyridyl Complexes, PhD Dissertation, Michigan State University, East Lansing, MI, 2018.

47. Zhang, K.; Ash, R.; Girolami, G. S.; Vura-Weis, J. Tracking the Metal-Centered Triplet in Photoinduced Spin Crossover of $[Fe(phen)_3]^{2+}$ with Tabletop Femtosecond M-Edge X-Ray Absorption Near-Edge Structure Spectroscopy. *J. Am. Chem. Soc*. **2019**, *141*, 17180–17188. https://doi.org/10.1021/jacs.9b07332.

48. Smeigh, A. L.; Creelman, M.; Mathies, R. A.; McCusker, J. K. Femtosecond Time-Resolved Optical and Raman Spectroscopy of Photoinduced Spin Crossover: Temporal Resolution of Low-to-High Spin Optical Switching. *J. Am. Chem. Soc*. **2008**, *130*, 14105–14107. https://doi.org/10.1021/ja805949s.

49. McCusker, J. K.; Walda, K. N.; Dunn, R. C.; Simon, J. D.; Magde, D.; Hendrickson, D. N. Subpicosecond $^1MLCT \rightarrow {}^5T_2$ Intersystem Crossing of Low-Spin Polypyridyl Ferrous Complexes. *J. Am. Chem. Soc.* **1993**, *115*, 298–307. https://doi.org/10.1021/ja00054a043.

50. Carey, M. C.; Adelman, S. L.; McCusker, J. K. Insights into the Excited State Dynamics of Fe(II) Polypyridyl Complexes from Variable-Temperature Ultrafast Spectroscopy. *Chem. Sci*. **2019**, *10*, 134–144. https://doi.org/10.1039/C8SC04025G.

51. Xie, C. L.; Hendrickson, D. N. Mechanism of Spin-State Interconversion in Ferrous Spin-Crossover Complexes: Direct Evidence for Quantum Mechanical Tunneling. *J. Am. Chem. Soc*. **1987**, *109*, 6981–6988. https://doi.org/10.1021/ja00257a013.

52. Britz, A.; Gawelda, W.; Assefa, T. A.; Jamula, L. L.; Yarranton, J. T.; Galler, A.; Khakhulin, D.; Diez, M.; Harder, M.; Doumy, G.; et al. Using Ultrafast X-Ray Spectroscopy to Address Questions in Ligand-Field Theory: The Excited State Spin and Structure of $[Fe(dcpp)_2]^{2+}$. *Inorg. Chem*. **2019**, *58*, 9341–9350. https://doi.org/10.1021/acs.inorgchem.9b01063.

53. Ardo, S.; Meyer, G. J. Photodriven Heterogeneous Charge Transfer with Transition-Metal Compounds Anchored to TiO_2 Semiconductor Surfaces. *Chem. Soc. Rev.* **2009,** *38*, 115–164. https://doi.org/10.1039/b804321n.

54. Ferrere, S.; Gregg, B. A. Photosensitization of TiO_2 by $[Fe^{II}$(2,2'-Bipyridine-4,4'-Dicarboxylic Acid)$_2(CN)_2]$: Band Selective Electron Injection from Ultra-Short-Lived Excited States. *J. Am. Chem. Soc.* **1998**, *120*, 843–844. https://doi.org/10.1021/ja973504e.

55. Tichnell, C. R.; Miller, J. N.; Liu, C.; Mukherjee, S.; Jakubikova, E.; Mccusker, J. K. Influence of Electrolyte Composition on Ultrafast Interfacial Electron Transfer in Fe-Sensitized TiO_2-based Solar Cells. *J. Phys. Chem. C* **2020**, *124*, 1794-1811. https://doi.org/10.1021/acs.jpcc.9b09404.

56. Gualandi, A.; Marchini, M.; Mengozzi, L.; Natali, M.; Lucarini, M.; Ceroni, P.; Cozzi, P. G.; Chimiche, S.; Ferrara, U. Organocatalytic Enantioselective Alkylation of Aldehydes with $[Fe(bpy)_3]Br_2$ Catalyst and Visible Light. *ACS Catal*. **2015**, *5*, 5927–5931. https://doi.org/10.1021/acscatal.5b01573.

57. Woodhouse, M. D.; McCusker, J. K. *Manuscript in preparation*.

58. Ashley, D. C.; Jakubikova, E. Tuning the Redox Potentials and Ligand Field Strength of Fe(II) Polypyridines: The Dual π-Donor and π-Acceptor Character of Bipyridine. *Inorg. Chem.* **2018**, *57*, 9907–9917. https://doi.org/10.1021/acs.inorgchem.8b01002.

59. Chábera, P.; Kjaer, K. S.; Prakash, O.; Honarfar, A.; Liu, Y.; Fredin, L. A.; Harlang, T. C. B.; Lidin, S.; Uhlig, J.; Sundström, V.; et al. Fe^{II} Hexa N-Heterocyclic Carbene Complex with a 528 ps Metal-To-Ligand Charge-Transfer Excited-State Lifetime. *J. Phys. Chem. Lett.* **2018**, *9*, 459–463. https://doi.org/10.1021/acs.jpclett.7b02962.

60. Kjær, K. S.; Kaul, N.; Prakash, O.; Chábera, P.; Rosemann, N. W.; Honarfar, A.; Gordivska, O.; Fredin, L. A.; Bergquist, K. E.; Häggström, L.; et al. Luminescence and Reactivity of a Charge-Transfer Excited Iron Complex with Nanosecond Lifetime. *Science* **2019,** *363*, 249–253. https://doi.org/10.1126/science.aau7160.

61. Braun, J. D.; Lozada, I. B.; Kolodziej, C.; Burda, C.; Newman, K. M. E.; van Lierop, J.; Davis, R. L.; Herbert, D. E. Iron(II) Coordination Complexes with Panchromatic Absorption and Nanosecond Charge-Transfer Excited State Lifetimes. *Nat. Chem*. **2019**, *11*, 1144-1150. https://doi.org/10.1038/s41557-019-0357-z.

62. Fatur, S. M.; Shepard, S. G.; Higgins, R. F.; Shores, M. P.; Damrauer, N. H. A Synthetically Tunable System to Control MLCT Excited-State Lifetimes and Spin States in Iron(II) Polypyridines. *J. Am. Chem. Soc*. **2017**, *139*, 4493–4505. https://doi.org/10.1021/jacs.7b00700.

63. Garakyaraghi, S.; McCusker, C. E.; Khan, S.; Koutnik, P.; Bui, A. T.; Castellano, F. N. Enhancing the Visible-Light Absorption and Excited-State Properties of Cu(I) MLCT Excited States. *Inorg. Chem*. **2018**, *57*, 2296–2307. https://doi.org/10.1021/acs.inorgchem.7b03169.

64. Endicott, J. E.; Perkovie, M. W.; Heeg, M. J.; Ryu, C. K.; Thompson, D. Ligand-Induced, Stereochemical Relaxation of Electronic Constraints in a Simple Chemical Process Examples from Hexaam(m)Ine Cr(III) Photophysics. In *Advances in Chemistry Series*; 1997; Vol. 253, pp 199–220. https://doi.org/10.1021/ba-1997-0253.ch012.

65. Treiling, S.; Wang, C.; Förster, C.; Reichenauer, F.; Kalmbach, J.; Boden, P.; Harris, J. P.; Carrella, L. M.; Rentschler, E.; Resch-Genger, U.; et al. Luminescence and Light-Driven Energy and Electron Transfer from an Exceptionally Long-Lived Excited State of a Non-Innocent Chromium(III) Complex. *Angew. Chemie - Int. Ed.* **2019**, 18075–18085. https://doi.org/10.1002/anie.201909325.

66. Claude, J. P.; Meyer, T. J. Temperature Dependence of Nonradiative Decay. *J. Phys. Chem.* **1995**, *99*, 51–54. https://doi.org/10.1021/j100001a010.

67. Collet, E.; Cammarata, M. Disentangling Ultrafast Electronic and Structural Dynamics with X-Ray Lasers. *Chem. Eur. J.* **2018**, *24*, 15696–15705. https://doi.org/10.1002/chem.201802105.

68. Auböck, G.; Chergui, M. Sub-50-Fs Photoinduced Spin Crossover in $[Fe(bpy)_3]^{2+}$. *Nat. Chem*. **2015**, *7*, 629–633. https://doi.org/10.1038/nchem.2305.

69. Ashley, D. C.; Jakubikova, E. Ray-Dutt and Bailar Twists in Fe(II)-Tris(2,2′-Bipyridine): Spin States, Sterics, and Fe–N Bond Strengths. *Inorg. Chem.* **2018**, *57*, 5585–5596. https://doi.org/10.1021/acs.inorgchem.8b00560.

CHAPTER 2. EXPERIMENTAL DETERMINATION OF THE MARCUS PARAMETERS FOR GROUND-STATE RECOVERY IN AN IRON(II) SPIN-CROSSOVER COMPLEX

2.1. Introduction[iii,iv]

Ideally, the first step in tackling the kinetic approach outlined in the first chapter of this dissertation is to identify the vibrational modes that describe the geometric distortions coupled to the ^{1,3}MLCT $\rightarrow$ $^{5}T_2$ intersystem crossing (ISC) in low-spin (LS) iron(II) polypyridyl chromophores. However, the ultrafast ^{3}MLCT excited-state lifetime (<150 fs) in most low-spin Fe(II) polypyridyls introduces substantial theoretical and technical barriers to directly extracting this information from traditional experiments. Therefore, I will first focus on defining the geometric changes associated with ground-state recovery (GSR), i.e. the $^{5}T_2 \rightarrow {}^{1}A_1$ conversion, which occurs typically on the order of nanoseconds.[1] Characterizing the geometric and electronic parameters associated with GSR is also of interest to the recent push to exploit this process for the indirect monitoring of magnetic storage information.[2,3]

For transition metal chromophores, there have been several methods developed to describe the nuclear coordinates involved in excited-state decay. In emissive complexes, fitting of emission profiles with vibronic fine structure to a Franck-Condon analysis can in general cleanly yield $\hbar\omega$, the averaged frequency of the mode(s) coupled to the emissive process.[4] Another option is resonance Raman, where the vibrational modes that occur concurrently with an optical transition

[iii] Some of the introduction of this chapter is also presented in the article: Carey, M. C.; Adelman, S. L.; McCusker, J. K. *Chem. Sci.* **2019**, *10*, 134-144.

[iv] The work in this chapter is a continuation of research started by Dr. Monica C. Carey. As such, an initial introduction into this work can be found in Carey, M. C. Achieving a Long-lived Charge-separated Fe(II) Chromophore: Insights into the Role of Reorganization Energy on the Ultrafast Photophysical Processes of d^6 Polypyridyl Complexes, PhD Dissertation, Michigan State University, East Lansing, MI, 2018.

can be experimentally described.[5] Both of these traditional methods are of no utility to defining the $^5T_2 \rightarrow {}^1A_1$ nuclear coordinate, as the decay of the $^5T_2$ is nonradiative and the optical signature of this transition in the ground-state absorption spectrum is usually completely obscured by $^1A_1 \rightarrow$ MLCT absorption features. Recently, there has been a growing body of work utilizing time-resolved optical pump/x-ray probe measurements with Fe(II) polypyridyl complexes.[6–10] For the $^5T_2 \rightarrow {}^1A_1$ process, the overall geometric changes between the two states can be defined, but so far determining which changes reflect kinetically relevant vibrations has been out of reach.[7] Furthermore, gaining access to the facilities which house the instruments necessary for these types of measurements can be difficult. Because of these obstacles, there has not been an undisputed assignment of specific modes that compose the GSR nuclear coordinate for LS Fe(II) polypyridyl chromophores. Due to the ~0.2 Å elongation of Fe-N bonds upon population of the $^5T_2$ state observed in several LS Fe(II) polypyridyls from steady-state[11] and time-resolved x-ray measurements,[12] the most commonly proposed candidate is a symmetric Fe-N breathing mode.[13] Yet simply because a given bond length changes during GSR does not signify that the vibrational mode associated with that distortion is coupled to the electronic transition, as it is unlikely that all of the 3N-6 possible modes for a given molecule are kinetically relevant.[14]

Therefore, to better define the electronic and nuclear parameters of the $^5T_2 \rightarrow {}^1A_1$ transition, Monica Carey and I used ultrafast variable-temperature transient absorption (VT-TA) spectroscopy to find the rate of nonradiative decay (k_{nr}) from the $^5T_2$ as a function of temperature on a series of low-spin iron(II) polypyridyl complexes.[15,16,v] The results from this work, as well as the assumptions used to arrive to conclusions about the nuclear coordinate for GSR, will be briefly summarized here, as they form the basis for the forthcoming research in this dissertation. First, k_{nr}

[v]All of the ultrafast variable-temperature transient absorption spectroscopy in the 2019 *Chem. Sci.* report was collected by Dr. Monica C. Carey.

as a function of temperature can be fit to the Arrhenius equation the activation energy (E_a) and frequency factor (A) were found from the Arrhenius relationship:

$$k_{nr} = A\exp\left\{\frac{-E_a}{k_B T}\right\} \tag{2.1}$$

where k_B is the Boltzmann constant and T is temperature. Then, a mathematical relationship between the Arrhenius model (eq. 2.1) and semi-classical Marcus theory (eq 2.2),

$$k_{nr} = \frac{2\pi}{\hbar}\left|H_{ab}\right|^2 \frac{1}{\sqrt{4\pi\lambda k_B T}}\exp\left(\frac{-(\lambda+\Delta G°)^2}{4\lambda k_B T}\right) \tag{2.2}$$

which relates k_{nr} at a given temperature to the electronic coupling matrix between the $^5T_2$ and $^1A_1$ states (H_{ab}), the $^1A_1/^5T_2$ free energy difference (ΔG°), and the reorganization energy (λ), was exploited:

$$E_a = \frac{(\lambda+\Delta G°)^2}{4\lambda} \tag{2.3}$$

$$A = \frac{2\pi}{\hbar}\left|H_{ab}\right|^2 \frac{1}{\sqrt{4\pi\lambda k_B T}} \tag{2.4}$$

The benefit of this approach is that the λ for GSR may be approximated from experimental data namely, E_a and A.

Generally, λ is the amount of energy required to change the geometry of the reactant ($^5T_2$) to the geometry of the product ($^1A_1$) without changing the electronic structure (Figure 2.1). λ reflects the change in geometry about a specific nuclear coordinate (ΔQ generally, $\Delta Q_{LF/GS}$ for the conversion from the $^5T_2$ ligand field state to the $^1A_1$ ground state):

$$\lambda = \frac{1}{2} f(\Delta Q)^2 \tag{2.5}$$

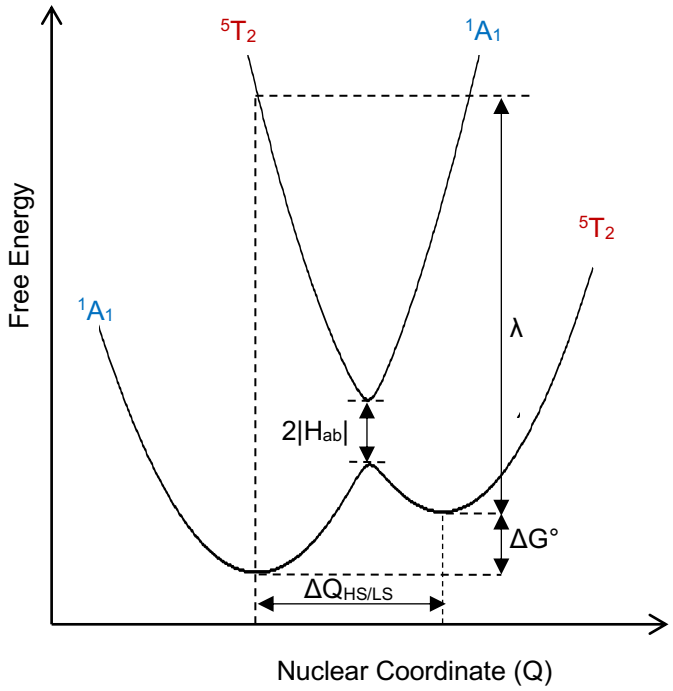

Figure 2.1. General diagram defining the pertinent Marcus variables for a low-spin Fe(II) polypyridyl complex along a unitless nuclear coordinate.

Where *f* is the force constant for the kinetically relevant vibrational mode. Thus, the reorganization energy reflects the degree of geometric distortion associated with a given electronic transition and can provide insight into similarities, or differences, between related complexes.[17] Ideally, the experimentally determined values for k_{nr} versus T would be used to unambiguously calculate λ for a series of complexes to begin to explore kinetically relevant geometric distortions for GSR. However, to explicitly solve for λ, we must also input values for either H_{ab} or ΔG°. When nonradiative decay models are applied in other transition metals, ΔG° is usually determined either from electrochemistry, an analysis of pertinent absorption features, or the emission spectral fitting mentioned above. Unfortunately, for LS Fe(II) polypyridyl complexes we are again thwarted by the previously-described lack of experimental probes to define the $^5T_2 \rightarrow {}^1A_1$ transition.

In light of these hurdles, it is clear that some approximations must be made in order to define the nuclear coordinate in LS Fe(II) complexes. One option is to calculate the $^5T_2/^1A_1$ free energy gap computationally, however current theoretical techniques are notoriously inaccurate and imprecise, and at best only trends in $\Delta\Delta G°$ can be surmised for a series of closely related complexes.[18] Therefore, we relied on a blended experimental and theoretical method to approximate $\Delta G°$ for LS Fe(II) complexes, summarized in eq. 2.6:

$$\Delta G^{\circ}_{complex} = \Delta G^{\circ}_{[Fe(bpy)_3]^{2+}} + nF\left(E^{ox}_{complex} - E^{ox}_{[Fe(bpy)_3]^{2+}}\right) \tag{2.6}$$

where we assume a value of $\Delta G°$ for a parent compound based on theoretical calculations, in this case $[Fe(bpy)_3]^{2+}$, and modulate $\Delta G°$ based off of the experimentally measured difference between the $Fe^{2+/3+}$ oxidation potential of the desired complex and that of the parent compound ($E^{ox}_{complex}$ and $E^{ox}_{[Fe(bpy)_3]^{2+}}$, respectively).

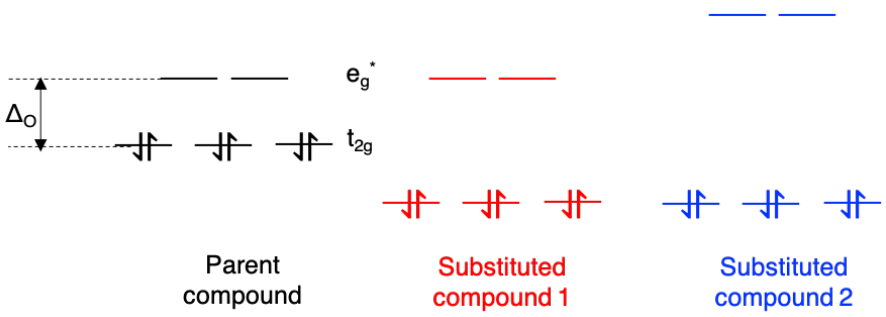

Figure 2.2. Schematic illustrating the limits of the electrochemical approximation to find $\Delta G°$ in low-spin iron(II) polypyridyl complexes.

The reasoning behind this approximation can be summarized by considering a theoretical parent compound, in which there is some ligand field splitting parameter (Δ_O) that gives rise to the free energy difference between the $^1A_1$ ground state and the lowest-energy ligand field state, the $^5T_2$ (Figure 2.2). The assumption summarized in eq. 2.6 is based on the fact that in LS Fe(II) pseudo-octahedral complexes, the oxidation potential measured electrochemically generally corresponds to the loss of an electron from the t_{2g} metal-based orbitals. So, across a series of

structurally related complexes, changes in the oxidation potential should correspond to either stabilization (shown in Figure 2.2 as "substituted compound 1") or destabilization of the t_{2g} orbitals, which results in a corresponding modulation of $\Delta G°$. However, the shortcomings of this approximation are clear for cases such as "substituted compound 2" in Figure 2.2. Using eq. 2.6, $\Delta G°$ of the two substituted compounds would be calculated as equal, despite the value of $\Delta G°$ actually being larger for compound 2. This highlights the fact that electronic effects due to σ-interactions are "invisible" electrochemically. The Jakubikova group has recently shown computationally that for Fe(II) chromophores with bipyridine-based ligands, π-interactions do tend to outweigh the effects of σ-interactions in overall impact on ligand-field strength,[19] however the inability for electrochemistry to assess these effects is a clear limitation to our electrochemical approximation of $\Delta G°$. Furthermore, electron-electron repulsion effects are neglected by eq. 2.6.

Despite these deficiencies, our 2019 *Chemical Science* report[15] and Monica C. Carey's dissertation[16] showed that this method of approximation for $\Delta G°$, when combined with VT-TA on a family of substituted $[Fe(bpy')_3]^{2+}$ complexes (bpy = 2,2'-bipyridine, bpy' = 4,4'-dimethyl-2,2'-bipyridine or 4,4'-di-*tert*-butyl-2,2'-bipyridine) and $[Fe(terpy)_2]^{2+}$ (terpy = 2,2':6,"-terpyridine), can still yield valuable insights into the nature of both the nuclear coordinate and electronics associated with GSR in LS Fe(II) polypyridyls. First, we found that the activation energy for the only *bis*-tridentate complex studied, $[Fe(terpy)_2]^{2+}$, was significantly larger than that of the bpy-

Table 2.1. $Fe^{2+/3+}$ oxidation potential (versus the Fc/Fc^+ couple), frequency factor, and activation energy for the $^5T_2 \rightarrow {}^1A_1$ conversion of four low-spin Fe(II) complexes in acetonitrile solutions. Reproduced from reference 15.

Complex	E^{ox} (V)	A (ps^{-1})	E_a (cm^{-1})
$[Fe(bpy)_3](PF_6)_2$	0.68	230 ± 20	310 ± 15
$[Fe(dmb)_3](PF_6)_2$	0.52	240 ± 20	345 ±10
$[Fe(dtbb)_3](PF_6)_2$	0.53	230 ± 15	315 ± 15
$[Fe(terpy)_2](PF_6)_2$	0.72	150 ± 55	755 ±70

based complexes (Table 2.1), indicating that the nuclear coordinate for GSR may be impacted by the change in coordination environment.

Table 2.2. Marcus parameters for four low-spin Fe(II) complexes. ΔG° is approximated according to the approximation outlined in eq. 2.6 and the electrochemical oxidation potentials given in Table 2.1. Reproduced from reference 15.

Complex	$\lvert H_{ab}\rvert^4/\lambda$	ΔG° (cm^{-1})	λ (cm^{-1})	H_{ab} (cm^{-1})
$[Fe(bpy)_3](PF_6)_2$	1/(30 ± 5)	-7300 ± 730	11000 ± 1100	4.4 ± 0.2
$[Fe(dmb)_3](PF_6)_2$	1/(33 ± 4)	-6000 ± 600	9700 ± 900	4.2 ± 0.1
$[Fe(dtbb)_3](PF_6)_2$	1/(29 ± 4)	-6100 ± 610	9500 ± 900	4.3 ± 0.2
$[Fe(terpy)_2](PF_6)_2$	1/(14 ± 9)	-7600 ± 760	14100 ± 1200	6.2 ± 1.2

We were able deduce the origin for the much greater E_a in $[Fe(terpy)_2]^{2+}$ than $[Fe(bpy)_3]^{2+}$ by comparing the calculated ΔG° and reorganization energies (Table 2.2). To determine these values, we used ΔG° = 7300 cm^{-1} for $[Fe(bpy)_3]^{2+}$ as calculated by Sutin using modified electron-transfer theory.[20] Then, ΔG° was found for the other three members of the series using eq. 2.6 and their $Fe^{2+/3+}$ oxidation potentials (Table 2.1). To account for the shortcomings in the electrochemical approximation, we used rather generous error bars of ±10% for our estimated ΔG° values. While it appears that terpy actually imparts a stronger ligand-field strength than bpy, which is manifested by the more positive oxidation potential in the respective Fe(II) complexes, this fact alone could not explain the increased E_a, as an increase in ΔG° should result in a decrease in E_a (Figure 2.1). When the reorganization energies associated with GSR were calculated, it became clear that the increase in E_a in $[Fe(terpy)_2]^{2+}$ must arise from an increase in λ, even with the large error induced by the uncertain ΔG° values. Our results reflect the computational predictions that the more strained coordination environment provided by terpy would force the Fe(II) complex to undergo both Fe-N breathing and torsional distortions[21] to recover the ground state from the $^5T_2$

It should be noted that while the values for λ have relatively large error associated with them, the relation $\lvert H_{ab}\rvert^4/\lambda$ is constrained by the experimentally-determined frequency factor (eq. 2.4). As such, we could determine H_{ab} values for these low-spin Fe(II) complexes with surprisingly

high degree of certainty, which is reflected by the relatively small error bars reported in Table 2.2. In addition, we hypothesized that the experimentally-determined $|H_{ab}|^4/\lambda$ ratios may further prove that the GSR nuclear coordinate in $[Fe(terpy)_2]^{2+}$ diverges from that of the $[Fe(bpy')_3]^{2+}$ complexes, as all of the $|H_{ab}|^4/\lambda$ ratios calculated were within error of each other, expect that of $[Fe(terpy)_2]^{2+}$.

Overall, from these previous studies we gained greater insights into the nature of the nuclear coordinate for GSR, yet a more specific definition of $\Delta Q_{LF/GS}$ is necessary to propose synthetic routes towards disruption and ultimately control this excited-state process. The biggest issue with this previous study was the approximation of $\Delta G°$, which hindered the accuracy of the calculated reorganization energies and prevented more definitive conclusions. Therefore, to remove this shroud of ambiguity and experimentally determine $\Delta G°$, λ, and H_{ab}, the Marcus parameters of an Fe(II) spin crossover (SCO) complex will be determined. SCO systems employ ligands that impart a weak enough ligand field strength such that the high-spin (HS) $^5T_2$ state is thermally accessible from the LS $^1A_1$, which remains the lowest-energy state.[22] Such a delicate energetic balance results in an equilibrium between the HS and LS states (eq. 2.7) that can be driven to either side with changes in temperature, pressure, and other external factors.[11]

$$^1A_1 \underset{k_{HL}}{\overset{k_{LH}}{\rightleftharpoons}} {}^5T_2 \tag{2.7}$$

The SCO phenomenon was first noted decades ago, and has since been an area of intense study due its importance in both the fundamental understanding of spin conversion in transition metals and its potential to advance applications such as heat sensing, pH determination, and information storage.[2,3]

For our purposes, SCO complexes will allow for the experimental determination of $\Delta G°$ between the $^1A_1$ and $^5T_2$ states. To do so, we will take advantage of the fact that the diamagnetic

LS and paramagnetic HS states have drastically different magnetic susceptibilities, enabling the use of magnetic measurements to define the basic thermodynamic parameters that are experimentally inaccessible for completely LS complexes. First, the temperature dependence of the measured magnetic susceptibility (χT) of a SCO complex can be modelled as behaving as an ideal solution[22,23] in the form of eq. 2.8:

$$\chi T = (\chi T)_{LT} + \frac{(\chi T)_{HT} - (\chi T)_{LT}}{1 + \exp\left(\frac{\Delta H}{R}\left(\frac{1}{T} - \frac{1}{T_{1/2}}\right)\right)} \tag{2.8}$$

where $(\chi T)_{LT}$ is the magnetic susceptibility at the low temperature limit, $(\chi T)_{HT}$ in the high temperature limit, ΔH is the change in enthalpy associated with SCO, R is the ideal gas constant, and $T_{1/2}$ is the temperature at which equimolar amounts of the LS and HS species are present, or $\Delta G° = 0$. As such, the change in entropy (ΔS) for the spin conversion processes can be found:

$$\Delta S = \frac{\Delta H}{T_{1/2}} \tag{2.9}$$

From parameters found from the ideal solution fit, the relative populations of the LS and HS states, here expressed as the mole fractions of two states (γ_{LS} and γ_{HS}), at every temperature can be found

$$\gamma_{HS} = \frac{\chi T_{obs} - \chi T_{LS}}{\chi T_{HS} - \chi T_{LS}} \tag{2.10}$$

$$1 = \gamma_{LS} + \gamma_{HS} \tag{2.11}$$

Then, the equilibrium constant for the spin conversion from the HS to LS states (K_{HL}) can be defined:

$$K_{HL} = \frac{\gamma_{LS}}{\gamma_{HS}} \tag{2.12}$$

It should be noted that it was chosen to define the equilibrium constant as written in order to be consistent with the ground-state recovery ($^5T_2 \rightarrow {}^1A_1$) process in low-spin Fe(II) complexes. Using the van't Hoff relation:

$$\Delta G^\circ = -RT \ln K_{HL} \tag{2.13}$$

ΔG° between the $^5T_2$ and $^1A_1$ states can be experimentally determined at every temperature at which χT is measured.

Once combined with VT-TA studies on the SCO complex, which will yield k_{nr} for GSR as a function of temperature, all of the variables necessary to find λ and H_{ab} from eq. 2.2. will have been acquired. Not only would this be the first instance of defining these parameters for a SCO complex, but these concrete values will serve as benchmarks to both our previous[15] and future results on LS complexes. To relate as closely as possible to this class of complexes, the SCO complex studied should be structurally very similar to them (i.e. t*ris*-polypyridyl in nature), as changes in coordination environment are expected to impact the GSR nuclear coordinate. At the time of writing, there have been hundreds of examples of Fe(II) SCO complexes;[24,25] however the

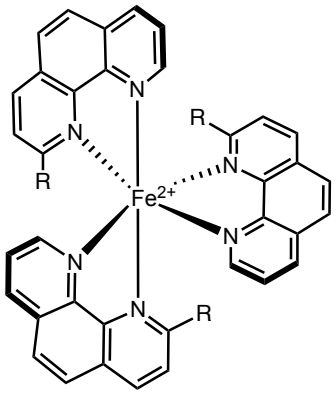

Figure 2.3. Drawing of a general $[Fe(2\text{-R-phen})_3]^{2+}$ complex.

pool of SCO complexes that have a *tris*-polypyridyl coordination motif is drastically smaller. In fact, the only potential family of complexes that might fit the bill is a series of $[Fe(2\text{-R-phen})_3]^{2+}$

complexes (Figure 2.3), where 2-R-phen is a 1,10-phenanthroline (phen) ligand with a mono-substitution to the position *ortho* to a nitrogen atom.

The identity of these substituents has a huge influence on the ground electronic state of the *tris*-Fe(II) compound. When R = H, the compound is the well-studied diamagnetic complex, $[Fe(phen)_3]^{2+}$, which is very closely related structurally and electronically to the prototypical low-spin Fe(II) complex $[Fe(bpy)_3]^{2+}$.[9] As first noted by Goodwin and coworkers[26] in 1968 and then expanded upon by several others,[27,28] the addition of a single methyl group to the phen ligand changes the electronic nature of the ground state of the corresponding Fe(II) complex, $[Fe(2\text{-Me-phen})_3]^{2+}$. The solid-state magnetic behavior of this complex was investigated with variable-temperature (VT) magnetic measurements and Mössbauer spectroscopy, revealing a temperature-dependent effective magnetic moment (μ_{eff}): 5.5 at room temperature and 3.4 at 97 K. On the heels of these results, researchers then extended the series, observing that $[Fe(2\text{-OMe-phen})_3]^{2+}$ also exhibits SCO in the solid state, while $[Fe\text{-}2\text{-Cl-phen})_3]^{2+}$ is strictly HS from room temperature down to 4.2 K.[27,29] The origin of the substituent effects on the ground-state of the $[Fe(2\text{-R-phen})_3]^{2+}$ complexes was hypothesized to be a result of intertwined steric and electronic effects, and in the discussion section of this chapter further evidence to support this will be provided.

These $[Fe(2\text{-R-phen})_3]^{2+}$ complexes constitute a tantalizing potential series to allow the explicit determination of λ and H_{ab} in geometrically relevant Fe(II) complexes. The first step in this process will be to confirm the SCO nature of $[Fe(2\text{-Me-phen})_3]^{2+}$ and $[Fe(2\text{-OMe-phen})_3]^{2+}$ in solution, as solid- and solution-phase magnetic behavior for a given complex can be notoriously incongruous due in part to lattice effects, cooperativity, phase changes, and ion-pairing.[11] Once established as a bona fide SCO complex in solution through VT magnetic measurements, the complex(es) will be studied with VT-TA to allow for Arrhenius and Marcus analyses and yield

unprecedented insight into the nature of the nuclear coordinate defining ground-state recovery in this class of chromophores.

2.2. Experimental

2.2.1. Synthesis

General. 2-Me-phen[30] and 2-Cl-phen[31] ligands were prepared according to the literature procedures. 1,10-phenanthroline (phen) was purchased from Oakwood Chemicals and used as received. Acetonitrile, methanol, and diethyl ether were dried over neutral alumina under nitrogen. ^{1}H NMR were collected on an Agilent DDR2 500 MHz spectrometer at the Max T. Rogers NMR facility at Michigan State University and referenced to residual solvent shifts. Unless otherwise noted, all reactions were conducted either using standard Schlenk techniques or in an inert atmosphere glove box (nitrogen-filled, Vacuum Atmospheres). Electrospray ionization mass spectra were obtained at the Michigan State University Mass Spectrometry and Metabolomics Core on a Waters G2-XS QTof mass spectrometer interfaced to a Waters Aquity UPLC. Elemental analyses were obtained through the analytical facilities at Michigan State University on samples that had been ground in a vial with a glass stir rod in an inert atmosphere glovebox and stored under vacuum overnight prior to analysis.

2-methoxy-1,10-phenanthroline (2-OMe-phen). The title compound was prepared with a modified version of the literature procedure.[32] Anhydrous MeOH (50 mL) was cooled in an ice bath. Sodium metal (1.1 g, 48 mmol) was cut into ~1 cm cubes, washed with hexanes and isopropanol, and added to MeOH (50 mL) slowly under nitrogen with vigorous stirring. The sodium was allowed to stir in MeOH until no sodium metal was visible. 2-Cl-phen (515 mg, 2.4 mmol) was added under nitrogen. The ice bath was removed and the reaction was refluxed under nitrogen for 16 h. The solvent was removed, and the orange residue was taken into water. The

orange suspension was extracted DCM (3 × 30 mL), dried over sodium sulfate, and the solvent was subsequently removed, yielding a yellow oil that solidified to a beige solid (439 mg, 87% yield) upon pumping in a vacuum desiccator. ^{1}H NMR (500 MHz, $CDCl_3$) 9.19 (d, J = 3.89 Hz, 1 H), 8.25 (d, J = 8.02, 1 H), 8.12 (d, J = 8.63, 1 H), 7.76 (d, J = 8.57, 1 H), 7.68 (dd, J_1 = 8.69, J_2 = 3.02, 1 H), 7.60 (m, 1 H), 7.14 (d, J = 8.62, 1 H), 4.33 (s, 3 H).

***tris*(1,10-phenanthroline)iron(II) tetrafluoroborate [Fe(phen)$_3$](BF$_4$)$_2$.** In a nitrogen-filled glovebox, phen (112 mg, 0.62 mmol) was dissolved in MeCN (5 mL). $Fe(BF_4)_2$•$2H_2O$ (50 mg, 0.19 mmol) was dissolved in MeCN (5 mL) and added dropwise to the phen solution with stirring, instantly causing a color change to bright cherry red. The resulting solution was stirred overnight, and enough Et_2O was added until precipitation of a red solid was induced. This precipitate was collected via filtration and washed with Et_2O. All spectroscopic characterization matched that in the literature.[33]

***tris*(2-R-1,10-phenanthroline)iron(II) tetrafluoroborate ([Fe(2-R-phen)$_3$](BF$_4$)$_2$).** In a nitrogen-filled glovebox, the 2-R-phen ligand (1.05 mmol) was dissolved in acetone (5 mL) in a pressure tube. $Fe(BF_4)_2$•$2H_2O$ (84 mg, 0.32 mmol) was dissolved in acetone (5 mL) and added dropwise over 2 min to the ligand with stirring. The resulting red solution was refluxed under nitrogen for 12 h. Upon cooling, Et_2O was added until very cloudy, and the suspension was allowed to sit for 1 h. The orange (in the case of [Fe(2-Me-phen)]$(BF_4)_2$ and [Fe(2-Cl-phen)]$(BF_4)_2$) or red precipitate (in the case of [Fe(2-OMe-phen)]$(BF_4)_2$) was collected via filtration and washed with Et_2O. X-ray quality crystals were grown from ether diffusion into 9:1 MeCN/MeOH solutions of [Fe(2-OMe-phen)$_3$]$(BF_4)_2$ and [Fe(2-Cl-phen)]$(BF_4)_2$ complexes, and 1:1 acetone/MeOH solutions of [Fe(2-Me-phen)]$(BF_4)_2$.

[Fe(2-OMe-phen)$_3$](BF$_4$)$_2$. HRMS (ESI-TOF) m/z: [M-2(BF$_4$)]$^{2+}$ calc'd for $C_{39}H_{30}N_6O_3Fe$: 343.0865, obs. 343.0886; Elemental Analysis: Calc'd: C, 54.46; H, 3.52; N 9.77. Found C, 54.21; H, 3.71; N, 9.79.

[Fe(2-Me-phen)$_3$](BF$_4$)$_2$. HRMS (ESI-TOF) m/z: [M-2(BF$_4$)]$^{2+}$ calc'd for $C_{39}H_{30}N_6Fe$: 319.0941, obs. 319.0948; Elemental Analysis: Calc'd: C, 57.68; H, 3.72; N, 10.35. Found: C, 57.05; H, 3.27; N, 10.01.

[Fe(2-Cl-phen)$_3$](BF$_4$)$_2$. HRMS (ESI-TOF) m/z: [M-2(BF$_4$)]$^{2+}$ calc'd for $C_{36}H_{21}N_6Cl_2Fe$: 349.0122, obs. 349.0137; Elemental Analysis: Calc'd: C, 49.51; H, 2.42; N, 9.62. Found: C, 49.10; H, 2.62; N, 9.55.

2.2.2. Physical Characterization

X-ray crystal structure determination. Single-crystal x-ray diffraction data were collected on suitable crystals of [Fe(2-OMe-phen)$_3$](BF$_4$)$_2$ and [Fe(2-Cl-phen)$_3$](BF$_4$)$_2$ mounted on a Bruker APEX-II CCD diffractometer with CuK$_\alpha$ radiation at the Center for Crystallographic Research at Michigan State University. These crystal structures have been submitted to the CCDC database and can be accessed by their CCDC accession numbers: [Fe(2-OMe-phen)$_3$](BF$_4$)$_2$ (CCDC number:1977342), [Fe(2-Cl-phen)$_3$](BF$_4$)$_2$ (CCDC number 1977386). Single crystals were grown of [Fe(2-Me-phen)$_3$](BF$_4$)$_2$, but all attempts to collect x-ray diffraction at MSU failed. Data were successfully collected at Rigaku on an XtaLAB Synergy Dualflex HyPix diffractometer equipped with an Oxford Cryosystems low-temperature device operating at 100.00(10) K. The crystal was either higher symmetry or whole molecule disordered, or both. As such, the crystal structure proved connectivity, however no attempt will be made to extract out meaningful bond lengths and angles.

Ground-state absorption spectroscopy. All room temperature extinction coefficient measurements were collected on approximately 0.5 mM solutions of each Fe(II) complex in spectrophotometric grade acetone (Sigma Aldrich) in a 1 cm quartz cuvette on a Cary 50 spectrophotometer.

Electrochemistry. Electrochemistry was performed using a CH Instruments potentiostat in a 0.1 M tetrabutylammonium hexafluorophosphate ($TBAPF_6$) acetone solution with a Pt working electrode, Pt counter electrode, and a Ag wire pseudo-reference electrode in an Ar-filled glovebox. Cyclic voltammetry measurements were conducted with a 100 mV/s scan rate to determine the reversibility of redox processes and differential pulse voltammetry was used to find their potentials. All potentials were internally referenced to the Fc/Fc^+ redox couple. $TBAPF_6$ was purchased from Oakwood Chemical Company and recrystallized from ethanol twice before use.

Solid-state Variable Temperature Magnetic Susceptibility Measurements. All measurements were performed on a Quantum Design MPMS 3 magnetometer cryogen free equipped with an EverCool He gas regulator interfaced to a Dell PC. Data were collected with an applied field of 1 T in DC mode and with 10 min of temperature equilibration at each temperature point before scanning began. DC moments were corrected for the diamagnetic contributions attributed to the straw and bag, as measured in blank experiments. Pascal's constants were used to correct for the diamagnetic contribution from the sample.[34] Crystalline samples were stored in a vacuum desiccator for one day prior to data collection. Approximately 3-5 mg of the sample were weighed out and placed in a weighed vacuum sealer bag (approximately 7 x 7 mm, sealed on 3 sides). The bag was then folded into a cylinder that was no longer than 6 mm and be placed into a plastic straw, centered on the sample holder, and inserted into the sample chamber, which was purged

three times prior to sealing. The absence of ferromagnetic impurities was confirmed by measuring the magnetic moment versus applied field (0-1 T) and ensuring a linear response.

Evans Method for Solution-phase Variable Temperature Magnetic Susceptibility Measurements.[35] In general, an approximately 5 mM solution of the compound under investigation was prepared in acetone-d_6 (Cambridge Isotope Laboratories) spiked with 3% v/v spectroscopic grade benzene (OmniSolv). This solution was added to a 5 mm glass insert (Michigan State University Department of Chemistry Glassblowing Facility). To a NMR tube was added acetone-d_6 spiked with 3% v/v spectroscopic grade benzene. The glass insert was placed inside this NMR tube and sealed tightly with a rubber septum, NMR tube cap, and parafilm. All measurements were conducted on a Varian 500 MHz spectrometer (Bastet) at the Max T. Rogers NMR facility at Michigan State University. The temperature of the sample was determined using a spectroscopic grade methanol standard following temperature equilibration at each temperature point for 5 min. Samples were allowed to equilibrate at each temperature for 10 min. The accuracy of this method was tested by measuring the effective magnetic moment (μ_{eff}) of tris(acetylacetonate) chromium(III) ($Cr(acac)_3$) in acetone-*d_6* from 210-310 K. μ_{eff} of the $Cr(acac)_3$ standard was measured as 3.85 ± 0.03 μ_B and completely temperature independent.[36] For all samples, a correction was applied to account for the change in density of the solvent with varying temperature[37] using the previously determined densities of acetone as a function of temperature,[38] as well as the difference in densities of acetone-d_6 (0.872 mg/cm^3) and acetone (0.7845 mg/cm^3). Diamagnetic contributions to the magnetic moment were corrected for using Pascal's constants.[34]

The molar susceptibility (χ) of the paramagnetic species was determined based on the frequency of the spectrometer (ν), the concentration of the species in the prepared sample ([C]),

corrected for changes in density as a function of temperature, and the observed difference in the shifts of the standard, in this case benzene, in the inner and outer tubes (Δν) (Equation 2.14).[39]

$$\chi = \frac{3000\Delta\nu}{4\pi\nu[C]} \tag{2.14}$$

After applying diamagnetic correction factors to χ using Pascal's constants,[34] the effective magnetic moment was calculated from the measured magnetic susceptibility (Equation 2.15):

$$\mu_{eff} = 2.828\sqrt{\chi T} \tag{2.15}$$

2.2.3. Variable-temperature optical spectroscopy

General. All variable temperature (VT) optical spectroscopy, with the exception of ultrafast transient absorption measurements, was conducted in a Janis SVT-100 optical cryostat equipped with two LakeShore resistive heaters with autotuning temperature controllers (Model 321). The vacuum jacket of the cryostat was pumped down to a pressure of $<1\text{x}10^{-4}$ Pa with a turbomolecular pump (Pfeiffer Vacuum HiCube 80 Eco pumping station) prior to the addition of liquid nitrogen. For nanosecond VT transient absorption measurements, a dynamic vacuum was maintained during data collection, but for all other VT measurements only a static vacuum was used. Room temperature data were collected in the cryostat before dropping down to the lowest temperature point to conserve cryogenic fluid. After the desired temperature was achieved, the temperature was held for 10 minutes before data collection began to ensure temperature equilibration.

Variable Temperature Ground-state Absorption Spectroscopy. Data were collected on a Perkin Elmer Lambda1050 spectrometer operating in single beam mode. A sample with a known concentration of the spin crossover complex was prepared in spectroscopic grade acetone to achieve a room temperature absorbance of approximately 0.1 au at the maximum visible absorbance in a 1 cm quartz tube. To derive the ground state absorption spectra of the LS and HS

species and thus guide time-resolved transient absorption measurements, the data were globally fit to a modified form of the Beer-Lambert law:[40]

$$Absorbance(T,\lambda) = b \cdot c_{total} \cdot \left(\gamma_{HS}(T) \cdot \varepsilon_{HS}(\lambda) + \left(1 - \gamma_{HS}(T)\right) \cdot \varepsilon_{LS}(\lambda)\right) \quad (2.16)$$

Where b is the path length of the cell, c_{total} is the concentration of the spin crossover complex, γ_{HS} is the mole fraction of the HS species (as determined by variable temperature magnetic susceptibility Evans measurements in the same solvent), ε_{HS} is the extinction coefficient of the HS species, and ε_{LS} the extinction coefficient of the LS species.

Variable Temperature Nanosecond Time-resolved Transient Absorption Spectroscopy. Data were collected using a Nd:YAG laser that has been generally described in the past,[41,42] but is now equipped with an Opotek Vibrant 355 LD tunable pulsed laser system with ~5 ns pulses coupled with an LP980 laser flash photolysis system (Edinburgh Instruments). Samples were prepared with spectrophotometric grade acetone in an Ar-filled glovebox (Vacuum Atmospheres) with an absorbance at the pump wavelength between 0.4-0.7 au in a 1 cm cryogenic quartz cuvette (FireflySci) as measured on a SSI400 CCD spectrometer. Pump power at the laser was between 1-3 mJ and linearity was checked using a 0.3 OD filter. Alignment of the cryostat in the TA setup was achieved by putting the white light in CW mode. This steady beam was used to ensure the probe could hit the sample and land on the monochromator slits, adjusting the cryostat both vertically and horizontally. During data collection, in addition to collecting scans with both the pump and probe hitting the sample, two backgrounds were collected and subtracted from the raw data: one with just the probe traversing the sample and the other just the pump. Depending on signal strength, 200-500 averages were collected at each temperature point to obtain the best possible signal-to-noise ratios. For transients with time constants less than 50 ns, multipeak fitting in Igor Pro (Version 6.37) was used to model the data as an exponentially modified Gaussian

distribution. For longer time constants, satisfactory fits were achieved using a single exponential function.

Ultrafast Variable Temperature Time-resolved Transient Absorption Spectroscopy. Measurements were conducted on samples in spectrophotometric grade acetone and following the procedure outlined in the 2019 report by Carey et al.[15] and Monica Carey's dissertation.[16]

2.3. Results and Discussion

2.3.1. Synthesis

In the original reports of the syntheses of each member of the $[Fe(2\text{-R-phen})_3]^{2+}$ series,[26–29] a wide variety of Fe(II) precursors, solvents, and reagent ratios were used. These procedures did result in the desired complexes, but the authors also noted that ferromagnetic impurities were present as well. Because we will be extracting thermodynamic parameters from the magnetic susceptibilities of these compounds, it is of the upmost importance to have pure Fe(II) complexes. Therefore, an amended synthetic route was pursued. In the first round of attempts, $FeCl_2 \bullet 2H_2O$ was added to 3.1 equivalents of a given ligand, a common condition for the synthesis of *tris*-polypyridyl iron(II) complexes in the literature and our lab. However, with this iron(II) precursor no desired product was observed for any member of the series besides the unsubstituted phen complex. Insight behind the failure of this route was gleaned by obtaining a crystal structure of the product formed from the 2-Me-phen synthesis: $[Fe(2\text{-Me-phen})_2Cl](PF_6)$ (Figure 2.4). Because

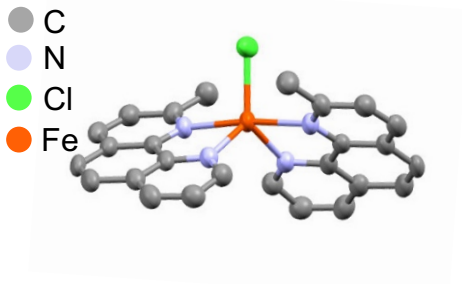

Figure 2.4. X-ray crystal structure of $[Fe(2\text{-Me-phen})_2Cl](PF_6)_2$. Hydrogen atoms and counteranion excluded for clarity.

relatively weak-field ligands are being employed, the chlorides in $FeCl_2 \bullet 2H_2O$ are too coordinating to allow for complete ligand substitution to occur, preventing the formation of the desired *tris*-complexes.

From this initial observation, an Fe(II) starting material with a less coordinating anion was employed, $Fe(BF_4)_2 \bullet 2H_2O$, and the complexation was performed at reflux to foment the formation of the thermodynamically favorable *tris* complex over the *bis* product. Acetone was used as the noncoordinating solvent and no metathesis from the tetrafluoroborate salt was necessary, as the tetrafluoroborate complexes were suitably soluble in a range of solvents. The ^{1}H NMR spectra of all members of the series when R ≠ H exhibit broad peaks from -60 to 80 ppm, preventing definitive structural analysis and indicate the presence of a paramagnetic species at room temperature.

2.3.2. Solid-state characterization: crystal structures and variable-temperature magnetic measurements

Although we are primarily concerned with the solution-phase magnetic behavior of the $[Fe(2\text{-R-phen})_3]^{2+}$ complexes, an investigation of their solid-state properties can yield insight into the origin of any SCO observed. Crystals of $[Fe(2\text{-OMe-phen})_3](BF_4)_2$ and $[Fe(2\text{-Cl-phen})_3](BF_4)_2$ obtained from room temperature complexations led to structures that contained both possible enantiomers, giving rise to unresolvable disorder in one of the 2-R-phen ligands. However,

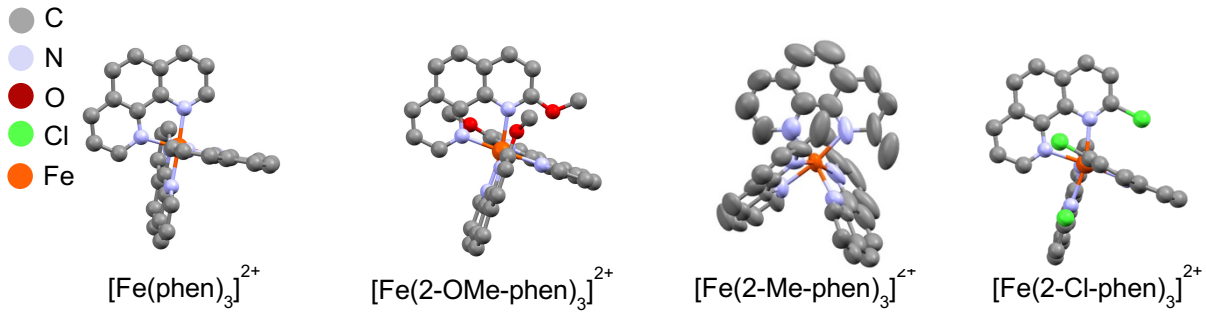

Figure 2.5. X-ray crystal structures of each member of the $[Fe(2\text{-R-phen})_3](BF_4)_2$. Counteranions and solvent molecules are excluded for clarity. $[Fe(phen)_3](BF_4)_2$ was originally collected by Panja et al. (reference 33).

conducting the complexation reactions at reflux alleviated these issues, as evidenced by their x-ray crystal structures (Figure 2.5). Unfortunately, all crystals of $[Fe(2\text{-Me-phen})_3](BF_4)_2$ grown resulted in very weak diffraction on MSU's instruments. Upon collection at Rigaku's facilities, higher quality data were obtained, however the data indicate a highly disordered structure. Most likely this disorder is a result of the presence of both Λ and Δ enantiomers within the asymmetric unit cell. As such, the crystal structure proves that the desired connectivity has been achieved, but no attempts will be made to extract out bond lengths and angles.

The impact of introducing a non-hydrogen substituent to the *ortho*-position on the phen ligands can be observed in the structural parameters of the three $[Fe(2\text{-R-phen})_3]^{2+}$ complexes with acceptable crystal structures (Table 2.3). In general, Fe-N bond lengths in LS complexes are ~1.96-2.00 Å, but for HS complexes they elongate to ~2.00-2.25 Å.[43] The longer bond lengths in the $^5T_2$ state is a consequence of antibonding e_g^* orbital population, which are unoccupied in the LS $^1A_1$ electron configuration. From these guidelines, we can expect at least some HS population in both $[Fe(2\text{-OMe-phen})_3]^{2+}$ and $[Fe(2\text{-Cl-phen})_3]^{2+}$, which exhibit significantly longer Fe-N bond lengths and greater deviations from ideal octahedral geometry than $[Fe(phen)_3]^{2+}$.[33]

Table 2.3. Select structural parameters from single crystal x-ray structures.

Complex	Average Fe-N bond length (Å)	Average trans-angle	Average cis-angle
$[Fe(phen)_3](BF_4)_2$[a]	1.97	175.9°	90.04°
$[Fe(2\text{-OMe-phen})_3](BF_4)_2$	2.15	169.0°	89.82°
$[Fe(2\text{-Cl-phen})_3](BF_4)_2$	2.21	168.1°	91.37°

[a]X-ray crystal structure from reference 33.

This conclusion is confirmed by examining the solid-state magnetic properties of crystalline samples of $[Fe(2\text{-OMe-phen})_3](BF_4)_2$ and $[Fe(2\text{-Cl-phen})_3](BF_4)_2$ using variable-temperature SQUID measurements (Figure 2.6). Although solid-state magnetic data for these

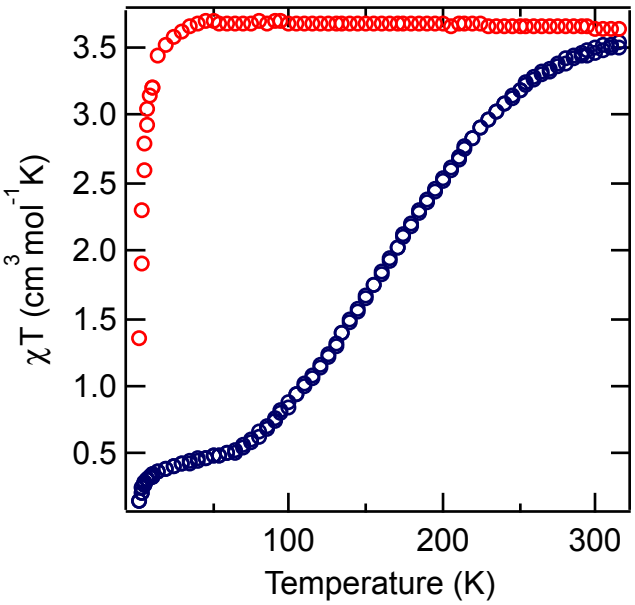

Figure 2.6. Magnetic susceptibility of crystalline samples of $[Fe(2\text{-Cl-phen})_3](BF_4)_2$ (red circles) and $[Fe(2\text{-OMe-phen})_3](BF_4)_2$ (blue circles). Both samples were collected at an applied field of 1 T from 2-315 K.

compounds are available in the literature, the presence of ferromagnetic impurities may have skewed those results.[27,29] In the recollected data, above approximately 50 K, χT of $[Fe(2\text{-Cl-phen})_3](BF_4)_2$ (Figure 2.6, blue circles) is essentially temperature independent at 3.68 $cm^3mol^{-1}K$ (μ_{eff} = 5.42). While this value is slightly higher than the spin-only value expected for a $^5T_2$ (4.9), most likely due to the effects of spin-orbit coupling, it falls well within the range of magnetic susceptibilities experimentally observed for HS Fe(II) complexes.[44]

Below ~50 K, the magnetic susceptibility begins to decrease drastically, an effect that can be attributed to zero-field splitting of a $^5T_2$ Fe(II) center. Overall, the magnetic behavior of crystalline $[Fe(2\text{-Cl-phen})_3](BF_4)_2$ is indicative of a HS Fe(II) complex, qualitatively matching literature reports.[27]

The magnetic measurements on crystalline $[Fe(2\text{-OMe-phen})_3](BF_4)_2$ (Figure 2.6, blue circles) revealed a gradual and incomplete spin-crossover: the magnetic susceptibility decreases from 3.54 $cm^3mol^{-1}K$ (μ_{eff} = 5.32) at 315 K to 0.48 $cm^3mol^{-1}K$ (μ_{eff} = 1.96) at 50 K. Some high-

spin fraction remains in $[Fe(2\text{-}OMe\text{-}phen)_3](BF_4)_2$ below 50 K, which again gives rise to zero-field splitting. Sterics alone cannot account for the fact that $[Fe(2\text{-}OMe\text{-}phen)_3]^{2+}$ has some low-spin population, but $[Fe(2\text{-}Cl\text{-}phen)_3]^{2+}$ is strictly high-spin, as a methoxy group is bulkier than a chlorine substituent and would therefore be predicted to be more likely to stabilize the HS state. Previous combined computational and experimental studies on over 25 SCO complexes have concluded that electron-withdrawing substituents can in some instances stabilize the $^5T_2$ state, but do just the opposite in others, depending on a finely-tuned balance between Fe-N σ- and π-effects that can be difficult to define without a large number of well-characterized structurally-related SCO complexes.[45]

2.3.3. Ground-state absorption spectra

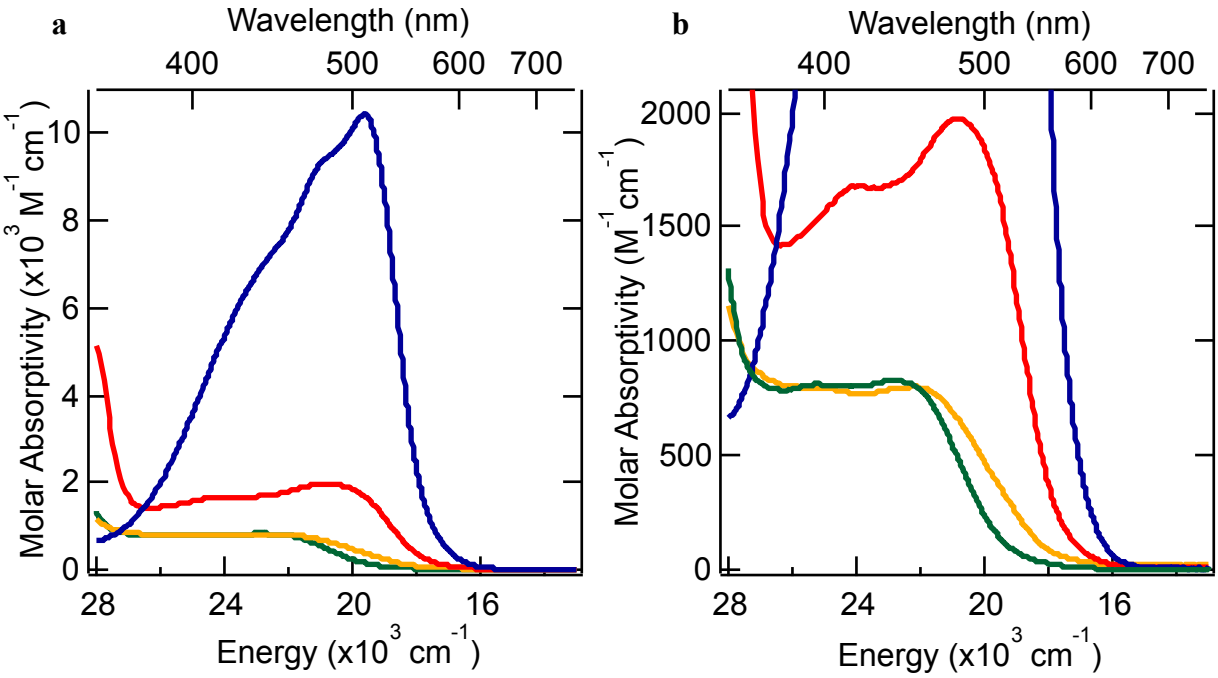

Figure 2.7. (a) Molar absorptivity of the four members of the $[Fe(2\text{-}R\text{-}phen)_3](BF_4)_2$ series in acetone at room temperature: $[Fe(phen)_3](BF_4)_2$ (blue), $[Fe(2\text{-}OMe\text{-}phen)_3](BF_4)_2$ (red), $[Fe(2\text{-}Me\text{-}phen)_3](BF_4)_2$ (yellow), and $[Fe(2\text{-}Cl\text{-}phen)_3](BF_4)_2$ (green) (b) A zoom-in of the ground-state absorption spectra of the R ≠ H $[Fe(2\text{-}R\text{-}phen)_3](BF_4)_2$ in acetone at room temperature.

Another sign of some HS population in these complexes is found in the ground-state absorption spectra of the series (Figure 2.7). For the diamagnetic $[Fe(phen)_3](BF_4)_2$ complex, the absorption spectrum strongly resembles that of many other low-spin *tris*-polypyridyl-iron(II) complexes,[15] with a broad, relatively intense (extinction coefficient of 1.0×10^4 $M^{-1}cm^{-1}$) absorption in the mid-visible region at 510 nm (19600 cm^{-1}), which can be assigned as $^1A_1 \rightarrow {}^{1,3}$MLCT transitions. Introduction of a non-hydrogen substituent to the *ortho*-position of the phenanthroline ligand drastically decreases the extinction coefficients of the Fe(II) complexes in the visible region by almost an order of magnitude and shifts the maxima of these features to bluer wavelengths. The lower molar absorptivity of these complexes is consistent with HS population at room temperature, as the oscillator strength of $^5T_2 \rightarrow {}^5$MLCT features is expected to be weaker than the MLCT transitions originating from low-spin ground states. This is due to the longer Fe-N bond lengths present in high-spin complexes, which decrease metal/ligand orbital overlap and attenuates π-back-bonding from the metal. From these measurements, it is clear that solution-phase magnetic data is necessary to determine if any of these members of the series are SCO and will enable the experimental determination of the free energy difference between the $^1A_1$ and $^5T_2$ states.

2.3.4. Temperature-dependent solution-phase magnetic behavior of $[Fe(2\text{-}R\text{-}phen)_3](BF_4)_2$

To investigate the magnetic behavior of the $[Fe(2\text{-}R\text{-}phen)_3]^{2+}$ series in solution, variable-temperature (VT) magnetic susceptibility measurements were conducted in acetone using Evans NMR method on all four complexes. First, $[Fe(phen)_3](BF_4)_2$ was found to be completely diamagnetic from 210-310 K, as expected for a LS Fe(II) compound. The explicit value of χT for this complex was below the detection limit of Evans method and therefore must be close to ~0 $cm^3mol^{-1}K$, consistent with the absence of unpaired electrons. On the opposite end of the spectrum, $[Fe(2\text{-}Me\text{-}phen)_3](BF_4)_2$ and $[Fe(2\text{-}Cl\text{-}phen)_3](BF_4)_2$ had magnetic behavior characteristic of a $^5T_2$

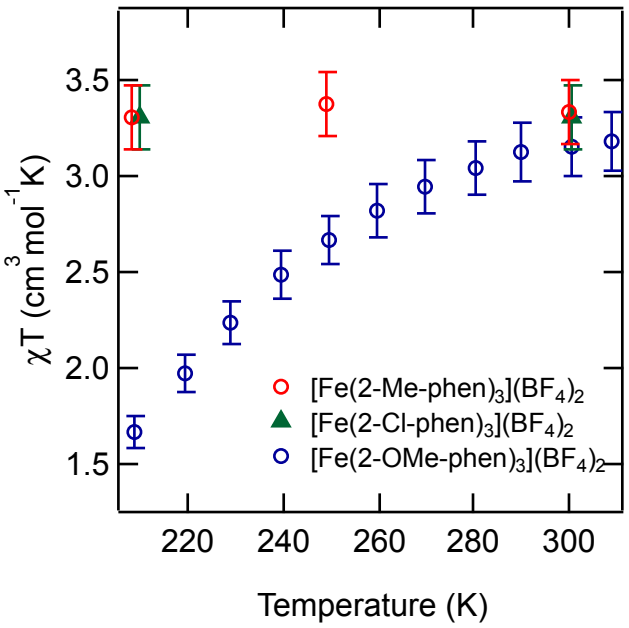

Figure 2.8. Magnetic susceptibility of $[Fe(2\text{-R-phen})_3](BF_4)_2$ series measured in ~5 mM acetone solution with Evans method.

HS state (3.34 and 3.30 $cm^3mol^{-1}K$, respectively) at room temperature and virtually no change in magnetic susceptibility upon cooling (Figure 2.8). It should be noted that 210 K was the lowest temperature accessible for these measurements not because of the freezing point of acetone (178.5 K), but due to the inability to shim the NMR magnet below this temperature. In both complexes, the measured χT values are higher than the spin-only value of 3.00 $cm^3mol^{-1}K$ for noninteracting HS Fe(II) due to orbital contributions to the moment.[44]

Finally, χT of $[Fe(2\text{-OMe-phen})_3](BF_4)_2$ at room temperature was close to that of the completely HS complexes, 3.18 $cm^3mol^{-1}K$ at 310 K. However, unlike the other members of the 2-R-phen series, χT of $[Fe(2\text{-OMe-phen})_3](BF_4)_2$ exhibited clear temperature dependence, dropping to 1.68 $cm^3mol^{-1}K$ at 210 K (Figure 2.8, blue circles), a hallmark of a SCO complex. To confirm that the temperature-dependent χT was not a consequence of ion-pairing, which can modulate the $^5T_2/^1A_1$ energy gap in some Fe(II) complexes,[46] variable-concentration VT Evans method was collected on $[Fe(2\text{-OMe-phen})]^{2+}$ (Figure 2.9).

No concentration dependence was observed over the experimentally accessible concentration range, so either ion-pairing is not occurring or it is not affecting the energy gap differently over this concentration range.

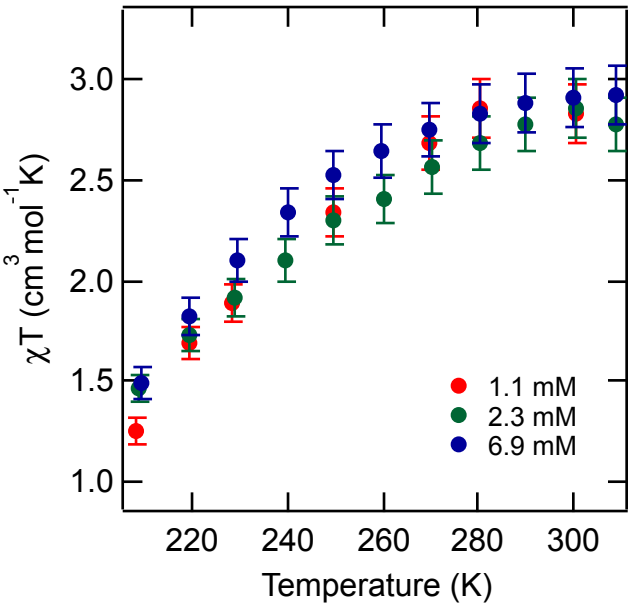

Figure 2.9. Magnetic susceptibility of $[Fe(2\text{-OMe-phen})_3](BF_4)_2$ in acetone at three different concentrations.

Therefore, $[Fe(2\text{-OMe-phen})_3]^{2+}$ will be the complex that will allow for the explicit determination of ΔG, and subsequently a more in-depth Marcus analysis of the $^5T_2 \rightarrow {}^1A_1$ transition. First, fitting the SCO complex's VT-magnetic data to the ideal solution model shown in eq. 2.8 while fixing χT_{LS} at 0 yields values for the change in enthalpy associated with SCO as well as $T_{1/2}$ (Figure 2.10a). The values for ΔH and ΔS (1200 ± 50 cm^{-1} and 5.5 ± 1 $cm^{-1}K^{-1}$, respectively) obtained from the fit fall within the those reported for other Fe(II) SCO complexes in solution.[40,47,48] The magnitudes of ΔH and ΔS indicate that $[Fe(2\text{-OMe-phen})_3]^{2+}$ is stable in an acetone solution, as higher values (>2500 cm^{-1} for ΔH and >10 $cm^{-1}K^{-1}$ for ΔS) have been observed for complexes that dissociate or undergo ligand exchange.[47]

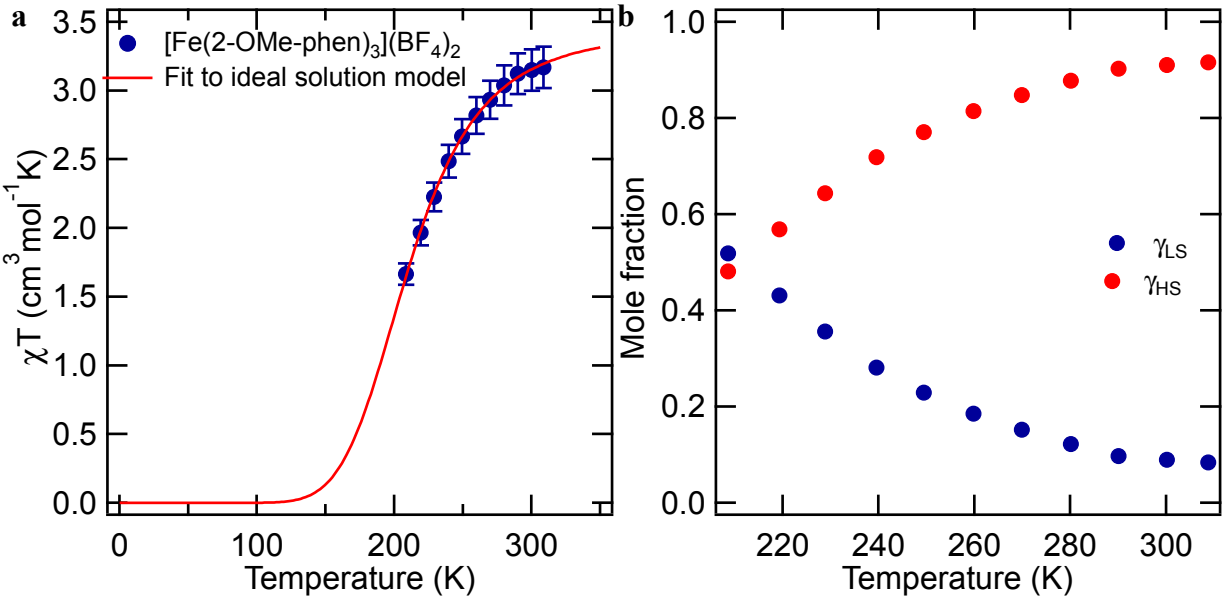

Figure 2.10. (a) Variable-temperature magnetic susceptibility of $[Fe(2\text{-}OMe\text{-}phen)_3]^{2+}$ in acetone, fit to an ideal solution model with χT_{LT} fixed at 0 to yield $\Delta H = 1200 \pm 50$ cm^{-1}, $T_{1/2} = 210 \pm 3$ K, $\chi T_{HT} = 3.46$ cm^{3}mol^{-1}K. (b) Mole fractions of the low-spin and high-spin states of $[Fe(2\text{-}OMe\text{-}phen)_3]^{2+}$ in acetone as a function of temperature.

The ideal solution fit predicted that for $[Fe(2\text{-}OMe\text{-}phen)_3]^{2+}$ in acetone, χT approaches 3.46 cm^{3}mol^{-1}K ($\mu_{HS} = 5.26 \pm 0.2$) in the high-temperature limit, and we will use this value as the completely HS magnetic susceptibility (χT_{HS}) for this complex. However, over the experimentally-accessible temperature range, $[Fe(2\text{-}OMe\text{-}phen)_3]^{2+}$ in acetone never achieves exclusive population of the low-spin state, which is common for SCO in solution as the absence of lattice effects and significant cooperativity tend to lead to more gradual spin conversion processes than those observed in solid state.[47] Therefore, we will assume that as $[Fe(2\text{-}OMe\text{-}phen)_3]^{2+}$ approaches 100% low-spin population, the magnetic susceptibility (χT_{LS}) is ~0 cm^{3}mol^{-1}K (as expected for a diamagnetic complex). The low-spin and high-spin mole fractions (γ_{LS} and γ_{HS}) may be calculated using equations 2.10 and 2.11 (Figure 2.10b), and subsequently the equilibrium constant for the $^5T_2 \rightarrow {}^1A_1$ conversion (K_{HL}) may be calculated (eq. 2.12).

A van't Hoff plot of the temperature dependence of K_{HL} (Figure 2.11a) is linear over the temperature range studied, indicating that ΔH and ΔS for spin conversion in this complex are not appreciably temperature dependent. In addition, the values for ΔH and ΔS found from the van't Hoff model correspond well to those calculated from the ideal solution model of the χT versus temperature data. ΔG° for the $^5T_2 \rightarrow {}^1A_1$ process, calculated from the K_{HL} values using eq. 2.13,

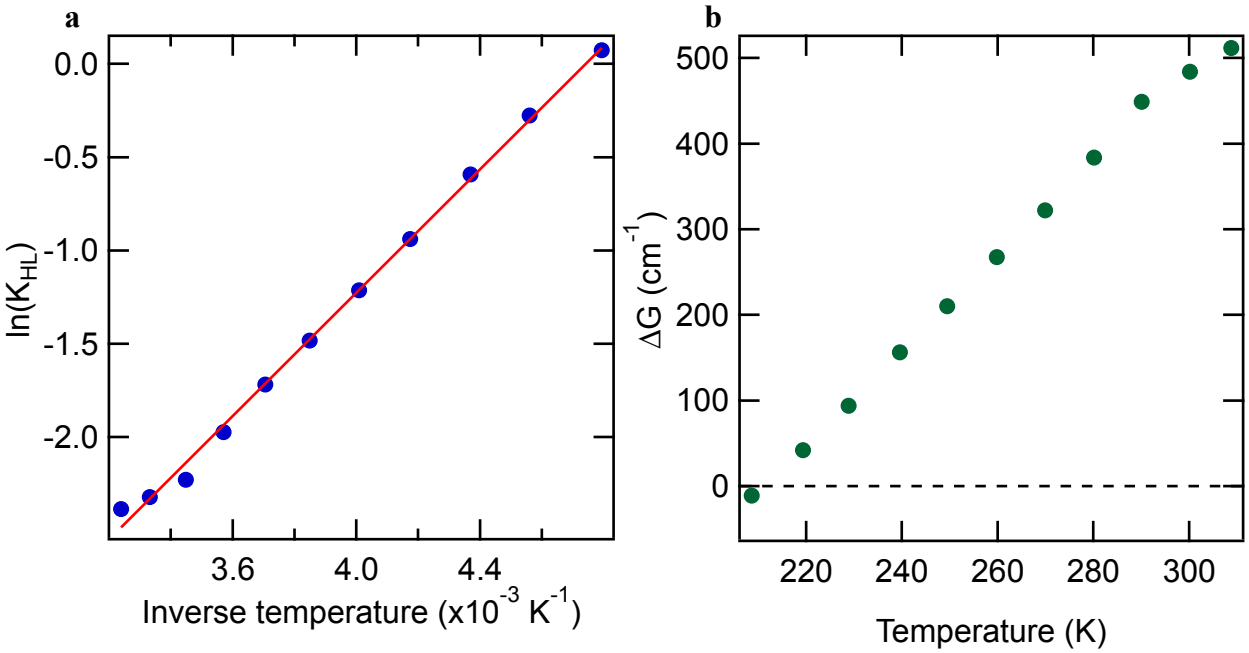

Figure 2.11. (a) van't Hoff plot of the calculated equilibrium constants for the $^5T_2 \rightarrow {}^1A_1$ conversion of $[Fe(2\text{-OMe-phen})_3](BF_4)_2$ in an acetone solution. The red line corresponds to a van't Hoff model to yield ΔH = 1200 cm^{-1} and ΔS = -5.4. (b) Calculated ΔG values as a function of temperature.

are displayed graphically in Figure 2.11b. The change in sign of ΔG° at the lowest temperature point, 210 K, reflects the favored population of the LS state at lower temperatures and the entropy-driven nature of the spin conversion process. This analysis of the temperature dependent magnetic measurements on the SCO complex $[Fe(2\text{-OMe-phen})_3]^{2+}$ have allowed for a detailed characterization of the thermodynamics of the spin conversion process, and will therefore enable

a more in-depth analysis of the $^5T_2 \rightarrow {}^1A_1$ recovery kinetics than ever before experimentally possible.

2.3.5. Electrochemistry

Although we do not need to approximate ΔG° for $[Fe(2\text{-OMe-phen})_3]^{2+}$ from electrochemistry, as the previously discussed VT magnetic susceptibility measurements have provided much more accurate values than would be possible using the electrochemical approximation given in eq. 2.6, electrochemical measurements will be necessary to approximate ΔG° for the low-spin complex $[Fe(phen)_3]^{2+}$. Cyclic voltammetry (Figure 2.12a) and differential pulse voltammetry of the low-spin complex in acetone revealed a quasi-reversible $Fe^{II/III}$ oxidation with $E_{1/2}$ = 695 mV (versus Fc/Fc^+), which is within error of the $Fe^{II/III}$ oxidation potential of $[Fe(bpy)_3]^{2+}$ in acetonitrile.[15] Therefore, from the approximation in eq. 2.6, the values of the $^5T_2/^1A_1$ free energy gaps in $[Fe(bpy)_3]^{2+}$ and $[Fe(phen)_3]^{2+}$ are identical at -7300 ± 730 cm^{-1}. The origin of the oxidation potential observed in $[Fe(2\text{-OMe-phen})_3]^{2+}$ (Figure 2.12b) is more

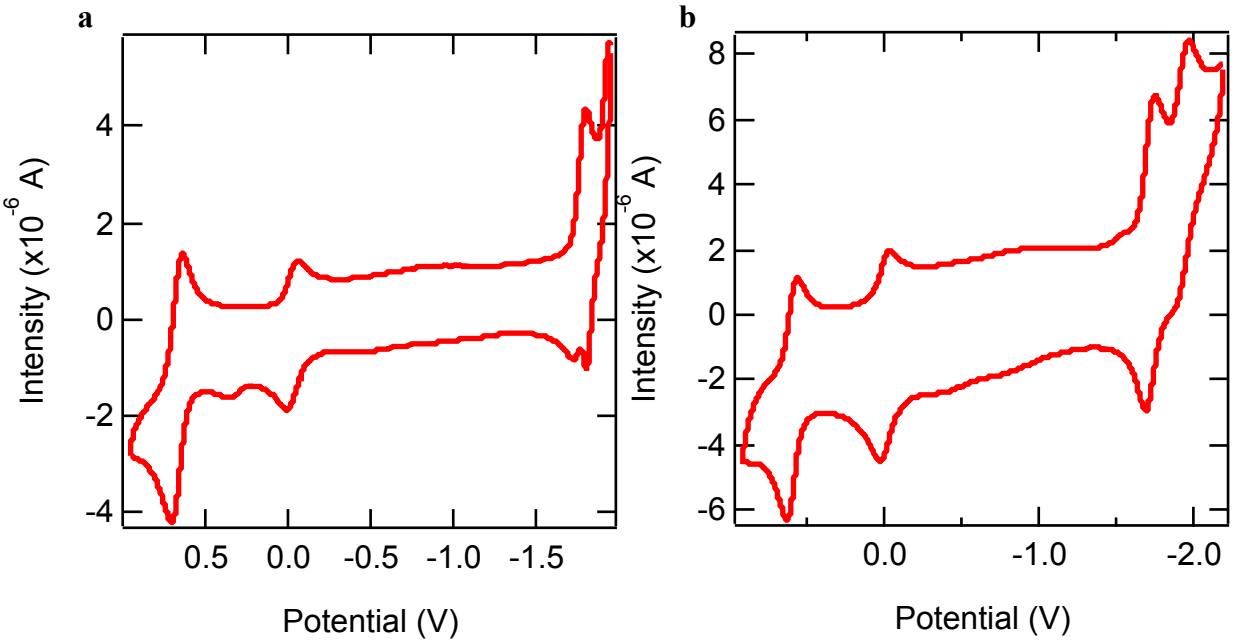

Figure 2.12. Cyclic voltammograms of (a) $[Fe(phen)_3](BF_4)_2$ and (b) $[Fe(2\text{-OMe-phen})_3](BF_4)_2$ in acetone solutions with 0.1 M $TBAPF_6$ and referenced internally to the Fc/Fc^+ couple.

ambiguous than that observed for a completely low-spin complex because 95% of the SCO complex is populating the $^5T_2$ state at room temperature. As such, when eq. 2.6 is used to approximate $\Delta G°$, a completely unrealistic value of -6570 ± 660 cm^{-1} is obtained, one that is in complete disagreement with the value calculated from magnetic measurements and if accurate, would indicate that $[Fe(2\text{-}OMe\text{-}phen)_3]^{2+}$ is a low-spin complex, which is clearly not true.

2.3.6. Variable-temperature ground-state absorption spectroscopy

The next step in unequivocally determining the Marcus parameters for ground-state recovery in the SCO complex $[Fe(2\text{-}OMe\text{-}phen)_3]^{2+}$ is to measure k_{nr} as a function of temperature. Our group has well-established procedures for collecting these data on LS Fe(II) complexes,[15,16] however the experiment is slightly more complicated in a spin-crossover complex. For the former class of compounds, to observe the decay of the photo-induced $^5T_2$ state down to the $^1A_1$ ground state, a pump wavelength is chosen that will achieve excitation into the $^1A_1 \rightarrow$ MLCT absorption feature, as in almost all known Fe(II) polypyridyls the transiently populated MLCT manifold undergoes ultrafast deactivation into the HS $^5T_2$ ligand field state, so when observing kinetics on timescales longer than ~10 ps, only ground-state recovery will be observed. However, for spin-crossover complexes, in which both the $^1A_1$ and $^5T_2$ states are populated, care must be taken to selectively excite into an absorption feature that originates from the $^1A_1$ to remain comparable to the kinetic studies on completely low-spin Fe(II) polypyridyls, as there are some studies that have reported photo-induced kinetics following excitation into a $^5T_2$-based absorption feature in spin-crossover complexes.[40,49] Therefore, to choose pump/probe combinations for VT transient

absorption, variable-temperature steady-state absorption was collected on [Fe(2-OMe-phen)$_3$](BF$_4$)$_2$ in an acetone solution.

At room temperature, 95% of [Fe(2-OMe-phen)$_3$]$^{2+}$ in solution is in the ^{5}T$_2$ state (Figure 2.10b), and correspondingly its ground-state absorption spectrum is typical of a high-spin complex: a broad absorption feature arising from ^{5}T$_2$ → ^{5}MLCT transitions (Figure 2.13a). As the sample is cooled (i.e. the population of the ^{1}A$_1$ state increases) the molar absorptivity of the MLCT feature increases and shifts to lower energies (Figure 2.13a), a result of the shorter Fe-N bond lengths in the low-spin state and higher oscillator strength of the ^{1}A$_1$ → ^{1,3}MLCT transitions. At the lowest temperature measured, the absorption spectrum of [Fe(2-OMe-phen)$_3$]$^{2+}$ more closely resembles that of the low-spin complex [Fe(phen)$_3$]$^{2+}$ than that of the high-spin [Fe(2-Cl-phen)$_3$]$^{2+}$ (Figure 2.7a), as the majority of the complex is now low-spin.

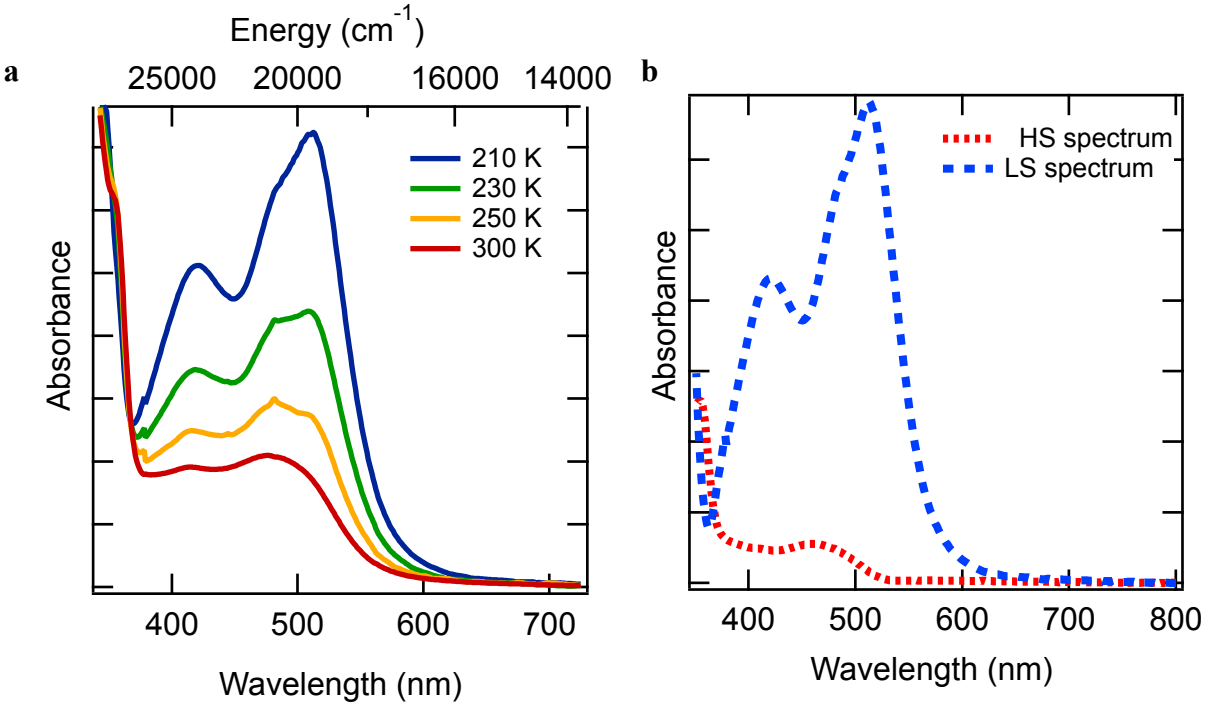

Figure 2.13. (a) Steady-state absorption spectrum of [Fe(2-OMe-phen)$_3$](BF$_4$)$_2$ in acetone collected at four different temperatures. (b) Calculated spectra of the completely high-spin and low-spin forms of [Fe(2-OMe-phen)$_3$](BF$_4$)$_2$ in acetone.

By extending the classic form of Beer's law to include absorption from both a low- and high-spin species in the same sample[40] (eq. 2.16), the data shown in Figure 2.13a can be fit using global analysis to extract out the predicted extinction coefficients of the completely low- and high-spin forms of $[Fe(2\text{-}OMe\text{-}phen)_3]^{2+}$ (Figure 2.13b), providing a guide to time-resolved absorption studies. The $^5T_2$ predicted spectrum lacks virtually any absorption at wavelengths redder than 540 nm, while the $^1A_1$ absorbs strongly from the near-UV to ~600 nm. Even in the range through which the absorption features of the $^1A_1$ and $^5T_2$ states overlap, i.e. bluer than 540 nm, the $^1A_1$ state has an extinction coefficient between 5-50 times higher than that of the $^5T_2$. Therefore, selective excitation from the $^1A_1$ may be achieved by using almost any pump wavelength in the visible region.

2.3.7. Variable-temperature transient absorption spectroscopy: A low-spin Fe(II) complex

For the spin-crossover complex $[Fe(2\text{-}OMe\text{-}phen)_3]^{2+}$, measuring k_{nr} as a function of temperature will provide the last experimentally-accessible variable necessary to determine the values of λ and H_{ab} that define the $^5T_2 \rightarrow {}^1A_1$ decay process. Since we would like to relate these findings to ground-state recovery of low-spin Fe(II) polypyridyl complexes in general, the Marcus parameters of the low-spin member of the $[Fe(2\text{-}R\text{-}phen)_3]^{2+}$ series, $[Fe(phen)_3]^{2+}$, will be determined in the manner described in our 2019 *Chemical Science* report[15] to have the closest structural and electronic analog possible. Then, the GSR dynamics of the SCO complex will be presented and put the approximated Marcus values into context.

Ground-state recovery of $[Fe(phen)_3](BF_4)_2$ in acetone solution was monitored at 510 nm following $^1A_1 \rightarrow {}^{1,3}$MLCT excitation at 537 nm at five temperature points from 210-293 K (Figure 2.14a). At room temperature, the lifetime of the $^5T_2$ excited state was measured as 1.20 ± 0.04 ns, within error of the 1.1 ± 0.1 ns lifetime that Tribollet et al. found for the same complex in acetonitrile,[49] as well as the lifetime of $[Fe(bpy)_3]Cl_2$ in acetone (Table 2.4).[16] The Arrhenius and

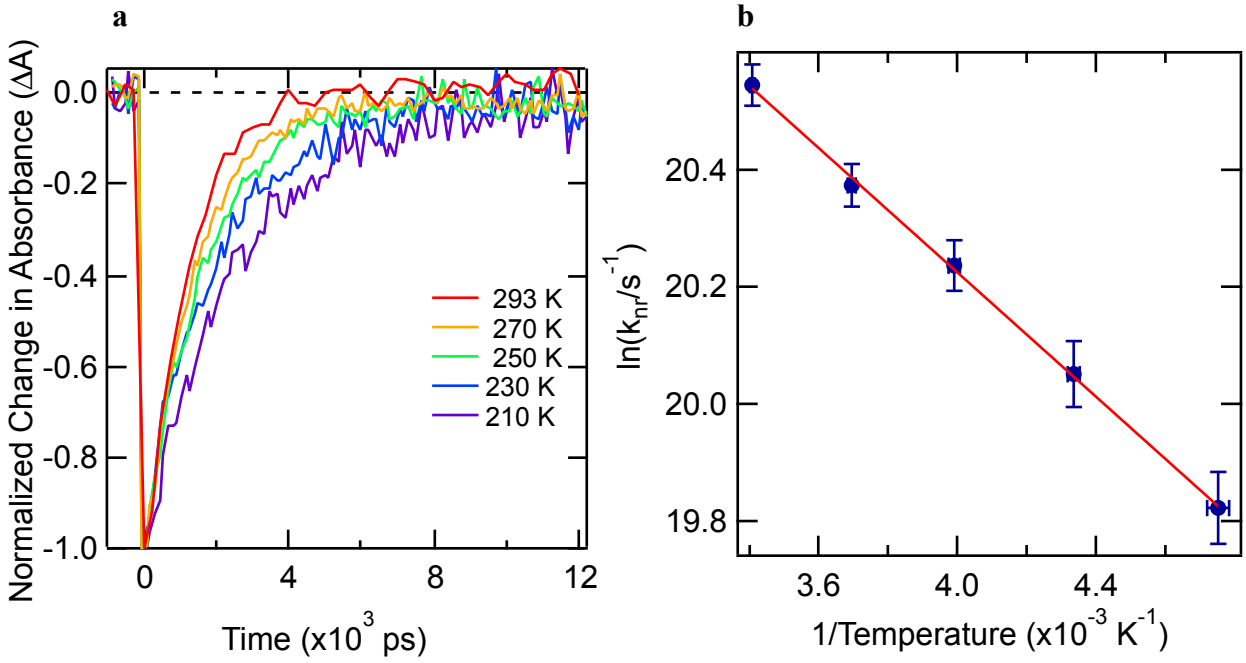

Figure 2.14. (a) Ground-state recovery kinetics of $[Fe(phen)_3]^{2+}$ in acetone solution monitoring at λ_{probe} = 510 nm following $^1A_1 \rightarrow {}^{1,3}$MLCT excitation at λ_{pump} = 537 nm. (b) Arrhenius plot for ground-state recovery of $[Fe(phen)_3]^{2+}$ in acetone from 210-293 K. The solid line represents a fit to the Arrhenius model to yield A = 200 ± 15 ps^{-1} and E_a = 370 ± 20 cm^{-1}. Plot shown is the average between two different data sets.

Marcus values obtained for $[Fe(phen)_3](BF_4)_2$ will be discussed in comparison to $[Fe(bpy)_3]^{2+}$, as our group has established that these parameters are not drastically altered upon introduction of substituents for $[Fe(bpy')_3]^{2+}$ (where bpy' = 4,4'-dimethyl-2,2'-bipyridine or 4,4'-di-*tert*-butyl-

Table 2.4. Summary of electrochemical and variable temperature transient absorption measurements for two low-spin iron(II) complexes.

Complex	ΔE^{ox} (V)	τ_{RT} (ns)	E_a (cm^{-1})	A (ps^{-1})
$[Fe(bpy)_3]Cl_2$*	0.68	1.13 ± 0.05	295 ±10	255 ± 20
$[Fe(phen)_3](BF_4)_2$	0.69	1.20 ± 0.04	370 ± 20	200 ± 15

*From Monica Carey's dissertation, reference 16.

2,2'-bipyridine), but are when the coordination environment is changed, i.e. in $[Fe(terpy)_2]^{2+}$ and $[Fe(dcpp)_2]^{2+}$ (terpy = 2,2':6,2"-terpyridine and dcpp = 2,6-bis(2-carboxypyridyl)pyridine).

Despite the practically identical room temperature behavior between $[Fe(phen)_3](BF_4)_2$ and $[Fe(bpy)_3]Cl_2$ (Table 2.4), differences between these two prototypical low-spin Fe(II) complexes become apparent when the GSR dynamics are studied as a function of temperature. An Arrhenius analysis of the temperature dependence of k_{nr} for GSR in $[Fe(phen)_3](BF_4)_2$ yielded an activation energy for the $^5T_2 \rightarrow {}^1A_1$ process of 370 ± 20 cm^{-1}, significantly larger than that found for $[Fe(bpy)_3]Cl_2$ in acetone (Table 2.4), as well as the activation energies measured for the entire series of substituted bpy complexes.[15] The larger barrier to GSR in $[Fe(phen)_3](BF_4)_2$ is most likely not a consequence of a significant change in ΔG° between the $^1A_1$ and $^5T_2$ states relative to the bpy-based complexes, as the oxidation potential of $[Fe(phen)_3](BF_4)_2$ is essentially identical to that of $[Fe(bpy)_3]^{2+}$ (Table 2.4) Instead, the larger barrier is more likely a consequence of the increased rigidity of phen versus bpy, which is also the reasoning behind the fact that the rate of nonradiative decay from the ^{3}MLCT in $[Ru(phen)_3]^{2+}$ is almost double that of $[Ru(bpy)_3]^{2+}$.[50] Accordingly, the value of λ in $[Fe(phen)_3]^{2+}$, is larger than that of $[Fe(bpy)_3]Cl_2$ (Table 2.5), but due to the large error bars introduced by the approximation of ΔG°, it is not significantly so. On the other hand, the electronic coupling constant for $[Fe(phen)_3]^{2+}$ is significantly smaller than that of $[Fe(bpy)_3]^{2+}$, and therefore their $|H_{ab}|^4/\lambda$ ratios are also outside of error from one another. The origin of these differences is not immediately obvious, as H_{ab} reflects the second order spin-orbit coupling

Table 2.5. Marcus parameters for two low-spin Fe(II) polypyridyl complexes in acetone at room temperature. ΔG° was found from the electrochemical approximation discussed in the text.

Complex	ΔG° (cm^{-1})	λ (cm^{-1})	H_{ab} (cm^{-1})	$\|H_{ab}\|^4/\lambda$
$[Fe(bpy)_3]Cl_2$	-7300 ± 730	10900 ± 1000	4.2 ± 0.2	1/(36 ± 5)
$[Fe(phen)_3](BF_4)_2$		11400 ± 800	3.6 ± 0.1	1/(20 ± 4)

*From Monica Carey's dissertation, reference 16.

between the $^5T_2$ and $^1A_1$ through a ^3T state, and therefore may suggest that, contrary to what the oxidation potentials suggest, the ligand field strength in $[Fe(phen)_3]^{2+}$ is not identical to that of $[Fe(bpy)_3]^{2+}$. However, we are unable to definitively reach this conclusion without a more accurate measure of $\Delta G°$ in these two low-spin complexes.

Carey et al. hypothesized that the magnitude of the $|H_{ab}|^4/\lambda$ ratios provide unique insight into the nature of the nuclear coordinate, especially because these values can be found directly from the experimentally-determined Arrhenius data, without making any approximations.[15] The intermediate $|H_{ab}|^4/\lambda$ ratio of $[Fe(phen)_3]^{2+}$, between that of $[Fe(bpy)_3]^{2+}$ (Table 2.5) and $[Fe(terpy)_2]^{2+}$ $(1/14 \pm 9)$[15], may be an indication that the increased rigidity of the phen ligand has an effect on the geometric distortions that drive the kinetics of GSR. However, the fact that the $|H_{ab}|^4/\lambda$ ratios, E_a, and A values are relatively similar between $[Fe(bpy)_3]^{2+}$ and $[Fe(phen)_3]^{2+}$ (i.e. not as drastically different as these parameters are between $[Fe(bpy)_3]^{2+}$, $[Fe(terpy)_3]^{2+}$, and $[Fe(dcpp)_2]^{2+}$)[16], is a good indication that describing the nuclear coordinate of phenanthroline-based Fe(II) complexes will provide relevant nuclear coordinate information for a broader class of Fe(II) chromophores.

2.3.8. Variable-temperature transient absorption spectroscopy: A spin-crossover Fe(II) complex

Guided by the previously discussed variable-temperature steady-state absorption measurements, the kinetics for ground-state recovery of $[Fe(2\text{-}OMe\text{-}phen)_3](BF_4)_2$ as a function of temperature were measured using nanosecond VT-TA (Figure 2.15a). At room temperature, the excited-state lifetime in acetone was 15 ± 1 ns, much longer than the $^5T_2$ lifetime in $[Fe(phen)_3](BF_4)_2$. Dropping in temperature, the lifetime at 210 K extended to 1.00 ± 0.01 μs, indicating a much larger barrier to GSR in this SCO complex than in all previously measured low-spin complexes. As a SCO complex, the observed rate constant for excited-state decay (k_{obs}) in

$[Fe(2\text{-}OMe\text{-}phen)_3]^{2+}$ is an amalgam of the rate constants for both the $^5T_2 \rightarrow {}^1A_1$ and $^1A_1 \rightarrow {}^5T_2$ processes (k_{HL} and k_{LH} respectively):[51]

$$k_{obs} = k_{HL} + k_{LH} \tag{2.17}$$

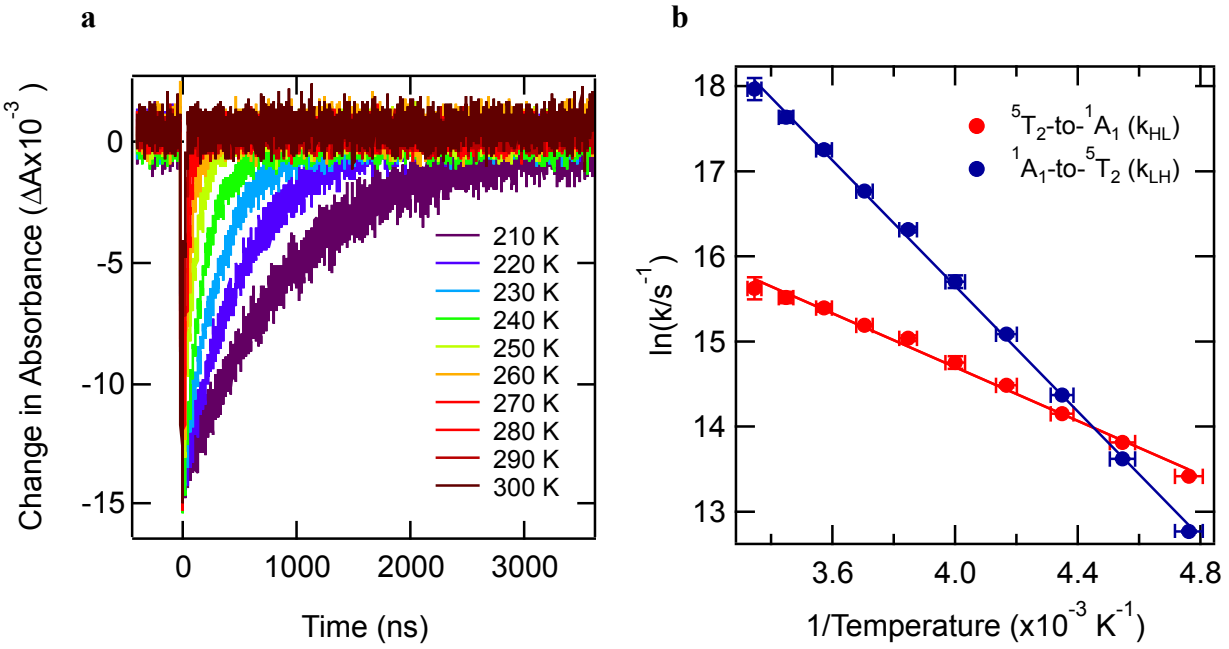

Figure 2.15. (a) Variable-temperature time-resolved absorption kinetic traces of $[Fe(2\text{-}OMe\text{-}phen)_3](BF_4)_2$ in an acetone solution. Over the temperature range 260-300 K, the kinetics were monitored at 510 nm following $^1A_1 \rightarrow$MLCT excitation at 540 nm and at lower temperatures, 210-250 K, the kinetics were monitored at 570 nm following $^1A_1 \rightarrow$MLCT excitation at 510 nm. (b) Arrhenius plots of k_{HL} (red) and k_{LH} (blue), with the solid lines as fits to the Arrhenius model. For k_{HL}, $E_a = 1100 \pm 20$ cm^{-1} and $A = 1.33 \times 10^9$ s^{-1} ($R^2 = 0.99$). For k_{LH} $E_a = 2560 \pm 80$ cm^{-1} and $A = 1.58 \times 10^{13}$ s^{-1} ($R^2 = 0.99$)

As such, we must extract the rate constants for each process from k_{obs} using the equilibrium constants determined from the previously discussed equilibrium constants:

$$K_{HL} = \frac{k_{LH}}{k_{HL}} \tag{2.18}$$

A subsequent Arrhenius analysis (Figure 2.15b) revealed a barrier to the $^5T_2 \rightarrow {}^1A_1$ conversion of 1100 ± 20 cm^{-1}, almost three times larger than the measured barrier in $[Fe(phen)_3](BF_4)_2$ (Figure 2.14c). Even larger, as expected, is the activation energy for the reverse process, the $^1A_1 \rightarrow {}^5T_2$

conversion ($E_a = 2560 \pm 200$ cm^{-1}), a process that does not occur in LS complexes. There are a few other reports of activation energies for the $^5T_2 \rightarrow {}^1A_1$ conversion in SCO complexes in solution; however the observed barrier in $[Fe(2\text{-OMe-phen})_3]^{2+}$ falls mid-range of those in the literature.[40,51,52]

Finally, using equations 2.3 and 2.4, λ and H_{ab} were calculated at every temperature point from the frequency factor and activation energy, inputting the ΔG° values found from magnetic susceptibility measurements. The electronic coupling constant was essentially invariable over the entire temperature range at 1.4 ± 0.2 cm^{-1} (Figure 2.16a) while the reorganization energies were moderately temperature dependent: 3300 ± 100 cm^{-1} at 300 K and 4600 ± 100 cm^{-1} at 210 K (*Figure 2.16*b). These experimentally-determined values for λ and H_{ab} for a SCO complex confirm that the magnitudes of the values for λ and H_{ab} predicted from ultrafast VT-TA and electrochemistry for $[Fe(bpy')_3]^{2+}$ are reasonable, and the $^5T_2 \rightarrow {}^1A_1$ conversion occurs within the

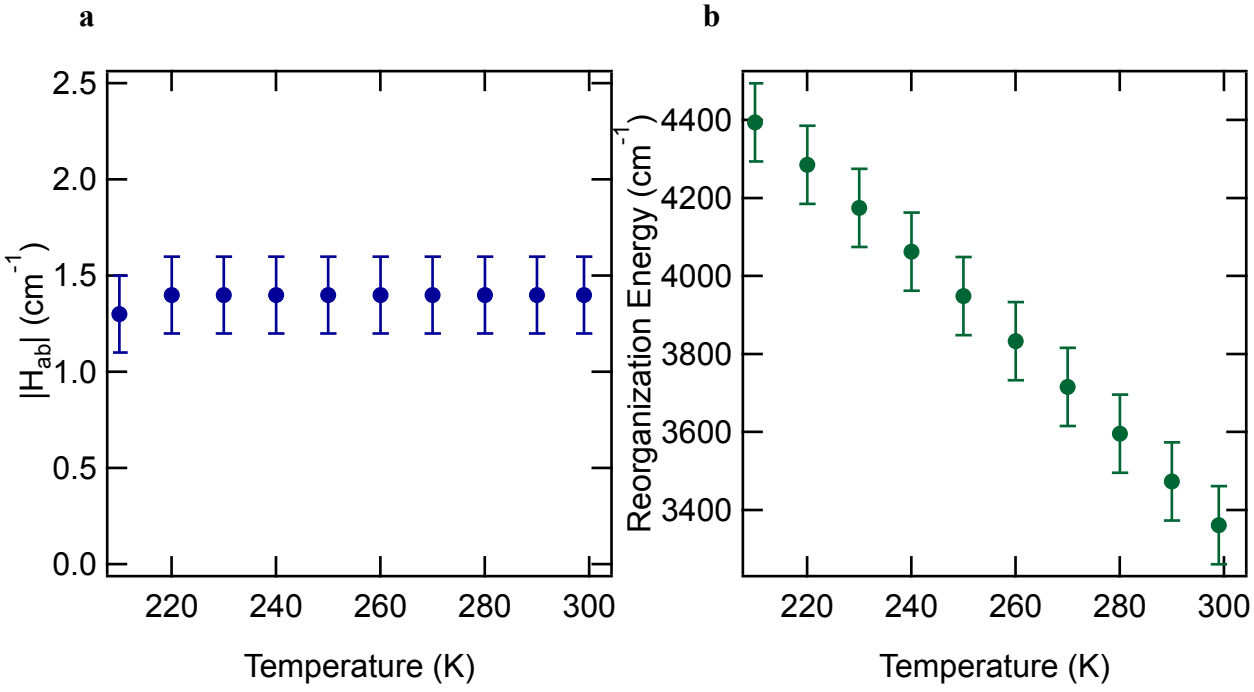

Figure 2.16. Calculated Marcus parameters found for $[Fe(2\text{-OMe-phen})_3](BF_4)_2$ in acetone from 210-300 K. (a) The electronic coupling constant (H_{ab}) and (b) The reorganization energy (λ) for the $^5T_2 \rightarrow {}^1A_1$ conversion.

Marcus normal region. The value for H_{ab} predicted previously from free ion terms by Jortner,[53] 170 cm^{-1}, is not accurate to describe the electronic coupling between the $^1A_1$ and $^5T_2$ states.

The approximately three times smaller value for λ in $[Fe(2\text{-}OMe\text{-}phen)_3]^{2+}$ than approximated for the low-spin complexes at room temperature makes sense when the relative magnitudes of the nuclear distortion between the $^5T_2$ and $^1A_1$ states ($\Delta Q_{HS/LS}$) are considered. Due to the steric and electronic perturbations from the 2-OMe substitution, $[Fe(2\text{-}OMe\text{-}phen)_3]^{2+}$ cannot adopt a $^1A_1$ geometry that is contracted as is possible in the low-spin state in $[Fe(phen)_3]^{2+}$. This is shown schematically in Figure 2.17: if the magnitude of $\Delta Q_{HS/LS}$ is decreased between a

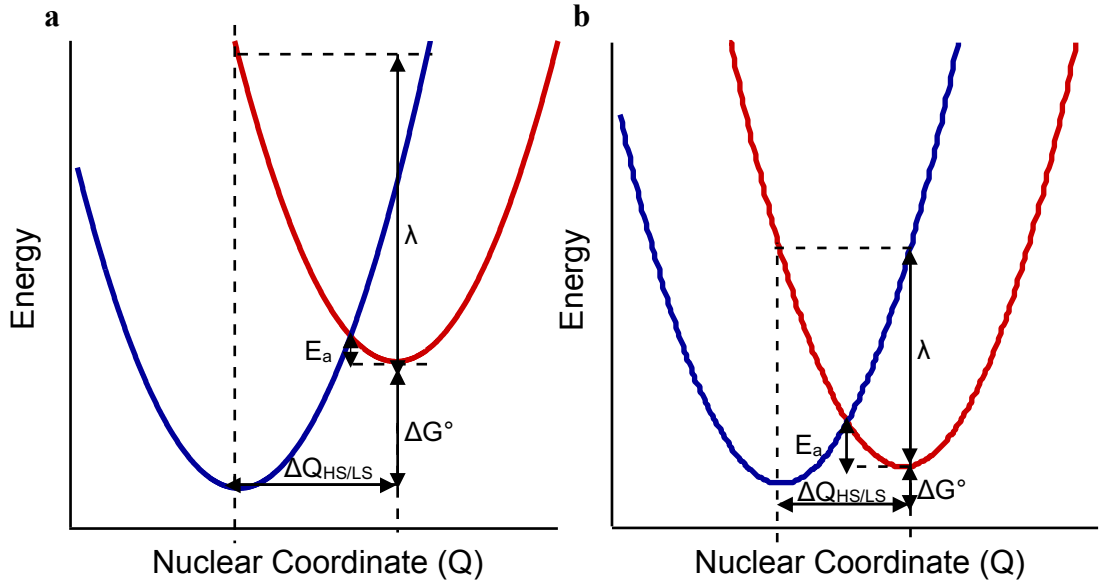

Figure 2.17. Hypothetical potential energy surfaces for the $^1A_1$ (blue traces) and $^5T_2$ (red traces) states for (a) a low-spin Fe(II) polypyridyl complex and (b) a spin-crossover complex.

low-spin complex (Figure 2.17a) to a spin-crossover complex (Figure 2.17b), the reorganization energy will decrease. This schematic also accounts for the smaller $^5T_2/^1A_1$ energy gap in a spin-crossover complex than a low-spin complex, which contributes to the larger barrier measured in the former. The lower H_{ab} value found in $[Fe(2\text{-}OMe\text{-}phen)_3](BF_4)_2$ than in the low-spin complexes may reflect the decreased ligand field strength, which should attenuate the degree of second-order coupling between the $^1A_1$ and $^5T_2$ states.

2.4. Concluding remarks

In this chapter, the thermodynamics of the equilibrium between the $^1A_1$ and $^5T_2$ states in a *tris*-polypyridyl Fe(II) spin-crossover complex, $[Fe(2\text{-OMe-phen})_3]^{2+}$, were determined in solution using variable-temperature magnetic measurements. When coupled to variable-temperature transient absorption spectroscopy, these experiments enabled a complete description of the Marcus parameters associated with the $^5T_2 \rightarrow {}^1A_1$ ground-state recovery process in the same complex, a feat that is currently impossible for low-spin Fe(II) complexes due to the inability to measure the $^5T_2 \rightarrow {}^1A_1$ driving force in these systems. The experimental determination of the values for λ and H_{ab} associated with GSR in $[Fe(2\text{-OMe-phen})_3]^{2+}$ is not only the first example of doing so, but also confirms the assumptions made in a previous report about the magnitudes of these values in low-spin Fe(II) complexes. With these experimental data in hand, we can now begin to dissect the reorganization energy into the vibrational modes that it reflects, as we are ultimately interested in defining the kinetically relevant geometric motions associated with excited-state evolution in Fe(II) polypyridyls. Most likely this will need to be done in collaboration with computational chemists, however in the next chapter of this dissertation I will attempt to do so through a mixture of experiment and theory. Expanding the approach outlined in this chapter to other Fe(II) SCO systems will demonstrate how general the values λ and H_{ab} found for $[Fe(2\text{-OMe-phen})_3]^{2+}$ are, and if changing the coordination environment (i.e. the nature of the donor atoms or the denticity of the ligands) will profoundly change the nature of the nuclear coordinate of GSR.

APPENDIX

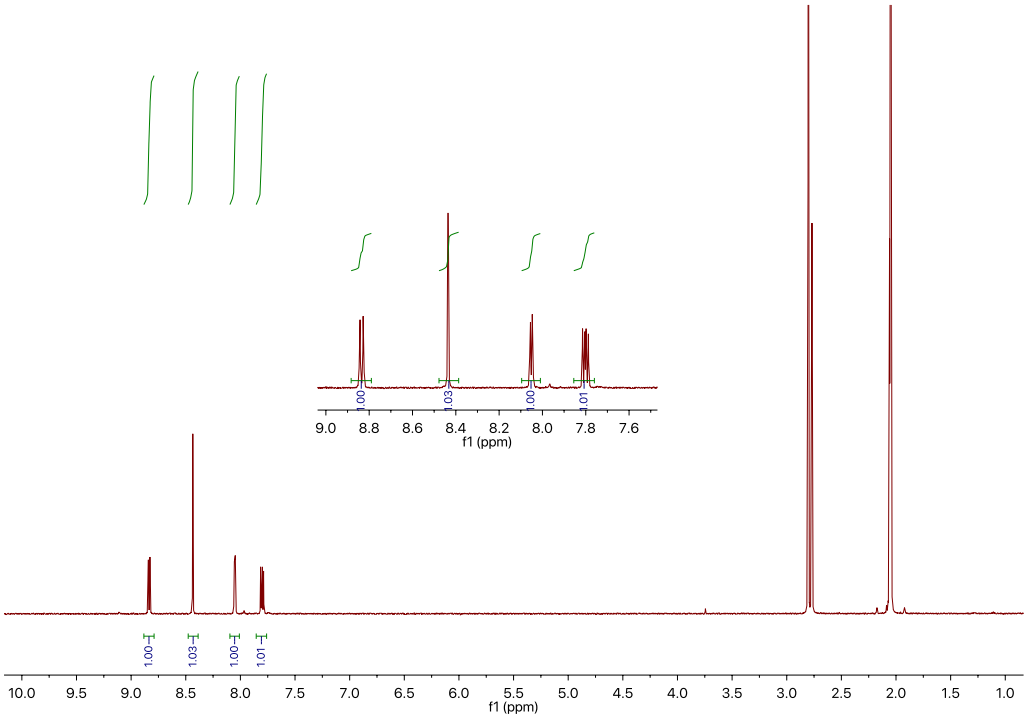

Figure 2.18. ^{1}H NMR of $[Fe(phen)_3](BF_4)_2$ in acetone-d_6.

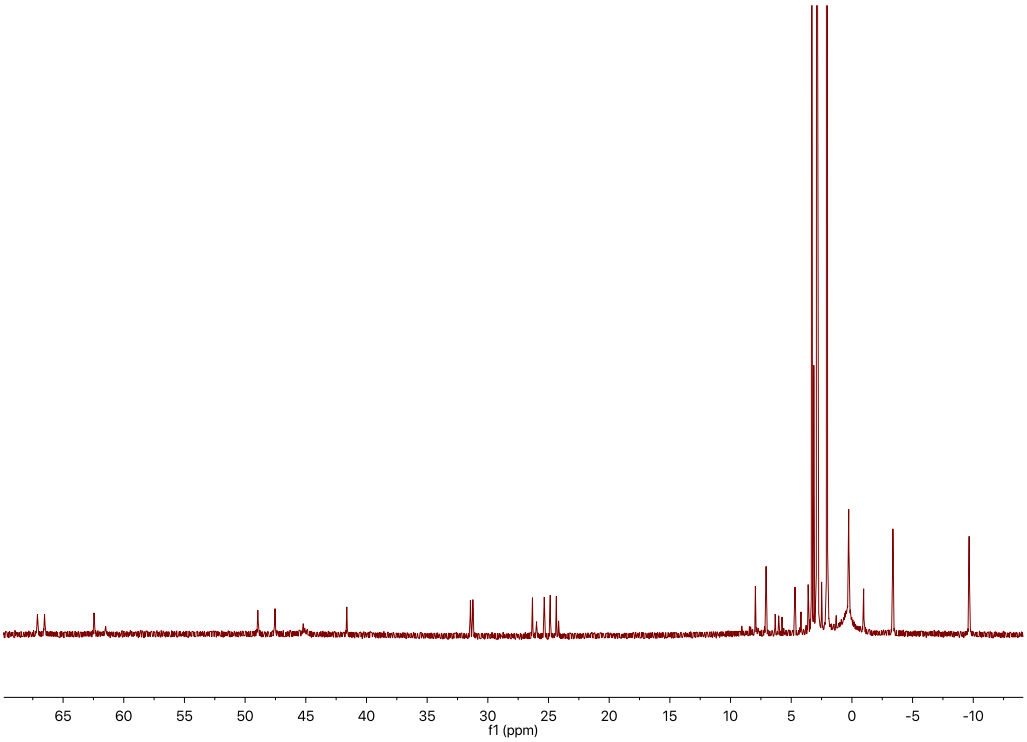

Figure 2.19. ^{1}H NMR of $[Fe(2\text{-}OMe\text{-}phen)_3](BF_4)_2$ in acetone-d_6.

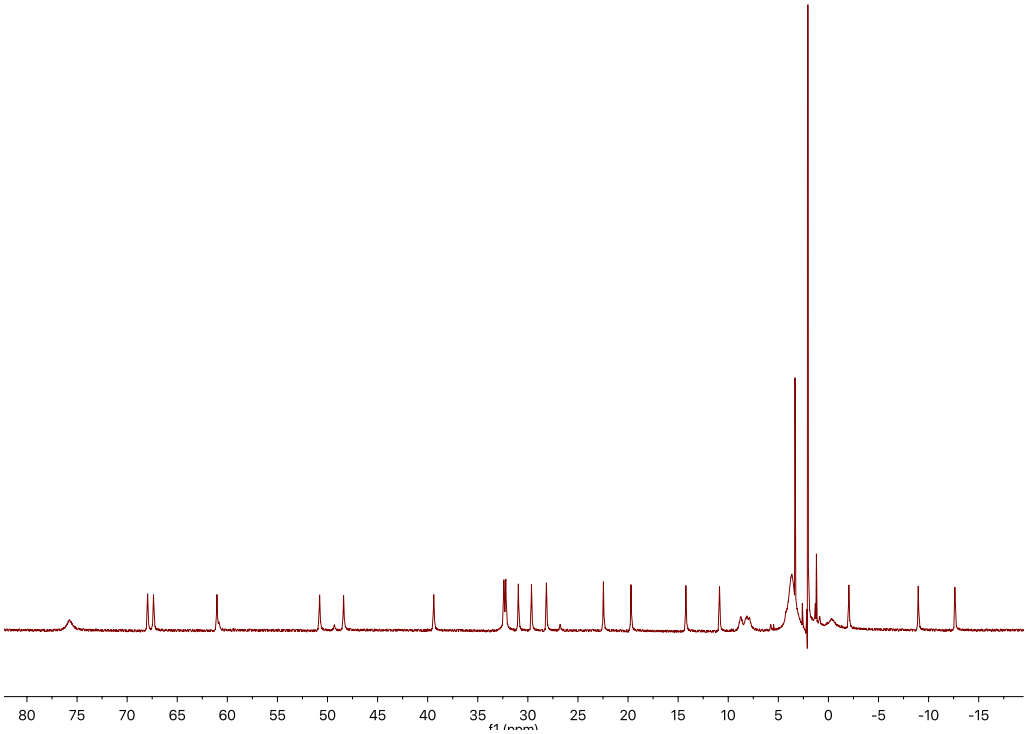

Figure 2.20. ^{1}H NMR of $[Fe(2\text{-}Cl\text{-}phen)_3](BF_4)_2$ in acetone-d_6.

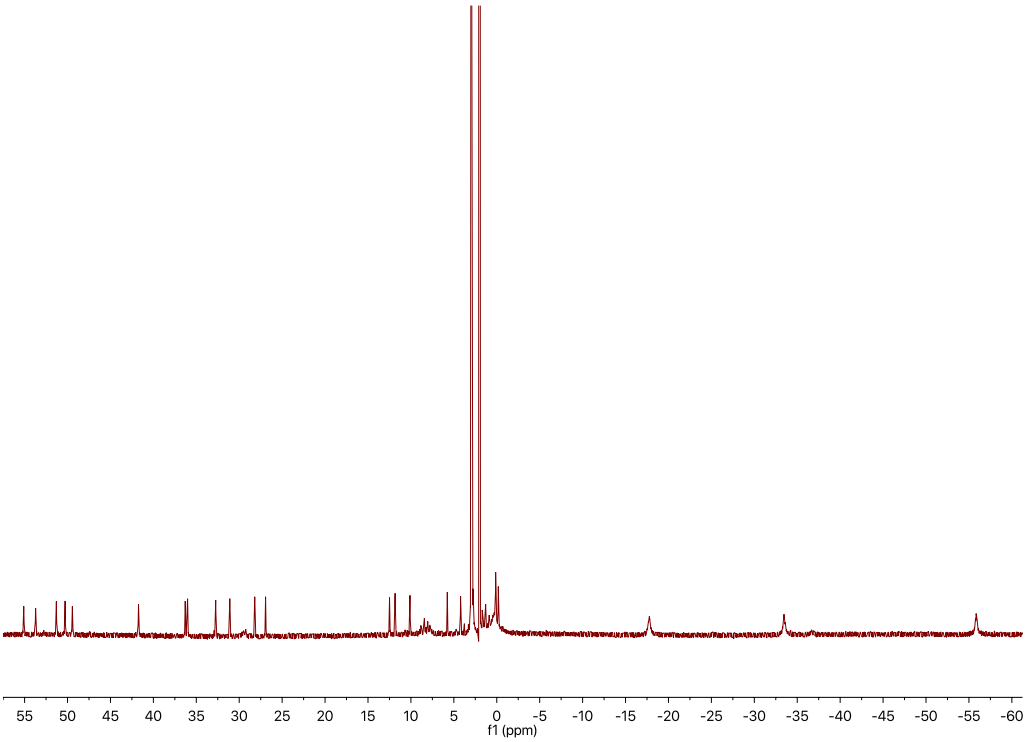

Figure 2.21. ^{1}H NMR of $[Fe(2\text{-}Me\text{-}phen)_3](BF_4)_2$ in acetone-d_6.

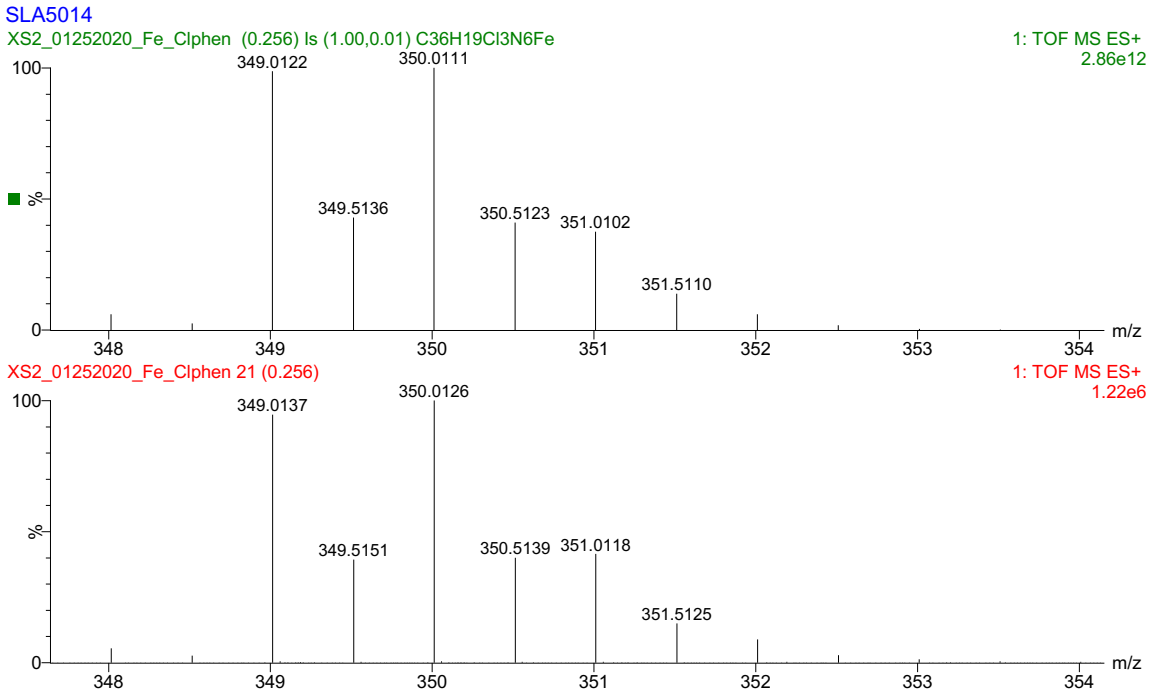

Figure 2.22. ESI-MS of $[Fe(2\text{-Cl-phen})_3](BF_4)_2$. Top: calculated isotope pattern for $[M-2(BF_4)]^{2+}$ ($C_{36}H_{21}N_6Cl_3Fe$). Bottom: experimental result.

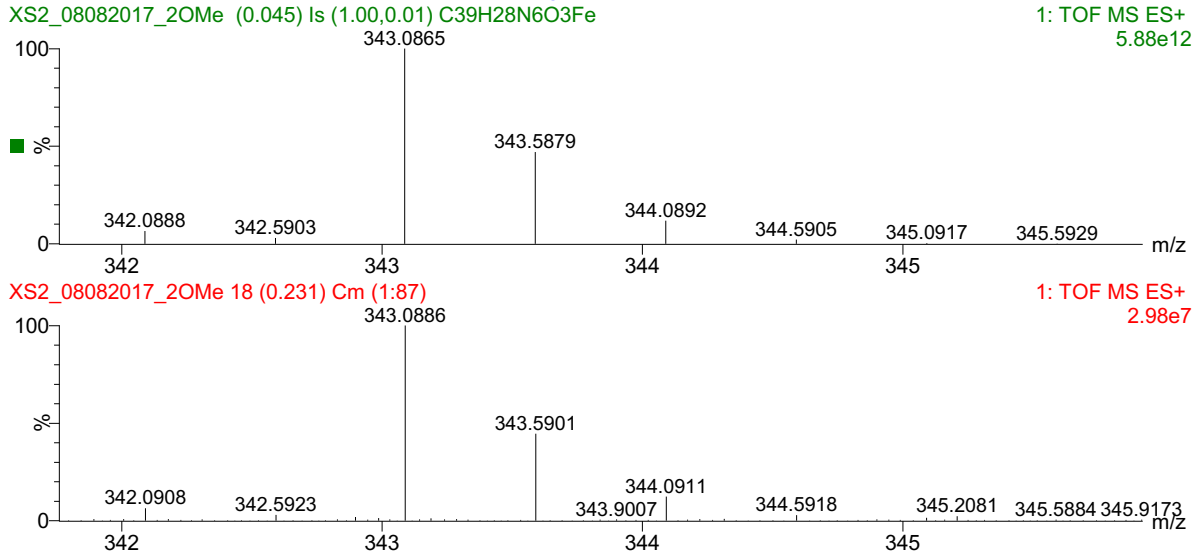

Figure 2.23. ESI-MS of $[Fe(2\text{-OMe-phen})_3](BF_4)_2$. Top: calculated isotope pattern for $[M-2(BF_4)]^{2+}$ ($C_{39}H_{30}N_6O_3Fe$). Bottom: experimental result.

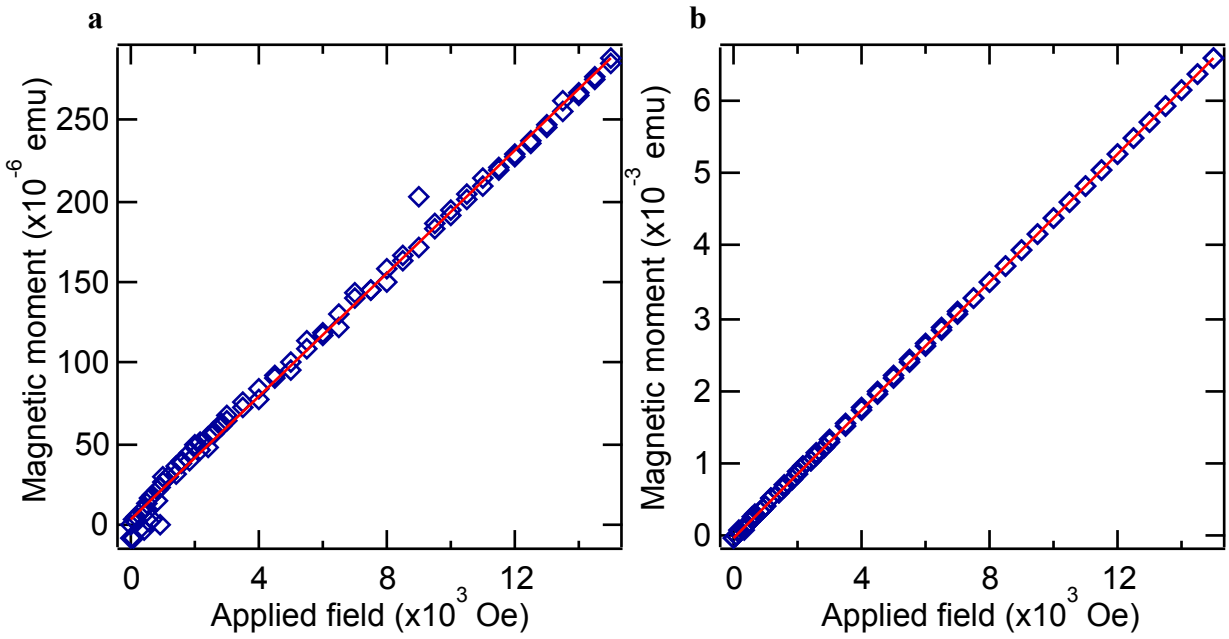

Figure 2.24. Field dependence of magnetic moment of crystalline samples of (a) [Fe(2-OMe-phen)$_3$](BF$_4$)$_2$ and (b) [Fe(2-Cl-phen)$_3$](BF$_4$)$_2$. Both samples were collected at 100 K and the red lines are fits of the data to a linear regression.

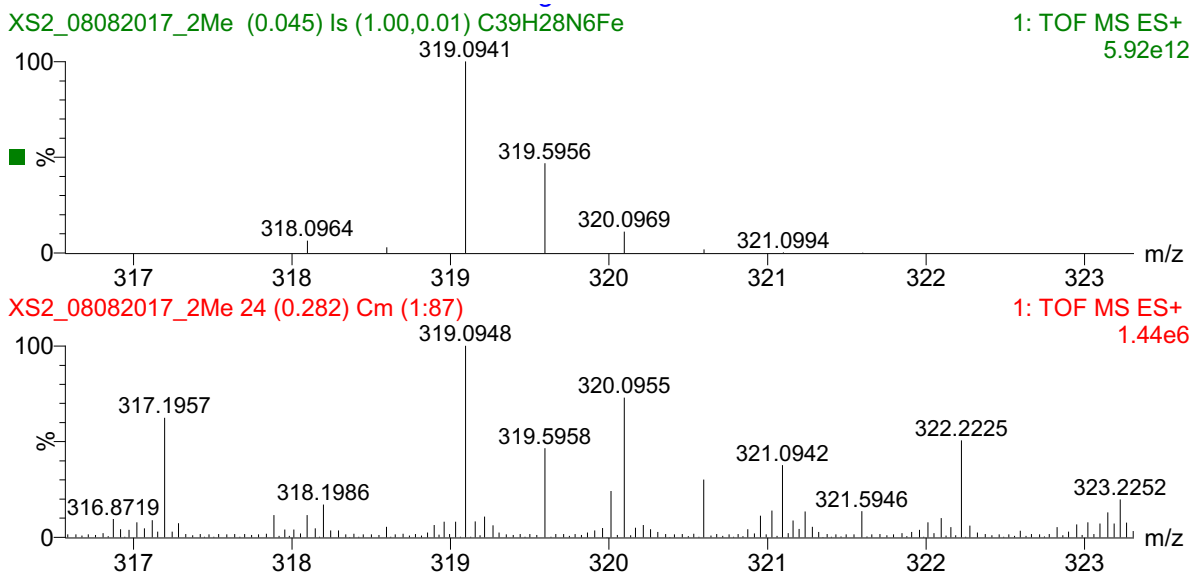

Figure 2.25. ESI-MS of [Fe(2-Me-phen)$_3$](BF$_4$)$_2$. Top: calculated isotope pattern for [M-2(BF$_4$)]$^{2+}$ (C$_{39}$H$_{30}$N$_6$Fe). Bottom: experimental result.

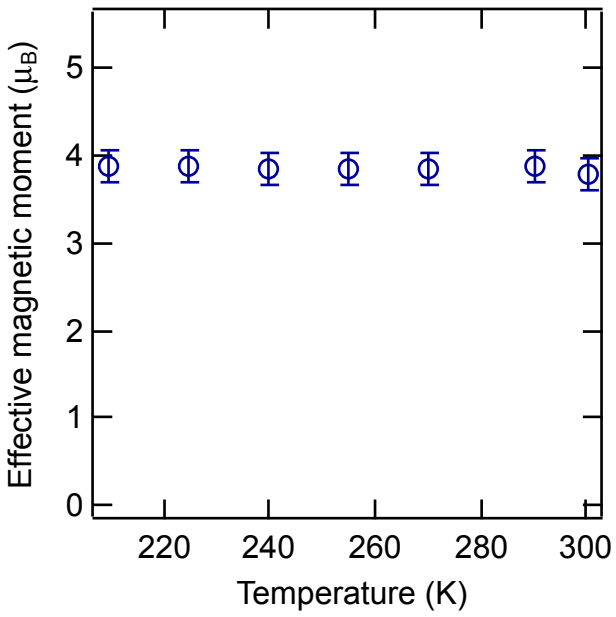

Figure 2.26. Effective magnetic moment of a 4 mM solution of $Cr(acac)_3$ in acetone using variable-temperature Evans method.

REFERENCES

REFERENCES

1. Brady, C.; McGarvey, J. J.; McCusker, J. K.; Toftlund, H.; Hendrickson, D. N. Time-Resolved Relaxation Studies of Spin Crossover Systems in Solution. In *Spin Crossover Transition Metal Compounds III*; Gütlich, P.; Goodwin, H. A., Eds.; Springer: Berlin, 2004, pp 1–22. https://doi.org/10.1007/b95420.

2. Létard, J.-F.; Guionneau, P.; Goux-Capes, L. Towards Spin Crossover Applications. In *Spin Crossover Transition Metal Compounds III*; Gütlich, P.; Goodwin, H. A., Eds.; Springer: Berlin, 2004, pp 221–249. https://doi.org/10.1007/b95429.

3. Senthil Kumar, K.; Ruben, M. Emerging Trends in Spin Crossover (SCO) Based Functional Materials and Devices. *Coord. Chem. Rev.* **2017**, *346*, 176–205. https://doi.org/10.1016/j.ccr.2017.03.024.

4. Claude, J. P.; Meyer, T. J. Temperature Dependence of Nonradiative Decay. *J. Phys. Chem.* **1995**, *99*, 51–54. https://doi.org/10.1021/j100001a010.

5. Caspar, J. V.; Westmoreland, T. D.; Allen, G. H.; Meyer, T. J.; Bradley, P. G.; Woodruff, W. H. Molecular and Electronic Structure in the Metal-to-Ligand Charge-Transfer Excited States of d^6 Transition-Metal Complexes in Solution. *J. Am. Chem. Soc.* **1984**, *106*, 3492–3500. https://doi.org/10.1021/ja00324a017.

6. Bressler, C.; Milne, C.; Pham, V.; ElNahhas, A.; van der Veen, R. M.; Gawelda, W.; Johnson, S.; Beaud, P.; Grolimund, D.; Kaiser, M.; Borca, C. N.; Infold, G.; Abela, R.; Chergui, M. Femtosecond XANES Study of the Light-Induced Spin Crossover Dynamics in an Iron(II) Complex. *Science* **2009**, *323*, 489–492.

7. Collet, E.; Cammarata, M. Disentangling Ultrafast Electronic and Structural Dynamics with X-Ray Lasers. *Chem. Eur. J.* **2018**, *24*, 15696–15705. https://doi.org/10.1002/chem.201802105.

8. Britz, A.; Gawelda, W.; Assefa, T. A.; Jamula, L. L.; Yarranton, J. T.; Galler, A.; Khakhulin, D.; Diez, M.; Harder, M.; Doumy, G.; et al. Using Ultrafast X-Ray Spectroscopy to Address Questions in Ligand-Field Theory: The Excited State Spin and Structure of $[Fe(dcpp)_2]^{2+}$. *Inorg. Chem.* **2019**, *58*, 9341–9350. https://doi.org/10.1021/acs.inorgchem.9b01063.

9. Zhang, K.; Ash, R.; Girolami, G. S.; Vura-Weis, J. Tracking the Metal-Centered Triplet in Photoinduced Spin Crossover of $[Fe(phen)_3]^{2+}$ with Tabletop Femtosecond M-Edge XANES . *J. Am. Chem. Soc.* **2019**, *141*, 17180–17188. https://doi.org/10.1021/jacs.9b07332.

10. Vankó, G.; Bordage, A.; Pápai, M.; Haldrup, K.; Glatzel, P.; March, A. M.; Doumy, G.; Britz, A.; Galler, A.; Assefa, T.; et al. Detailed Characterization of a Nanosecond-Lived Excited State: X-Ray and Theoretical Investigation of the Quintet State in Photoexcited $[Fe(terpy)_2]^{2+}$. *J. Phys. Chem. C* **2015**, *119*, 5888–5902. https://doi.org/10.1021/acs.jpcc.5b00557.

11. Gütlich, P.; Goodwin, H. A. Spin Crossover—An Overall Perspective; In *Spin Crossover Transition Metal Compounds III*; Gütlich, P.; Goodwin, H. A., Eds.; Springer: Berlin, 2012, pp 1–47. https://doi.org/10.1007/b13527.

12. Gawelda, W.; Pham, V. T.; Benfatto, M.; Zaushitsyn, Y.; Kaiser, M.; Grolimund, D.; Johnson, S. L.; Abela, R.; Hauser, A.; Bressler, C.; et al. Structural Determination of a Short-Lived Excited Iron(II) Complex by Picosecond X-Ray Absorption Spectroscopy. *Phys. Rev. Lett.* **2007**, *98*, 6–9. https://doi.org/10.1103/PhysRevLett.98.057401.

13. Tuchagues, J.-P.; Bousseksou, A.; Molnár, G.; McGarvey, J. J.; Varret, F. The Role of Molecular Vibrations in the Spin Crossover Phenomenon. In *Spin Crossover Transition Metal Compounds III*; Gütlich, P.; Goodwin, H. A., Eds.; Springer: Berlin, 2004, pp 84–103. https://doi.org/10.1007/b95423.

14. McCusker, J. K.; Rheingold, A. L.; Hendrickson, D. N. Variable-Temperature Studies of Laser-Initiated $^5T_2 \rightarrow {}^1A_1$ Intersystem Crossing in Spin-Crossover Complexes: Empirical Correlations between Activation Parameters and Ligand Structure in a Series of Polypyridyl Ferrous Complexes. *Inorg. Chem.* **1996**, *35*, 2100–2112. https://doi.org/10.1021/ic9507880.

15. Carey, M. C.; Adelman, S. L.; McCusker, J. K. Insights into the Excited State Dynamics of Fe(II) Polypyridyl Complexes from Variable-Temperature Ultrafast Spectroscopy. *Chem. Sci*. **2019**, *10*, 134–144. https://doi.org/10.1039/C8SC04025G.

16. Carey, M. C. Achieving a Long-Lived Charge-Separated Fe(II) Chromophore: Insights into the Role of Reorganization Energy on the Ultrafast Photophysical Processes of d^6 Polypyridyl Complexes, PhD Dissertation, Michigan State University, East Lansing, MI, 2018.

17. Barbara, P. F.; Meyer, T. J.; Ratner, M. A. Contemporary Issues in Electron Transfer Research. *J. Phys. Chem*. **1996**, *100*, 13148–13168. https://doi.org/10.1021/jp9605663.

18. Bowman, D. N.; Jakubikova, E. Low-Spin versus High-Spin Ground State in Pseudo-Octahedral Iron Complexes. *Inorg. Chem*. **2012**, *51*, 6011–6019. https://doi.org/10.1021/ic202344w.

19. Ashley, D. C.; Jakubikova, E. Tuning the Redox Potentials and Ligand Field Strength of Fe(II) Polypyridines: The Dual π-Donor and π-Acceptor Character of Bipyridine. *Inorg. Chem*. **2018**, *57*, 9907–9917. https://doi.org/10.1021/acs.inorgchem.8b01002.

20. Sutin, N. Nuclear, Electronic, and Frequency Factors in Electron Transfer Reactions. *Acc. Chem. Res*. **1982**, *15*, 275–282. https://doi.org/10.1021/ar00081a002.

21. Nance, J.; Bowman, D. N.; Mukherjee, S.; Kelley, C. T.; Jakubikova, E. Insights into the Spin-State Transitions in $[Fe(tpy)_2]^{2+}$: Importance of the Terpyridine Rocking Motion. *Inorg. Chem*. **2015**, *54*, 11259–11268. https://doi.org/10.1021/acs.inorgchem.5b01747.

22. Kahn, O. *Molecular Magnetism*, 1st ed.; VCH Publishers: New York, 1993.

23. Siretanu, D.; Li, D.; Buisson, L.; Bassani, D. M.; Holmes, S. M.; Mathonière, C.; Clérac, R. Controlling Thermally Induced Electron Transfer in Cyano-Bridged Molecular Squares: From Solid State to Solution. *Chem. Eur. J.* **2011**, *17*, 11704–11708. https://doi.org/10.1002/chem.201102042.

24. Toftlund, H.; McGarvey, J. J. Iron(II) Spin Crossover Systems with Multidentate Ligands. In *Spin Crossover Transition Metal Compounds III*; Gütlich, P.; Goodwin, H. A., Eds.; Springer: Berlin, 2004, pp 151–166. https://doi.org/10.1007/b13532.

25. Goodwin, H. A. Spin Crossover in Iron(II) Tris(Diimine) and Bis(Terimine) Systems. In *Spin Crossover Transition Metal Compounds III*; Gütlich, P.; Goodwin, H. A., Eds.; Springer: Berlin, 2004, pp 59–90. https://doi.org/10.1007/b13529.

26. Goodwin, H. A.; Sylva, R. N. Magnetic Properties of the Tris(2-Methyl-1,10-phenanthroline)iron(II) ion. *Aust. J. Chem*. **1968**, *21*, 83–90. https://doi.org/10.1071/CH9680083.

27. Fleisch, J.; Hasselbach, K.; Hasselbach, K. High Spin-Low Spin Transition in Substituted Phenanthroline Complexes of Iron(II) Journal de Physique Colloques, **1974**, *35*, C6-659-C6-662.

28. Fleisch, J.; Gütlich, P.; Hasselbach, K. M.; Müller, W. New Aspects of the High Spin-Low Spin Transition in Tris(2-Methyl-1,10-phenanthroline)iron(II) Perchlorate. *Inorg. Chem.* **1976**, *15*, 958–961. https://doi.org/10.1021/ic50158a046.

29. Fleisch, J.; Gutlich, P.; Hasselbach, K. M. Thermally Induced Spin Transition in Tris(2-Methoxy-1,10-phenanthroline)iron(II) Perchlorate. Variable-Temperature Mössbauer, Magnetic Susceptibility, and Far-Infrared Measurements. *Inorg. Chem*. **1977**, *16*, 1979–1984.

30. Poole, R. A.; Bobba, G.; Cann, M. J.; Frias, J. C.; Parker, D.; Peacock, R. D. Synthesis and Characterisation of Highly Emissive and Kinetically Stable Lanthanide Complexes Suitable for Usage "in Cellulo." *Org. Biomol. Chem*. **2005**, *3*, 1013–1024. https://doi.org/10.1039/b418964g.

31. Krapcho, A. P.; Lanza, J. B. Improved Synthesis of 2-Chloro- and 2,9-Dichloro-1,10-Phenanthrolines. *Org. Prep. Proced. Int.* **2007**, *39*, 603–608. https://doi.org/10.1080/00304940709458644.

32. Krapcho, A. P.; Sparapani, S. Facile Acidic Hydrolysis and Displacement Reactions of 2-Chloro- and 2,9-Dichloro-1,10-Phenanthroline. *J. Heterocycl. Chem*. **2008**, *45*, 1167.

33. Panja, A. Mononuclear Cobalt(III) and Iron(II) Complexes with Diimine Ligands: Synthesis, Structure, DNA Binding and Cleavage Activities, and Oxidation of 2-Aminophenol. *Polyhedron* **2012**, *43*, 22–30. https://doi.org/10.1016/j.poly.2012.05.041.

34. Bain, G. A.; Berry, J. F. Diamagnetic Corrections and Pascal's Constants. *J. Chem. Educ*. **2008**, *85*, 532. https://doi.org/10.1021/ed085p532.

35. Evans, D. F. The Determination of the Paramagnetic Susceptibility of Substances in Solution by Nuclear Magnetic Resonance. *J. Chem. Soc.* **1959**, 2003–2005. https://doi.org/10.1039/jr9590002003.

36. Sharma, R. P.; Bhasin, K. K. $Cr(acac)_3$ as a New Calibrant for Magnetic Susceptibility Experiments. *Chem. Soc. Japan* **1986**, *59*, 1603–1604.

37. Ostfeld, D.; Cohen, I. A. A Cautionary Note on the Use of the Evans Method for Magnetic Moments. *J. Chem. Educ*. **1972**, *49*, 829. https://doi.org/10.1021/ed049p829.

38. Archibald, E. H.; Ure, W. The Temperature and Viscosity of Acetone at Low Temperatures. *J. Chem. Soc. Trans*. **1924**, *125*, 725–731.

39. Crawford, T. H.; Swanson, J. Temperature Dependent Magnetic Measurements and Structural Equilibria in Solution. *J. Chem. Educ*. **1971**, *48*, 382–386. https://doi.org/10.1021/ed048p382.

40. Fatur, S. M.; Shepard, S. G.; Higgins, R. F.; Shores, M. P.; Damrauer, N. H. A Synthetically Tunable System to Control MLCT Excited-State Lifetimes and Spin States in Iron(II) Polypyridines. *J. Am. Chem. Soc*. **2017**, *139*, 4493–4505. https://doi.org/10.1021/jacs.7b00700.

41. Picraux, L. B.; Smeigh, A. L.; Guo, D.; McCusker, J. K. Intramolecular Energy Transfer Involving Heisenberg Spin-Coupled Dinuclear Iron − Oxo Complexes. *Inorg. Chem.* **2005**, *44*, 7846–7859. https://doi.org/10.1021/ic0506761.

42. Damrauer, N. H.; Boussie, T. R.; Devenney, M.; McCusker, J. K. Effects of Intraligand Electron Delocalization, Steric Tuning, and Excited-State Vibronic Coupling on the Photophysics of Aryl-Substituted Bipyridyl Complexes of Ru(II). *J. Am. Chem. Soc*. **1997**, *119*, 8253–8268. https://doi.org/10.1021/ja971321m.

43. Toftlund, H. Spin Equilibria in Iron(II) Complexes. *Coord. Chem. Rev*. **1989**, *94*, 67–108. https://doi.org/10.1016/0010-8545(89)80045-1.

44. Carlin, R. L. *Magnetochemistry*; Springer-Verlag Berlin Heidelberg: Berlin, 1986.

45. Kershaw Cook, L. J.; Kulmaczewski, R.; Mohammed, R.; Dudley, S.; Barrett, S. A.; Little, M. A.; Deeth, R. J.; Halcrow, M. A. A Unified Treatment of the Relationship Between Ligand Substituents and Spin State in a Family of Iron(II) Complexes. *Angew. Chemie Int. Ed*. **2016**, *55*, 4327–4331. https://doi.org/10.1002/anie.201600165.

46. Conti, A. J.; Xie, C. L.; Hendrickson, D. N. Tunneling in Spin-State Interconversion of Ferrous Spin-Crossover Complexes. Concentration Dependence of Apparent Activation Energy Determined in Solution by Laser-Flash Photolysis. *J. Am. Chem. Soc*. **1989**, *111*, 1171–1180. https://doi.org/10.1021/ja00186a002.

47. Shores, M. P.; Klug, C. M.; Fiedler, S. R. Spin-State Switching in Solution. In *Spin-Crossover Materials: Properties and Applications*; 2013; pp 281–301. https://doi.org/10.1002/9781118519301.ch10.

48. Kepp, K. P. Theoretical Study of Spin Crossover in 30 Iron Complexes. *Inorg. Chem*. **2016**, *55*, 2717–2727. https://doi.org/10.1021/acs.inorgchem.5b02371.

49. Tribollet, J.; Galle, G.; Jonusauskas, G.; Deldicque, D.; Tondusson, M.; Letard, J. F.; Freysz, E. Transient Absorption Spectroscopy of the Iron(II) $[Fe(phen)_3]^{2+}$ Complex: Study of the Non-Radiative Relaxation of an Isolated Iron(II) Complex. *Chem. Phys. Lett.* **2011**, *513*, 42–47. https://doi.org/10.1016/j.cplett.2011.07.048.

50. Juris, A.; Balzani, V.; Barigelletti, F.; Campagna, S.; Belser, P.; Von Zelewsky, A. Ru(II) Polypyridine Complexes: Photophysics, Photochemistry, Electrochemistry, and Chemiluminescence. *Coord. Chem. Rev*. **1988**, *84*, 85–277.

51. Stock, P.; Deck, E.; Hohnstein, S.; Korzekwa, J.; Meyer, K.; Heinemann, F. W.; Breher, F.; Hörner, G. Molecular Spin Crossover in Slow Motion: Light-Induced Spin-State Transitions in Trigonal Prismatic Iron(II) Complexes. *Inorg. Chem*. **2016**, *55*, 5254–5265. https://doi.org/10.1021/acs.inorgchem.6b00238.

52. Stock, P.; Pędziński, T.; Spintig, N.; Grohmann, A.; Hörner, G. High Intrinsic Barriers against Spin-State Relaxation in Iron(II)-Complex Solutions. *Chem. Eur. J*. **2013**, *19*, 839–842. https://doi.org/10.1002/chem.201203784.

53. Buhks, E.; Navon, G.; Bixon, M.; Jortner, J. Spin Conversion Processes in Solutions. *J. Am. Chem. Soc.* **1980**, *102*, 2918–2923. https://doi.org/10.1021/ja00529a

CHAPTER 3. A SEMI-CLASSICAL AND QUANTUM-MECHANICAL ANALYSIS OF GROUND-STATE RECOVERY IN AN IRON(II) SPIN-CROSSOVER COMPLEX

3.1. Introduction

In Chapter 2, λ and H_{ab}, the reorganization energy and the electronic coupling constant for $^5T_2 \rightarrow {}^1A_1$ decay in an Fe(II) spin-crossover complex, were found. These experimentally-determined values served as validation for those approximated in low-spin Fe(II) complexes.[1] However, the ultimate goal of this dissertation is to exert kinetic control over the MLCT $\rightarrow {}^5T_2$ decay. To do so, the nature of the nuclear coordinate describing this electronic transition, i.e. which vibrational modes are coupled to nonradiative excited-state evolution, must be identified. Therefore, in this chapter we will delve more deeply into nonradiative decay models that can describe ground-state recovery in the spin-crossover complex $[Fe(2\text{-}OMe\text{-}phen)_3](BF_4)_2$ in an effort to define the kinetically relevant vibrational mode(s) for this process. Then, information about the geometric distortions important between the ground state and ^{3}MLCT excited state will be gained using a Ru(II) analog of the spin-crossover complex. Together, these experimentally-grounded analyses will provide the necessary information to better define, and subsequently disrupt through synthetic modification, the nuclear coordinate for excited-state evolution in an Fe(II) spin-crossover complex.

3.1.1. Nonradiative decay theory applied to ground-state recovery

For the purposes of the subsequent discussion, a brief summary of the origins of two commonly employed models of nonradiative decay will be provided, highlighting the major assumptions implied as well as the differences between the two. However, the details of the mathematics behind their derivations will not be discussed in detail, as they have been extensively

presented elsewhere. Some excellent resources are Don DeVault's book on quantum-mechanical tunneling in biological systems[2], a broad review on electron transfer,[3] and a more recent review of quantum effects in biology.[4] A good starting point for the comparison of nonradiative decay models is the so-called "golden rule"[2,3,5–10]

$$k_{nr} = \frac{2\pi}{\hbar}\left|H_{ab}\right|^2 \bullet FC \tag{3.1}$$

where the rate constant (k_{nr}) is related to the electronic coupling constant between the reactant and

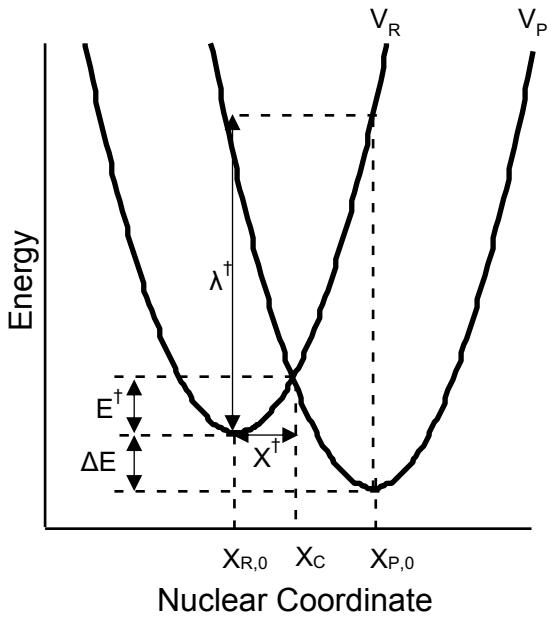

Figure 3.1. Diabatic energy curves for the reactant and product of an electron transfer. See text for a description of parameters. Reproduced from Barbara, et al.

product (H_{ab}) and FC is the Franck-Condon overlap factor. Here, the Born-Oppenheimer rule has been followed and the electronic and nuclear terms are treated separately. The two non-radiative decay models differ in that the FC overlap factor is either treated classically in the case of Marcus and quantum mechanically in the case of Jortner.

Marcus theory has its origins in transition state theory and was developed to describe electron transfer reactions both at electrodes and in solution.[11–14] The Eyring equation (eq. 3.2) was the basis of Marcus theory, with k_{nr} as function of the probability of an electronic

rearrangement occurring (κB) and the probability of traversing a barrier, which requires a free energy of activation ($\Delta G^{\dagger}$).

$$k_{nr} = \kappa B \exp\left(\frac{\Delta G^{\dagger}}{k_B T}\right) \tag{3.2}$$

Marcus expanded upon the $\Delta G^{\dagger}$ term by considering harmonic potential energy curves for the reactant (V_R) and product (V_P) described by identical frequencies, with equilibrium geometries of $X_{R,0}$ and $X_{P,0}$, respectively, along a one-dimensional nuclear coordinate (Figure 3.1). The equations for the parabolas associated with the reactant and product are:

$$V_R = \frac{k_H \left(X - X_{R,0}\right)^2}{2} + E_R \tag{3.3}$$

$$V_P = \frac{k_H \left(X - X_{P,0}\right)^2}{2} + E_P \tag{3.4}$$

E_R and E_P are the energies of the reactant and product in their equilibrium geometries and k_H is the force constant for the vibration describing the motion along the nuclear coordinate. The angular frequency (ω) of this vibration can be described as

$$\omega = \left(\frac{k_H}{M}\right)^{1/2} \tag{3.5}$$

where M is the reduced mass of the oscillator. If we define the change in equilibrium geometry along the nuclear coordinate (ΔQ) as

$$\Delta Q = X_{R,0} - X_{P,0} \tag{3.6}$$

then we can also define the reorganization energy (λ), or the amount of energy required to change the geometry from $X_{R,0}$ to $X_{P,0}$ without transferring an electron, as:

$$\lambda = \frac{k_H \left(\Delta Q\right)^2}{2} = \frac{M\omega^2 \left(\Delta Q\right)^2}{2} \tag{3.7}$$

The reorganization energy of a given electron transfer event is affected by both intramolecular rearrangement, or inner-sphere reorganization energy (λ_i), and changes in the solvent environment, or outer-sphere reorganization energy (λ_o). We must prepare for the fact that the value of λ_i may contain contributions from more than one intramolecular vibrational mode if the nuclear coordinate describing ground-state recovery in Fe(II) polypyridyls is multi-dimensional, as λ_i will be a summation of all values of λ describing the coupled vibrational modes:

$$\lambda_i = \sum_l \lambda_{i,l} = \tfrac{1}{2} \sum_l f_l \left(\Delta Q\right)^2 \tag{3.8}$$

with *f* as the force constant for a given vibrational mode. Keeping this in mind, we can describe the activation energy ($E^\dagger$), for an electron transfer reaction that proceeds along the nuclear coordinate $X^\dagger$:

$$X^\dagger = X_C - X_{R,0} \tag{3.9}$$

as:

$$E^\dagger = \frac{k_H \left(X^\dagger\right)^2}{2} \tag{3.10}$$

So now, $E^\dagger$ can be described in terms of the geometric changes that occur along the relevant nuclear coordinate, ΔQ, and the energy difference between the reactant and product (ΔE):

$$E^\dagger = \frac{k_H \left(\Delta Q - X^\dagger\right)^2}{2} - \Delta E \tag{3.11}$$

Combining equations 3.7, 3.10, and 3.11 yields:

$$E^\dagger = \frac{\left(\lambda + \Delta E\right)^2}{4\lambda} \tag{3.12}$$

The energy terms (E_R, E_P, ΔE, and $E^\dagger$), used in equations 3.3-3.12 can be replaced with their free energy analogs (G_R, G_P, $\Delta G°$, and $\Delta G^\dagger$) if we assume that there is no entropic contribution to the

free energy terms, or $\Delta S° = \Delta S^{\dagger} = 0$. We will use the free energy terms in the subsequent discussions of Marcus theory and will address the non-zero value of $\Delta S°$ in the application of the theory for the $^5T_2/^1A_1$ conversion in Fe(II) systems.

While the derivation for the nuclear motion pertinent to electron transfer was treated classically by Marcus, the probability of electron transfer (κB) was instead treated quantum mechanically, following the formulation of Landau and Zener[2]:

$$\kappa B = \frac{2\pi}{\hbar}\left|H_{ab}\right|^2 \frac{1}{\sqrt{4\pi\lambda k_B T}} \tag{3.13}$$

Where $|H_{ab}|$ is the magntidue of the electronic coupling matrix between the reactant and the product. To describe H_{ab} in the ground-state recovery process in Fe(II) complexes specifically, there is no direct coupling term between the $^1A_1$ and $^5T_2$ states, only second-order spin-orbit coupling through a $^3T_1$ state, as described by Griffith:[15]

$$\left\langle {}^1A_{1g}\left|\hat{H}_{ab}\right|{}^3T_{1g}\right\rangle = -\sqrt{6}\zeta \tag{3.14}$$

$$\left\langle {}^5T_{2g}\left|\hat{H}_{ab}\right|{}^3T_{1g}\right\rangle = \sqrt{3}\zeta \tag{3.15}$$

where ζ is the spin-orbit coupling constant for Fe(II). Consequently, the electronic coupling constant relevant to this discussion is:

$$H_{ab} = -3\sqrt{2}\zeta^2\left(\frac{1}{\Delta E_1} + \frac{1}{\Delta E_2}\right) \tag{3.16}$$

and

$$\Delta E_1 = E({}^3T_1) - E({}^5T_2) \tag{3.17}$$

$$\Delta E_2 = E({}^3T_1) - E({}^1A_1) \tag{3.18}$$

Inserting equations 3.12 and 3.13 into Eyring's original equation (eq. 3.2) yields:

$$k_{nr} = \frac{2\pi}{\hbar}|H_{ab}|^2 \frac{1}{\sqrt{4\pi\lambda k_B T}} \exp\left[\frac{-\left(\lambda + \Delta G^{\circ}\right)^2}{4\lambda k_B T}\right] \tag{3.19}$$

the semi-classical form of the Marcus equation used in Chapter 2 of this dissertation, with a classical treatment of nuclear motion, represented by the Franck-Condon overlap factor in eq. 3.1. This condition is only valid for temperatures at which the molecule is fully vibrationally excited, or the accessible thermal energy is much larger than the spacing of the vibrational levels on the reactant and product surfaces, i.e. $k_B T \gg \hbar\omega$. While Marcus' semi-classical equation has garnered wide-spread use, it erroneously predicts that as the temperature of system approaches 0 K, the rate should also approach 0 s^{-1}. This is simply not true from many electron transfer reactions,[2,4] calling for the consideration of non-classical nuclear motion.

In 1980, Joshua Jortner applied a quantum-mechanical model for nonradiative decay to spin conversion in first-row transition metals in solution, and his initial approximations showed promise in modelling the data available at the time.[16] In this theory, the electron transfer event is not considered the result of going *over* a barrier, but instead is modelled as going *through* a barrier. In other words, the nuclear motion is treated quantum-mechanically, which allows for nuclear tunneling and therefore a non-zero electron transfer rate at low temperatures. Here we will simply consider nuclear tunneling as the result of overlap between the vibrational wavefunctions associated with the product and reactant surfaces, shown schematically in Figure 3.2, which is an expansion of the potential energy surfaces in Figure 3.1.

First, we will consider the effects of quantum-mechanical tunneling qualitatively, then we will show the expressions used to derive a relationship between k_{nr} and temperature. In the example shown in Figure 3.2, at very low temperatures ($k_B T \ll \hbar\omega$), only the n = 0 vibrational state is

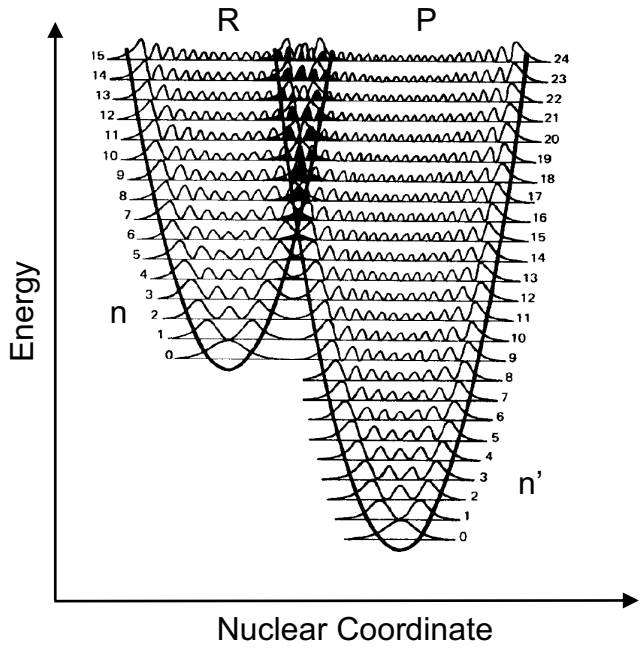

Figure 3.2. Energy surfaces of the reactant (R) and product (P) of an electron transfer reaction along a unitless one-dimensional nuclear coordinate. n and n' refer to the vibrational states of the reactant and product, respectively. Reproduced from DeVault book.

populated on the reactant surface. Because there is some overlap of the vibrational wavefunctions between the n = 0 vibrational state on the reactant surface and the n' = 9 vibrational state on the product surface, nuclear tunneling can occur, so even at these low temperatures the rate of electron transfer is non-zero. As the temperature is increased, thermal population of higher vibrational states increases in the reactant (following a Boltzmann distribution), thus increasing the amount of overlap between the vibrational wavefunctions associated with the reactant and product electronic surfaces, thereby increasing the probability of nuclear tunneling and the rate of electron transfer. When the temperature is high enough that $k_BT \gg \hbar\omega$, the rate of electron transfer may be sufficiently described by the Arrhenius model, however nuclear tunneling is still the dominant mechanism for electron transfer and the observed rate may be described as the sum of the different rates of tunneling from the reactant to each vibrational level of the product. More generally, when

$k_BT \gg \hbar\omega$, the fully quantum mechanical and semi-classical models should converge and both accurately predict the temperature dependence of k_{nr}.

Quantitatively, Jortner begins his derivation from a nonadiabatic form of the Golden rule,[2,16] i.e. an expansion of the expression in eq. 3.1:

$$k_{nr} = \frac{2\pi}{\hbar} g_f A_{\chi i \phi i} \sum_{\chi f \phi f} \delta\left(\Delta E + E^c_{\chi f} + E^s_{\phi f} - E^c_{\chi i} - E^s_{\phi i}\right) \bullet \left| \left\langle \Psi_i \left| H_{ab} \right| \Psi_f \right\rangle \left\langle \chi_i \mid \chi_f \right\rangle \left\langle \phi_i \mid \phi_f \right\rangle \right|^2 \quad (3.20)$$

Where g_f is the degeneracy of the final electronic state and $A_{\chi i \phi I}$ is an operation that thermally averages the vibrational states of the reactant, or initial state:

$$A\nu_{\chi i \phi i}(...) = \frac{1}{Z^c_i Z^s_i} \sum_{\chi i \phi i} \exp\left\{ \frac{-\left(E^c_{\chi i} + E^s_{\phi i}\right)}{k_B T} \right\} (...) \quad (3.21)$$

In this expression the Z_i terms represent the partition functions of the solvent (Z^s) and intramolecular motion of the complex (Z^c):

$$Z^s_i = \sum_{\chi i} \exp\left\{ \frac{-E^s_{\chi i}}{k_B T} \right\} \quad (3.22)$$

$$Z^c_i = \sum_{\phi i} \exp\left\{ \frac{-E^c_{\phi i}}{k_B T} \right\} \quad (3.23)$$

It should be noted that a nonadiabatic expression for spin conversion in solution is only appropriate if the electronic coupling between the two states is small, i.e.

$$\frac{\left| H_{ab} \right|^2}{\hbar\omega\sqrt{\lambda k_B T}} < 1 \quad (3.24)$$

We know that this condition is met by plugging in the values for H_{ab} and λ measured for an iron(II) spin crossover complex in Chapter 2 and assuming that the frequency of the mode coupled to the

spin conversion process is greater than 1 cm^{-1}. By combining equations 3.20-3.23, the quantum-mechanical expression can be condensed into eq. 3.25:

$$k_{nr} = \frac{2\pi}{\hbar} g_f \left| H_{ab} \right|^2 F \tag{3.25}$$

by expressing the thermally averaged nuclear Franck-Condon vibrational overlap factor as F. An analytical expression for F can be defined by making two main assumptions. First, the solvent can be represented by low frequency modes, such that $\hbar\omega_s << k_B T$, and therefore these modes can be represented by E_s, the semi-classical solvent reorganization energy. Second, the spacing between the vibrational levels in the reactant and product will be assumed to be large and identical, and it follows that the nuclear coordinate describing the conversion from reactant to product can be defined by a single mode. Then the Franck-Condon factor can be expressed as:

$$F = \frac{1}{\hbar\omega} \bullet \exp\left\{ -\frac{\lambda}{\hbar\omega} \coth x - px \right\} \bullet I_p \left(\frac{\lambda}{\hbar\omega \sinh x} \right) \tag{3.26}$$

Where I_p is the modified Bessel function of order p:

$$I_p = \left(\frac{x}{2} \right)^p \sum_{k=0}^{\infty} \frac{\left(\frac{x^2}{2} \right)^k}{k!(m+k)!} \tag{3.27}$$

and

$$x = \frac{\hbar\omega}{2k_B T} \tag{3.28}$$

$$p = \frac{\Delta E}{\hbar\omega} \tag{3.29}$$

Combining together these descriptions and considering that for spin conversion in Fe(II) complexes, where $g_f = 1$, an expression for the rate may be defined as:

$$k_{nr} = \frac{2\pi}{\hbar^2\omega}\left|H_{ab}\right|^2 \exp\left\{\frac{-\lambda}{\hbar\omega}\coth\left(\frac{\hbar\omega}{2k_BT}\right) - \frac{\Delta E}{2k_BT}\right\} \bullet I_p\left(\frac{\lambda}{\hbar\omega\sinh\left(\frac{\hbar\omega}{2k_BT}\right)}\right) \qquad (3.30)$$

Eq. 30 is the form of Jortner's nonradiative decay theory that will be applied to ground-state recovery in an Fe(II) SCO complex in this chapter.

In this analysis, we will first simply observe whether or not temperature independence of k_{nr} for GSR of $[Fe(2\text{-OMe-phen})_3]^{2+}$ occurs over the experimentally-accessible temperature range (for these studies, 145-300 K). This finding will reveal if the semi-classical model is sufficient to describe the $^5T_2 \rightarrow {}^1A_1$ conversion in solution, i.e. if the $k_BT \gg \hbar\omega$ condition is fulfilled, or if the quantum-mechanical model is necessary and the frequency of the vibrational mode defining this segment of the nuclear coordinate is small compared to the thermal energy available at low temperatures. From there, we will fit the k_{nr} versus temperature data with eq. 30 over a span of $\hbar\omega$ values and qualitatively evaluate the model's ability to reproduce the experimental data. The frequencies that provide reasonable fits can be visualized with DFT frequency calculations to get an idea of the geometric distortions that describe $\Delta Q_{LF/GS}$, the nuclear coordinate of ground-state recovery. Various iterations of this analysis have been attempted before in the past, namely by Hendrickson and coworkers on a SCO complex in a polystyrene matrix[17]and through a glass-to-fluid transition[18], and also by Hauser on low-spin Fe(II) complexes in dilute crystal mixtures and embedded in polymer matrices.[19] However, there have been serious shortcomings with the work done in solution, and as such they will be overcome here.

3.1.2. Franck-Condon analysis of emission from a MLCT excited-state

We are attempting to not only identify $\Delta Q_{LF/GS}$, but also the nuclear coordinate defining the $^{1,3}MLCT \rightarrow {}^5T_2$ conversion ($\Delta Q_{MLCT/LF}$). As this process typically occurs on sub-200 fs timescales,[20,21] variable temperature time-resolved measurements would have little practical significance, ruling out direct approaches to define $\Delta Q_{MLCT/LF}$. Therefore, a more indirect route to defining $\Delta Q_{MLCT/LF}$ will be taken. After identifying the modes composing $\Delta Q_{LF/GS}$ using the analysis described above, the nuclear coordinate between the $^1A_1$ and ^{3}MLCT excited state, $\Delta Q_{MLCT/GS}$, will also be identified (Figure 3.3). Our computational collaborators, Jakubikova and coworkers, have done DFT and complete active space self-consistent field calculations[22,23] on $[Fe(terpy)_2]^{2+}$ and $[Fe(bpy)_3]^{2+}$ to determine which geometric distortions provide low-energy pathways for the $^{1,3}MLCT \rightarrow {}^5T_2$ conversion. With experimental values of $\hbar\omega$ for $\Delta Q_{MLCT/GS}$ and $\Delta Q_{LF/GS}$ to benchmark these types of calculations, the Jakubikova group can establish which geometric motions are the lowest energy pathway at the intersection of $\Delta Q_{MLCT/GS}$ and $\Delta Q_{LF/GS}$.

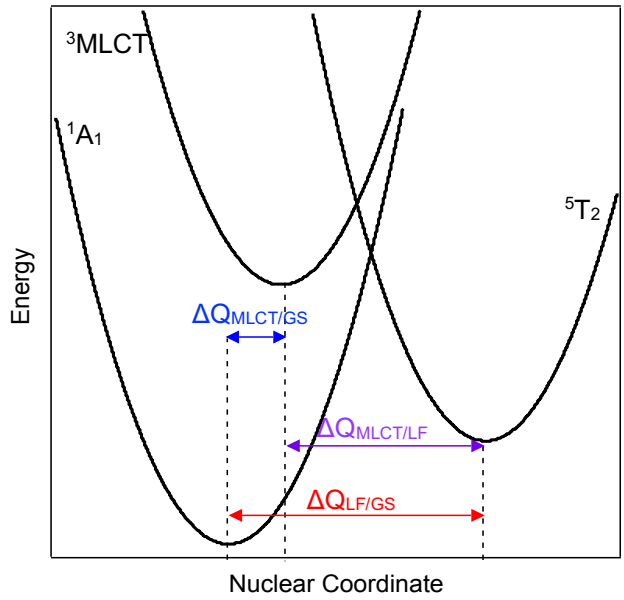

Figure 3.3. Schematic of relevant potential surfaces along a one-dimensional nuclear coordinate.

To define $\Delta Q_{MLCT/GS}$, a ruthenium(II) analog of the spin-crossover complex used to find $\Delta Q_{LF/GS}$ will be utilized. The geometric changes associated with the ^{3}MLCT excited state compared to the ground state are largely ligand-based.[24–26] Therefore, as long as identical ligand systems are used, information about the geometric distortions that occur with the $^3MLCT \rightarrow {}^1A_1$ decay in a Ru(II) complex should be a good approximation to those that occur in the corresponding Fe(II) complex. Ru(II) polypyridyl complexes tend to have emissive ^{3}MLCT excited states, and their steady-state emission profiles can be fit to a single-mode Franck-Condon analysis (eq. 3.31)[27] to yield $\hbar\omega_M$, the average frequency coupled to the $^3MLCT \rightarrow {}^1A_1$ intersystem crossing.

$$I(\tilde{\nu}) = \sum_{\nu_M=0}^{5} \left\{ \left(\frac{E_0 - \nu_M \hbar\omega_M}{E_0} \right)^3 \left(\frac{S_M^{\nu_M}}{\nu_M!} \right) \exp\left[-4\ln(2) \left(\frac{\tilde{\nu} - E_0 + \nu_M \hbar\omega_M}{\Delta\tilde{\nu}_{0,1/2}} \right)^2 \right] \right\} \qquad (3.31)$$

In this equation, the intensity of emitted light (I) at a given frequency $\tilde{\nu}$ can be defined by the zero-point energy difference between the emitting state and the ground state (E_0), spectral bandwidth ($\Delta\tilde{\nu}_{0,1/2}$), the vibrational spacing ($\hbar\omega_M$), an index ν_M that runs over the number of vibrational levels of $\hbar\omega_M$ in the ground state that serve as the final vibronic states, and Huang-Rhys factor (S_M), which is reflective of the relative displacement between the two states involved in the emissive process. This analysis provides a comparatively straight-forward route to describe $\Delta Q_{MLCT/GS}$. Combining these two approaches, one comparing the ability of semi-classical and quantum-mechanical nonradiative decay theories to model the temperature dependence of k_{nr} in an Fe(II) spin-crossover molecule and the other utilizing a Ru(II) to analog of the SCO complex, should yield information about $\Delta Q_{LF/GS}$ and $\Delta Q_{MLCT/GS}$ and provide the experimental data necessary to predict how these two portions of the nuclear coordinate intersect.

3.2. Experimental section

3.2.1. Synthesis

General synthesis. Unless otherwise noted, all reactions were conducted either using standard Schlenk techniques or in an inert atmosphere glove box (nitrogen-filled, Vacuum Atmospheres). Tetrakis(dimethylsulfoxide) ruthenium(II) dichloride was prepared according to the literature procedure[28] by Dr. Daniela Arias-Rotondo. 2-methoxy-1,10-phenanthroline and [Fe(2-R-phen)$_3$](BF_4)$_2$ were prepared according to the procedures given in Chapter 2. MeOH, MeCN, and Et_2O were bubble degassed with nitrogen, dried over activated neutral alumina, and pumped into an inert atmosphere glovebox. Anhydrous acetone was purchased from Acros Organics. All other reagents and solvents were purchased from either Sigma Aldrich, Acros Organics, or Oakwood Chemical Company and used as received. Size-exclusion chromatography was performed with SorbaDex lipophilic hydrophilic gel filtration matrix (Sorbtech). ^{1}H NMR were collected on a Agilent DDR2 500 MHz spectrometer and referenced to residual solvent shifts. Electrospray ionization mass spectra were obtained at the Michigan State University Mass Spectrometry and Metabolomics Core on a Waters G2-XS QToF mass spectrometer interfaced to a Waters Aquity UPLC. Elemental analyses were obtained through the analytical facilities at Michigan State University on samples that had been ground in a vial with a glass stir rod in an inert atmosphere glovebox and stored under vacuum overnight prior to analysis.

***tris*(2-methoxy-1,10-phenanthroline)ruthenium(II) tetrafluoroborate.** In a 2-neck flask, 2-OMe-phen (167 mg, 0.79 mmol) was dissolved in EtOH/H_2O (50 mL/25 mL). The solution was bubble degassed with N_2 for 30 min and the flask was wrapped in foil to exclude light. Ru(DMSO)$_4Cl_2$ (116 mg, 0.24 mmol) was added under nitrogen and the suspension was degassed for 10 min. AgOTf (15 mg, 0.59 mmol) was added under nitrogen and the suspension was refluxed

for 48 h while monitoring the reaction by ESI-MS to watch for the disappearance of Ru(2-OMe-phen)$_2$Cl$_2$. After cooling to RT, the reaction was filtered through Celite, and the solvent was removed from the bright orange filtrate. The orange solid was dissolved in H_2O (5 mL), and $NaBF_4$ (263 mg, 2.4 mmol) was added. The orange solution was stirred overnight, resulting in an orange precipitate, which was collected via filtration and washed with H_2O. Excess sodium salts were removed by size-exclusion chromatography in MeOH. X-ray quality crystals were grown from diethyl ether diffusion into acetone/methanol solutions of the complex. ^{1}H NMR (500 MHz, acetone-d$_6$) 8.78 (m, 3 H), 8.65 (d, J = 8.98, 1 H), 8.59 (m, 2 H), 8.11-8.40 (m, 8 H), 8.01 (d, J = 5.0, 1 H), 7.63 (m, 3 H), 7.50 (m, 3 H), 3.37 (s, 3 H) . Sufficient concentrations of the compound could not be achieved to obtain a clear ^{13}C NMR spectrum. HRMS (ESI-TOF) m/z: $[M\text{-}2(BF_4)]^{2+}$ calc'd for $C_{39}H_{30}N_6O_3Ru$: 366.0717, obs. 366.0661; Elemental analysis (% calc'd, % found) for $C_{39}H_{30}N_6O_3RuB_2F_8$: C (51.74, 49.97) H (3.34, 3.50) N (9.28, 9.20).

3.2.2. Physical Characterization

X-ray crystal structure determination. Single-crystal x-ray diffraction data were collected on suitable crystals of [Ru(2-OMe-phen)$_3$](BF$_4$)$_2$ mounted on a Bruker APEX-II CCD diffractometer with MoK$_\alpha$ radiation at the Center for Crystallographic Research at Michigan State University, and the crystal structure data may be obtained from the CCDC accession code 1875433.

Solution-phase Variable Temperature Magnetic Susceptibility Measurements. All measurements were performed on a Quantum Design MPMS 3 magnetometer cryogen free equipped with an EverCool He gas regulator interfaced to a Dell PC. Data were collected with an applied field of 1 T in DC mode and with 10 min of temperature equilibration at each temperature point before scanning. DC moments were corrected for the diamagnetic contributions attributed to the straw and solvent, as measured in blank experiments. Pascal's constants were used to correct

for the diamagnetic contribution from the sample.[29] Calibration was performed by measuring the magnetic susceptibility a 1 mM solution of analytically pure $Cr(acac)_3$ in 9:1 methanol-d_4/ethanol-d_6. Sample preparation was performed in the procedure suggested by Dr. Rodolphe Clérac of the Centre de Recherche Paul Pascal. Crystalline samples were stored in a vacuum desiccator for one day prior to data collection and an approximately 1 mM solution in methanol-d_4/ethanol-d_6 were made. Extensive sonication (~30 min) was required to achieve this concentration for all solutions prepared, but care was taken to ensure the sample did warm significantly above room temperature. Using a food sealer, a seal was made in a plastic straw (Cancun Mexican Grill, Okemos, MI) at the appropriate length to ensure sample centering once in the magnetometer. 100 μL of the 1 mM solution was placed in the sealed straw. The straw was flushed with Ar and a second seal was made 2 inches above the first, perpendicular to the original seal. The sample was then loaded into the magnetometer and the sample chamber was evacuated. Following this preliminary evacuation, the sample was removed from the magnetometer and checked to ensure no leaks in the sealed straw. The density of the plastic straw is of the upmost importance for this sample preparation method, as straws that are too thin will form seals that are prone to leaking and straws that are too thick will not form a strong seal. The absence of ferromagnetic impurities was confirmed by measuring the magnetic moment versus applied field (0-1 T) and ensuring a linear response.

Room temperature steady-state emission spectroscopy. Steady-state emission was collected on samples prepared in an Ar-filled glovebox with an absorbance between 0.1-0.2 at the excitation wavelength, as measured on a SSI400 CCD spectrometer, in matched 1 cm quartz cuvettes (FireFlySci) and adapted at the MSU Glassblowing Shop to extend the neck of the cell and enable sealing with PTFE Kontes valves to ensure air-free measurements. Data were collected on a Horiba Fluorolog-3 fluorimeter and corrected for instrumental response using a NIST standard of spectral

irradiance (Optronic Laboratories, Inc., OL220 M tungsten quartz lamp). Background scans of the solvent in the cell with the Xe lamp on and off were both subtracted from the sample data. Emission quantum yields of the samples (Φ_x) were found relative to the emission quantum yield of a standard (Φ_{std}), in this case $[Ru(bpy)_3](PF_6)_2$, by the following equation:

$$\Phi_x = \Phi_{std}\left(\frac{I_x/A_x}{I_{std}/A_{std}}\right)\left(\frac{\eta_x}{\eta_{std}}\right)^2 \tag{3.32}$$

Where I_x and I_{std} are the measured emission intensities of the sample and standard, A_x and A_{std} are the absorbances of the sample and standard are the excitation wavelength, and η_x and η_{std} are the refractive indices of the solutions (assumed to be equal to the refractive indices of the neat solvent).[28] The value of Φ_{std}, in the case of $[Ru(bpy)_3](PF_6)_2$ in degassed acetonitrile, is 0.095.[30]

Low-temperature steady-state emission spectroscopy. Absolute quantum yields at 77 K were collected on samples prepared in an Ar-filled glovebox in solutions of spectroscopic grade 9:1 MeOH/EtOH (Alfa Aesar/Acros Organics) in sealed quartz test tubes with a round cross section and an absorbance at the excitation wavelength of 0.2-0.4, as measured on a SSI400 CCD spectrometer. Data were collected on Hamamatsu Photonic Quantaurus absolute PL QY spectrometer (C11347) using the liquid nitrogen accessory.

Room-temperature time-resolved emission spectroscopy. Data were collected on Professor Gary Blanchard's time-correlated single-photon counting (TCSPC) system, which has been described previously.[31] Briefly, the system is fit with a CW passively mode-locked light source, diode-pumped Nd:YVO4 laser (Spectra Physics Vanguard) with 13 ps pulses; this laser's output pumps a cavity-dumped dye laser (Coherent 702-2), which generates 5 ps pulses in the 430-850 nm range. Samples were prepared in spectroscopic-grade acetone (Acros Organics) in an Ar-filled glovebox using the same cells as for room temperature steady-state emission measurements.

Resonance Raman. Data were collected with the assistance of Allison Stettler using equipment in Professor Proshlyakov's lab at Michigan State University using 488 nm excitation (200 mW) in a spinning cell to prevent sample degradation. The scattered light was collected at 90° relative to the incident light and analyzed using a single polychromator (model TRIAX 550; Jobin Yvon) equipped with an imaging CCD detector (model 5000; Jobin Yvon).

Variable Temperature Nanosecond Time-resolved Transient Absorption Spectroscopy. Data were collected by the procedure given in Chapter 2 of this dissertation on samples prepared in an Ar-filled glovebox in 9:1 solutions of spectroscopic grade MeOH/EtOH.

Density Functional Theory Calculations. Geometry optimizations and frequency calculations were conducted for the $^1A_1$ and $^5T_2$ electronic states of $[Fe(2\text{-}OMe\text{-}phen)_3]^{2+}$ and $[Fe(2\text{-}Cl\text{-}phen)_3]^{2+}$ using the Gaussian 16 package[32] with B3LYP, the Becke 3-parameter hybrid density functional based on the correlation function of Lee, Yang, and Parr[33–36] and the 6-311G(d, p) Pople-type basis set.[37–41] X-ray crystal structures were used as the starting point for geometry optimizations of both the $^1A_1$ and $^5T_2$ states. To ensure that the optimized structures were global, not local, minima, the frequency calculations were checked for the absence of negative frequencies.

Fitting to Marcus and Jortner Models. A fitting procedure for both models was written in Mathematica by Stephen Yuwono and subsequently edited, inputting the experimental values for k_{nr}, ΔG, and T, and in the case of the Jortner model, $\hbar\omega$. The average values of λ and H_{ab}, as calculated from the methods outlined in Chapter 2, were the starting guesses in the fitting.

3.3. Results and Discussion

3.3.1. Magnetic susceptibility and variable-temperature ground-state recovery of [Fe(2-OMe-phen)$_3$](BF$_4$)$_2$ in 9:1 methanol/ethanol

The synthetically accessible SCO complex selected for the initial semi-classical and quantum-mechanical descriptions of ground-state recovery was [Fe(2-OMe-phen)$_3$](BF$_4$)$_2$, whose synthesis, ground-state recovery, and magnetic characterization from 210-300 K in acetone were given Chapter 2 of this dissertation. For our intended comparison of the semi-classical and quantum-mechanical theories of ground-state recovery, it would be beneficial to go as low as possible in temperature while remaining in fluid solution, as it is expected to see a divergence between Marcus and Jortner's theories at low temperatures. Therefore, the magnetic susceptibility of [Fe(2-OMe-phen)$_3$](BF$_4$)$_2$, was measured in a solution of 9:1 methanol/ethanol, at solvent

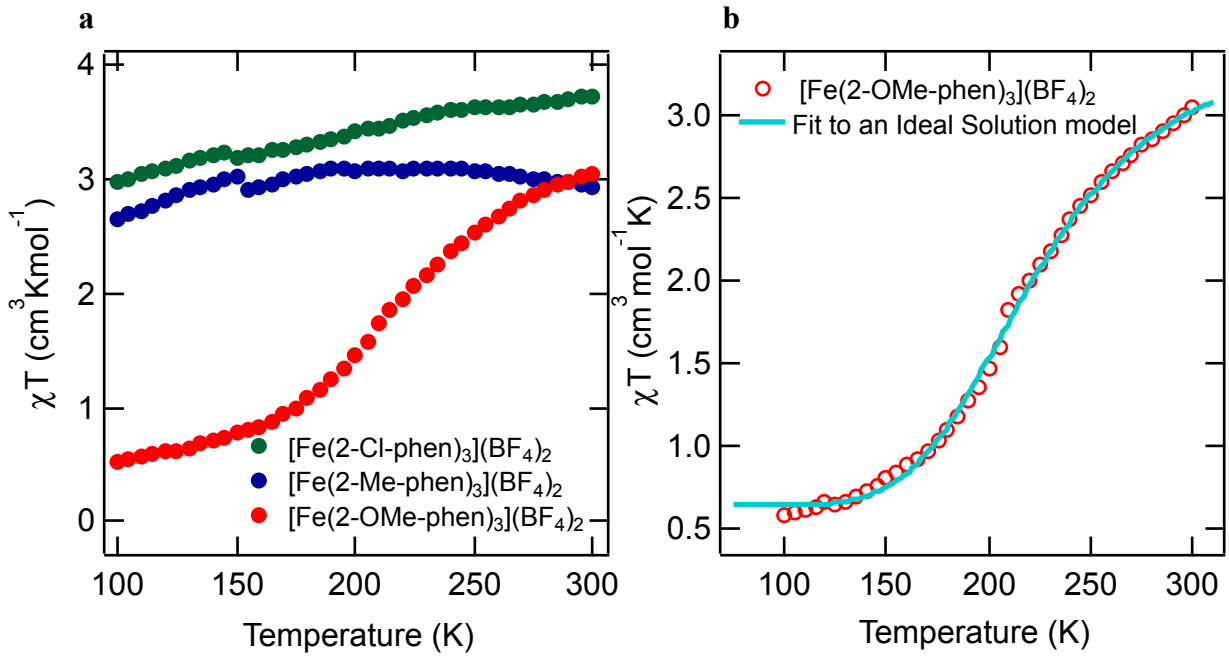

Figure 3.4. (a) Magnetic susceptibility of three Fe(II) complexes in 1 mM solutions in 9:1 methanol-d$_4$/ethanol-d$_6$, collected at an applied field of 1 T. (b) Magnetic susceptibility of [Fe(2-OMe-phen)$_3$](BF$_4$)$_2$ in 9:1 methanol-d$_4$/ethanol-d$_6$, collected with with an applied field of 1 T and fit to an ideal solution model to yield $\Delta H = 1090 \pm 25$ cm^{-1} and $T_{1/2} = 225 \pm 2$ K.

mixture that has a freezing point of ~145 K. In another deviation from the procedure given in Chapter 2, temperature-dependent magnetic susceptibility measurements were collected using SQUID magnetometry instead of Evans NMR method, as with the latter technique it was not possible at temperatures below 210 K due to the inability of the NMR magnet to shim at these lower temperatures.

Figure 3.4 displays the variable-temperature magnetic measurements of three Fe(II) complexes in approximately 1 mM methanol-d_4/ethanol-d_6 solutions from 100-300 K. Qualitatively analogous to the data presented in Chapter 2, only $[Fe(2\text{-}OMe\text{-}phen)_3]^{2+}$ displays SCO behavior, while $[Fe(2\text{-}Me\text{-}phen)_3]^{2+}$ and $[Fe(2\text{-}Cl\text{-}phen)_3]^{2+}$ are essentially only high-spin in fluid solution. The minor dependence on the magnetic moment of $[Fe(2\text{-}Cl\text{-}phen)_3]^{2+}$ on temperature could indicate some slight population of the low-spin state upon cooling, however this population does not exceed ~10%. The slight lowering of χT of $[Fe(2\text{-}Me\text{-}phen)_3]^{2+}$ at higher temperatures may be attributed to spin-orbit coupling.[42] It is not unusual to observe solvent-dependent magnetic behavior of Fe(II) complexes with ligands that impose a ligand-field strength close to the SCO region, however in the case of the $[Fe(2\text{-}R\text{-}phen)_3]^{2+}$ series it is apparent that any fluctuations in the relative ligand field strengths of these complexes is not significant enough to impact their SCO character, or lack thereof.

From the magnetic data of $[Fe(2\text{-}OMe\text{-}phen)_3]^{2+}$, it becomes apparent that the magnetic moment plateaus at ~0.61 $cm^3mol^{-1}K$ (μ_{eff} = 2.2), well above the expected spin-only value for a completely low-spin Fe(II) complex (0 $cm^3mol^{-1}K$). This may arise due to temperature independent paramagnetism.[43] Because of this plateauing at lower temperatures, the ideal solution model cannot extrapolate a reasonable value of $(\chi T)_{LS}$, or the magnetic susceptibility of the completely low-spin form of $[Fe(2\text{-}OMe\text{-}phen)_3]^{2+}$. As such, in the same analysis outlined in

Chatper 2, the mole fraction of the high-spin (γ_{HS}) and low-spin (γ_{LS}) species at every temperature was found with the expression:

$$\gamma_{HS} = \frac{\chi T - (\chi T)_{LS}}{(\chi T)_{HS} - (\chi T)_{LS}} \tag{3.33}$$

With $(\chi T)_{LS}$ approximated as 0 $cm^3mol^{-1}K$ and $(\chi T)_{HS}$, the magnetic susceptibility of the completely HS form of $[Fe(2\text{-}OMe\text{-}phen)_3]^{2+}$, taken as 3.52 $cm^3mol^{-1}K$ from the ideal solution fit. With the relative concentrations of the high- and low-spin states at each temperature in hand, the equilibrium constant (K_{eq}) defining the HS/LS equilibrium can be found as a function of temperature, subsequently allowing for the determination of $\Delta G°$ using the van't Hoff relation:

$$\Delta G° = -RT \ln K_{eq} \tag{3.34}$$

Just as k_{nr} was measured for the ground-state recovery process in $[Fe(2\text{-}OMe\text{-}phen_3]^{2+}$ from the transiently populated $^5T_2$ state as a function of temperature in an acetone solution with variable-

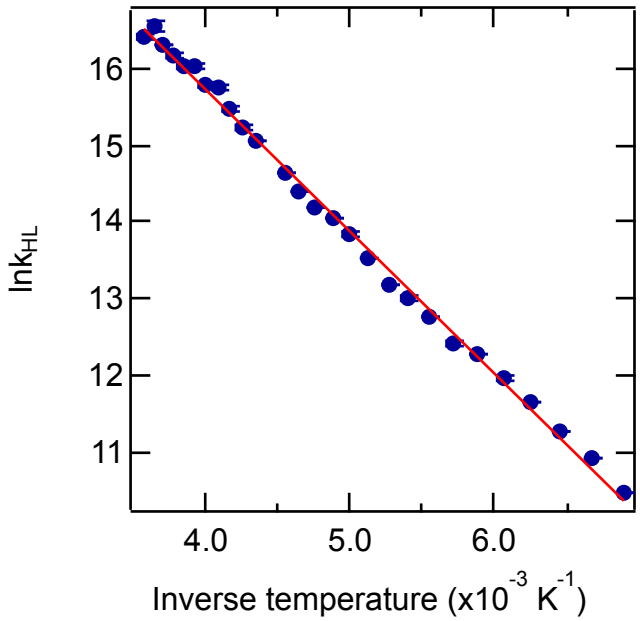

Figure 3.5. Arrhenius plot of k_{HL} from variable-temperature transient absorption spectroscopy of $[Fe(2\text{-}OMe\text{-}phen)_3](BF_4)_2$ in 9:1 methanol/ethanol, with the solid line as the fit to the Arrhenius model, yielding $E_a = 1260 \pm 40$ cm^{-1} and $A = 9.37 \times 10^9$ s^{-1} ($R^2 = 0.99$).

temperature transient absorption spectroscopy (VT-TA) in Chapter 2, the measurements were conducted in 9:1 methanol/ethanol solutions. Using K_{eq} from magnetic measurements, k_{HL} was extracted from the observed rate constants at each temperature, and the Arrhenius plot for k_{HL} yielded the activation energy (E_a) and frequency factor (A) for the $^5T_2 \rightarrow {}^1A_1$ conversion (Figure 3.5). It should be noted that k_{HL} is dependent on temperature over this temperature range (145-300 K).

The barrier measured for the $^5T_2 \rightarrow {}^1A_1$ conversion in this alcohol solution is higher than that measured in acetone (Table 3.1), which can be explained by examining the experimentally-determined values of $\Delta G°$ (from the magnetic data) and λ (from the combined Arrhenius and Marcus analysis described in Chapter 2 and reference 1). At 300 K, $\Delta G°$ is smaller in 9:1 methanol/ethanol than in acetone, which on its own would result in the opposite trend in activation energies than observed. However, λ in the 9:1 methanol/ethanol solution is much higher than in acetone, which overrides the effects of the decreased $\Delta G°$ and raises the $^5T_2/{}^1A_1$ barrier. This increase in λ upon changing solvent highlights the outer sphere component (λ_o) of the total reorganization energy. In this specific case, one could imagine hydrogen-bonding between the methoxy substituent on the ligand and solvent being more prevalent in the alcohol solution than in acetone, raising λ_o. Although the exact value for the dielectric constant of the 9:1 methanol/ethanol solution has not been measured, it is expected to higher than that of acetone (20.7 at 298 K), as the dielectric constants of its components are both higher (MeOH = 32.7, EtOH = 24.3 at 298 K). Therefore, it is not expected that the differences summarized in Table 3.1 are due to changes in

Table 3.1. Parameters defining the $^5T_2 \rightarrow {}^1A_1$ conversion in $[Fe(2\text{-OMe-phen})_3](BF_4)_2$ in acetone and 9:1 methanol/ethanol at 300 K.

Parameter	Acetone	9:1 MeOH/EtOH
E_a (cm^{-1})	1100 ± 20	1260 ± 40
$\Delta G°$ (cm^{-1})	510 ± 20	365 ± 5
λ (cm^{-1})	3300 ± 100	5800 ± 200

ion-pairing upon changing the solvent, as no ion-pairing was observed in acetone (Chapter 2), and ion-pairing becomes less probable with increasing dielectric constant.

3.3.2. Comparison of semi-classical and quantum-mechanical models of nonradiative decay

Now that we have experimental data for $\Delta G°$ and k_{HL} in fluid solution from 145-300 K, we can begin to compare the ability of the semi-classical (eq. 3.19) and quantum-mechanical (eq. 3.30) theories to model these data. First, k_{HL} as function of temperature and $\Delta G°$ was fit according to Marcus theory (Figure 3.6). As is evident from the ability of the semi-classical theory to fit the data, even at lower temperatures (Figure 3.5 and 3.6b), the condition that $k_BT \gg \hbar\omega$ is fulfilled. If the kinetically relevant mode for ground-state recovery were characterized by a frequency of

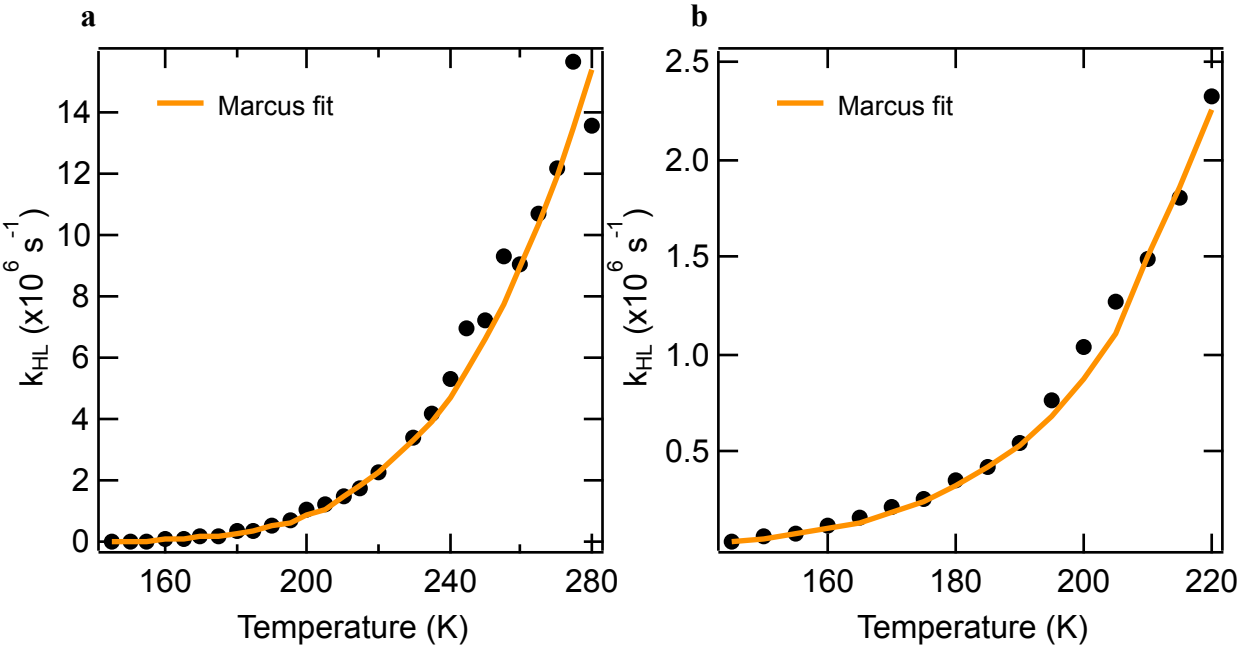

Figure 3.6. Rate of nonradiative decay from the $^5T_2 \rightarrow {}^1A_1$ in $[Fe(2\text{-OMe-phen})_3](BF_4)_2$ in 9:1 methanol/ethanol as a function of temperature. Black dots are individual data points, and the orange line is the fit to Marcus theory to yield $\lambda_{avg} = 3350 \pm 250$ cm^{-1} and $H_{ab} = 1.7 \pm 0.4$ cm^{-1}. (a) Data and fit from 145-280 K. (b) Data and fit from 145-220 K.

250 cm^{-1} as suggested by Hauser for a series of other low-spin and spin-crossover complexes,[44] this condition would not be met. Indeed, for a 250 cm^{-1} mode, k_BT is equal to $\hbar\omega$ at 360 K, and

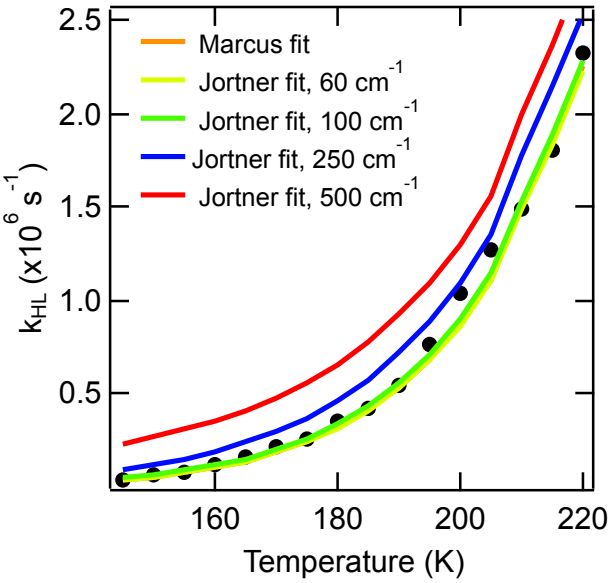

Figure 3.7. Semi-classical (Marcus) and quantum-mechanical (Jortner) fits of the temperature dependence of k_{HL} in $[Fe(2\text{-OMe-phen})_3](BF_4)_2$ in 9:1 methanol/ethanol.

therefore we would expect to observe some temperature independent kinetics over the temperatures studied here. The mere fact that no temperature independent kinetics are observed for ground-state recovery in $[Fe(2\text{-OMe-phen})_3]^{2+}$ from 145-300 K, and therefore the semi-classical theory for nonradiative decay can sufficiently model its behavior, suggests that the kinetically relevant mode is below 150 cm^{-1}, within the limits of a single-mode approximation.

We can further our analysis by fitting k_{HL} versus temperature with the quantum-mechanical model, eq. 30, while fixing $\hbar\omega$ at various frequencies and examining their fits (Figure 3.7) as well as their associated values of λ_{avg} and H_{ab} (Table 3.2). When the frequency of the mode is fixed at 60 cm^{-1} and 100 cm^{-1}, the fits to the data, λ_{avg}, and H_{ab} are all indistinguishable from those

Table 3.2. Values of λ and H_{ab} obtained from semi-classical and quantum-mechanical fits.

Fit	λ_{avg} (cm^{-1})	H_{ab} (cm^{-1})
Marcus	3350 ± 250	1.7 ± 0.4
Jortner 60 cm^{-1}	3350 ± 250	1.7 ± 0.4
Jortner 100 cm^{-1}	3300 ± 250	1.6 ± 0.4
Jortner 250 cm^{-1}	3450 ± 230	1.7 ± 0.4
Jortner 500 cm^{-1}	5000 ± 300	4.3 ± 1.0

associated with the semi-classical fitting. Small but noticeable systematic over-estimations of k_{nr} are seen when $\hbar\omega$ is increased to 250 cm^{-1}, but the parameters associated with this fit are still within error of the lower-frequency fits. Increasing $\hbar\omega$ to 500 cm^{-1} results in a clearly unsatisfactory fit, and the values found for λ_{avg} and H_{ab} are well above those calculated for the semi-classical theory. It should be noted that although both models assume that the driving force associated with the electron transfer process of interest is temperature independent, i.e. there is no entropic component to $\Delta G°$, they both are capable of adequately reproducing the experimental temperature dependence of k_{nr}, despite the fact that this assumption is not acceptable for the $^5T_2 \rightarrow {}^1A_1$ conversion. We were able to circumvent this constraint by independently measuring $\Delta G°$ over the entire solution-phase temperature range, allowing us to fit k_{nr} as function of both temperature and the driving force, thereby accounting for the small but non-zero ΔS associated with ground-state recovery.

The convergence of the semi-classical and quantum-mechanical theories for nonradiative decay when $\hbar\omega$ is less 250 cm^{-1} and the fact that the semi-classical theory can effectively model the data down to 145 K provides experimental evidence that $\Delta Q_{LF/GS}$ is defined by a vibrational mode that has a frequency of less than 250 cm^{-1}. The largest caveat to this conclusion is that these models operate under a single-mode approximation, and therefore instead of representing a unique vibrational mode, this limit for the value of $\hbar\omega$ could represent the average between two or more modes, including those associated with the solvent. While this most certainly is the case, we argue that to reach such a low average frequency, if assuming a multi-mode coordinate, low frequency modes must be important nonetheless. There is a formulation of the quantum-mechanical theory that accounts for a multi-configuration nuclear coordinate,[45] however because reasonable fits can

be obtained with the single-mode theory, the significance of a multi-coordinate analysis would not be clear.

3.3.3. Visualization of low-frequency modes in $[Fe(2\text{-}OMe\text{-}phen)_3]^{2+}$ with DFT frequency calculations

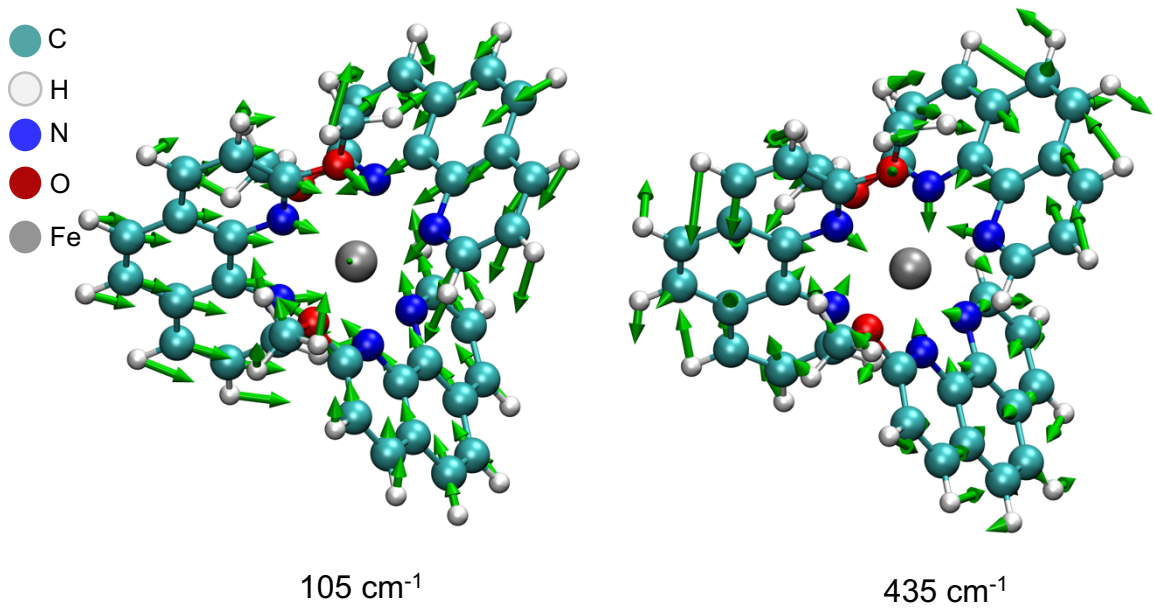

Figure 3.8. Diagrams of geometric distortions associated with 105 cm^{-1} and 435 cm^{-1} modes of the $^5T_2$ state of $[Fe(2\text{-}OMe\text{-}phen)_3]^{2+}$, as predicted by DFT frequency calculations. Visual molecular dynamic figures were prepared by Bryan C. Paulus.

Now, we would like to visualize the geometric distortions associated with vibrational modes at frequencies lower than 250 cm^{-1}. Therefore, DFT frequency calculations were conducted on $[Fe(2\text{-}OMe\text{-}phen)_3]^{2+}$ in the $^5T_2$ state in solution. In general, the modes below 250 cm^{-1} were characterized by Fe-N bond deformations, while above this threshold the vibrations are related to distortions of the ligands. This contrast is highlighted by comparing two modes that both have Fe-N stretching character: 105 and 435 cm^{-1} frequencies (Figure 3.8). The higher frequency mode, which according to our quantum-mechanical analysis is not a good representation of the kinetically relevant mode for ground-state recovery, has a high degree of ligand bending motion

accompanying the changes in Fe-N bond lengths and angles. On the other hand, the 105 cm^{-1} mode has very little twisting of the ligand, only translational motion in response to the changing Fe-N bond lengths. This confirms previous hypotheses that the geometric changes coupled to the $^5T_2 \rightarrow {}^1A_1$ conversion are Fe-N in character, and that synthetically modifying the ligand backbone would have little effect on $\Delta Q_{LF/GS}$.[46,47]

3.3.4. $\Delta Q_{MLCT/GS}$ from spectral analysis of $[Ru(2\text{-}OMe\text{-}phen)_3](BF_4)_2$

With a firm grasp on the identity of $\Delta Q_{LF/GS}$, we can turn our attention to defining $\Delta Q_{MLCT/GS}$ using the Ru(II) analog of $[Fe(2\text{-}OMe\text{-}phen)_3]^{2+}$. First, $[Ru(2\text{-}OMe\text{-}phen)_3](BF_4)_2$ was synthesized by modifying a procedure by Hammarström and co-workers for synthesizing sterically strained polypyridyl Ru(II) complexes,[48] where the chlorides of the $Ru(DMSO)_4Cl_2$ starting material are stripped off with Ag^+ in the presence of the ligand at reflux. Synthesis of the *tris*-compound was achieved, but a high-quality crystal structure was elusive, as two of the three 2-OMe-phen ligands were highly disordered due to the presence of both enantiomers (Figure 3.9a). The absorption spectrum of $[Ru(2\text{-}OMe\text{-}phen)_3]^{2+}$ (Figure 3.9b, green trace) is typical of a Ru(II) polypyridyl complex,[49] with a broad $^1A_1 \rightarrow$ MLCT absorption feature centered at 465 nm. At room temperature, following excitation into this MLCT absorption, the complex is very weakly emissive (Figure 3.9b). This emissive feature is barely above the detection limit of our fluorimeter, so only an approximate radiative quantum yield (Φ_r) of ~1×10^{-4} can be found, two orders of magnitude lower than the benchmark Ru(II) polypyridyl, $[Ru(bpy)_3]^{2+}$, for which $\Phi_r = 9.5 \times 10^{-2}$.[30]

Time-resolved emission on $[Ru(2\text{-}OMe\text{-}phen)_3]^{2+}$ in acetone was collected on a total-correlated single photon counting instrument with the help of Professor Gary Blanchard, as the excited-state lifetime was below the IRF of our nanosecond system. Following excitation into the MLCT absorption feature, the ^{3}MLCT excited-state lifetime was found to be 1.90 ± 0.01 ns (Figure

3.9c), significantly reduced from the ^{3}MLCT lifetime in $[Ru(bpy)_3]^{2+}$, 950 ns.[50] Insight into the

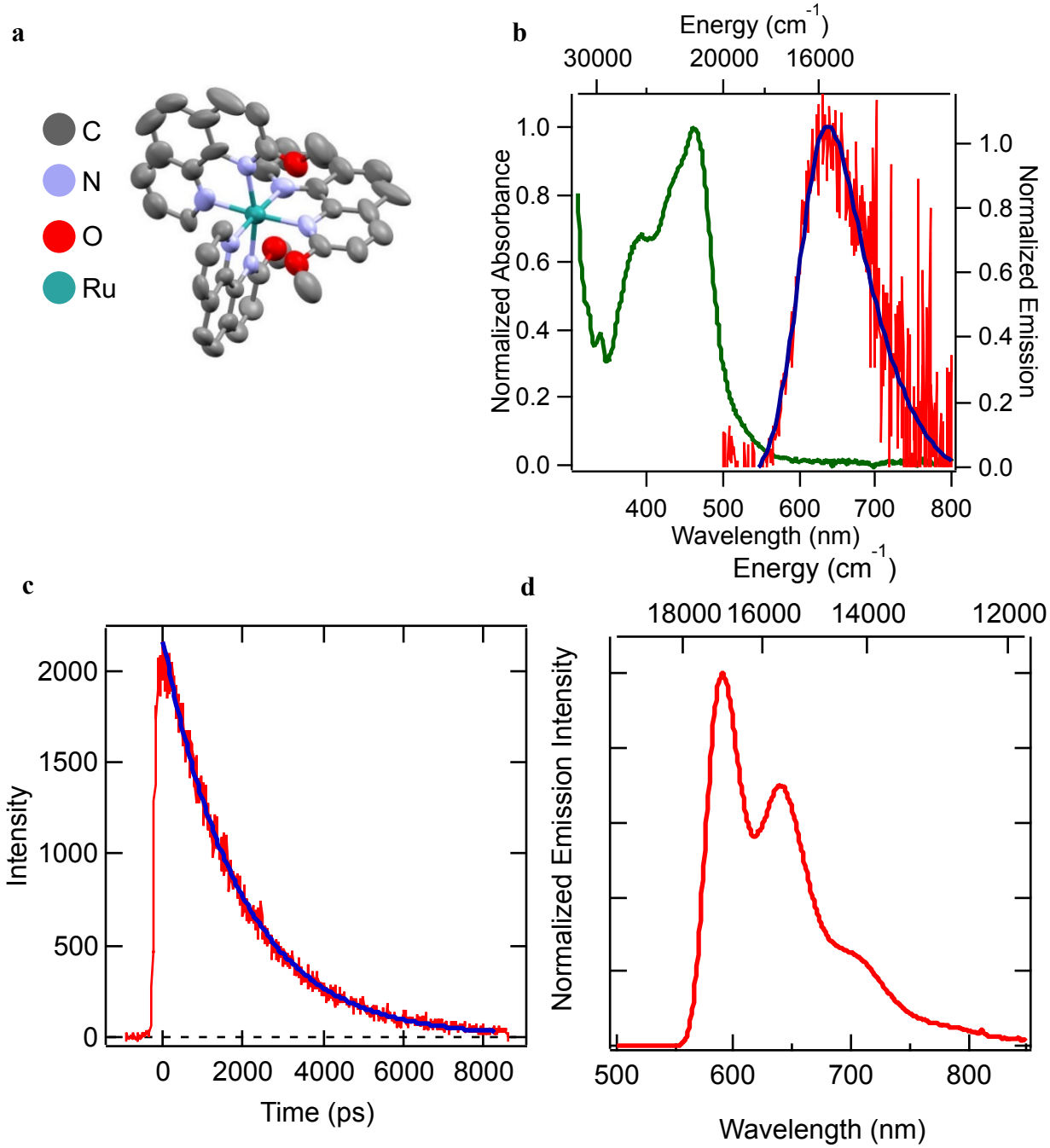

Figure 3.9. (a) X-ray crystal structure of $[Ru(2\text{-OMe-phen})_3](BF_4)_2$. Counteranions and hydrogen atoms have been omitted for clarity. (b) Room temperature ground state absorption (green trace) and steady-state emission of $[Ru(2\text{-OMe-phen})_3](BF_4)_2$ (red trace). Emission spectrum was collected in deoxygenated acetone following excitation at 475 nm, blue line represents a fit to an asymmetric double sigmoidal function. (c) Time-resolved emission of $[Ru(2\text{-OMe-phen})_3](BF_4)_2$ in acetone monitoring at 610 nm following excitation at 475 nm, fit to a single exponential (blue trace) to yield a time constant of $\tau = 1.9 \pm 0.01$ ns. (d) Steady-state emission of $[Ru(2\text{-OMe-phen})_3](BF_4)_2$ in 4:1 methanol/ethanol at 77 K, exciting at 475 nm.

origin of the low Φ_r and short ^{3}MLCT excited-state lifetime observed in $[Ru(2\text{-OMe-phen})_3]^{2+}$ can be gleaned from examining the radiative (k_r) and nonradiative rates of decay from the ^{3}MLCT.[vi] While in $[Ru(bpy)_3]^{2+}$ k_{nr} is only one order of magnitude faster than k_r (9.53×10^5 and 10.0×10^4 s^{-1}, respectively),[50] in $[Ru(2\text{-OMe-phen})_3]^{2+}$ k_{nr} far outpaces k_r (5.3×10^8 and 5.3×10^4 s^{-1}, respectively). The increase in k_{nr} for $[Ru(2\text{-OMe-phen})_3]^{2+}$ is likely a result of the presence of lower-energy ^{3}T ligand-field excited states, which provide nonradiative decay pathways from the ^{3}MLCT, than in $[Ru(bpy)_3]^{2+}$ and other complexes utilizing stronger-field ligands. It is unsurprising that 2-OMe-phen imparts a weak enough ligand-field strength to diminish emission from the ^{3}MLCT so greatly, as this effect has been reported in $[Ru(6\text{-Me-bpy})_3]^{2+}$ (6-Me-bpy = 6-methyl-2,2'-bipyridine).[51]

However, at 77 K in a solvent glass, the nonradiative deactivation into ligand-field states slows to such an extent that a well-resolved steady-state emission spectrum with vibronic progressions can be observed (Figure 3.9d). From a single-mode Franck-Condon analysis[52] of this low-temperature spectrum to eq. 3.31, a value of 1320 cm^{-1} is obtained for $\hbar\omega$, the vibrational mode coupled to the $^3\text{MLCT} \rightarrow {}^1A_1$ transition. This frequency falls within the range reported for numerous Ru(II) polypyridyl complexes,[50,53] and corresponds to aromatic C=C bond stretches, consistent with the fact that geometric distortions associated with the ^{3}MLCT excited state relative to the ground state are mostly ligand-based.[24–26]

3.4. Concluding remarks

A convergence of semi-classical and quantum-mechanical theories of nonradiative decay to describe the temperature dependence of k_{nr} for the $^5T_2 \rightarrow {}^1A_1$ process in a polypyridyl Fe(II) spin-crossover complex, $[Fe(2\text{-OMe-phen})_3]^{2+}$, was observed only when the frequency of the mode

[vi] $\Phi_r = k_r/k_{obs}$ and $k_{obs} = k_r + k_{nr}$

coupled to this transition is less than 250 cm^{-1}. Coupled with DFT frequency calculations, these results have allowed us to conclude that $\Delta Q_{LF/GS}$ is defined by Fe-N stretching and torsional modes, and that deformations of the ligand backbone are not kinetically relevant. Furthermore, a single-mode Franck-Condon analysis of the low-temperature steady-state emission spectrum of the Ru(II) analog to the Fe(II) SCO complex determined that the average frequency of the vibrational modes coupled to the $^3MLCT \rightarrow {}^1A_1$ transition is 1320 cm^{-1}. We can translate these findings to describe $\Delta Q_{MLCT/GS}$ in $[Fe(2\text{-}OMe\text{-}phen)_3]^{2+}$ as composed of aromatic C=C bond stretching in the ligand. These experimentally grounded conclusions about the nature of $\Delta Q_{LF/GS}$ and $\Delta Q_{MLCT/GS}$ can be used as benchmarks for computational work to elucidate how these two segments of the nuclear intersect and glean which geometric distortions are coupled to the $MLCT \rightarrow {}^5T_2$ transition in $[Fe(2\text{-}OMe\text{-}phen)_3]^{2+}$. Although the characterization of both $[Fe(2\text{-}OMe\text{-}phen)_3]^{2+}$ and $[Ru(2\text{-}OMe\text{-}phen)_3]^{2+}$ suggest that these complexes are typical of their class and therefore the results presented here can be extended to other Fe(II) polypyridyl complexes, the application of this approach should be combined to other Fe(II) SCO complexes to confirm this assumption. Specifically, studying Fe(II) SCO complexes with different coordination environments and varying the denticity of the coordinating ligands would be useful to investigating how general the results presented on $[Fe(2\text{-}OMe\text{-}phen)_3]^{2+}$ are. Finally, one of the most robust manners to prove that specific modes are relevant for a given electronic transition is to synthetically modify a molecule to target these modes and look for changes in the excited-state dynamics that suggest perturbation of a given nuclear coordinate. Attempts along these lines for low-spin Fe(II) polypyridyls are presented in the next chapter of this dissertation.

APPENDIX

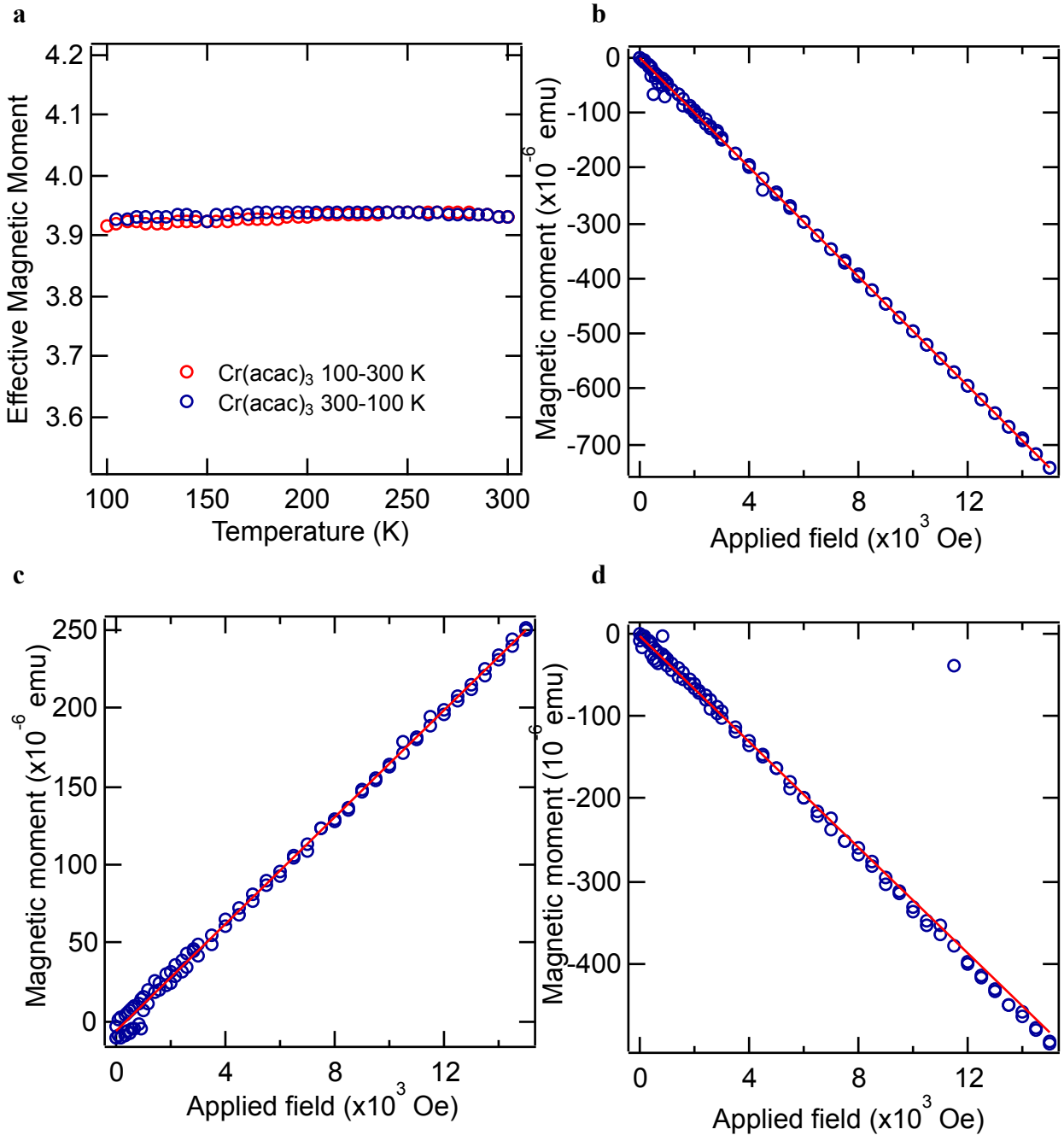

Figure 3.10. (a) Calibration of solution-phase SQUID methodology with $Cr(acac)_3$ in a 9:1 methanol/ethanol solution, collected in DC mode with an applied field of 1 T. (b-d) Variable field magnetic measurements in 9:1 methanol/ethanol solutions at 100 K of (b) $[Fe(2\text{-}OMe\text{-}phen)_3](BF_4)_2$, (c) $[Fe(2\text{-}Cl\text{-}phen)_3](BF_4)_2$, and (d) $[Fe(2\text{-}Me\text{-}phen)_3](BF_4)_2$. The red lines are fits to a linear regression.

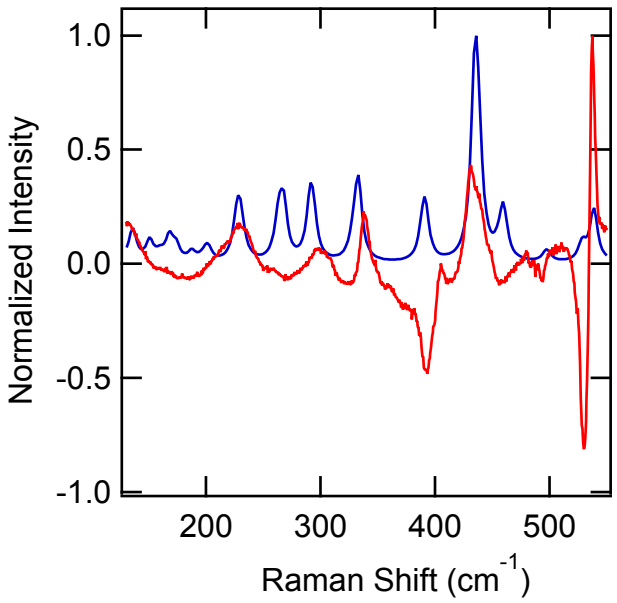

Figure 3.11. Red trace: Resonance Raman of $[Fe(2\text{-}OMe\text{-}phen)_3](BF_4)_2$ in acetone using 488 nm excitation. Collected in Professor Proshlyakov's laboratory with the assistance of Allison Stettler. Blue trace: DFT frequency calculations' predicted Raman spectrum of the $^5T_2$ of $[Fe(2\text{-}OMe\text{-}phen)_3]^{2+}$ in acetone.

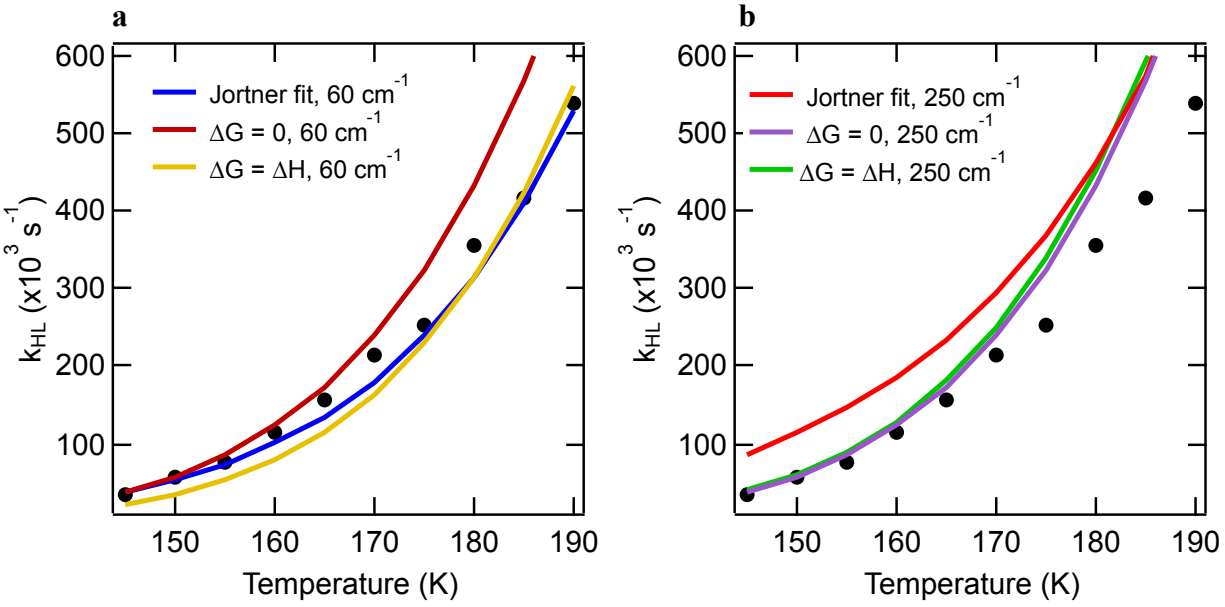

Figure 3.12. Fits of the temperature dependence of k_{HL} in $[Fe(2\text{-}OMe\text{-}phen)_3](BF_4)_2$ in 9:1 methanol/ethanol, fixing $\Delta G° = 0$ cm^{-1} or ΔH (1090 cm^{-1}) and $\hbar\omega$ to (a) 60 cm^{-1} and (b) 250 cm^{-1}.

REFERENCES

REFERENCES

1. Carey, M. C.; Adelman, S. L.; McCusker, J. K. Insights into the Excited State Dynamics of Fe(II) Polypyridyl Complexes from Variable-Temperature Ultrafast Spectroscopy. *Chem. Sci*. **2019**, *10*, 134–144. https://doi.org/10.1039/C8SC04025G.

2. DeVault, D. *Quantum-Mechanical Tunnelling in Biological Systems*, Second Ed.; University of Cambridge: New York, 1984.

3. Barbara, P. F.; Meyer, T. J.; Ratner, M. A. Contemporary Issues in Electron Transfer Research. *J. Phys. Chem.* **1996**, *100*, 13148–13168.

4. Brookes, J. C. Quantum Effects in Biology: Golden Rule in Enzymes, Olfaction, Photosynthesis and Magnetodetection. *Proc. R. Soc. A* **2017**, *473*. https://doi.org/10.1098/rspa.2016.0822.

5. Newton, M. Electron Transfer Reactions in Condensed Phases. *Annu. Rev. Phys. Chem.* **1984**, *35*, 437–480. https://doi.org/10.1146/annurev.physchem.35.1.437.

6. Newton, M. D. Quantum Chemical Probes of Electron-Transfer Kinetics: The Nature of Donor-Acceptor Interactions. *Chem. Rev*. **1991**, *91*, 767–792. https://doi.org/10.1021/cr00005a007.

7. Marcus, R. A.; Sutin, N. Electron Transfers in Chemistry and Biology. *Biochemica et Biophysica Acta* **1985**, *811*, 265–322. https://doi.org/10.1016/0304-4173(85)90014-X.

8. Mikkelsen, K. V.; Ratner, M. A. Electron Tunneling in Solid-State Electron-Transfer Reactions. *Chem. Rev*. **1987**, *87*, 113–153. https://doi.org/10.1021/cr00077a007.

9. Kestner, N. R.; Logan, J.; Jortner, J. Thermal Electron Transfer Reactions in Polar Solvents. *J. Phys. Chem*. **1974**, *78*, 2148–2166. https://doi.org/10.1021/j100614a017.

10. Marcus, R. A. Electron Transfer Reactions in Chemistry. Theory and Experiment. *Rev. Mod. Phys*. **1993**, *65*, 599–610. https://doi.org/10.1103/RevModPhys.65.599.

11. Marcus, R. A. On the Theory of Oxidation-Reduction Reactions Involving Electron Transfer: I. *J. Chem. Phys*. **1956**, *24*, 966–978.

12. Marcus, R. A. On the Theory of Electron-Transfer Reactions: VI. Unified Treatment for Homogeneous and Electrode Reactions. *J. Chem. Phys*. **1965**, *43*, 679–701.

13. Marcus, R. A. Electron Transfer Reactions. In *Chemische Elementarprozesse*; Hartmann, H., Ed.; Springer-Verlag: Berlin, 1968; pp 348–356.

14. Marcus, R. A. Electron Transfer and Tunneling in Chemical and Biological Systems. In *Light-induced charge separation in biology and chemistry*; Gerischer, H., Katz, J. J., Eds.; Dahlem Konferenzen, Verlag Chemie: Berlin, 1979; pp 15–43.

15. Griffith, J. S. *Theory of Transition Metal Ions*; Cambridge University Press: New York, 1961.

16. Buhks, E.; Navon, G.; Bixon, M.; Jortner, J. Spin Conversion Processes in Solutions. *J. Am. Chem. Soc.* **1980**, *102*, 2918–2923. https://doi.org/10.1021/ja00529a009.

17. Xie, C. L.; Hendrickson, D. N. Mechanism of Spin-State Interconversion in Ferrous Spin-Crossover Complexes: Direct Evidence for Quantum Mechanical Tunneling. *J. Am. Chem. Soc*. **1987**, *109*, 6981–6988. https://doi.org/10.1021/ja00257a013.

18. Conti, A. J.; Xie, C. L.; Hendrickson, D. N. Tunneling in Spin-State Interconversion of Ferrous Spin-Crossover Complexes. Concentration Dependence of Apparent Activation Energy Determined in Solution by Laser-Flash Photolysis. *J. Am. Chem. Soc*. **1989**, *111*, 1171–1180. https://doi.org/10.1021/ja00186a002.

19. Hauser, A. Intersystem Crossing in Fe(II) Coordination Compounds. *Coord. Chem. Rev*. **1991**, *111*, 275–290.

20. Monat, J. E.; McCusker, J. K. Femtosecond Excited-State Dynamics of an Iron(II) Polypyridyl Solar Cell Sensitizer Model. *J. Am. Chem. Soc*. **2000**, *122*, 4092–4097. https://doi.org/10.1021/ja992436o.

21. Gawelda, W.; Cannizzo, A.; Pham, V.-T.; van Mourik, F.; Bressler, C.; Chergui, M.; Mourik, F. Van; Bressler, C.; Chergui, M. Ultrafast Nonadiabatic Dynamics of $[Fe(II)(bpy)_3)]^{2+}$ in Solution. *J. Am. Chem. Soc*. **2007**, *129*, 8199–8206. https://doi.org/10.1021/ja070454x.

22. Nance, J.; Bowman, D. N.; Mukherjee, S.; Kelley, C. T.; Jakubikova, E. Insights into the Spin-State Transitions in $[Fe(tpy)_2]^{2+}$: Importance of the Terpyridine Rocking Motion. *Inorg. Chem*. **2015**, *54*, 11259–11268. https://doi.org/10.1021/acs.inorgchem.5b01747.

23. Ashley, D. C.; Jakubikova, E. Ray-Dutt and Bailar Twists in Fe(II)-Tris(2,2′-bipyridine): Spin States, Sterics, and Fe–N Bond Strengths. *Inorg. Chem*. **2018**, *57*, 5585–5596. https://doi.org/10.1021/acs.inorgchem.8b00560.

24. Caspar, J. V.; Westmoreland, T. D.; Allen, G. H.; Meyer, T. J.; Bradley, P. G.; Woodruff, W. H. Molecular and Electronic Structure in the Metal-to-Ligand Charge-Transfer Excited States of d^6 Transition-Metal Complexes in Solution. *J. Am. Chem. Soc*. **1984**, *106*, 3492–3500. https://doi.org/10.1021/ja00324a017.

25. Gawelda, W.; Johnson, M.; De Groot, F. M. F.; Abela, R.; Bressler, C.; Chergui, M. Electronic and Molecular Structure of Photoexcited $[Ru^{II}(bpy)_3]^{2+}$ Probed by Picosecond

X-Ray Absorption Spectroscopy. *J. Am. Chem. Soc*. **2006**, *128*, 5001–5009. https://doi.org/10.1021/ja054932k.

26. Sato, T.; Nozawa, S.; Tomita, A.; Hoshino, M.; Koshihara, S. Y.; Fujii, H.; Adachi, S. I. Coordination and Electronic Structure of Ruthenium(II)-tris-2,2′-bipyridine in the Triplet Metal-to-Ligand Charge-Transfer Excited State Observed by Picosecond Time-Resolved Ru K-Edge XAFS. *J. Phys. Chem. C* **2012**, *116*, 14232–14236. https://doi.org/10.1021/jp3038285.

27. Claude, J. P.; Meyer, T. J. Temperature Dependence of Nonradiative Decay. J. *Phys. Chem*. **1995**, *99*, 51–54. https://doi.org/10.1021/j100001a010.

28. McCusker, C. E.; McCusker, J. K. Synthesis and Spectroscopic Characterization of CN-Substituted Bipyridyl Complexes of Ru(II). *Inorg. Chem*. **2011**, *50*, 1656–1669. https://doi.org/10.1021/ic102085b.

29. Bain, G. A.; Berry, J. F. Diamagnetic Corrections and Pascal's Constants. *J. Chem. Educ*. **2008**, *85*, 532. https://doi.org/10.1021/ed085p532.

30. Suzuki, K.; Kobayashi, A.; Kaneko, S.; Takehira, K.; Yoshihara, T.; Ishida, H.; Shiina, Y.; Oishi, S.; Tobita, S. Reevaluation of Absolute Luminescence Quantum Yields of Standard Solutions Using a Spectrometer with an Integrating Sphere and a Back-Thinned CCD Detector. *Phys. Chem. Chem. Phys*. **2009**, *11*, 9850–9860. https://doi.org/10.1039/b912178a.

31. Pillman, H. A.; Blanchard, G. J. Effects of Energy Dissipation on Motional Dynamics in Unilamellar Vesicles. *J. Phys. Chem. B* **2010**, *114*, 13703–13709. https://doi.org/10.1021/jp1045723.

32. Frisch, M. J.; Trucks, G. W.; Schlegel, H. B.; Scuseria, G. E.; Robb, M. A.; Cheeseman, J. R.; Scalmani, G.; Barone, V.; Petersson, G. A.; Nakatsuji, H.; et al. Gaussian 16, Revision B.01. Gaussian Inc: Wallington, CT 2016.

33. Becke, A. D. Density-Functional Thermochemistry. III. The Role of Exact Exchange. *J. Chem. Phys*. **1993**, *98*, 5648–5652. https://doi.org/10.1063/1.464913.

34. Lee, C.; Hill, C.; Carolina, N. Development of the Colle-Salvetti Correlation-Energy Formula into a Functional of the Electron Density. *Chem. Phys. Lett*. **1989**, *162*, 165–169. https://doi.org/10.1016/0009-2614(89)85118-8.

35. Stephens, P. J.; Devlin, F. J.; Chabalowski, C. F.; Frisch, M. J. Ab Initio Calculation of Vibrational Absorption and Circular Dichroism Spectra Using Density Functional Force Fields. *J. Phys. Chem*. **1994**, *98*, 11623–11627. https://doi.org/10.1021/j100096a001.

36. Koch, W.; Holthausen, M. C. *A Chemist's Guide to Density Functional Theory*, Second Edition, Second.; John Wiley & Sons: Chichester, 2001.

37. Krishnan, R.; Binkley, J. S.; Seeger, R.; Pople, J. A. Self-Consistent Molecular Orbital Methods. XX. A Basis Set for Correlated Wave Functions. *J. Chem. Phys*. **1980**, *72*, 650–654. https://doi.org/10.1063/1.438955.

38. McLean, A. D.; Chandler, G. S. Contracted Gaussian Basis Sets for Molecular Calculations. I. Second Row Atoms, Z=11-18. *J. Chem. Phys*. **1980**, *72*, 5639–5648. https://doi.org/10.1063/1.438980.

39. Wachters, A. J. H. Gaussian Basis Sets for Molecular Wavefunctions Containing Third-Row Atoms. *J. Chem. Phys*. **1970**, *52*, 1033–1036. https://doi.org/10.1007/BF00529105.

40. Hay, P. J. Gaussian Basis Sets for Molecular Calculations. The Representation of 3d Orbitals in Transition-Metal Atoms. *J. Chem. Phys*. **1977**, *66*, 4377–4384. https://doi.org/10.1063/1.433731.

41. Raghavachari, K.; Trucks, G. W. Highly Correlated Systems. Excitation Energies of First Row Transition Metals Sc-Cu. *J. Chem. Phys*. **1989**, *91*, 1062–1065. https://doi.org/10.1063/1.457230.

42. Carlin, R. L. *Magnetochemistry*; Springer-Verlag Berlin Heidelberg: Berlin, 1986.

43. Kahn, O. *Molecular Magnetism*, 1st ed.; VCH Publishers: New York, 1993.

44. Hauser, A. Light-Induced Spin Crossover and the High-Spin to Low-Spin Relaxation. In *Spin Crossover in Transition Metal Compounds II*; Gütlich, P.; Goodwin, H. A., Eds.; Springer-Verlag, 2004; pp 155–198.

45. Jortner, J. Temperature Dependent Activation Energy for Electron Transfer between Biological Molecules. *J. Chem. Phys*. **1976**, *64*, 4860–4867. https://doi.org/10.1063/1.432142.

46. Stock, P.; Deck, E.; Hohnstein, S.; Korzekwa, J.; Meyer, K.; Heinemann, F. W.; Breher, F.; Hörner, G. Molecular Spin Crossover in Slow Motion: Light-Induced Spin-State Transitions in Trigonal Prismatic Iron(II) Complexes. *Inorg. Chem*. **2016**, *55*, 5254–5265. https://doi.org/10.1021/acs.inorgchem.6b00238.

47. Petzold, H.; Djomgoue, P.; Hörner, G.; Lochenie, C.; Weber, B.; Rüffer, T. Bis-Meridional Fe^{2+} Spincrossover Complexes of Phenyl and Pyridyl Substituted 2-(pyridin-2-yl)-1,10-phenanthrolines. *Dalt. Trans.* **2018**, *47*, 491–506. https://doi.org/10.1039/c7dt02320k.

48. Abrahamsson, M.; Lundqvist, M. J.; Wolpher, H.; Johansson, O.; Eriksson, L.; Bergquist, J.; Rasmussen, T.; Becker, H. C.; Hammarström, L.; Norrby, P. O.; et al. Steric Influence on the Excited-State Lifetimes of Ruthenium Complexes with Bipyridyl-alkanylene-pyridyl Ligands. *Inorg. Chem*. **2008**, *47*, 3540–3548. https://doi.org/10.1021/ic7019457.

49. Juris, A.; Balzani, V.; Barigelletti, F.; Campagna, S.; Belser, P.; Von Zelewsky, A. Ru(II) Polypyridine Complexes: Photophysics, Photochemistry, Electrochemistry, and Chemiluminescence. *Coord. Chem. Rev*. **1988**, *84*, 85–277.

50. McCusker, C. E.; McCusker, J. K. Synthesis and Spectroscopic Characterization of CN-Substituted Bipyridyl Complexes of Ru(II). *Inorg. Chem*. **2011**, *50*, 1656–1669. https://doi.org/10.1021/ic102085b.

51. Sun, Q.; Mosquera-Vazquez, S.; Lawson Daku, L. M.; Guénée, L.; Goodwin, H. A.; Vauthey, E.; Hauser, A. Experimental Evidence of Ultrafast Quenching of the ^{3}MLCT Luminescence in Ruthenium(II) Tris-bipyridyl Complexes via a ^{3}dd State. *J. Am. Chem. Soc*. **2013**, *135*, 13660–13663. https://doi.org/10.1021/ja407225t.

52. Arias-Rotondo, D. M. Photo-Induced Electron and Energy Transfer in Donor-Acceptor Systems Featuring a Spin-Coupled Metal Dimer, PhD Dissertation, Michigan State University, East Lansing, MI, 2018.

53. Damrauer, N. H.; Weldon, B. T.; McCusker, J. K. Theoretical Studies of Steric Effects on Intraligand Electron Delocalization: Implications for the Temporal Evolution of MLCT Excited States. *J. Phys. Chem. A* **1998**, *102*, 3382–3397. https://doi.org/10.1021/jp9805095.

CHAPTER 4. ATTEMPTED SYNTHESIS OF HEXADENTATE FE(II) SPIN-CROSSOVER COMPLEXES

4.1. Introduction

The analysis described in Chapters 2 and 3 is quite similar to that described in Hendrickson and coworker's 1987 report[1] on complex believed to exhibit SCO behavior: a member of a series of closely related complexes, $[Fe((6\text{-Me-py})_{3-x}(py)_x tren)]^{2+}$ **(**Figure 4.1). In this series, a methyl substituent is systematically introduced to the 6-position of each pyridyl group, and each additional methyl group lowers the ligand-field strength of the hexadentate ligand. As a result, the Fe(II) complex with the unsubstituted pyridyl ligand (complex **1** in Figure 4.1) is completely low-spin, and the Fe(II) complex with the completely methylated ligand is strictly high-spin (complex **4**) in solution. Consequently, asymmetric methyl substitution (complexes **2** and **3**) were shown to result in complexes that had temperature-dependent magnetic and optical properties, indicating their characterization as SCO complexes. This series seemed to provide an excellent platform to probe

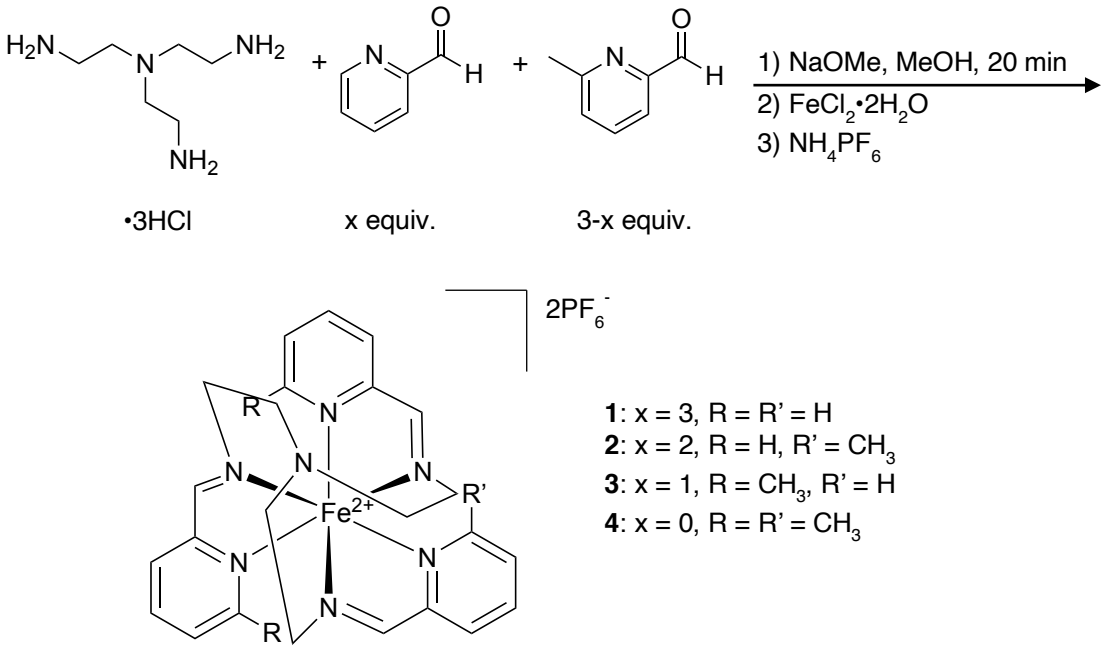

Figure 4.1. General synthetic scheme to prepare the complexes of the $[Fe((6\text{-Me-py})_{3-x}(py)_x tren)](PF_6)_2$ series.

the mechanism of SCO, as such it was the subject of numerous reports in the 1980s, including Hendrickson's.[2]

However, there was a glaring issue with these works: complexes **2** and **3** contained significant impurities of the other members of the series as a result of the synthetic route used to prepare them (Figure 4.1), where stoichiometric amounts of the 6-substituted and unsubstituted pyridinecarboxaldehydes were used in the imine condensation with tris(2-aminoethyl)amine (tren). Although the elemental analyses of complexes **2** and **3** indicated that the complexes were pure, the difference between the calculated mass percentages of carbon, hydrogen, and nitrogen for all four members of the series are actually within the experimental error of the measurement. However, high-resolution mass spectrometry collected by Lindsey Jamula[3] on complexes **2** and **3** prepared in this manner clearly show the presence of other members of the series. This fact casts doubt onto Hendrickson's results, as all of the data collected on what was assumed to be complex **3** is actually a convolution of three different complexes, all with distinct thermodynamic and electronic parameters. As the $[Fe((6\text{-Me-py})_{3-x}(py)_x tren)]^{2+}$ series contains two closely related SCO complexes, it would be an ideal platform to apply the semi-classical and quantum-mechanical analyses outlined in this chapter's introduction, as they would provide two new data points with unambiguous values of $\Delta G°$. Therefore, a path towards obtaining pure SCO complexes **2** and **3** was pursued.

4.2. Experimental section

4.2.1. Synthesis

General synthesis. Unless otherwise noted, all reactions were conducted either using standard Schlenk techniques or in an inert atmosphere glove box (nitrogen-filled, Vacuum Atmospheres). Tris-2(aminoethyl)amine was purchased from Alfa Aesar and vacuum distilled from potassium

hydroxide and activated carbon (Norbit pellets, Sigma Aldrich) twice, or until colorless, prior to use. 4 Å molecular sieves (Acros Organics) were activated by flame drying and cooling the sieves under vacuum three times before storing under nitrogen. Tris(2-tris(2-pyridin-2-ylmethylene)amino)ethyl)amine iron(II) hexafluorophosphate ($[Fe(trenpy_3)](PF_6)_2$),[4] tri-tert-butyl (nitrilotris(ethane-2,1-diyl))tricarbamate ($trenBoc_3$)[5] and *o*-iodoxybenzoic acid (IBX)[6] were prepared according to the literature procedures. MeOH, DCM, MeCN, THF, Et_2O were bubble degassed with nitrogen, dried over activated neutral alumina, and pumped into an inert atmosphere glovebox. Anhydrous DMF and acetone were purchased from Acros Organics. NH_4OH refers to aqueous 30% ammonium hydroxide from Jade Scientific. All other reagents and solvents were purchased from either Sigma Aldrich, Acros Organics, or Oakwood Chemical Company and used as received. Silica gel was purchased either from Silicycle (Silica Flash 60 Å porosity, 40-63μm/230-400 mesh) or Sorbtec (Premium Rf 60 Å porosity, 40-75 μm/200-400 mesh). A ninhydrin TLC developing stain was prepared by dissolving 1 g of ninhydrin in 50 mL of ethanol. To develop TLC plates, the spotted TLC plates were dipped into the ninhydrin stain and heated to 80°C. ^1H NMR were collected on an Agilent DDR2 500 MHz spectrometer and referenced to residual solvent shifts. Electrospray ionization mass spectra were obtained at the Michigan State University Mass Spectrometry and Metabolomics Core on a Waters G2-XS QToF mass spectrometer interfaced to a Waters Aquity UPLC. Elemental analyses were obtained through the analytical facilities at Michigan State University on samples that had been ground in a vial with a glass stir rod in an inert atmosphere glovebox and stored under vacuum overnight prior to analysis.

tris(2-tris(2-pyridin-2-ylmethylene)amino)ethyl)amine ($trenpy_3$). Tren (500 mg, 3.4 mmol) was dissolved in MeCN (5 mL) and activated 4 Å molecular sieves were added. 2-pyridinecarboxaldehyde (1.1 g, 10.3 mmol) was dissolved in MeCN (3 mL) and added dropwise.

The beige suspension was stirred overnight, filtered through Celite, and the solvent was removed. The yellow oil was triturated with Et_2O three times to remove any excess 2-pyridinecarboxaldehyde, yielding the pure product as an orange oil (705 mg, 50% yield). All characterization data matched those in the literature.[7]

tris[N-(2-pyridylmethyl)-2-aminoethyl]amine (TPAA). Prepared according to Deroche et al,[8] with minor modifications. $Trenpy_3$ (705 mg, 1.7 mmol) was dissolved in MeOH (10 mL), and 10% palladium on carbon (84 mg) was added under nitrogen. A negative pressure was pulled on the flask, and a hydrogen-filled balloon was added. The black suspension stirred for 12 h, filtered through Celite, and the solvent was removed, yielding 582 mg (83% yield) of the product as a yellow oil. All characterization data matched those in the literature.[8]

tris(2-tris(2-pyridin-2-ylmethylene)amino)ethyl)amine iron(II) hexafluorophosphate $[Fe(trenpy_3)](PF_6)_2$ prepared from oxidation/reduction of $[Fe(TPAA)]^{3+}$. TPAA (582 mg, 1.4 mmol) was dissolved in anhydrous DMF (10 mL). Anhydrous $FeCl_3$ (225 mg, 1.4 mmol) was added to the ligand, prompting a color change from yellow to deep green. After stirring for 3 h, the solution was pumped/purged with N_2 five times, then cannula transferred into a flask charged with IBX (1.29 g, 4.6 mmol). After stirring under N_2 for 3 h at room temperature, the suspension had turned to a deep purple color. The suspension was filtered, and NaI (210 mg, 1.4 mmol) was added to filtrate, which was allowed to stir for 1 h under N_2. NH_4PF_6 (2.3 g, 14 mmol) was added, and the dark purple solution was stirred for 1 h. Et_2O was added until cloudy, then the purple precipitate was collected by filtration. The solid was dissolved in a minimum amount of acetone, crashed out with Et_2O, and collected again by filtration. ^1H NMR of this dark purple solid matched that of the independently prepared $[Fe(trenpy_3)](PF_6)_2$, with no paramagnetic impurities observed.

tert-butyl (2-(bis(2-aminoethyl)amino)ethyl)carbamate (trenBoc). Prepared from the literature procedures[9–11] with several modifications. A solution of tren (730 mg, 5 mmol) in DCM (75 mL) was cooled in a dry ice/acetone bath under nitrogen. Di-tert-butyl-dicarbonate (220 mg, 1 mmol) in DCM (25 mL) was added dropwise over 1 h at -78 °C. The reaction was allowed to warm to room temperature and stir overnight. Once the solvent was removed, a solution of the crude product was prepared with 10:4:1 $CHCl_3$/MeOH/NH_4OH (18 mg of crude product/mL of eluent), and this solution was filtered through a plug of silica (Sigma Aldrich) until no product was detected in the eluent by TLC developed with ninhydrin. The solvent was removed from the filtrate, and again enough of the 10:4:1 $CHCl_3$/MeOH/NH_4OH eluent was added to reach a concentration of 18 mg/mL, and from this solution the product was obtained via purification by column chromatography with silica gel (Sorbtech) and10:4:1 $CHCl_3$/MeOH/NH_4OH eluent (383 mg, 50% yield). ^{1}H NMR (500 MHz, CD_3OD) 3.12 (t, J = 6.2 Hz, 2 H), 2.70 (t, J = 5.8 Hz, 4 H), 2.53 (m, 6 H), 1.44 (s, 9 H); ^{13}C NMR (CD_3OD): 157.41, 78.72, 55.44, 54.33, 38.48, 38.23, 37.29. HRMS (ESI-TOF) m/z: $[M + H]^+$ calcd for $C_{11}H_{26}N_4O_2$ 247.2134; Found 247.2147.

tert-butyl (2-(bis(2-((pyridin-2-ylmethyl)amino)ethyl)amino)ethyl)carbamate (trenpy$_2$Boc). trenBoc (383 mg, 1.56 mmol) was dissolved in MeCN (10 mL) and added to activated 4 Å molecular sieves, to which 2-pyridinecarboxaldehyde (334 mg, 3.12 mmol) was added dropwise. The pink suspension was stirred overnight at room temperature, filtered through Celite, and the solvent was removed to yield an orange oil (594 mg, 1.39 mmol, 89% yield) that was used without purification for the next step. ^{1}H NMR (500 MHz, $CDCl_3$) 8.62 (d, J = 4.8 Hz, 2 H), 8.36 (s, 2 H), 7.94 (d, J = 7.9 Hz, 2 H), 7.70 (t, J = 7.6 Hz, 2 H), 7.29 (m, 2 H), 5.44 (s, 1 H), 3.76 (t, J = 6.3 Hz, 4 H), 3.20 (m, 2 H), 2.93 (t, J = 6.4 Hz, 4 H), 2.73 (t, J = 5.3 Hz, 2 H), 1.36 (s, 9 H).

This oil (unreduced trenpy$_2$Boc) was dissolved in MeOH (10 mL) and 10% Pd/C (78 mg) was added. A vacuum was pulled on the flask and a hydrogen-filled balloon was added to the flask. The black suspension was stirred overnight under a hydrogen atmosphere, filtered through celite, and the solvent was removed to yield a light yellow oil (534 mg, 1.25 mmol, 80% yield over two steps) that was used without further purification. ^{1}H NMR (500 MHz, $CDCl_3$) 8.49 (d, J = 4 Hz, 2 H), 7.57 (t, J = 9 Hz, 2 H), 7.28 (2 H, partially obscured by solvent signal), 7.11 (m, 2 H), 3.89 (s, 2 H), 3.19 (m, 2 H), 2.72 (t, J = 5.7 Hz, 2 H), 2.64 (t, J = 5.5 Hz, 2 H), 2.57 (t, J = 5.4 Hz, 2 H), 1.38 (s, 9 H). HRMS (ESI-TOF) m/z: $[M+H]^+$ calcd for $C_{23}H_{36}N_6O_2$ 429.2978; found 429.3022.

N^1-(2-aminoethyl)-N^2-(pyridin-2-ylmethyl)-N^1-(2-((pyridin-2-ylmethyl)amino)ethyl)ethane-1,2-diamine (trenpy$_2$). Trenpy$_2$Boc (534 mg, 1.25 mmol) was dissolved in 3 M HCl in EtOAc (12.4 mL) and stirred at room temperature for 3 h. The solvent was removed, and the yellow oil was washed with Et_2O. 2 M NaOH was added to the yellow oil until the pH reached 12. The solvent was removed from the yellow suspension, and the gummy solid was suspended in DCM and filtered. The solvent was removed from the filtrate to yield a yellow oil (315 mg, 0.96 mmol, 77% yield). ^{1}H NMR (500 MHz, $CDCl_3$) 8.49 (d, J = 4.8 Hz, 2 H), 7.59 (t, J = 7.6 Hz, 2 H), 7.28 (2 H, partially obscured by solvent signal), 7.11 (m, 2 H), 8.87 (s, 4 H), 2.70 (m, 5 H), 2.61 (m, 5 H), 2.47 (t, J = 6 Hz, 2 H). HRMS (ESI-TOF) m/z: $[M+H]^+$ calcd for $C_{18}H_{28}N_6$ 329.2454; found 329.2460.

Benzyl-(2-((2-(((benzyloxy)carbonyl)(pyridin-2-ylmethyl)amino)ethyl)(2-((tert-butoxycarbonyl)amino)ethyl)amino)ethyl)(pyridin-2-ylmethyl)carbamate (trenpy$_2$Cbz$_2$Boc). Trenpy$_2$Boc (222 mg, 0.52 mmol) was sonicated with $NaHCO_3$ (124 mg, 1.5 mmol) in H_2O (2 mL) and then chilled in an ice bath. Benzyl chloroformate (177 mg, 1.04 mmol) was dissolved in THF (4 mL) and added dropwise. This solution was stirred at 0 °C for 2 h, poured

into brine, and extracted into EtOAc (3 × 10 mL). The organic fractions were combined and dried with Na_2SO_4. The crude product was obtained following removal of the solvent as a light yellow oil. See ^1H NMR in the appendix. HRMS (ESI-TOF) m/z: $[M+H]^+$ calcd for desired product $C_{39}H_{48}N_6O_6$ 697.3713 obs 697.3688, $[M+H]^+$ calcd for undesired side product ($trenpy_2Cbz_3Boc$) $[M+H]^+$ $C_{47}H_{54}N_6O_8$ 831.4081 obs 831.4089.

4.3. Results and Discussion

The first obvious avenue was purification of complexes **2** and **3** following their preparation outlined in the 1980s literature (Figure 4.1). However, this turned out to be no easy task, as all attempts using chromatographic separations or recrystallization to isolate each individual complex of the $[Fe((6\text{-Me-py})_{3-x}(py)_xtren)]^{2+}$ failed. The imines in the free ligands are highly susceptible towards hydrolysis, and consequently their chromatographic isolation was also unsuccessful. So, an alternate route was proposed (Figure 4.2), utilizing protection of a single primary amine of tren, which would allow for the addition of 6-R-pyridinecarboxaldehyde via an imine condensation. Subsequent reduction of these imines is essential due to their susceptibility towards hydrolysis under acidic conditions, which are necessary to cleave the Boc protecting group. Reduction of the imines also eliminates the possibility of transimination[12–14] after the primary amine is freed from Boc protection, which could scramble the 2-R-pyridyl groups intermolecularly and lose the desired intramolecular asymmetry. Following this proposed route, once the third primary amine is unprotected, the opposite 6-R-pyridinecarboxaldehyde can be introduced via a second imine condensation and subsequent reduction, again to minimize chances of hydrolysis.

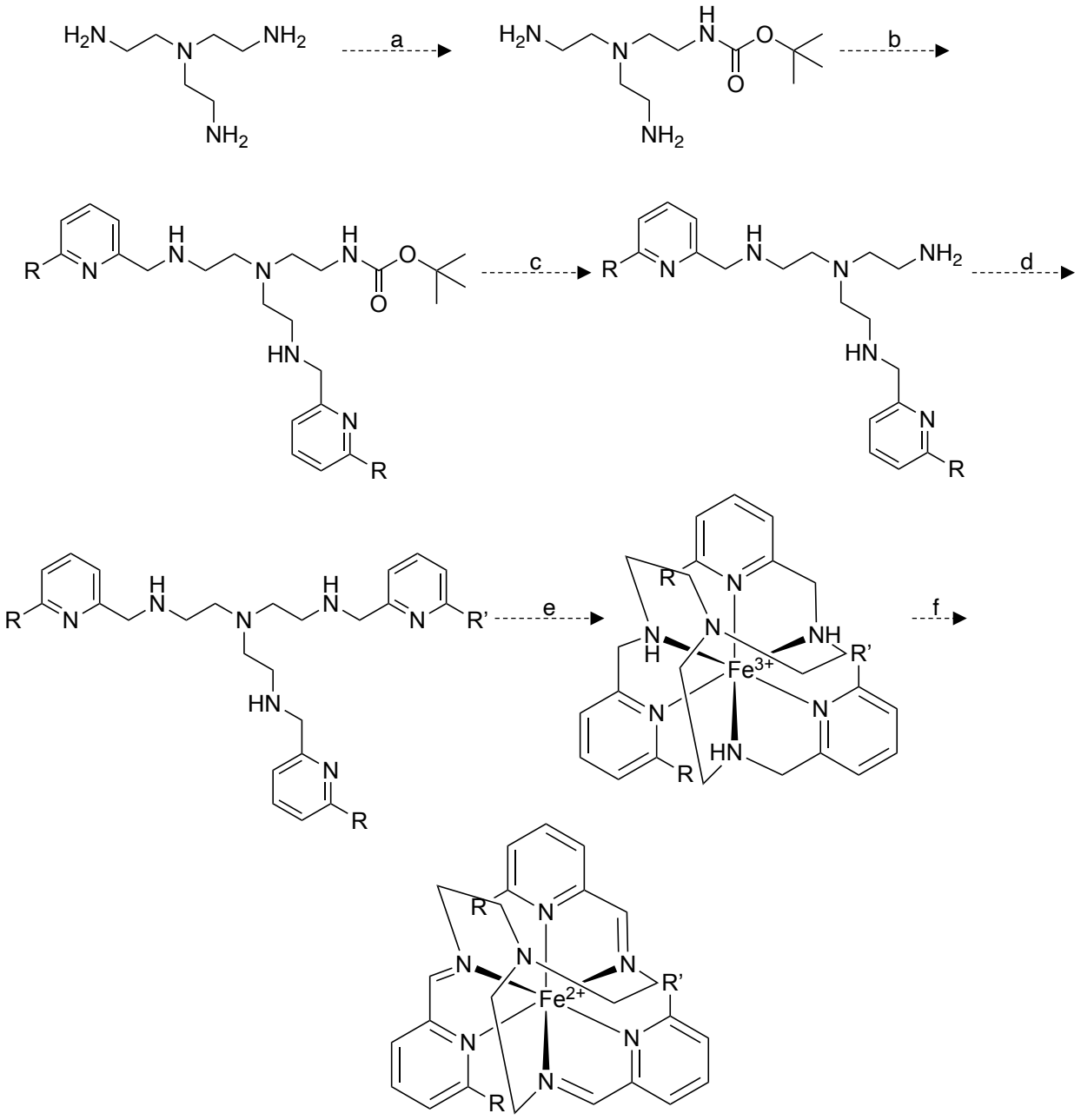

Figure 4.2. Proposed synthetic route to pure complexes **2** and **3**. General reagents and conditions: a) Boc_2O b) 1) 6-R-2-pyridinecarboxaldedyde 2) reduction c) deprotection of Boc-amine d) 1) 6-R'-2-pyridinecarboxaldehyde 2) reduction 3) $FeCl_3$ f) 1) oxidation of amines to imines 2) reduction of Fe^{3+} to Fe^{2+}.

At this point in the proposed synthetic route, the desired asymmetry has been introduction, however the secondary amines must be oxidized back to imines. Because of the ease of hydrolysis, I proposed to bind the reduced form of the asymmetric ligand to Fe(III), which should form a stable

complex,[15] unlike the corresponding Fe(II) complex, for which there is a precedence of instability in the case of $[Fe(TPAA)]^{2+}$ (where TPAA = tris[N-(2-pyridylmethyl)-2-aminoethyl]amine, or the reduced version of the ligand for complex **1**).[16] Then, oxidation of the imines can occur without fear of hydrolysis. Once the desired ligand is formed on the Fe(III) scaffold, the metal center can be reduced to yield the pure SCO complex.

Before I started the synthesis proposed in Figure 4.2, I wanted to confirm that the chemistry-on-the complex approach in step "f" was feasible. First, the oxidant chosen was o-

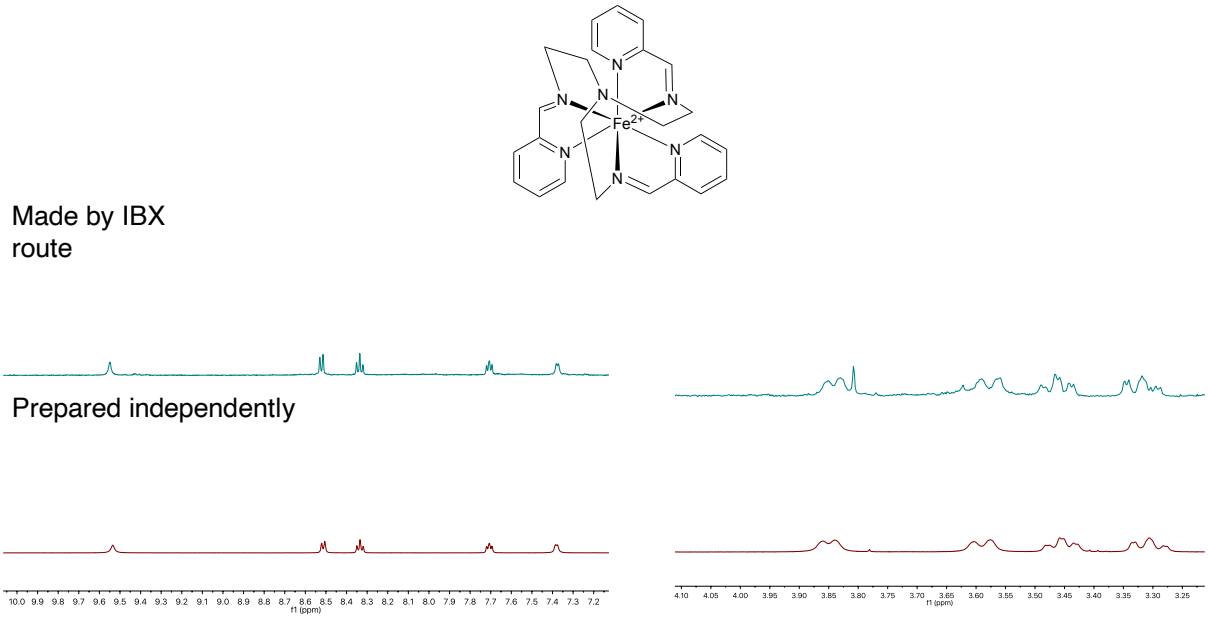

Figure 4.3. Comparison of the ^{1}H NMR spectra of complex **1** prepared from the amine oxidation and Fe(III)-reduction of $[Fe(TPAA)]^{3+}$ (top spectrum) and prepared from the route given in Figure 4.2 (bottom spectrum).

iodoxybenzoic acid (IBX) due to the literature precedence of its ability to oxidize secondary amines with electron-withdrawing substituents to imines under mild conditions.[17] Then, its ability to oxidize secondary amines bound to a metal center was tested on $[Fe(TPAA)]^{3+}$. Using a 3.3:1 ratio of IBX/$[Fe(TPAA)]^{3+}$ followed by reduction of the metal center with sodium iodide resulted in the formation of complex **1**, which was indistinguishable from an independently prepared sample (Figure 4.3).

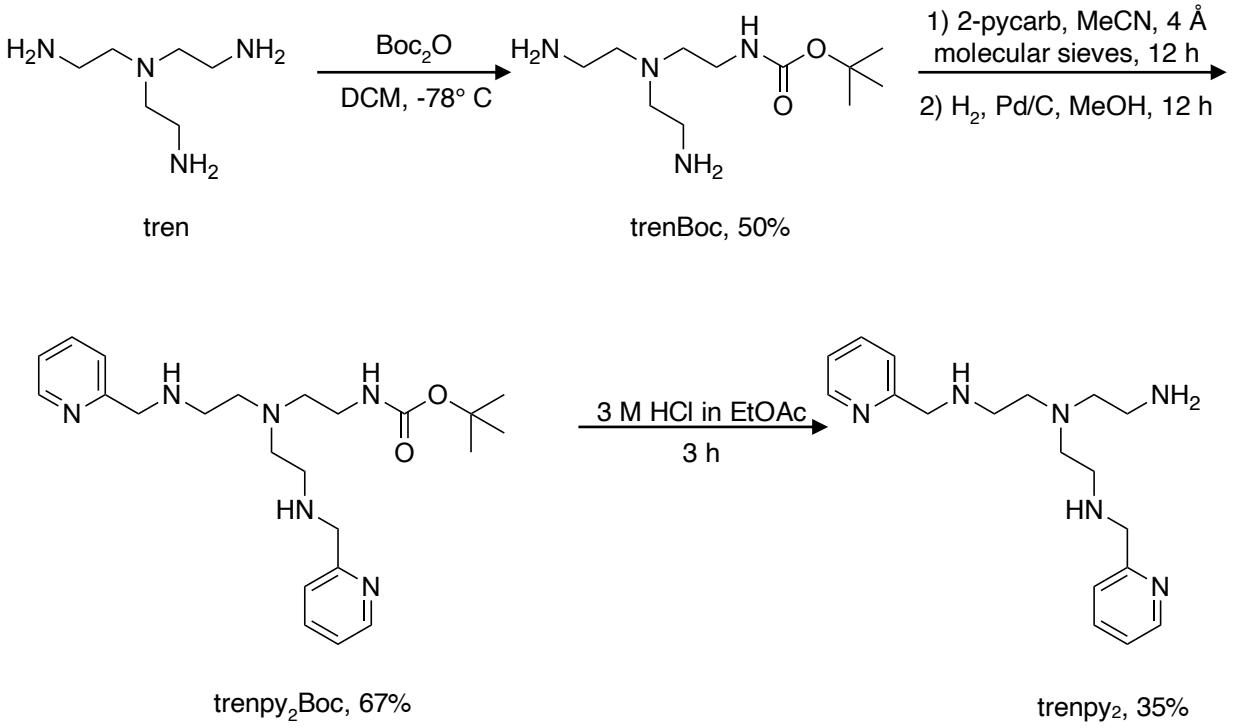

Figure 4.4. Synthesis of $trenpy_2$, an intermediate to complex **2**.

Bolstered by these initial results, the synthesis of complex **2** began (Figure 4.4) by isolating trenBoc from the crude product of the addition of Boc_2O (di-tert-butyl dicarbonate) to tren, which contained the desired product as well as bis- and tris-protected tren.[9–11] Next, while the literature suggests a large array of reaction conditions for similar imine condensations and subsequent reductions,[8,15] the synthesis of $trenpy_2Boc$ was highest yielding and purest when the imine condensation of trenBoc with 2-pyridinecarboxaldehyde (2-pycarb) was carried out in dry MeCN and 4 Å molecular sieves, followed by reduction with H_2 with Pd/C. Several different Boc-deprotection conditions have been suggested, from thermolytic cleavage to the addition of strong acids, however the reasoning behind the chosen deprotection routes is generally undiscussed.[18] As such, many different deprotection conditions were tested on the triply protected tren, $trenBoc_3$,[5] and only 3 M HCl in EtOAc[19] cleanly removed the Boc carbamate to yield completely unprotected tren, indicating that $trenpy_2$ could also be synthesized from this deprotection route.

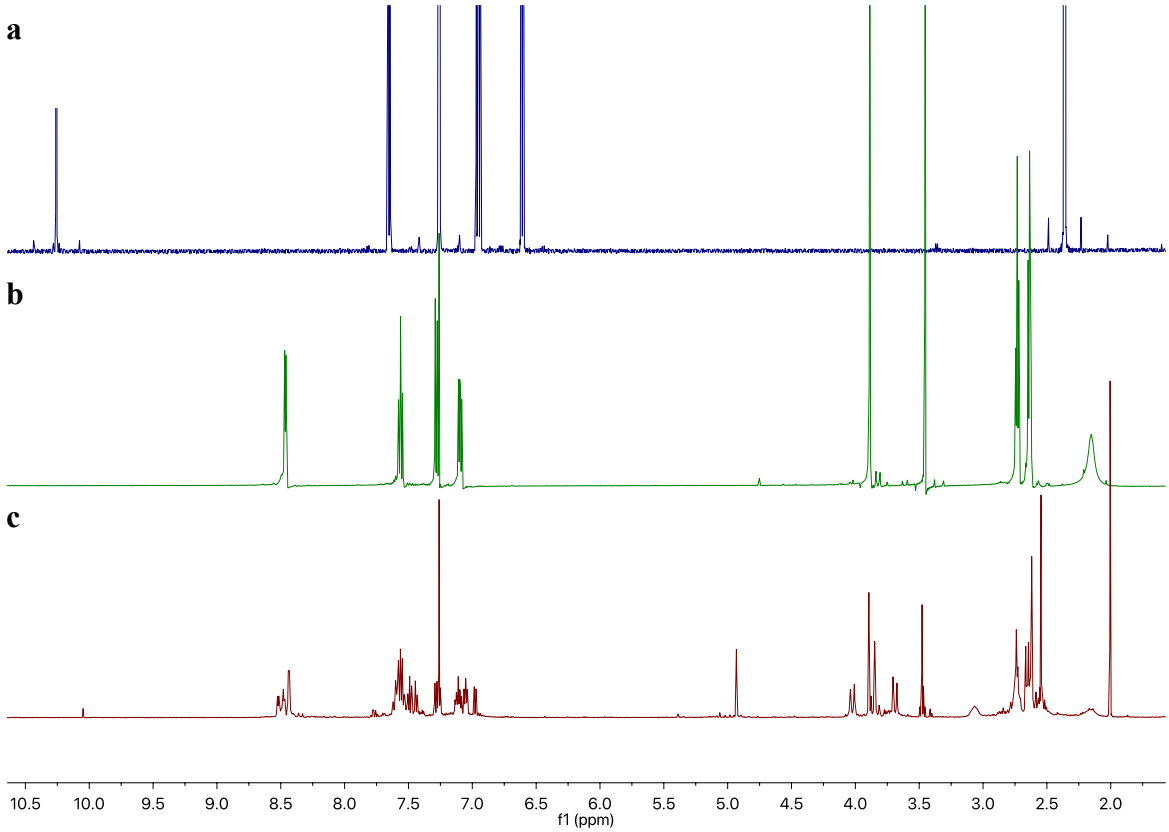

Figure 4.5. ^{1}H NMR of (a) 6-methyl-2-pyridinecarboxaldehyde (6-Me-2-pycarb) (b) tris[N-(2-pyridylmethyl)-2-aminoethyl]amine (TPAA) and c) 6-Me-pycarb + TPAA, all in $CDCl_3$ at room temperature.

Indeed, trenpy$_2$ was successfully isolated. Regrettably, the next step, condensation with 6-methyl-2-pyridinecarboxaldehyde (6-Me-pycarb) did not go as planned. Instead of simply adding the substituted pyridine to the primary amine, several inseparable side products were formed. To probe what is happening in this reaction, a test was performed: 6-Me-2pycarb was added to TPAA in an NMR tube, and then the ^{1}H NMR spectrum was immediately collected (Figure 4.5). As can be seen in Figure 4.5, a reaction is occurring despite the absence of a primary amine. The secondary amines are reacting with the aldehyde, which has been shown to occur rapidly in solution,[13] meaning that step "d" in Figure 4.2 is not a viable step towards synthesizing pure complexes **2** and **3**.

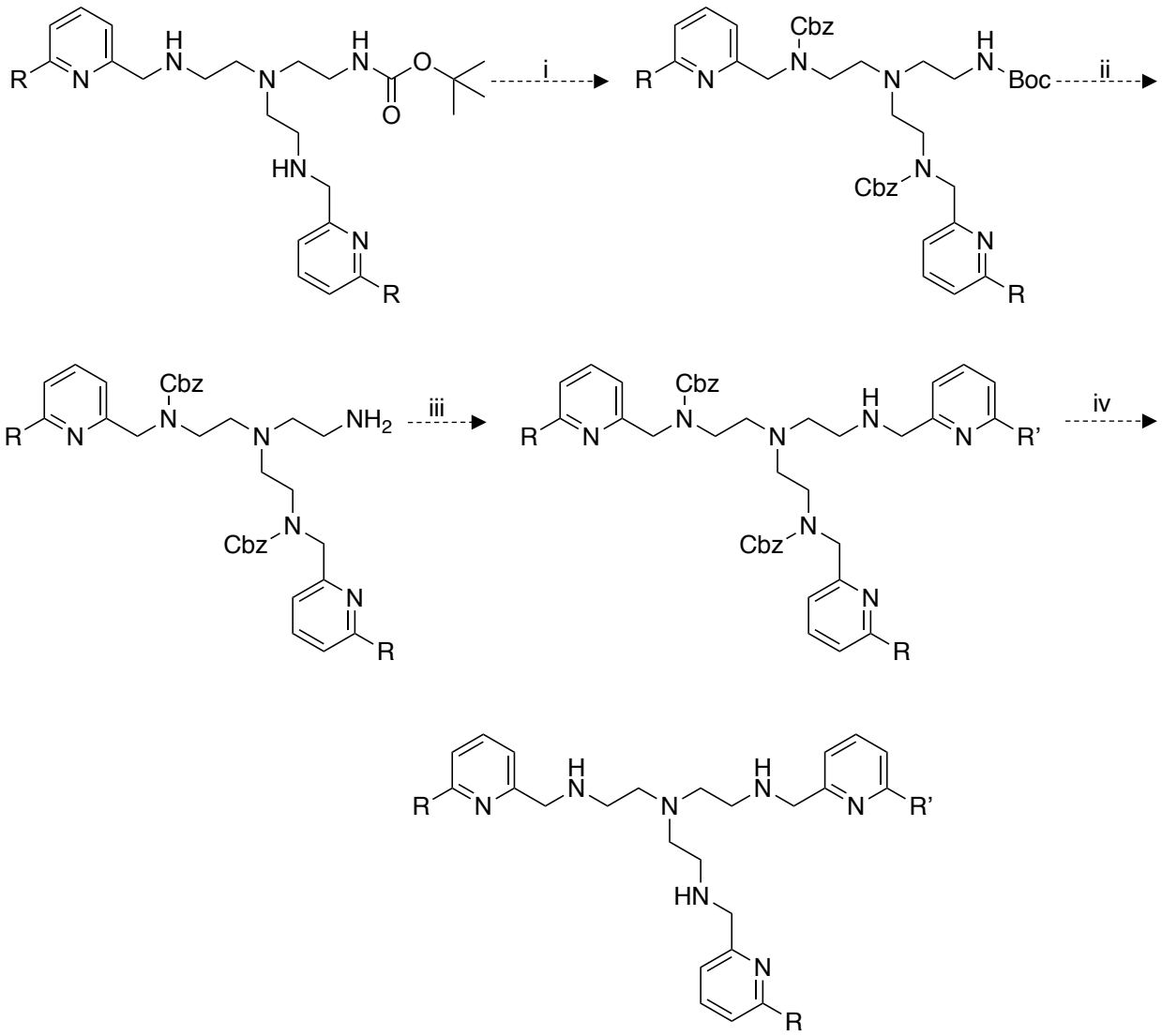

Figure 4.6. Proposed addendum to route in Figure 4.2, where carboxybenzyl (Cbz) carbamates are introduction (step i) prior to acidic Boc deprotection (step ii), imine formation with 6-R'-2-pyridinecarboxaldehyde and subsequent reduction with $NaBH_4$ (step iii). Step iv will be Cbz deprotection with H_2 and Pd/C.

One way to get around this issue of secondary amine reactivity is to protect them with a group stable to the acidic conditions used to remove the Boc protecting group. An obvious choice is Cbz (carboxybenzyl) group, which is cleaved under reductive conditions. And so, the proposed route to was amended prior to Boc deprotection to include Cbz protection of the secondary amines (Figure 4.6). However, when introduction of the Cbz groups was attempted on trenpy$_2$Boc, HRMS showed that not only was the desired product formed, but also the compound shown in Figure 4.7,

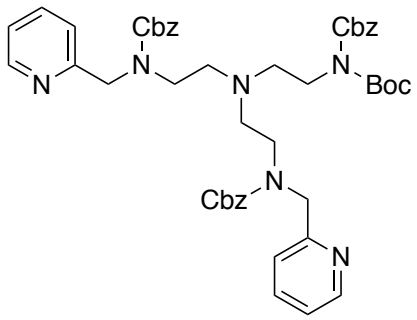

Figure 4.7. Over-protected trenpy$_2$Boc, where the Boc-protected nitrogen has also formed a carbamate with Cbz.

where the Boc carbamate also reacts with CbzCl. All attempts to separate these compounds were unsuccessful. In the hope that future products would be purifiable, Boc deprotection was performed under the same conditions for the Cbz-free ligand, however the product was afflicted by the same issue.

Different conditions to install the Cbz group, i.e. shorter reaction times, lower temperatures, or a different Cbz starting material, could be investigated in the hope that the unfavorable double protection of the Boc carbamate be avoided, however a route with fewer steps and separation problems would be ideal. Unfortunately, the general reactions[12–14] outlined in Figure 4.8 plague most conceivable routes towards the preparation of the ligands of complexes **2**

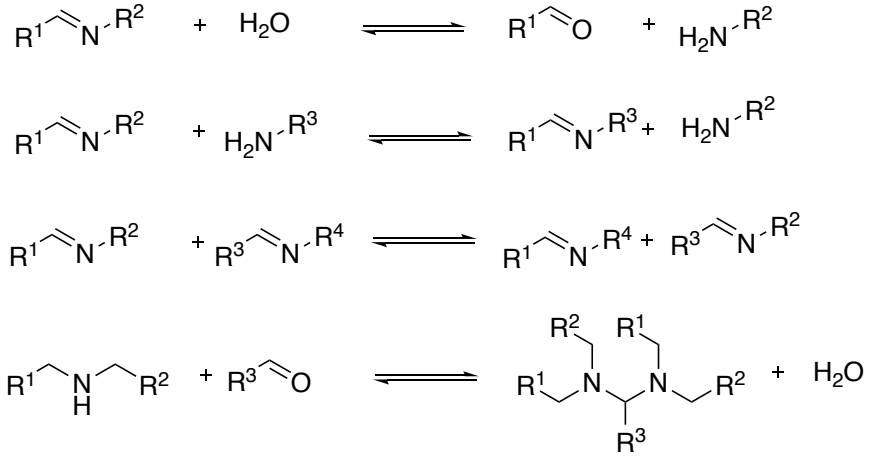

Figure 4.8. General summary of equilibrium reactions that are possible between imines, primary and secondary amines, aldehydes, and water. All result in scrambling of R groups or the formation of side products undesirable for the isolation of pure SCO complexes **2** and **3**. Made with data presented in references 12-14.

and **3** and make their synthesis much more complicated than first envisioned. Therefore, due to the indubitably formidable synthetic route that would have to proposed and embarked upon to isolate pure complexes **2** and **3**, we decided to abandon these SCO complexes.

4.4. Conclusion

At first glance, the $[Fe((6\text{-}Me\text{-}py)_{3-x}(py)_xtren)]^{2+}$ series presents an appealing group of Fe(II) polypyridyl complexes for the determination of the nuclear coordinate associated with excited-state evolution for hexadentate Fe(II) chromophores. However, due to the reactivity and instability of imines, the synthetic effort required to cleanly isolate the two spin-crossover Fe(II) complexes has proven to be an insurmountable barrier for the in-depth characterization required for the desired analysis. The most promising route towards the isolation of SCO complexes **2** and **3** may simply be the chromatographic separation of the crude reaction mixture containining complexes **1**-**4** prepared by the original synthetic route used in the previous reports of their characterization.

APPENDIX

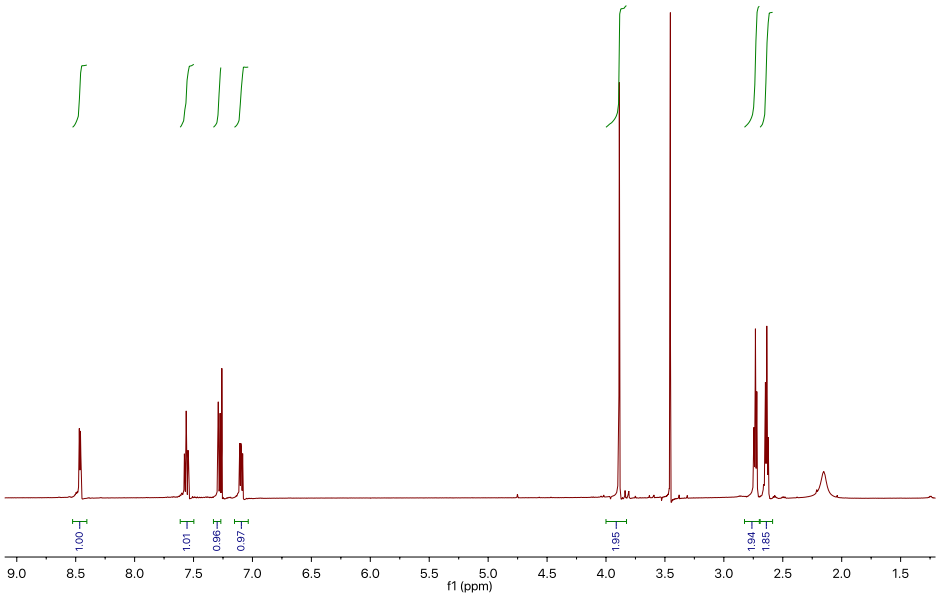

Figure 4.9. ^{1}H NMR of TPAA in $CDCl_3$.

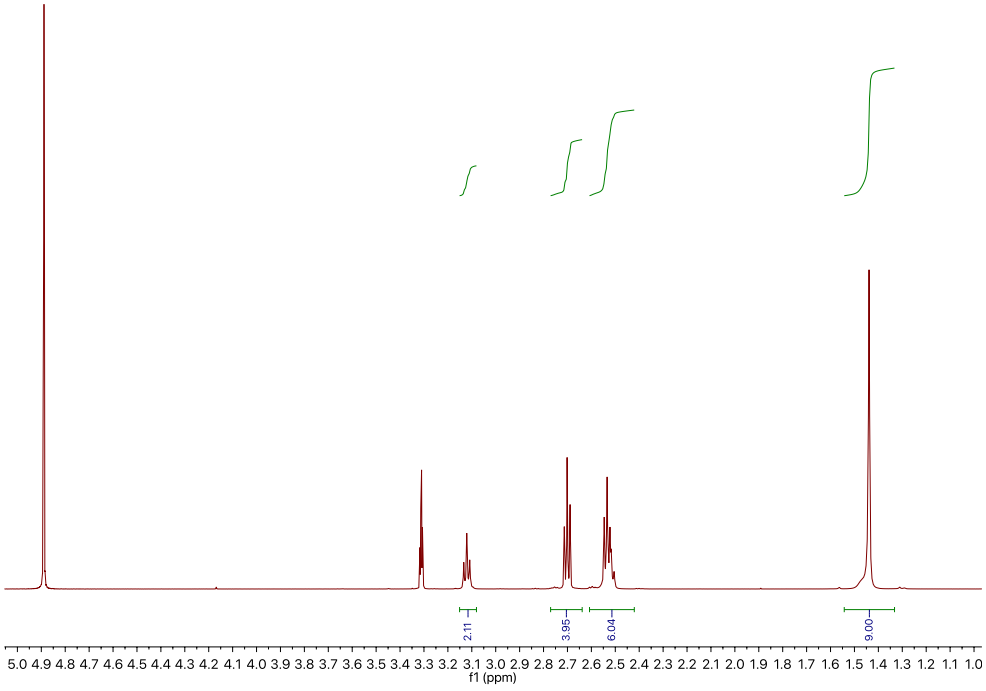

Figure 4.10. ^{1}H NMR of trenBoc in CD_3OD.

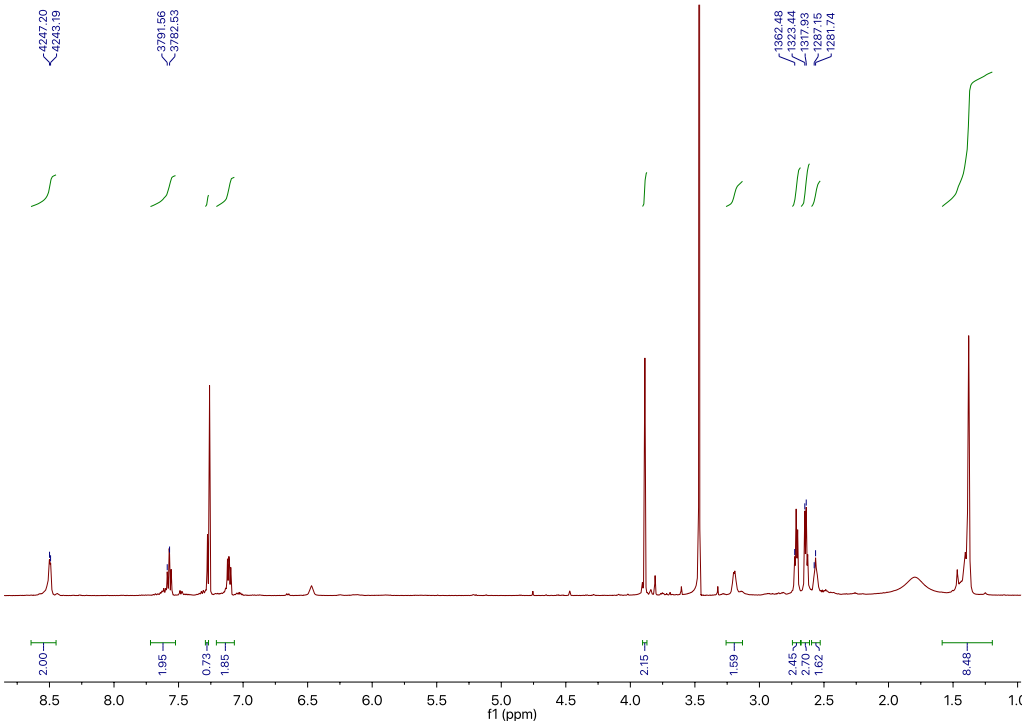

Figure 4.11. ^{1}H NMR of trenpy$_2$Boc in $CDCl_3$.

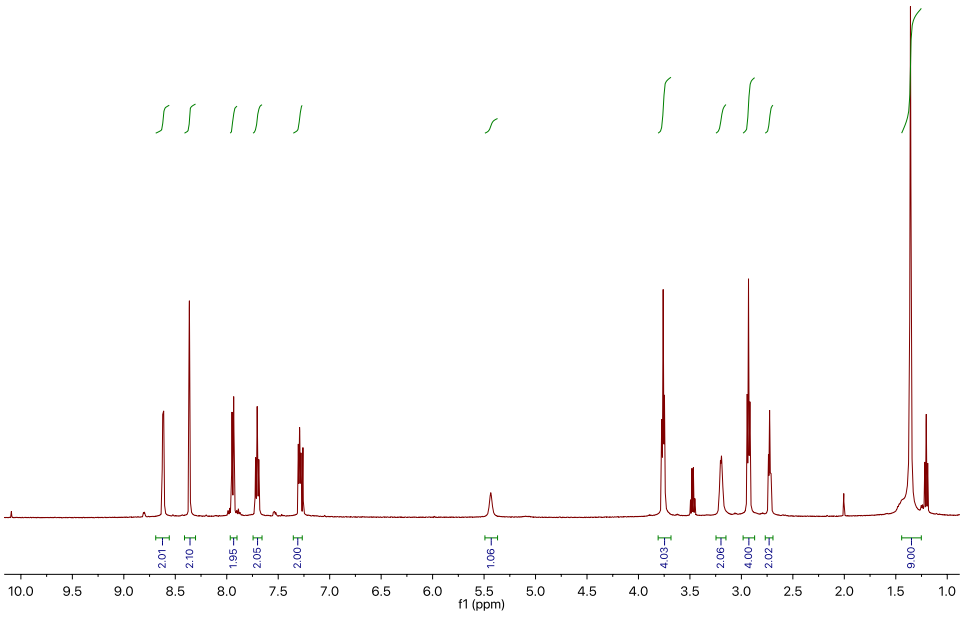

Figure 4.12. ^{1}H NMR of unreduced trenpy$_2$Boc in $CDCl_3$.

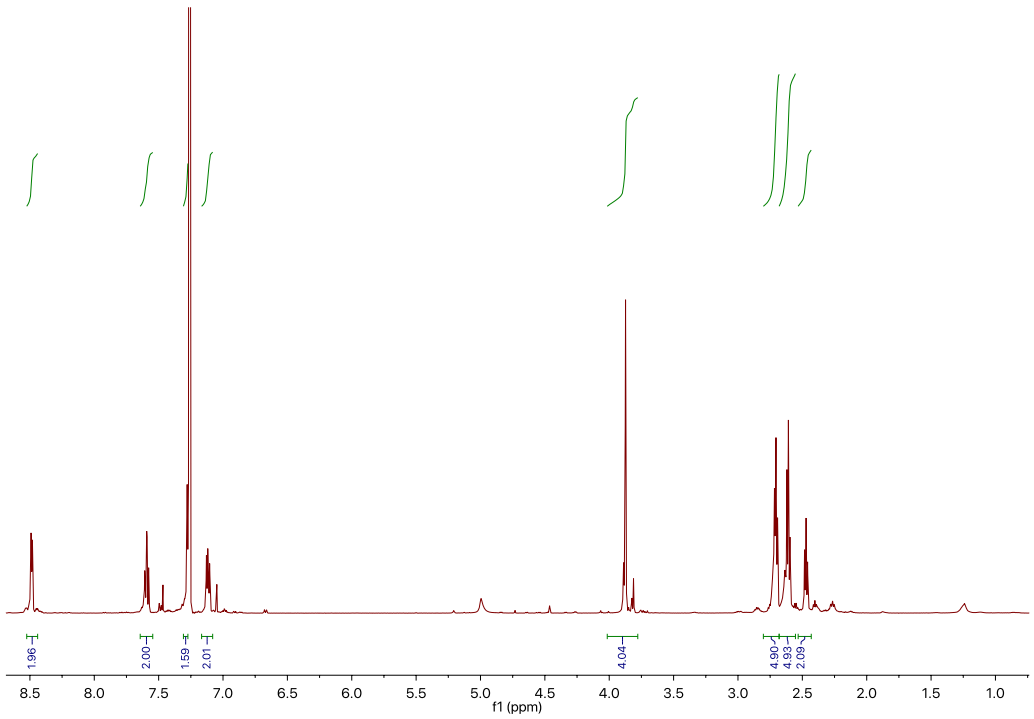

Figure 4.13. ^{1}H NMR of trenpy$_2$ in $CDCl_3$.

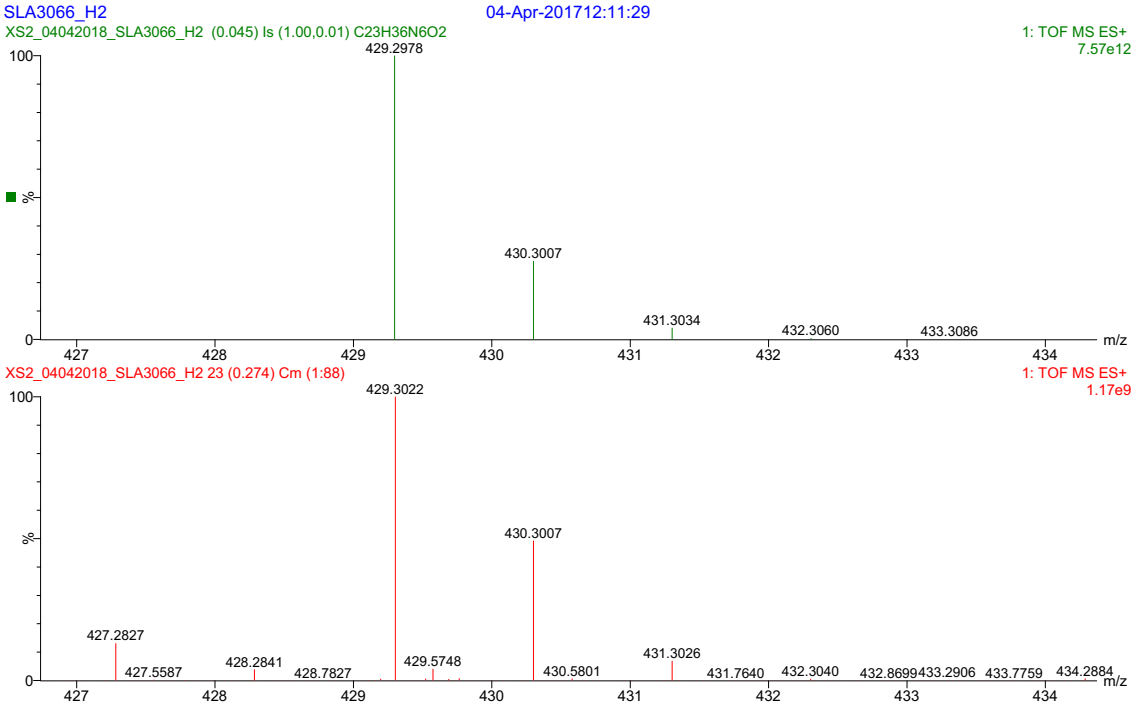

Figure 4.14. ESI-MS of trenpy$_2$Boc. Top: predicted isotope pattern for $C_{23}H_{36}N_6O_2$. Bottom: experimental result.

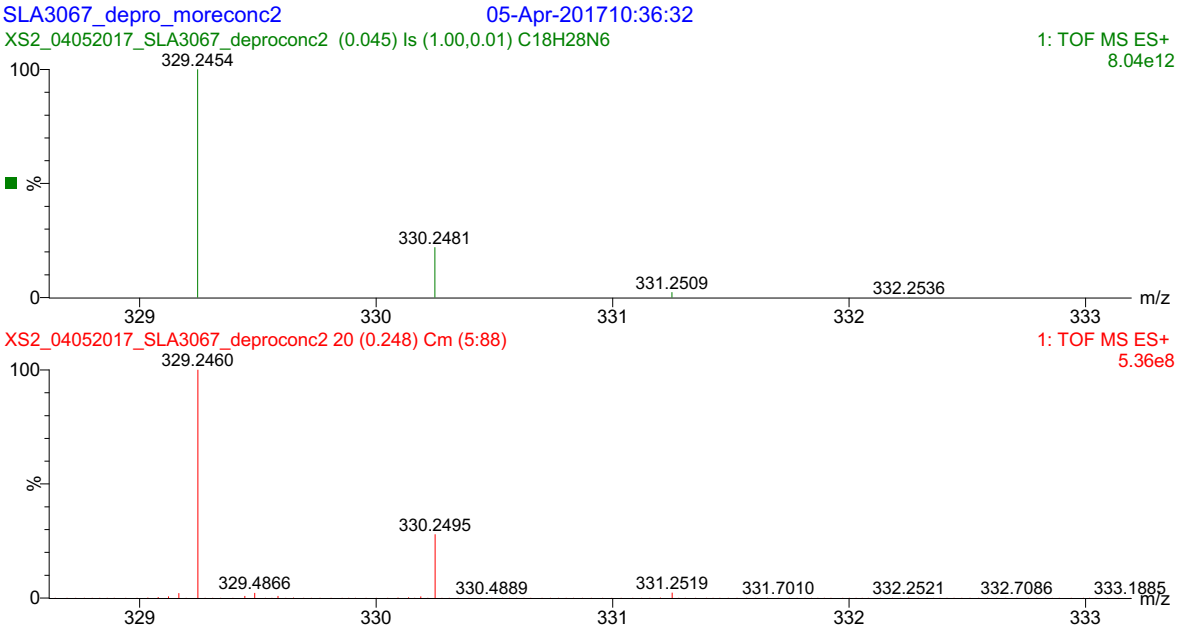

Figure 4.15. ESI-MS of trenpy$_2$. Top: calculated isotope pattern for $[M+H]^+$ ($C_{18}H_{28}N_6$). Bottom: experimental result.

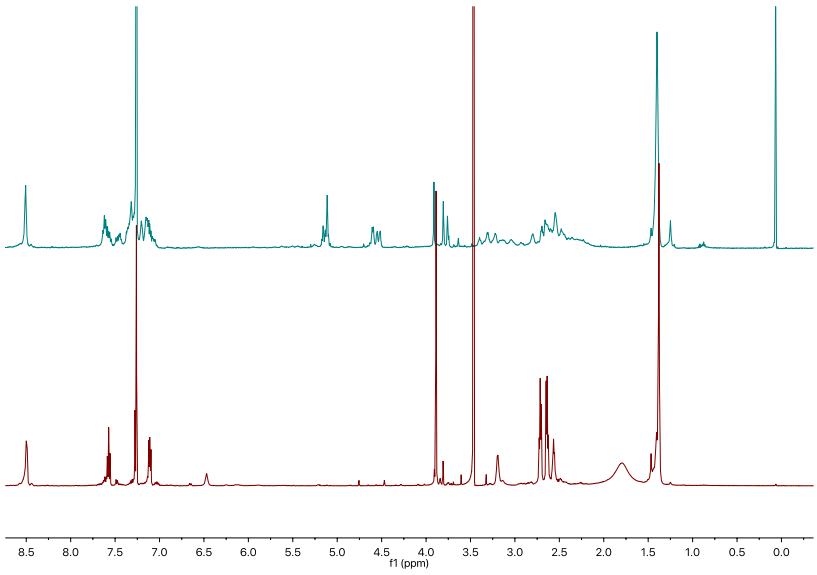

Figure 4.16. ^{1}H NMR of (top) trenpy$_2$Boc + CbzCl and (bottom) trenpy$_2$Boc, both in $CDCl_3$.

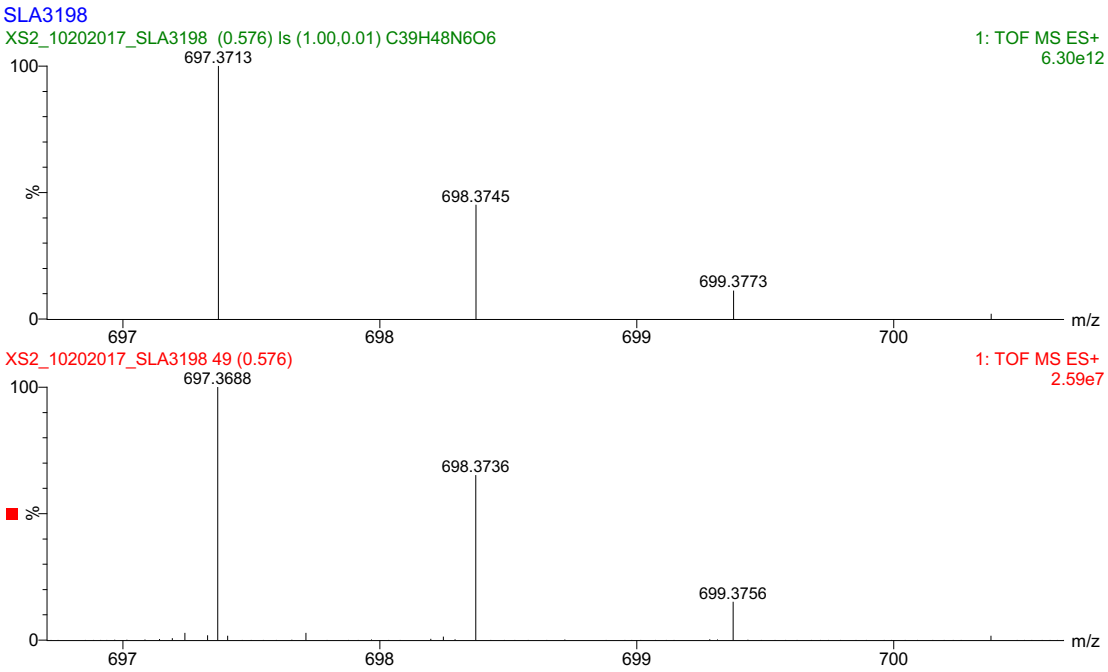

Figure 4.17. ESI-MS of crude trenpy$_2$Cbz$_2$Boc. Top: calculated isotope pattern for the desired product $[M+H]^+$ ($C_{39}H_{48}N_6O_6$). Bottom: experimental result.

REFERENCES

REFERENCES

1. Xie, C. L.; Hendrickson, D. N. Mechanism of Spin-State Interconversion in Ferrous Spin-Crossover Complexes: Direct Evidence for Quantum Mechanical Tunneling. *J. Am. Chem. Soc.* **1987**, *109*, 6981–6988. https://doi.org/10.1021/ja00257a013.

2. Hoselton, M. A.; Wilson, L. J.; Drago, R. S. Substituent Effects on the Spin Equilibrium Observed with Hexadentate Ligands on Iron(II). *J. Am. Chem. Soc*. **1975**, *97*, 1722–1729. https://doi.org/10.1021/ja00840a017.

3. Jamula, L. L. Exploring Design Strategies to Tune the Electronic Structure and Ultrafast Dynamics of Iron(II) Polypyridyl Chromophores, PhD Dissertation, Michigan State University, East Lansing, MI, 2013.

4. Smeigh, A. L. Ultrafast Dynamics Associated with the Transition Metal-Based Sensitizers for Titanium Dioxide Based Solar Cells, PhD Dissertation, Michigan State University, East Lansing, MI, 2007.

5. Ghanem, N.; Martinez, J.; Stien, D. A New High-Loading Water-Soluble Scavenger for Anhydrides, Acid Chlorides and Isocyanates. *Tetrahedron Lett*. **2002**, *43*, 1693–1695. https://doi.org/10.1016/S0040-4039(02)00125-9.

6. Frigerio, M.; Santagostino, M.; Sputore, S. A User-Friendly Entry to 2-Iodoxybenzoic Acid (IBX). *J. Org. Chem*. **1999**, *64*, 4537–4538.

7. Jäntti, A.; Wagner, M.; Suontamo, R.; Kolehmainen, E.; Rissanen, K. Schiff-Base Podates X-Ray , NMR and Ab Initio Molecular-Orbital Studies of the Cadmium(II) Complexes of Linear and Three-Armed Podands in Solution and Solid-state. *Eur. J. Inorg. Chem.* **1998**, 1555–1562.

8. Deroche, A.; Morgenstern-Badarau, I.; Cesario, M.; Guilhem, J.; Keita, B.; Nadjo, L.; Houée-Levin, C. A Seven-Coordinate Manganese(II) Complex Formed with a Single Tripodal Heptadentate Ligand as a New Superoxide Scavenger. *J. Am. Chem. Soc*. **1996**, *118*, 4567–4573. https://doi.org/10.1021/ja9525081.

9. Cleij, M. C.; Scrimin, P.; Tecilla, P.; Tonellato, U. Efficient and Highly Selective Copper(II) Transport across a Bulk Liquid Chloroform Membrane Mediated by Lipophilic Dipeptides. *J. Org. Chem*. **1997**, *62*, 5592–5599. https://doi.org/10.1021/jo9703257.

10. Boon, J. M.; Lambert, T. N.; Smith, B. D.; Beatty, A. M.; Ugrinova, V.; Brown, S. N. Structure/Activity Study of Tris(2-Aminoethyl)Amine-Derived Translocases for Phosphatidylcholine. *J. Org. Chem*. **2002**, *67*, 2168–2174.

11. Hong, S. Y.; Tobias, G.; Al-Jamal, K. T.; Ballesteros, B.; Ali-Boucetta, H.; Lozano-Perez, S.; Nellist, P. D.; Sim, R. B.; Finucane, C.; Mather, S. J.; et al. Filled and Glycosylated Carbon Nanotubes for in Vivo Radioemitter Localization and Imaging. *Nat. Mater*. **2010**, *9*, 485–490. https://doi.org/10.1038/nmat2766.

12. Ciaccia, M.; Cacciapaglia, R.; Mencarelli, P.; Mandolini, L.; Di Stefano, S. Fast Transimination in Organic Solvents in the Absence of Proton and Metal Catalysts. A Key to Imine Metathesis Catalyzed by Primary Amines under Mild Conditions. *Chem. Sci*. **2013**, *4*, 2253–2261. https://doi.org/10.1039/c3sc50277e.

13. Kovaříček, P.; Meister, A. C.; Flídrová, K.; Cabot, R.; Kovaříčková, K.; Lehn, J. M. Competition-Driven Selection in Covalent Dynamic Networks and Implementation in Organic Reactional Selectivity. *Chem. Sci*. **2016**, *7*, 3215–3226. https://doi.org/10.1039/c5sc04924e.

14. Ciaccia, M.; Di Stefano, S. Mechanisms of Imine Exchange Reactions in Organic Solvents. *Org. Biomol. Chem*. **2015**, *13*, 646–654. https://doi.org/10.1039/C4OB02110J.

15. Nagano, T.; Hirano, T.; Hirobe, M. Superoxide-Dismutase Mimics Based on Iron In vivo. *J. Biol. Chem*. **1989**, *264*, 9243–9249.

16. Morgenstern-Badarau, I.; Lambert, F.; Philippe Renault, J.; Cesario, M.; Maréchal, J. D.; Maseras, F. Amine Conformational Change and Spin Conversion Induced by Metal-Assisted Ligand Oxidation: From the Seven-Coordinate Iron(II)-TPAA Complex to the Two Oxidized Iron(II)-$(py)_3$tren Isomers. Characterization, Crystal Structures, and Density Functional Study. *Inorganica Chim. Acta* **2000**, *297*, 338–350. https://doi.org/10.1016/S0020-1693(99)00363-1.

17. Nicolaou, K. C.; Mathison, C. J. N.; Montagnon, T. O-Iodoxybenzoic Acid (IBX) as a Viable Reagent in the Manipulation of Nitrogen- and Sulfur-Containing Substrates: Scope, Generality, and Mechanism of IBX-Mediated Amine Oxidations and Dithiane Deprotections. *J. Am. Chem. Soc*. **2004**, *126*, 5192–5201. https://doi.org/10.1021/ja0400382.

18. Protection for the Amino Group. In *Greene's Protective Groups in Organic Synthesis*; Wuts, P. G. M., Ed.; John Wiley & Sons, 2014; pp 895–1193.

19. Stahl, G. L.; Walter, R.; Smith, C. W. General Procedure for the Synthesis of Mono-N-Acylated 1,6-Diaminohexanes. *J. Org. Chem*. **1978**, *43*, 2285–2286. https://doi.org/10.1021/jo00405a045.

CHAPTER 5. ALTERING THE NUCLEAR COORDINATE OF MLCT DEACTIVATION WITH CRYPTAND LIGANDS

5.1. Introduction[vii,viii]

The overarching goal of this dissertation is to identify and subsequently disrupt, through synthetic modification, the nuclear coordinate defining the MLCT → $^5T_2$ decay in low-spin iron(II) polypyridyl complexes to prolong the lifetime of the MLCT excited state. In the previous chapters of this dissertation, I have attempted to unequivocally identify the kinetically relevant vibrational modes associated with excited-state evolution in this class of chromophores. In addition, results obtained by other groups using a slew of time-resolved ultrafast x-ray spectroscopy and computational techniques have given us, at the very least, a general idea of which modes may be fruitful to target synthetically. Therefore, in this chapter, I will first provide an overview of the geometric changes that have been hypothesized to be relevant during excited-state evolution, and then describe in detail a ligand scaffold that I have chosen to exploit to achieve disruption of the excited-state nuclear coordinate in this class of chromophores.

First, there has been a long-standing belief that MLCT deactivation occurs along a nuclear coordinate that can be best described as a symmetric Fe-N breathing mode. This assumption is based on the fact that Fe-N bond lengths change significantly during excited-state evolution. In the ^{3}MLCT excited state, the electron configuration can be approximated as $(t_{2g})^5(e_g)^0(\pi^*)^1$ and there is no significant population of antibonding e_g^* orbitals. Upon decay into the $^5T_2$ ligand field

[vii] Some of the results and discussion of this chapter are also presented in the article: Paulus, B. C.[‡]; Adelman, S. L.[‡]; Jamula. L. L; McCusker, J. K. *Nature*, **2020**, *Accepted.*

[viii] The work in the chapter is a continuation of research started by Dr. Lindsey L. Jamula and done in collaboration with Bryan C. Paulus. All of the ultrafast transient absorption measurements and DFT calculations discussed in this chapter were performed by Bryan.

(LF) excited state, which may be formalized by a $(t_{2g})^4(e_g)^2(\pi^*)^0$ electron configuration, the antibonding Fe-N orbitals become doubly occupied. This shift of electron density into e_g^* antibonding orbitals decreases the amount of metal-ligand orbital overlap and consequently elongates the Fe-N bonds. A similar, if not more exaggerated, bond extension occurs during the $^1A_1 \rightarrow {}^5T_2$ conversion due to the same increase in population of e_g^* orbitals.[1,2] This Fe-N bond elongation in the $^5T_2$ excited state compared to the $^1A_1$ has been experimentally quantified in several different LS and SCO Fe(II) compounds and is typically on the order of 10% change in Fe-N bond distances.[2–6] For example, in $[Fe(bpy)_3]^{2+}$ (bpy = 2,2'-bipyridine) in aqueous solution, the average extension of Fe-N bond distances was found to be 0.19 ± 0.03 Å by picosecond x-ray absorption spectroscopy.[1] These observations have encouraged the adoption of the Fe-N breathing mode as the presumed kinetically-relevant mode for excited-state evolution. In addition, it has been common to draw conclusions about the MLCT → LF conversion from the results of studies on ground-state recovery (GSR, i.e. the $^5T_2 \rightarrow {}^1A_1$ process) in LS Fe(II) polypyridyl complexes because of the predicted similarity in geometries of the low-spin (LS) ground state and ^{3}MLCT excited state as well as the spin-forbidden nature ($\Delta S = 2$) for both processes. The validity of this assumption is not clear at this time.

This paradigm of a symmetric Fe-N breathing motion driving MLCT deactivation has not been completely stalwart. In 1979, Purcell showed that torsional modes must be invoked in an angular overlap model interpretation of the rapid racemization of $[Fe(phen)_3]^{2+}$.[7] Ever since, there has been a growing body of work that suggests a one-dimensional Fe-N breathing mode picture for excited-state evolution in Fe(II) polypyridyls may be incomplete. Hendrickson and coworkers[8] used variable-temperature transient absorption (VT-TA) spectroscopy to determine the Arrhenius parameters associated with GSR in a series of LS Fe(II) complexes with ligands imposing varying

degrees of hinderance towards torsional motion. They reported a correlation between a complex's Arrhenius parameters and the relative flexibility about a twisting axis, suggesting the potential kinetic relevance of twisting motions in GSR. Collet and coworkers[9] have used optical pump, x-ray probe spectroscopy on an Fe(II) SCO complex, $Fe(phen)_2(SCN)_2$, to observe vibrational coherences active during the GSR process of this complex. These studies indicated that upon population of the e_g^* orbitals in the $^5T_2$ excited state, the complex's Fe-N bonds impulsively elongated and then Fe-N torsional and bending modes dissipated excess vibrational energy. This study concluded that Fe-N breathing alone is not sufficient to describe GSR.

Computational work has been done on $[Fe(bpy)_3]^{2+}$ to show that the MLCT → $^5T_2$ nuclear coordinate may be multidimensional. Jakubikova and coworkers[10] showed that in this complex, both Fe-N breathing and torsional modes (classic and dancing Bailar, Ray-Dutt twists) are energetically feasible pathways for intersystem crossing from the ^{3}MLCT → $^5T_2$. This is especially true if a ^3T intermediate state is invoked, and proof for such an intermediate in $[Fe(bpy)_3]^{2+}$ has been provided experimentally.[11] In addition to the work focusing on bidentate ligands, there is a significant body of work investigating the nuclear coordinate for excited-state evolution in $[Fe(terpy)_2]^{2+}$ (terpy = 2,2':6',2"-terpyridine), where the tridentate ligand forces the ground-state geometry to adopt a much more strained coordination environment than observed in $[Fe(bpy)_3]^{2+}$. In 2015, a series of reports investigating $[Fe(terpy)_2]^{2+}$ with time-resolved x-ray techniques,[5,6,12] DFT calculations,[13] and continuous shape measures[12] showed that in order to accurately represent the nuclear coordinate of GSR in this complex, torsional modes must be included, specifically axial bending.

Finally, in Chapter 3 of this dissertation, it was shown that low-frequency (<100 cm^{-1}) modes compose the nuclear coordinate of the $^5T_2$ → $^1A_1$ transition in an Fe(II) SCO complex, and

the ^{3}MLCT → $^1A_1$ transition for its Ru(II) analog can be defined by a ~1320 cm^{-1} mode. Physically, these frequencies correspond to Fe-N bond deformations (breathing and torsional motions) and aromatic C=C stretching, respectively. These two segments of the nuclear coordinate must intersect during the MLCT → LF deactivation, signifying that targeting these geometric changes could have an impact on excited-state evolution. From this overview, it is clear that a large body of work has attempted to identify kinetically relevant modes for the ^{3}MLCT → $^5T_2$ intersystem crossing (ISC). While we have made strides to experimentally identify these modes and rationalize the results theoretically, one thing is abundantly clear: large geometric distortions occur during the electronic transition in question. Therefore, we set out to do something that may seem quite simple: can we disrupt all geometric distortions that may occur during excited-state evolution? To do this, we need the right ligand.

A ligand first made by Lehn and coworkers[14] (Figure 5.1) seemed a promising candidate to achieve this goal. This cage ligand (L) retains a *tris*-2,2'-bipyridine coordination environment, ideal to compare to the very well characterized $[Fe(bpy)_3]^{2+}$. But, the three bpy units are tethered together on two ends by tren-based imine caps (tren = tris(2-aminoethyl)amine), which could introduce enough of a gross restriction on both Fe-N bond elongation and torsion that some degree of nuclear coordinate disruption could be achieved during the excited-state evolution, specifically

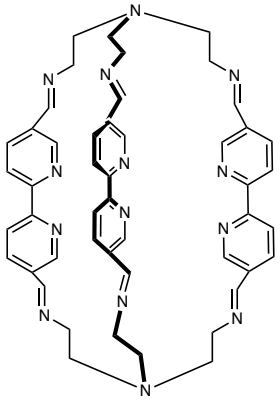

Figure 5.1. Drawing of cage ligand that will be discussed in this chapter and referred as "L."

the MLCT → $^5T_2$ conversion. In the forthcoming discussion, I will describe the synthesis of several coordination compounds with this ligand and their spectroscopic characterization, including evidence that we have achieved our goal of prolonging the MLCT excited-state lifetime in an iron(II) polypyridyl complex through disruption of the nuclear coordination defining excited-state evolution.

5.2. Experimental

5.2.1. Synthesis

General. All chemicals were purchased from Sigma Aldrich, Acros Organics, Alfa Aesar, or Oakwood Chemical Company and used as received unless otherwise noted. 5,5'-dimethylhydroxy-2,2'-bipyridine,[15] $[Cu(MeCN)_4](BAr^F)$,[16] and $[Fe(MeCN)_6](BAr^F)_2$[17] were synthesized from the literature procedures. $NaBAr^F$ was provided by Dr. Kelly Aldrich. All manipulations were carried out in a nitrogen- or argon-filled glovebox (Vacuum Atmospheres) unless otherwise noted. MeCN, DCM, and diethyl ether were dried over activated neutral alumina under nitrogen. Tris(2-aminoethyl)amine (tren) was distilled over KOH and activated carbon twice prior to use. ^{1}H NMR were collected on an Agilent 500 MHz spectrometer at the Max T. Rogers NMR facility at Michigan State University in $CDCl_3$, DMSO-d_6 or MeCN-d_3. $CDCl_3$ and MeCN-d_3 which were dried over 4 Å molecular sieves and deoxygenated with five cycles of freeze-pump-thawing. All signals are reported in ppm and referenced to the solvent residual signals. The data are reported as (s = singlet d = doublet t = triplet m = multiplet, coupling constant(s) in Hz, integration). ^{13}C NMR spectra were collected on an Agilent 125 MHz spectrometer at the same facility and referenced to the solvent residual signals. Electrospray ionization (ESI) high-resolution mass spectrometry (HRMS) was collected on at the Michigan State University Mass Spectrometry and Metabolomics Core using a Waters G2-XS QTof mass spectrometer interfaced to a Waters Aquity UPLC.

Elemental analysis was performed at Michigan State University by Rui Huang on samples that had been recrystallized a minimum of two times, dried in a vacuum desiccator, pumped into an inert atmosphere glovebox and ground in a glass vial, then stored in one of the antechambers under vacuum overnight. Immediately prior to collection of combustion analysis, the samples were again placed under an inert atmosphere and sealed within a larger glass vial, and wrapped with parafilm to transfer from the glovebox to the elemental analysis facilities. This method greatly reduced the incidence of the observation of hydrates.

5,5'-diformyl-2,2'-bipyridine (dfb). The title compound was prepared via a modified procedure outlined for substituted terpyridine synthesis.[18] To a 250 mL 2-necked flask under N_2, dry DCM (150 mL) was added and cooled to -78 °C. Freshly distilled oxalyl chloride (3.27 mL, 38 mmol) was added. Freshly distilled DMSO (4.9 mL, 70 mmol) was added dropwise over 20 min. 5,5'-dimethylhydroxy-2,2'-bipyridine (3.27 g, 15 mmol), dissolved in 50 mL DCM and 50 mL DMSO was added dropwise over 30 min. The resulting white suspension was stirred at -78°C for 3 h. The reaction was warmed to -30 °C and TEA (100 mL) was added dropwise. The reaction was warmed to RT and H_2O (100 mL) was added. The organic layer was separated and the aqueous layer was extracted 3 × 100 mL into DCM. The combined organic layers were washed with brine, then dried with $MgSO_4$. The solvent was removed to yield 2.32 g of a yellow powder (73% yield). ^{1}H NMR (500 MHz, DMSO-d_6) 10.20 (s, 1H), 9.25 (d, J = 2.03 Hz, 1H), 8.68 (d, J = 8.16 Hz, 1H), 8.45 (dd, J_1 = 8.26 Hz, J_2 = 2.12 Hz, 1H). ^{13}C NMR (125 MHz, DMSO-d_6) 192.54, 152.00, 138.02, 132.14, 122.37, 109.91.

Cage ligand (L). To a stirred solution of tren (0.71 g, 0.48 mmol) in MeCN (5 mL) was added dfb (0.15 g, 0.705 mmol) dropwise as a suspension in MeCN (10 mL). The resulting orange slurry was

stirred for 12 h at RT, filtered and washed with Et_2O, yielding 0.15 g of an orange powder (75% yield). All spectroscopic characterization of the product matches that in the literature.[14]

Reduced cage ligand (LH). L (0.082 g, 0.1 mmol) was suspended in dry 2:3 MeOH/DCM (20 mL) and cooled under N_2 in an ice bath. $NaBH_4$ (0.076 g, 2 mmol) was slowly added under positive pressure. The suspension was stirred at room temperature for 24 h. 1 M NaOH (15 mL) was added to the yellow suspension, and the organic layer was separated. The aqueous layer was extracted with $CHCl_3$ (3 × 15 mL). All organic layers were combined, washed with saturated Na_2CO_3, and dried over K_2CO_3. The solvent was removed, yielding 0.073 g of a white powder (88% yield). It should be noted that the results of this synthesis were highly variable and often would result in an impure product that could be purified on a silica gel column with 80:20:4 DCM/MeOH/NH_4OH in very poor yield. ^{1}H NMR (500 MHz, $CDCl_3$) 8.37 (d, J = 2.13 Hz, 1H), 7.78 (d, J = 8.08 Hz, 1H), 7.31 (dd, J_1 = 8.12, J_2 = 2.15, 1 H), 2.93 (t, J_1 = 10.45, J_2 = 5.03, 2 H), 2.71 (t, J_1 = 10.49, J_2 = 5.5, 2 H).

$[Fe(dfb)_3](PF_6)_2$. To a stirred suspension of dfb (0.113 g, 0.53 mmol) in MeCN (5 mL), $FeCl_2 \cdot 2H_2O$ (0.026 g, 0.16 mmol) in MeCN (5 mL) was added dropwise. The green solution was stirred under nitrogen at 30°C for 12 h, during which time the solution lightened to a murky yellow. Upon cooling to room temperature, NH_4PF_6 (0.26 g, 16 mmol) in MeCN (5 mL) was added to the green solution, instantly turning the solution deep blue. After stirring at RT for 3 h, the solvent was reduced and Et_2O was added until cloudy. The blue precipitate was collected by filtration and washed with Et_2O. X-ray quality single crystals were grown from vapor diffusion of Et_2O into MeCN solutions of $[Fe(dfb)(PF_6)_2$. ^{1}H NMR (500 MHz, CD_3CN) 9.86 (s, 1H), 8.82 (d, J = 8.32 Hz, 1H), 8.59 (d, 8.91 Hz, 1H), 7.81 (s, 1H). ^{13}C NMR (125 MHz, CD_3CN) 188.96, 161.28, 156.92,

137.85, 133.31, 126.00. HRMS (ESI-TOF) m/z: $[M-2(PF_6)]^{2+}$ calc'd for $[C_{36}H_{24}N_6O_6Fe]^{2+}$ 346.0554 obs. 346.0586.

$[Fe(L)](PF_6)_2$. To a stirred suspension of **L** (0.15 g, 0.18 mmol) in MeCN (5 mL) was added $FeCl_2 \cdot 2H_2O$ (0.03 g, 0.18 mmol) in MeCN (5 mL) dropwise over 5 min. The dark purple solution was stirred overnight and NH_4PF_6 (0.30 g, 1.8 mmol) in MeCN (5 mL) was added to the blue suspension, rapidly leading to a dark purple solution. After stirring at RT for 3 h, the solution was filtered through Celite. The solvent was removed in vacuo, dissolved in the minimal amount of MeCN, and Et_2O was added until the solution turned cloudy. The resulting purple precipitate was filtered and washed with Et_2O. X-ray quality single crystals were grown from vapor diffusion of Et_2O into MeCN solutions of $[Fe(L)(PF_6)_2$. ^1H NMR (500 MHz, CD_3CN) 8.89 (d, J = 8.53 Hz, 1H), 8.61 (s, 1H), 8.35 (s, 1H), 8.18 (d, J = 8.03 Hz), 4.03 (m, 1H), 3.67 (m, 1H), 3.57 (m, 2H). ^{13}C NMR (125 MHz, CD_3CN) 163.06, 159.35, 153.17, 140.14, 137.76, 126.06, 55.16, 53.79. HRMS (ESI-TOF) m/z: $[M-2(PF_6)]^{2+}$ calc'd for $[C_{48}H_{48}N_{14}Fe]^{2+}$ 438.1768 obs. 438.1780.

$[Cu_2Fe(L)](PF_6)_4$. To a stirred suspension of **L** (0.15 g, 0.18 mmol) in MeCN (5 mL) was added $[Cu(MeCN)_4]PF_6$ (0.15 g, 0.4 mmol) in MeCN (5 mL) dropwise over 5 min. The resulting green suspension was stirred for 3 h at RT. Then, $FeCl_2 \cdot 2H_2O$ (0.03 g, 0.18 mmol) in MeCN (5 mL) was added dropwise over 5 min. The dark maroon solution was stirred overnight, then filtered through a pad of Celite. After removing the solvent from the filtrate in vacuo, NH_4PF_6 (0.30 g, 1.8 mmol) in MeCN (5 mL) was added, then Et_2O was added until the solution turned cloudy. The resulting maroon precipitate was filtered and washed with Et_2O. X-ray quality single crystals were grown from vapor diffusion of Et_2O into MeCN solutions of $[Cu_2Fe(L)](PF_6)_4$. ^1H NMR (500 MHz, CD_3CN) 8.68 (s, 1H), 8.57 (d, J = 8.17 Hz, 1H), 8.26 (s, 1H), 8.24 (d, J = 8.06 Hz, 1H), 3.77 (t, J = 13.17 Hz, 1H), 3.69 (dd, J_1 = 13.65 Hz, J_2 = 3.46 Hz), 3.14 (dd, J_1 = 13.71 Hz, J_2 = 3.66 Hz, 1H),

3.05 (m, 1H). ^{13}C NMR (125 MHz, CD_3CN), d 161.84, 161.40, 152.67, 139.69, 136.72, 125.35, 61.93, 52.50 HRMS (ESI-TOF) m/z: $[M\text{-}4(PF_6)]^{4+}$ calc'd for $[C_{48}H_{48}N_{14}Cu_2Fe]^{4+}$ 251.0531 obs. found 251.0578; Elemental analysis (% calc'd, % found for $C_{48}H_{48}N_{14}Cu_2FeP_2F_{12}$): C (36.40, 36.40) H (3.06, 3.15) N (12.38, 12.27).

$[FeCu_2(L)](BAr^F)_4$. To a stirred solution of L (38 mg, 0.05 mmol) in THF (5 mL) was added $[Cu(MeCN)_4](BAr^F)$ (96 mg, 0.09 mmol) in THF (2 mL). The resulting green solution was stirred for 12 h at RT. $[Fe(MeCN)_6](BAr^F)_2$ (85 mg, 0.04 mmol) in THF (2 mL) was added dropwise over 5 min. The dark maroon solution was stirred for 12 h and filtered through Celite. The solvent was removed from the filtrate yielding a maroon film (60% yield). ^{1}H NMR (500 MHz, CD_3CN) 8.67 (d, J = 1.6, 1H), 8.56 (d, J = 8.19, 1 H), 8.24 (s, 1H), 8.22 (d, J = 1.7, 1H), 7.68 (m, 4 H), 3.70 (m, 2H), 3.09 (m, 2H); ^{13}C NMR (125 MHz, CD_3CN) 161.73, 161.13, 152.57, 139.67, 136.71, 129.19-130.39 (m), 128.62, 126.46, 125.19, 124.30, 122.13, 61.84, 52.42; HRMS (ESI-TOF) m/z: $[M\text{-}2(BAr^F)]^{2+}$ calc'd for $[C_{112}H_{72}N_{14}Cu_2FeB_2F_{48}]^{2+}$ 1365.1732 obs. 1365.1721; $[M\text{-}(BAr^F)]^{3+}$ calc'd for $[C_{80}H_{60}N_{14}Cu_2FeBF_{24}]^{3+}$ 622.4265 obs. 622.4298; $[M\text{-}4(BAr^F)]^{4+}$ calc'd for $[C_{48}H_{48}N_{14}Cu_2Fe]^{4+}$ 251.0531 obs. 251.0578.

$[Cu_2Zn(L)](PF_6)_4$. To a stirred suspension of L (0.15 g, 0.18 mmol) in MeCN (5 mL) was added $[Cu(MeCN)_4]PF_6$ (0.15 g, 0.4 mmol) in MeCN (5 mL) dropwise over 5 min. The resulting green suspension was stirred for 3 h at RT. Then, $ZnCl_2$ (0.025 g, 0.18 mmol) in MeCN (5 mL) was added dropwise over 5 min. The yellow solution was stirred overnight, then filtered through a pad of Celite. After removing the solvent from the filtrate in vacuo, NH_4PF_6 (0.30 g, 1.8 mmol) in MeCN (5 mL) was added, Et_2O was added until the yellow solution turned cloudy. The resulting orange precipitate was filtered and washed with Et_2O. X-ray quality single crystals were grown from vapor diffusion of Et_2O into MeCN solutions of $[Cu_2Zn(L)](PF_6)_4$. ^{1}H NMR (500 MHz,

CD_3CN) 9.03 (d, J = 1.62 Hz, 1H), 8.75 (s, 1H), 8.65 (d, J = 8.26 Hz, 1H), 8.45 (dd, J_1 = 8.25 Hz, J_2 = 1.99 Hz, 1H), 3.89 (m, 1H), 3.75 (m, 1H), 3.16 (m, 2H). ^{13}C NMR (125 MHz, CD_3CN), 161.68, 151.22, 146.66, 143.52, 134.84, 125.25, 62.44, 52.33. HRMS (ESI-TOF) m/z: [M-4(PF_6)]$^{4+}$ calc;d for $[C_{48}H_{48}N_{14}Cu_2Zn]^{4+}$ 253.0514 obs. 253.0527.

$[Ag_{1.5}Fe(L)](PF_6)_x$. In the dark, to a stirred suspension of L (0.05 g, 0.06 mmol) in a foil-wrapped flask, $AgPF_6$ (0.03 g, 0.13 mmol) in MeCN (2 mL) was added dropwise. After stirring for 5 min at RT, $Fe(BF_4)_2 \cdot 2H_2O$ (0.02 g, 0.06 mmol) in MeCN (2 mL) was added dropwise. The reaction stirred overnight at RT in the dark, then filtered through a pad of Celite. The solvent was reduced in vacuo, and NH_4PF_6 (0.10 g, 0.6 mmol) in MeCN (2 mL) was added. Et_2O was added until the solution turned cloudy. The resulting dark purple precipitate was filtered and washed with Et_2O. X-ray quality single crystals were grown from vapor diffusion of Et_2O into MeCN solutions of the crude product. The obtained product clearly contained $[Fe(L)]^{2+}$ and other byproducts by ^1H NMR.

$[Fe(LH)](PF_6)_2$. To a suspension of the LH (0.02 g, 0.02 mmol) in MeCN (2 mL) was added $FeCl_2 \cdot 2H_2O$ (0.003 g, 0.02 mmol) in MeCN (1 mL). The suspension instantly turned into a bright cherry red solution. After stirring at RT overnight, NH_4PF_6 (0.03 g, 0.2 mmol) in MeCN (2 mL) was added. The solvent was reduced in vacuo to ~1 mL, and Et_2O was added until cloudy. The red precipitate was collected via filtration and washed with Et_2O. X-ray quality crystals were grown from Et_2O diffusion into dilute solutions of the product in MeCN. The product was sparingly soluble in most solvents, resulting in a poorly resolved NMR spectrum, as such no coupling constants are reported. ^1H NMR (500 MHz, CD_3CN) 8.37 (d, 1 H), 7.98 (m, 1 H), 7.24 (s, 1 H), 3.75 (m, 1 H), 3.14 (m, 2 H), 3.02 (m, 1 H).

5.2.2. Physical Measurements

X-ray crystal structure determination. Single crystal X-ray diffraction was collected on suitable crystals mounted on a Bruker APEX-II CCD diffractometer with CuK_α radiation at the Center for Crystallographic Research at Michigan State University. The following crystal structures have been submitted to the CCDC data base and can be accessed by their CCDC accession numbers: $[Fe(L)](PF_6)_2$ (1904822), $[FeCu_2(L)](PF_6)_4$ (187542), and $[ZnCu_2(L)](PF_6)_4$ (190480).

Ground-state absorption spectroscopy. Molar absorptivity was collected on a PerkinElmer Lambda 1050 spectrometer in 1 cm quartz cuvettes in spectrophotometric grade MeCN (Sigma Aldrich).

Electrochemistry. Electrochemistry was performed using a CH Instruments potentiostat in a 0.1 M tetrabutylammonium hexafluorophosphate ($TBAPF_6$) MeCN solution with a Pt working electrode, Pt counter electrode, and a Ag wire pseudo-reference electrode in an Ar-filled glovebox. Cyclic voltammetry measurements were conducted with a 100 mV/s scan rate to determine the reversibility of redox processes and differential pulse voltammetry was used to find their potentials. All potentials were internally referenced to the Fc/Fc^+ redox couple. $TBAPF_6$ was purchased from Oakwood Chemical Company and recrystallized from ethanol twice before use.

Spectroelectrochemistry. Spectroelectrochemistry was performed in a similar manner as previously described,[19] with some slight modifications: all measurements were carried out in an Ar-filled glovebox in spectrophotometric grade MeCN (Sigma Aldrich) with 0.1 M $TBAPF_6$ using a Pine Research Pt honeycomb combination working/reference electrode and Ag wire pseudo-reference electrode controlled by a CH Instruments potentiostat. The solutions were prepared so the absorbance of the solution was ~0.4 at the maximum of the MLCT absorption feature as

measured with a SSI400 CCD spectrometer. Spectra were collected every 30 s for 10 min with a ~100 mV overpotential applied for a reductive or oxidative process under investigation.

Variable-temperature time-resolved transient absorption spectroscopy. Nanosecond time-resolved transient absorption measurements were collected on the desired Fe(II) complexes dissolved spectrophotometric grade solvent, either MeCN (Sigma Aldrich) or 9:1 MeOH/EtOH, and prepared in an Ar-filled glovebox (VacAtm). Ambient temperature samples were prepared in 1 cm quartz cuvettes that were originally purchased from FireFlySci and modified in house with the addition of a Kontes valve to allow sealing of the sample under inert atmosphere. Variable-temperature measurements were conducted following the procedure outlined in Chapter 2, and all nanosecond transient absorption spectra were collected on the same instrument described in that chapter. All samples were checked for degradation by comparing the UV-Vis absorption spectrum of the sample before and after TA measurements and no changes were observed.

Ultrafast time-resolved transient absorption spectroscopy. Except for the GSR of $[Fe(dfb)_3]^{2+}$, which was collected by Hayden Biessel, all ultrafast data were collected by Bryan C. Paulus and described in detail both in his dissertation[20] and our article[21] describing the ultrafast behavior of $[Fe(L)](PF_6)_2$ and $[Cu_2Fe(L)]^{4+}$**.**

5.3. Results and Discussion

5.3.1. Ligand synthesis

The synthesis of the macrocyclic hexaimine ligand, here simply denoted as L, was originally described by Lehn and coworkers from the condensation of 5,5'-diformyl-2,2'-bipyridine (dfb) and tris(2-aminoethyl)amine (tren).[14] However, the conditions detailed in this report were vague as to the actual experimental conditions used to isolate the dfb starting material. Therefore, Lindsey Jamula[22] devised a straightforward step-wise synthetic scheme to transform

the commercially available 5,5'-dimethyl-2,2'-bipyridine (5,5'-dmb) into the desired starting material (Figure 5.2). This synthetic route was easily performed on a multi-gram scale. It should be noted that the common route for the synthesis of 4,4'-dfb, oxidation of either the dialcohol[23] or dmb[24] using selenium dioxide, was unsuccessful in the synthesis of 5,5'-dfb. The imine

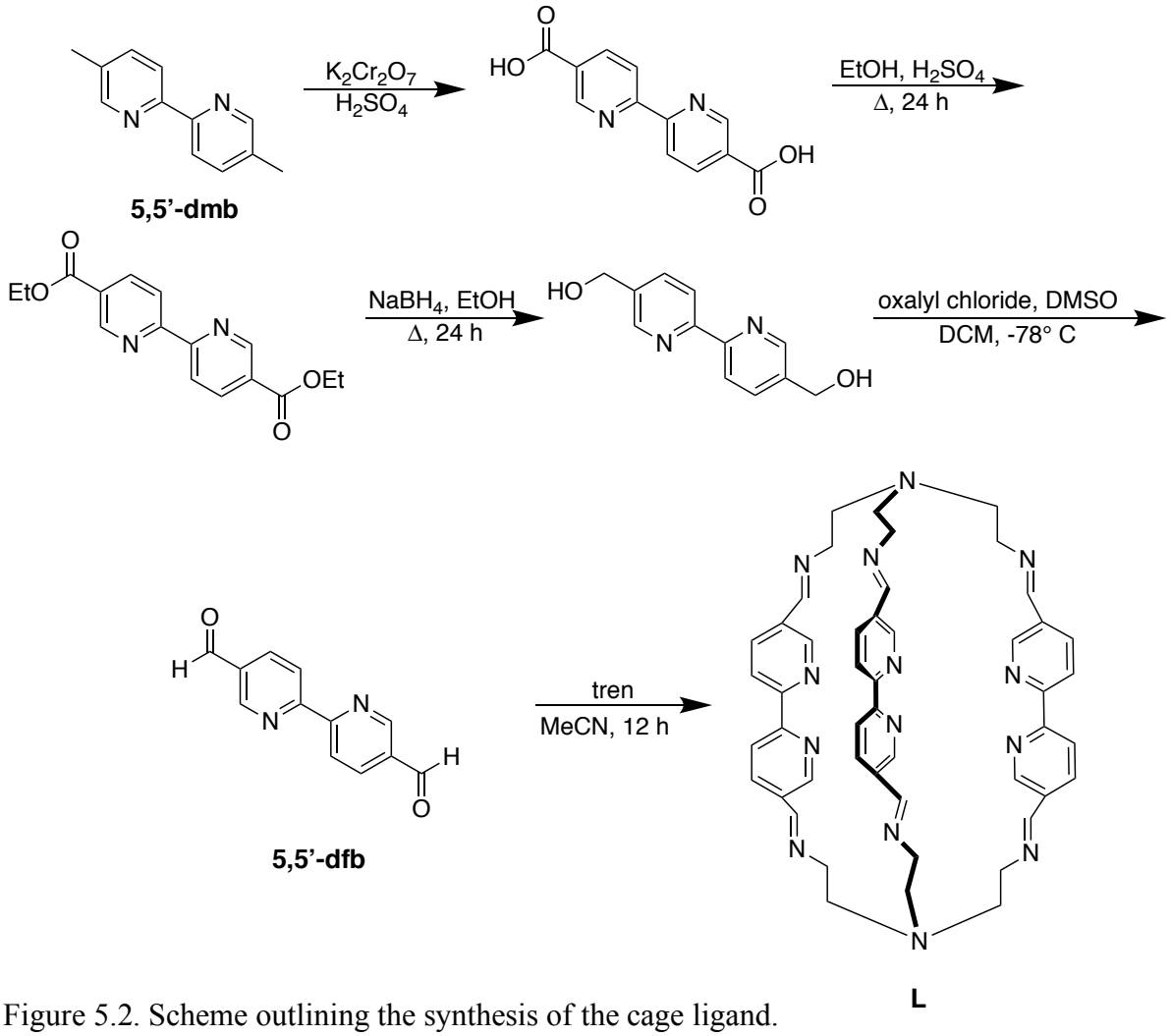

Figure 5.2. Scheme outlining the synthesis of the cage ligand.

condensation that assembles the macrocyclic ligand was efficient at smaller scales, however scaling this reaction up to any larger than 200 mg of dfb resulted in the formation of inseparable side products, presumably due to the highly insoluble nature of both the dialdehyde starting material and the product itself; efficient stirring during the dropwise addition of dfb is crucial even at smaller scales.

5.3.2. Synthesis and ground-state characterization of $[Fe(dfb)_3]^{2+}$ and $[Fe(L)]^{2+}$

The synthesis of $[Fe(L)](PF_6)_2$ was achieved through the well-accepted method[8,22,25] of the dropwise addition of $FeCl_2 \bullet 2H_2O$ to a suspension of L in acetonitrile, followed by the metathesis of the highly insoluble chloride salt to hexafluorophosphate complex. Over 24 h, $[Fe(L)](PF_6)_2$ showed no instability towards atmospheric conditions and there were no indications of paramagnetic impurities by ^1H NMR or Evans method for magnetic susceptibility. However, in addition to the peaks ascribed to the protons on the ligand of $[Fe(L)]^{2+}$ as drawn in Figure 5.1, there was also a broad peak in the aromatic region of the ^1H NMR spectrum in dry CD_3CN that disappeared when one drop of D_2O is added to the NMR tube, indicating the presence of an exchangeable proton in the complex (Figure 5.3).

All of the other peaks in the spectrum of $[Fe(L)]^{2+}$remained unperturbed regardless of the presence or absence of D_2O, and no shifting of the exchangeable protons was observed at lower temperatures. 2-dimensional NMR investigations yielded no additional information about these exchangeable protons The fact that the integration of the ^1H NMR spectrum of $[Fe(L)]^{2+}$ is consistent with the structure shown in Figure 5.1, as well as the absence of an aldehyde proton, indicates that the imines of the cage are intact in solution. Therefore, we must conclude that the

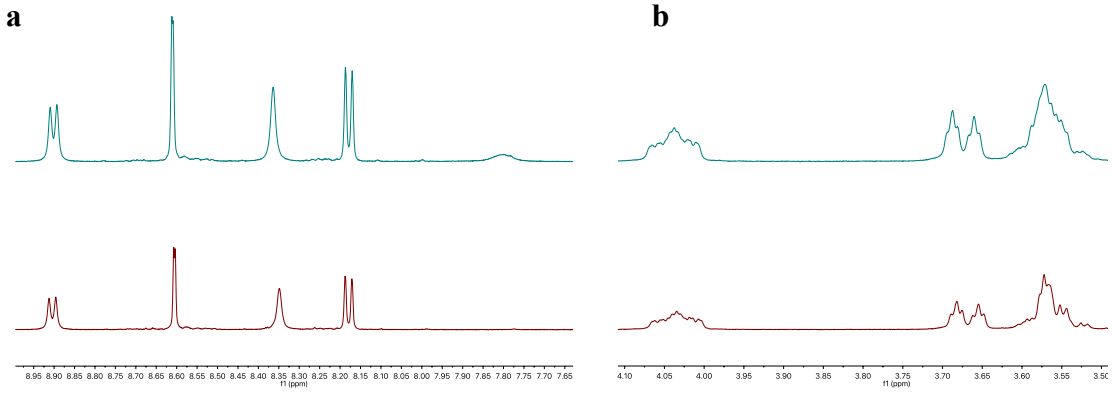

Figure 5.3. (a) Aromatic region of the ^1H NMR spectra of $[Fe(L)](PF_6)_2$ in CD_3CN in absence (teal trace) and presence (red trace) of D_2O. (b) Aliphatic region of the ^1H NMR spectra of $[Fe(L)](PF_6)_2$ in CD_3CN in absence (teal trace) and presence (red trace) of D_2O.

caps of the cage are able to hydrogen-bond to protons that are scavenged from trace water in solution. Unfortunately, the x-ray crystal structure of $[Fe(L)](PF_6)_2$ (Figure 5.4c) is not of high enough quality to prove or disprove this hypothesis. To have a link between the benchmark

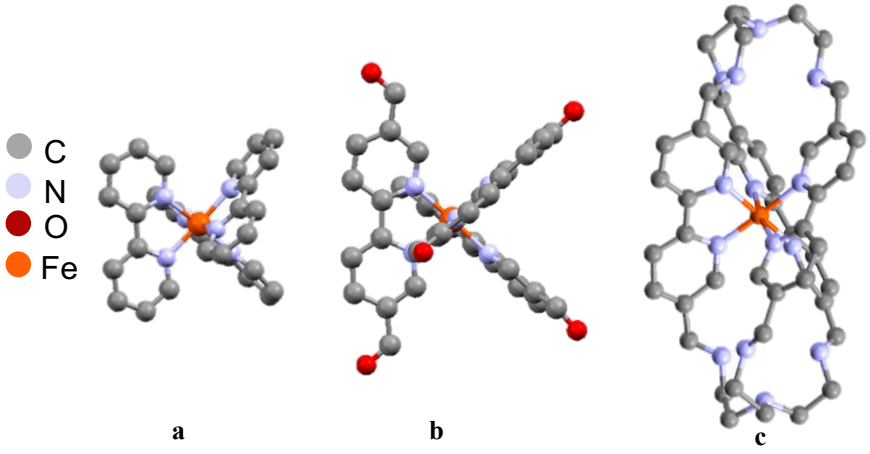

Figure 5.4. X-ray crystal structures of (a) $[Fe(bpy)_3](PF_6)_2$, (b) $[Fe(dfb)_3](PF_6)_2$, (c) $[Fe(L)](PF_6)_2$. Counteranions and hydrogen atoms are excluded from all crystal structures for clarity.

$[Fe(bpy)_3]^{2+}$ complex and the new macrocyclic $[Fe(L)]^{2+}$ complex, the *tris*-5,5'-diformyl-2,2'-bipyridine iron(II) complex ($[Fe(dfb)]^{2+}$) was also prepared. The electronic effects induced by the 5,5'-diformyl substituents in dfb should be similar to those introduced by the imine moieties in the cage ligand,[26] but the structural ramifications of tethering together the three bpy ligands expected in $[Fe(L)]^{2+}$ will be absent in $[Fe(dfb)_3]^{2+}$.

Table 5.1. Selected structural parameters of the three complexes in Figure 5.4.

Complex	Fe-N distance (Å)	*Cis* N-Fe-N angles	*Trans* N-Fe-N angles
$[Fe(bpy)_3](PF_6)_2$[a]	1.9670 ± 0.0004	81.86–94.31°	174.61°
$[Fe(dfb)_3](PF_6)_2$	1.961 ± 0.0009	81.93-96.13°	177.30-177.36°
$[Fe(L)](PF_6)_2$	1.958 ± 0.05	81.37-95.54°	170.25-175.46

a: Taken from reference 27.

By comparing the x-ray crystal structures of $[Fe(bpy)_3]^{2+}$,[27] $[Fe(dfb)_3]^{2+}$, and $[Fe(L)]^{2+}$ (Figure 5.4), it is clear that tethering together the three bpy moieties has a large impact on the coordination geometry of Fe(II). In fact, because of the almost helical twisting of the cage ligand

adopted to accommodate chelation of the Fe(II), $[Fe(L)]^{2+}$ is actually closer to D_{3h} symmetry than D_3, the typical symmetry of *tris*-bidentate transition metal complexes. The ramifications of these disparate local symmetries are evident in the extinction coefficient of the visible $^1A_1 \rightarrow$ MLCT

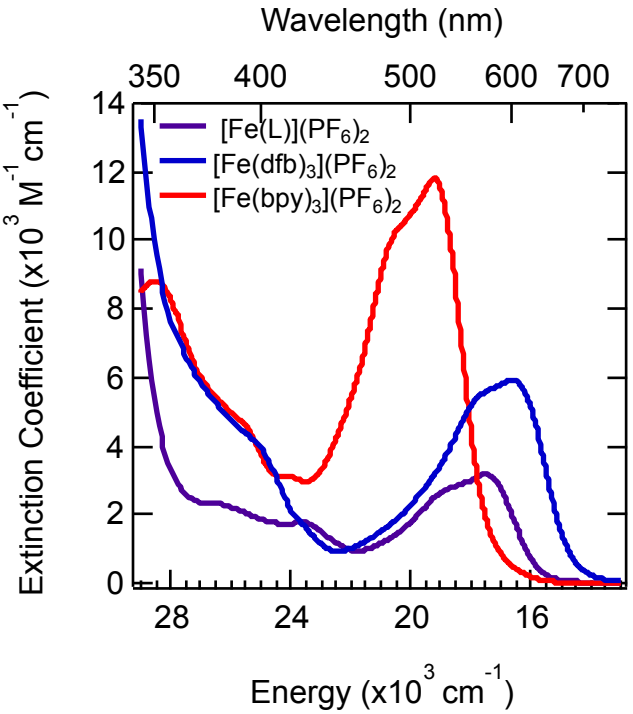

Figure 5.5. Ground state absorption spectra of $[Fe(L)](PF_6)_2$, $[Fe(dfb)_3](PF_6)_2$, and $[Fe(bpy)_3](PF_6)_2$ in acetonitrile at room temperature.

absorption feature in $[Fe(L)]^{2+}$ (Figure 5.5), which at its maximum only reaches 3160 $M^{-1}cm^{-1}$, whereas for $[Fe(bpy)_3]^{2+}$ the same feature has an extinction coefficient of 11750 $M^{-1}cm^{-1}$.[28] This absorption feature in both $[Fe(dfb)_3]^{2+}$ and $[Fe(L)]^{2+}$ is significantly red-shifted compared to that of $[Fe(bpy)_3]^{2+}$, presumably due to the increase in delocalization of the π-system and electron-withdrawing nature of the aldehyde and imine moieties.

Electrochemical measurements were performed on $[Fe(L)]^{2+}$ to further characterize the electronics of this new low-spin Fe(II) complex (Figure 5.6). Unfortunately, the aldehyde functional groups in $[Fe(dfb)_3]^{2+}$ reacted under electrochemical conditions and prevented the observation of both Fe^{II} oxidation and ligand reduction events. In $[Fe(L)]^{2+}$, an irreversible $Fe^{II/III}$

oxidation potential occurs at 0.90 V (versus Fc/Fc^+), which is almost 225 mV more positive than that of $[Fe(bpy)_3]^{2+}$ under the same conditions (0.68 V).[28] compared to 17500 cm^{-1} (570 nm) observed in the absorption spectrum. In octahedral Fe(II) complexes, the origin of the oxidation sampled electrochemically can be characterized as the loss of an electron from the formally π-bonding t_{2g} orbitals. Therefore, in the limit of octahedral symmetry, the more positive oxidation potential in $[Fe(L)]^{2+}$ versus that in $[Fe(bpy)_3]^{2+}$ represents a stabilization of the t_{2g} orbitals. Although the change in symmetry between the two complexes slightly muddles this conclusion, it is quite reasonable that the π-withdrawing nature of the imines coupled into the π-system of the macrocycle ligand would stabilize the t_{2g} orbitals.

The first reduction event of $[Fe(L)]^{2+}$ is highly irreversible, so only an approximation of the reduction potential at -1.3 V (versus Fc/Fc^+) can be surmised from cyclic voltammetry and differential pulse voltammetry. Even with this estimation, it can be noted that the reduction of $[Fe(L)]^{2+}$ is more positive than that of $[Fe(bpy)_3]^{2+}$, supporting the previously stated conclusions about the nature of the relatively electron deficient π-system in $[Fe(L)]^{2+}$. Despite the irreversible

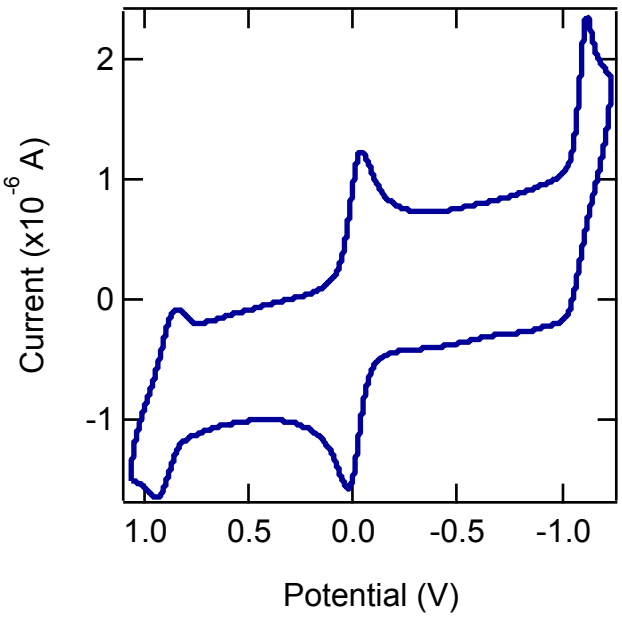

Figure 5.6. Cyclic voltammogram of $[Fe(L)](PF_6)_2$.

nature of the redox potentials, the approximate energy of the MLCT excited state, as calculated as the sum of the oxidation potential of the metal center and the reduction potential of the ligand, is actually quite close to the observed λmax of the absorption feature: 17900 cm^{-1} (560 nm) from cyclic voltammetry compared to 17500 cm^{-1} (570 nm) observed in the absorption spectrum.

5.3.3. Ground-state recovery of $[Fe(dfb)_3]^{2+}$ and $[Fe(L)]^{2+}$

We ultimately are concerned with the MLCT → LF transition this new $[Fe(L)]^{2+}$ chromophore, yet we can still gain insight into the overall nuclear coordinate of excited state evolution by studying the ground-state recovery (GSR) dynamics of the complex. The differential electronic absorption spectrum on the nanosecond timescale following excitation into the MLCT manifold of $[Fe(L)]^{2+}$ in acetonitrile (Figure 5.7a) is characteristic[29] of the $^5T_2$ ligand field excited state in other low-spin Fe(II) complexes, with a ground-state bleach (GSB) of the visible MLCT

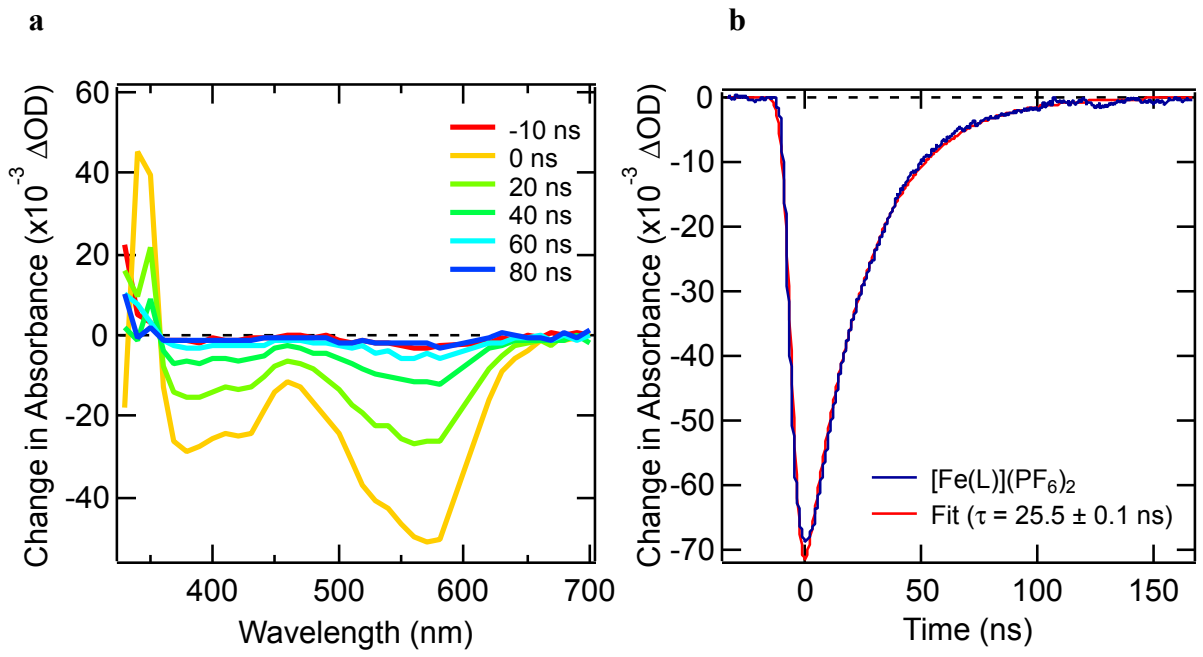

Figure 5.7. (a) Change in absorbance of $[Fe(L)](PF_6)_2$ in acetonitrile following excitation at λ_{pump} = 600 nm. (b) Single-wavelength transient absorption kinetics of $[Fe(L)](PF_6)_2$ in acetonitrile at room temperature monitored at λ_{probe} = 580 nm following excitation at λ_{pump} = 610 nm. Data were fit to an exponential modified Gaussian model to yield a time constant of $\tau = 25.5 \pm 0.1$ ns.

absorption feature and an excited-state absorption in the near-UV from the red-shifting of the ligand-based π-to-π* absorption. Recovery of the $^1A_1$ ground-state can be fit with a single exponential function, yielding a time constant of 24 ± 2 ns (Figure 5.7b), much longer than the 1.05 ± 0.02 ns[28] lifetime reported for $[Fe(bpy)_3](PF_6)_2$ in the same solvent. Perhaps more significantly, the GSR lifetime for $[Fe(L)](PF_6)_2$ is also almost twenty times longer than the 1.34 ± 0.05 ns lifetime of $[Fe(dfb)_3](PF_6)_2$ in the same solvent.[ix] These comparatively slower ground-state recovery dynamics for $[Fe(L)](PF_6)_2$ are not outside of the realm of possibility for low-spin Fe(II) polypyridyls, for example GSR occurs with τ = 55 ns in another hexadentate Fe(II) complex, $[Fe(tren(py)_3)]^{2+}$ (where $tren(py)_3$ refers to tris(2-tris(2-pyridin-2-ylmethylene)amino)ethyl)amine).[30]

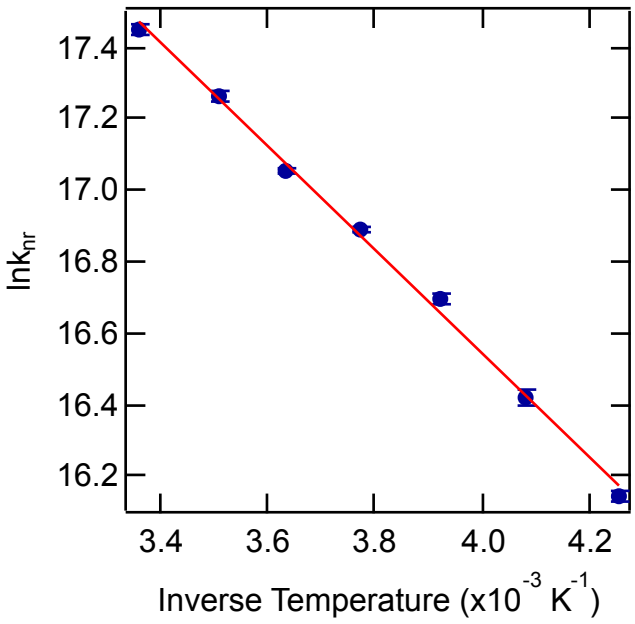

Figure 5.8. Arrhenius plot describing the temperature dependence of the rate of ground-state recovery of $[Fe(L)](PF_6)_2$ in acetonitrile, monitored at λ_{probe} = 590 nm following excitation at λ_{pump} = 620 nm. The red line is a fit to the Arrhenius equation (R^2 = 0.99), yield E_a = 1010 ± 50 cm^{-1} and A = 5.2 × 10^9 s^{-1} (200 ± 20 ps^{-1}).

[ix] These data were collected by Hayden Biessel and are presented in the appendix of this chapter (Figure 5.49).

Table 5.2. Summary of kinetic data, Arrhenius, and Marcus parameters for four low-spin Fe(II) complexes.

Complex	RT lifetime (ns)	E_a (cm^{-1})	A (ps)	$\Delta G°$ (cm^{-1})	λ (cm^{-1})	H_{ab} (cm^{-1})
$[Fe(bpy)_3]^{2+}$, *a*	1.05 ± 0.02	310 ± 15	230 ± 20	-7300 ± 730	11000 ± 1000	4.4 ± 0.2
$[Fe(terpy)_2]^{2+}$, *a*	5.2 ± 0.1	755 ± 70	240 ± 20	-7600 ± 760	14100 ± 1200	6.2 ± 1.2
$[Fe(trenpy_3)]^{2+}$, *b*	55 ± 5	1200 ± 100	200 ± 50	-6300 ± 630	14700 ± 1400	4.4 ± 0.4
$[Fe(L)]^{2+}$	**25 ± 2**	**1010 ± 50**	**200 ± 20**	**-9200 ± 920**	**17700 ± 1400**	**4.1 ± 0.2**

a: Carey, M. C.; Adelman, S. L.; McCusker, J. K. *Chem. Sci.* **2019**, *10*, 134-144 *b*: Arrhenius parameters from Brown, A. M. PhD dissertation, Michigan State University, 2011, $\Delta G°$ calculated from electrochemical data collected by M. D. Woodhouse. All complexes in the table have hexafluorophosphate counteranions and are in an acetonitrile solution. See text for the assumptions made in the calculation of these thermodynamic parameters.

As discussed in Chapter 2, it is difficult to disentangle energetic and nuclear coordinate factors that dictate the lifetimes of individual LS Fe(II) complexes. However, an Arrhenius treatment of the rate constant for ground-state recovery as a function of temperature may be illustrative of the mechanism by which the lifetime for this process extends by a factor of almost 25 for $[Fe(L)]^{2+}$ compared to $[Fe(bpy)_3]^{2+}$, especially when analyzed in the context of previously published Arrhenius parameters. Therefore, variable-temperature time-resolved absorption spectroscopy (VT-TA) was conducted on $[Fe(L)]^{2+}$ in MeCN (Figure 5.8). Marcus parameters for the $^5T_2 \rightarrow {}^1A_1$ conversion, namely the reorganization energy (λ) and the electronic coupling constant between the two states (H_{ab}), were calculated from the observed activation energy (E_a) and frequency factor (A) for GSR in $[Fe(L)]^{2+}$. The value for the free energy gap between the $^5T_2$ and $^1A_1$ states ($\Delta G°$) was approximated from electrochemical data, as described in Chapter 2 and Carey et al.[28] A comparison of these values for a series of low-spin Fe(II) complexes studied by the McCusker group is given in Table 5.2. First, when comparing the activation energies given in Table 5.2, it is immediately apparent that complexes with hexadentate ligands ($[Fe(trenpy_3)]^{2+}$ and $[Fe(L)]^{2+}$) have substantially larger barriers towards GSR than complexes with bi- and tridentate ligands ($[Fe(bpy)_3]^{2+}$ and $[Fe(terpy)_2]^{2+}$, respectively). By consulting eq. 5.1, these results could signify

$$E_a = \frac{(\lambda + \Delta G°)^2}{4\lambda} \quad (5.1)$$

that the LF strengths imposed by the hexadentate ligands are weaker (i.e. ΔG° is less negative) than that of the lower dentate ligands. In the case of $[Fe(tren(py)_3)]^{2+}$, ΔG° is in fact less negative than seen for $[Fe(bpy)_3]^{2+}$ and $[Fe(terpy)_2]^{2+}$, likely a consequence of the mixed imine/pyridine nature of the donor nitrogen atoms. However, the expected $^1A_1/^5T_2$ energy gap in $[Fe(L)]^{2+}$ is actually the largest of the four complexes, which on its own would lead to a lower activation

Table 5.3. Summary of kinetic data, Arrhenius and Marcus parameters for $[Fe(L)](PF_6)_2$ in 9:1 MeOH/EtOH.

Complex	RT lifetime (ns)	E_a (cm^{-1})	A (ps)	λ (cm^{-1})	H_{ab} (cm^{-1})
$[Fe(L)]^{2+}$	14 ± 1	630 ± 20	580 ± 30	16000 ± 1300	2.3 ± 0.1

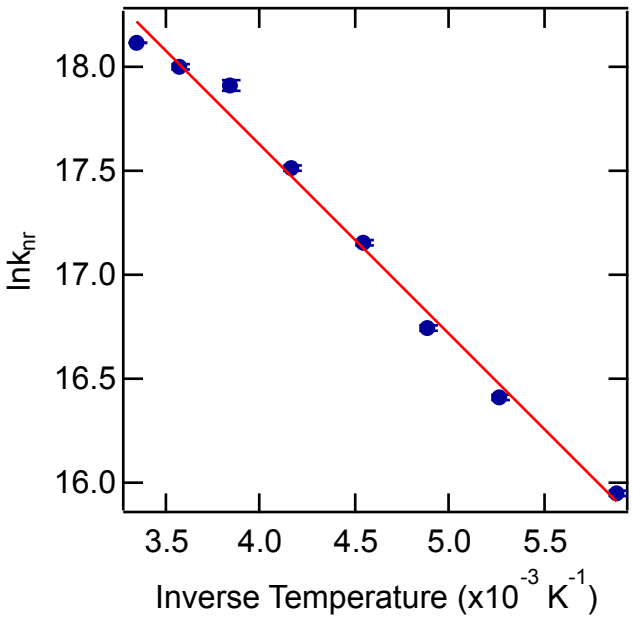

Figure 5.9. Arrhenius plot of the temperature dependence of the rate of nonradiative decay for ground-state recovery in $[Fe(L)]^{2+}$ in a 9:1 MeOH/EtOH solution. λ_{probe} = 540 nm and λ_{pump} = 570 nm. Line represents the fit to the Arrhenius equation (R^2 = 0.98) to yield E_a = 630 ± 20 cm^{-1} and A = (1.74 ± 0.2) × 10^9 s^{-1} (580 ± 30 ps^{-1}).

energy, the opposite of what is observed experimentally. So, it is clear that any effects imparted by a more favorable driving force in $[Fe(L)]^{2+}$ is offset by a higher reorganization energy. Indeed,

the value for λ at nearly 18,000 cm^{-1} approximated for an iron(II) polypyridyl is the largest reported to date.

The origin of this significant increase in λ for $[Fe(L)]^{2+}$ is not immediately obvious, as the values for λ given in Table 5.2 reflect structural reorganization due to both inner-sphere (λ_i) and outer-sphere (λ_o) structural reorganizations. To assess the contribution of λ_o, which originates from solute-solvent interactions, the temperature-dependence of GSR in $[Fe(L)]^{2+}$ was also collected in a 9:1 MeOH/EtOH solution (Figure 5.9). The alcohol nature of this solvent system is expected to interact differently with $[Fe(L)]^{2+}$ than acetonitrile, not only due to the lower dielectric constant expected for the alcohol solution than that of neat acetonitrile (dielectric constants: MeOH = 32.7, EtOH = 24.3 versus MeCN = 38.8 at 298 K),[31] but also due to the presence of the imine caps on both ends of the molecule that could hydrogen bond with alcoholic solvents. Unlike previous studies of $[Fe(bpy)_3]^{2+}$ in a variety of organic solvents, which showed practically no significant impact on the measured Arrhenius and Marcus parameters,[32] the $^5T_2$ lifetime in $[Fe(L)]^{2+}$ dropped by almost half by changing solvent, and there was also huge difference observed in the $^5T_2 \rightarrow {}^1A_1$ barrier (Tables 5.2 and 5.3). This would seem to indicate that there are significant solute-solvent interactions contributing to the kinetics of GSR. However, when λ and H_{ab} values were calculated by assuming that ΔG° does not change significantly between solvents, λ_{MeCN} and λ_{OH} were within error of each other. The factor that does change significantly is the electronic coupling constant, a reflection of the much smaller frequency factor measured for $[Fe(L)]^{2+}$ in the alcohol solution. Unfortunately, VT-TA and electrochemistry alone cannot fully explain these results, but a combination of ab initio molecular dynamics[33] and x-ray measurements (emission and diffuse scattering),[34–36] such as those conducted to described the photo-induced changes in solvation of

$[Fe(bpy)_3]^{2+}$ in water, could yield more insight into the origin of the discrepancies in GSR of $[Fe(L)]^{2+}$ in different solvents.

Ground-state characterization and VT-TA experiments on $[Fe(L)]^{2+}$ suggest that by employing this macrocyclic cage ligand, we may have enabled a higher degree of geometric distortion to occur during GSR, as evidenced by its high activation energy as well as the large reorganization energy in acetonitrile in comparison to other LS Fe(II) complexes. While further investigations are necessary to firmly describe the origin(s) of these findings, as well as the large discrepancies between the Arrhenius parameters for GSR in two different solvents, the simple comparison between the GSR dynamics of $[Fe(dfb)_3]^{2+}$ and $[Fe(L)]^{2+}$ shows that tethering together three bidentate ligands has a profound impact on the room-temperature GSR dynamics of the LS polypyridyl complexes.

5.3.4. MLCT excited-state deactivation of $[Fe(dfb)_3]^{2+}$ and $[Fe(L)]^{2+}$

A thorough investigation of the GSR dynamics of $[Fe(L)]^{2+}$ has revealed that the cage ligand employed to chelate Fe(II) may be affecting the nuclear coordinate, but the real question is: have we affected the lifetime of the coveted charge-separated MLCT excited state? This question will be answered via an investigation of the ultrafast excited-state dynamics with transient absorption (TA) spectroscopy. First, a spectral tag of the MLCT excited state must be identified to guide TA measurements. Spectroelectrochemistry was used to predict the differential absorption spectrum of the MLCT excited state in $[Fe(L)]^{2+}$, taking advantage of the fact that a MLCT can be formalized as the concomitant oxidation of the metal center ($Fe^{II} \rightarrow Fe^{III}$) and reduction of a bpy ligand ($bpy \rightarrow bpy^{\bullet -}$). Thus, monitoring the absorption spectrum of the complex while applying either an oxidative or reductive potential can roughly represent those two individual processes,

and the sum of the two spectra is a qualitative guide for the differential TA spectrum of the MLCT excited state.

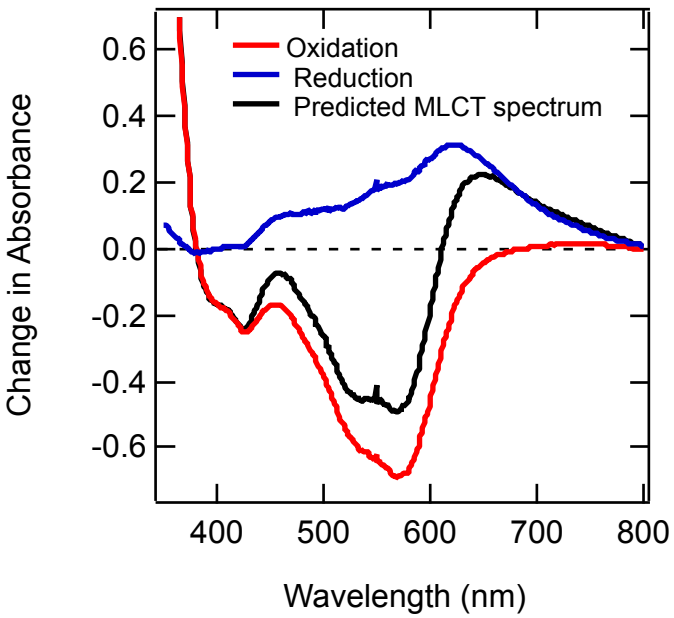

Figure 5.10. Change in the absorbance spectrum of $[Fe(L)](PF_6)_2$ in acetonitrile with 0.1 M $TBAPF_6$ with an applied oxidative potential of 1 V vs Fc/Fc^+ (red trace) or an applied reductive potential of -1.2 V vs Fc/Fc^+ (blue trace). The sum of these two spectra yield a predicted absorption spectrum of a MLCT excited state (black trace).

As is typical of *tris*-polypyridyl d^6 transition metal complexes,[19] oxidation of the metal center results in a loss of the visible MLCT absorption and a red-shift of the ligand-centered $\pi \rightarrow \pi^*$ peak (Figure 5.10, red trace). Reduction of the ligand, on the other hand, leads to broad absorption throughout the visible region, a hallmark of a bpy-based radical anion (Figure 4.10, blue trace). The sum of these two spectra simulate the MLCT transient absorption spectrum (Figure 5.10, black trace), and can be compared to the nanosecond time-resolved full spectrum data (Figure 5.7a), which we know is the TA spectrum of the $^5T_2$ excited state. The mid-visible to near-infrared TA spectrum of the $^5T_2$ is dominated by a GSB, with ΔA approaching zero at longer wavelengths. However, the calculated MLCT spectrum from spectroelectrochemistry predicts that this excited state should have an absorption feature at wavelengths >600 nm, suggesting that probing in this

region and looking for an initially positive signal that either returns to baseline or transitions to a GSB would be diagnostic of the MLCT→ $^5T_2$ transition in $[Fe(L)]^{2+}$.

With this guide, Bryan Paulus conducted ultrafast transient absorption on $[Fe(L)]^{2+}$, which are described in detail in his dissertation[20] and our article regarding the ultrafast behavior of iron(II) cage complexes.[21] His results will be briefly summarized here, as they provide important foundations for forthcoming discussions. The ultrafast time-resolved full spectrum of $[Fe(L)]^{2+}$ in acetonitrile showed the absence of any positive signal red of 600 nm (Figure 5.11), and instead matched in sign the time-resolved spectrum obtained at nanosecond timescales, indicating a very fast deactivation of the MLCT excited state into the $^5T_2$ ligand field excited state. Single wavelength kinetics revealed a time constant for MLCT excited state decay as 110 ± 30 fs, typical of the reported lifetimes for other low-spin iron(II) polypyridyl complexes.[11,29,37,38] Due to the instability of $[Fe(dfb)_3]^{2+}$ in electrochemical measurements, instead of collecting

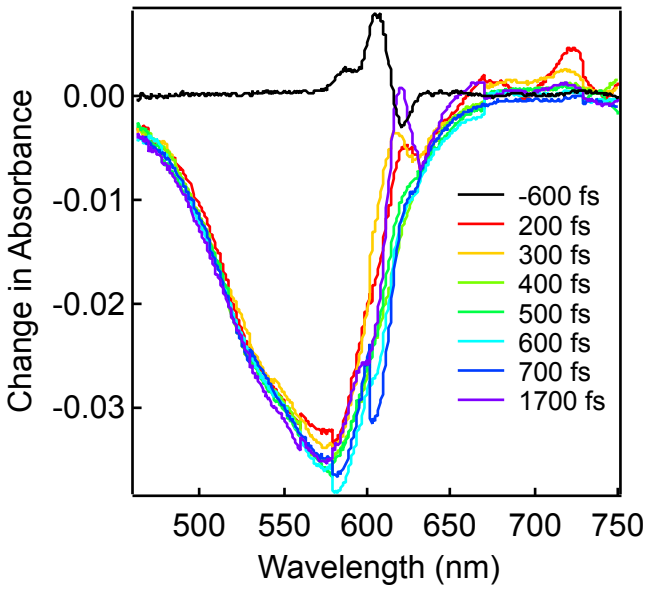

Figure 5.11. Femtosecond time-resolved absorption data of $[Fe(L)](PF_6)_2$ acquired in CH_3CN solution. Full spectrum data collected over the first few ps following MLCT excitation at 600 nm. The anomalous features near 600 nm are due to scattered light from the excitation source. Reproduced from reference 20.

spectroelectrochemistry on the complex to identify the spectral tag of its MLCT excited state, it was assumed that it would qualitatively match that of $[Fe(L)]^{2+}$, with the minimum of the GSB occurring at a wavelength that corresponds to the maximum of the MLCT absorption feature in the ground-state absorption spectrum. Bryan Paulus found that the lifetime of the MLCT in $[Fe(dfb)_3]^{2+}$ was very short, sub-100 fs.[x] From these measurements, we can conclude that despite lowering the MLCT energy significantly from that observed in $[Fe(bpy)_3]^{2+}$ (by ~1700 cm^{-1} for $[Fe(L)]^{2+}$ and 2600 cm^{-1} for $[Fe(dfb)_3]^{2+}$) and changing the Fe-N coordination geometry by tying together the bpy moieties in $[Fe(L)]^{2+}$, essentially no change to the MLCT $\rightarrow$ $^5T_2$ timescale was imparted.

Despite the disappointment of the unremarkable MLCT excited-state lifetime for $[Fe(L)]^{2+}$, the ultrafast TA data yielded additional information about the shorter timescale kinetics:

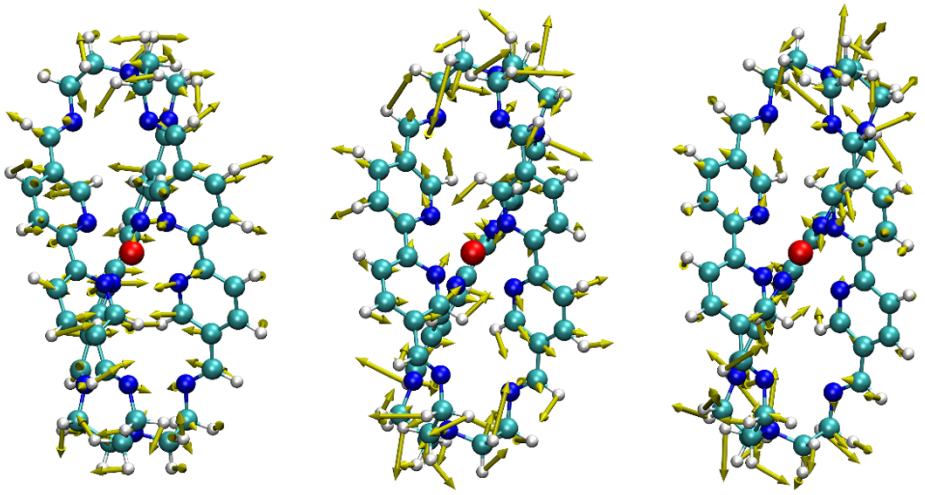

Figure 5.12. DFT calculated vector displacement diagrams of the observed coherently excited vibrational modes of $[Fe(L)](PF_6)_2$ in acetonitrile. Reproduced from reference 21.

[x] The very fast time constant and low signal intensity for the MLCT deactivation in this complex prevented a more precise determination of this lifetime.

vibrational coherences, observed as oscillatory features superimposed onto the single wavelength kinetics. A fast Fourier transform (FFT) and linear-predictive singular value decomposition (LPSVD) analyses of these features revealed the vibrational frequencies that give rise to these coherent artifacts. To visualize the geometric motions associated with these specific vibrational modes, Bryan Paulus performed DFT frequency calculations on both the ground state ($^1A_1$) and lowest-energy excited state ($^5T_2$) of the $[Fe(L)]^{2+}$ molecule.[20] He found that all of the experimentally observed modes could be reproduced by motions of the molecule in the $^5T_2$ state that involved both changes in Fe-N bond lengths and angles that were coupled to extensive distortions of the imine cap in the $^5T_2$ ligand field state of the complex (specifically the modes given in Figure 5.12).

By observing vibrational modes that may be active[xi] during the MLCT → $^5T_2$ decay with transient absorption, a pathway towards disruption of the excited-state nuclear coordinate presents itself: could hampering movement of the imine caps of the $[Fe(L)]^{2+}$ complex through synthetic modification of the ligand affect the vibrational modes coupled to MLCT excited state deactivation to such an extent that we could observe a change in the rate of the MLCT → $^5T_2$ transition? Fortunately, the cage ligand provides a relatively simple way to tie up the imine caps: tetrahedral coordination of a metal cation.

5.3.5. Synthesis of trinuclear cage compounds

Indeed, there was a precedence for coordination of transition metals in the tetrahedral environment provided by the imine caps of this Lehn cage ligand while maintaining octahedral

[xi] At the point of writing, we are unable to conclusively state whether or not the vibrational modes observed from coherent oscillations in ultrafast transient absorption are kinetically relevant (i.e. define the nuclear coordinate for excited-state decay) or are simply spectator modes. Some insight into this question may be given by the dephasing times for the coherent oscillations. However, this discussion is beyond the scope of this work and these details are explored in much greater detail in Bryan C. Paulus' dissertation.

coordination of Fe(II). A previous McCusker group member, Lindsey Jamula, was able to obtain a disordered crystal structure of $[FeCu_2(L)]^{4+}$, with the motive of using the Cu(I) as a pathway towards intramolecular "flash-quench," whereby in the Fe-based MLCT excited state the ostensibly Fe(III) center is reductively quenched by the nearby Cu(I), isolating the bpy-based radical and potentially prolonging its lifetime.[22] While Cu(I) was convenient for this flash-quench system, in our current scenario we would actually prefer a photoredox inert transition metal to avoid difficult-to-interpret kinetic data. Therefore, the best candidate for coordination of the imine caps was Li^+: its ionic radius in a tetrahedral environment is almost identical to that of Cu(I), there should be no possibility for photoredox activity, and there are examples in the literature of tetrahedral imine lithium compounds.[39,40]

Although ideal in theory, $[FeLi_2(L)]^{4+}$ could not be isolated, despite employing many different lithium starting materials, solvents, reaction temperatures, reaction times, and order of addition of Fe^{2+} and Li^+ sources. Ultimately, we must conclude that there simply is not a sufficient driving force for the coordination of Li^+ in this particular ligand scaffold. Following this conclusion, the syntheses of $[FeNa_2(L)]^{4+}$ and $[FeK_2(L)]^{4+}$ were attempted, but again to no avail. Next, the synthesis of $[FeZn_2(L)]^{6+}$ was attempted, starting from $[Fe(L)]^{2+}$ in hopes of avoiding

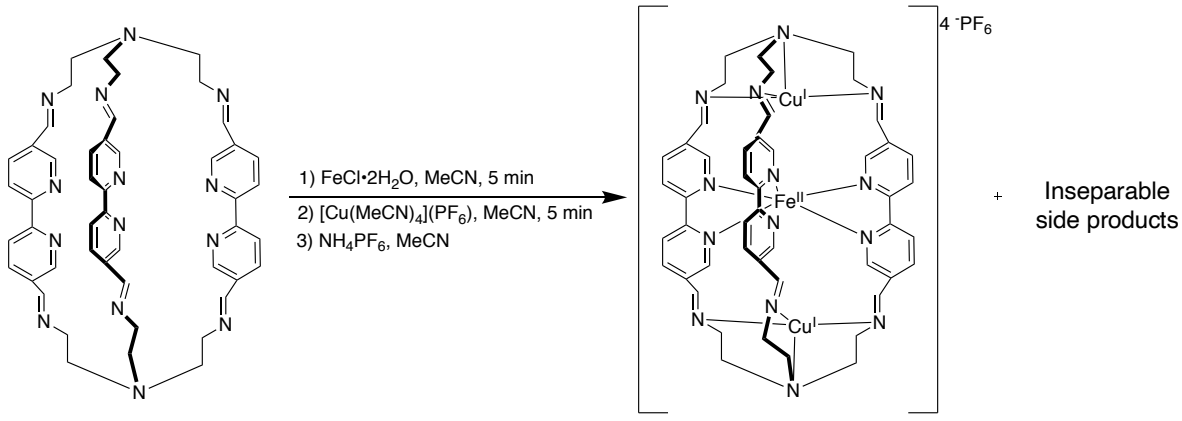

Figure 5.13. Synthetic route employed by Lindsey Jamula to synthesize impure $[FeCu_2(L)](PF_6)_4$.

octahedral coordination of Zn^{2+} and forcing it into the tetrahedral sites. After short reaction times at room temperature, no reaction was observed. On the other hand, at longer reaction times or elevated temperatures, Fe^{2+} was actually replaced by Zn^{2+}, and no signs of $[FeZn_x(L)]^{n+}$ (x = 1, 2; n = 2 + 2x) were detected in mass spectrometry. There is precedence of the preferred thermal stability of octahedral Zn^{2+} over Fe^{2+}, and there have been studies that suggest that the formation constants of Zn^{2+} coordination with polypyridyl ligands is higher than the analogous formation of Fe^{2+} complexes.[41]

Therefore, because the synthesis of a trinuclear $[FeX_2(L)]^{n+}$ complex where X is a photoredox inert metal was not viable, the previously synthesized $[FeCu_2(L)]^{4+}$ was revisited in hopes that we could selectively monitor Fe-based dynamics spectroscopically. But first, the purity of the complex needed to be addressed. When synthesized via the procedure outlined by Lindsey Jamula (Figure 5.13),[22] the ^1H NMR of the complex indicated the presence of a ~20% impurity. Recrystallization of the impure $[FeCu_2(L)]^{4+}$ increased the relative concentration of the impurity and introduced new peaks to the ^1H NMR. All column chromatography (on silica, neutral and basic alumina, and LH-20 size exclusion resin) either resulted in no improvement in the purity of the complex or in complex decomposition.

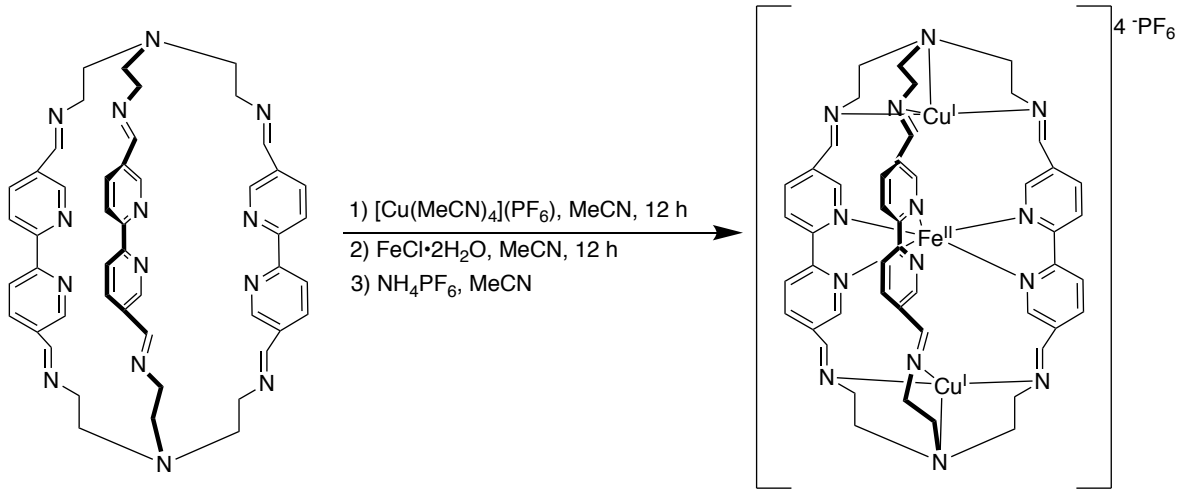

Figure 5.14. Modified synthetic route to obtain pure $[FeCu_2(L)](PF_6)_4$.

However, amending the reaction conditions resulted in analytically pure complex (Figure 5.14). By adding the Cu(I) starting material to the cage ligand first and allowing ample time for coordination prevented incomplete copper complexation and helped pull the highly insoluble ligand into solution. Then Fe(II) could be added, rapidly causing an obvious color change from green to maroon. Again, a relatively long reaction time (12 h) was provided to ensure as much coordination of Fe(II) as possible. Filtering the reaction mixture through Celite prior to anion exchange removed any uncoordinated ligand and the highly insoluble $[Fe(L)]Cl_2$. With these side products removed, the tetracationic complex could be metathesized to the hexafluorophosphate salt, not only resulting in a pure compound by elemental analysis, but a high-quality crystal structure without the disorder originally observed. To begin to assign spectral features derived from the presence of Cu(I), $[ZnCu_2(L)]^{4+}$ was also synthesized following the same synthetic route outlined in Figure 5.14, but replacing $FeCl_2 \bullet 2H_2O$ with $ZnCl_2$.

5.3.6. Structural characterization of trinuclear cages

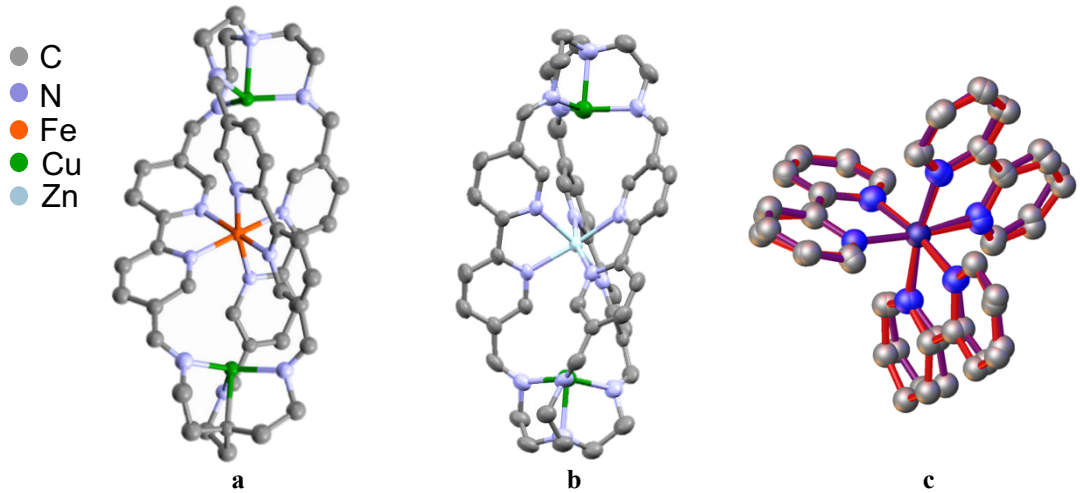

Figure 5.15. X-ray crystal structures of (a) $[FeCu_2(L)](PF_6)_4$ and (b) $[ZnCu_2(L)](PF_6)_4$. Hydrogen atoms, solvent molecules, and counteranions are excluded for clairity. (c) Overlay of the $[Fe(bpy)_3]^{2+}$ cores from the crystal structures of $[Fe(L)]^{2+}$ (*red bonds*) and $[FeCu_2(L)]^{4+}$ (*purple bonds*).

The crystals of both trinuclear complexes (Figure 5.15a-b) were monoclinic in the $P2_1/c$ space group, differing from the orthorhombic Ibam crystal of $[Fe(L)]^{2+}$. However, the local coordination geometries of the octahedral Fe(II) centers were indistinguishable from one another in the $[Fe(L)]^{2+}$ and $[FeCu_2(L)]^{4+}$ complexes (Figure 5.15c)[xii], suggesting that any spectroscopic differences between the two would not arise from geometric factors. The average Cu-Fe distance in $[FeCu_2(L)]^{4+}$ is 4.99 Å, a sign that electronic communication between the two metals is unlikely.

5.3.7. Ground state absorption of trinuclear complexes

From a comparison of the ground state absorption spectra of $[Fe(L)]^{2+}$ and $[FeCu_2(L)]^{4+}$ complexes in acetonitrile, it is clear that the mid-visible Fe-based MLCT manifold is not greatly affected by the addition of coordinated Cu(I) atoms in $[FeCu_2(L)]^{4+}$ (Figure 5.16). This feature is slightly red-shifted in the $[FeCu_2(L)]^{4+}$ complex by ~350 cm^{-1} relative to $[Fe(L)]^{2+}$ and is most

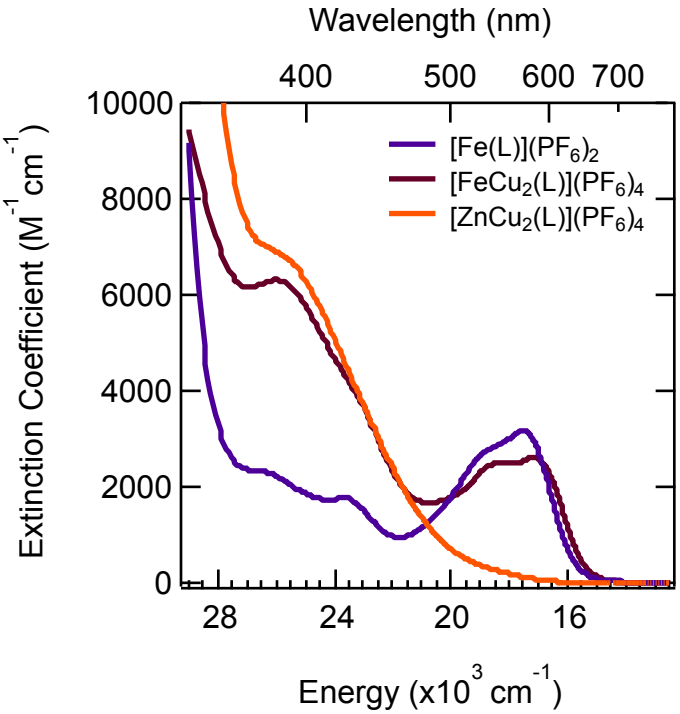

Figure 5.16. Ground-state absorption spectra of $[Fe(L)](PF_6)_2$, $[FeCu_2(L)](PF_6)_4$, and $[ZnCu_2(L)](PF_6)_4$ in acetonitrile at room temperature.

[xii] The overlay of the crystal structures of $[Fe(L)]^{2+}$ and $[FeCu_2(L)]^{4+}$ was prepared by Dr. Richard J. Staples.

likely the consequence of the electron-withdrawing effect of copper coordination to the imine caps. The presence of the ~6500 $M^{-1}cm^{-1}$ feature near 26000 cm^{-1} in both $[ZnCu_2(L)]^{4+}$ and $[FeCu_2(L)]^{4+}$ complexes suggests it is copper-based, probably a $Cu^{I} \rightarrow L$ MLCT.The fact that there are not strong deviations in the absorption spectrum of $[FeCu_2(L)]^{4+}$ from the features observed in $[Fe(L)]^{2+}$ and $[ZnCu_2(L)]^{4+}$ confirms the absence of electronic perturbation to the Fe and Cu systems.

5.3.8. Electrochemistry of trinuclear complexes

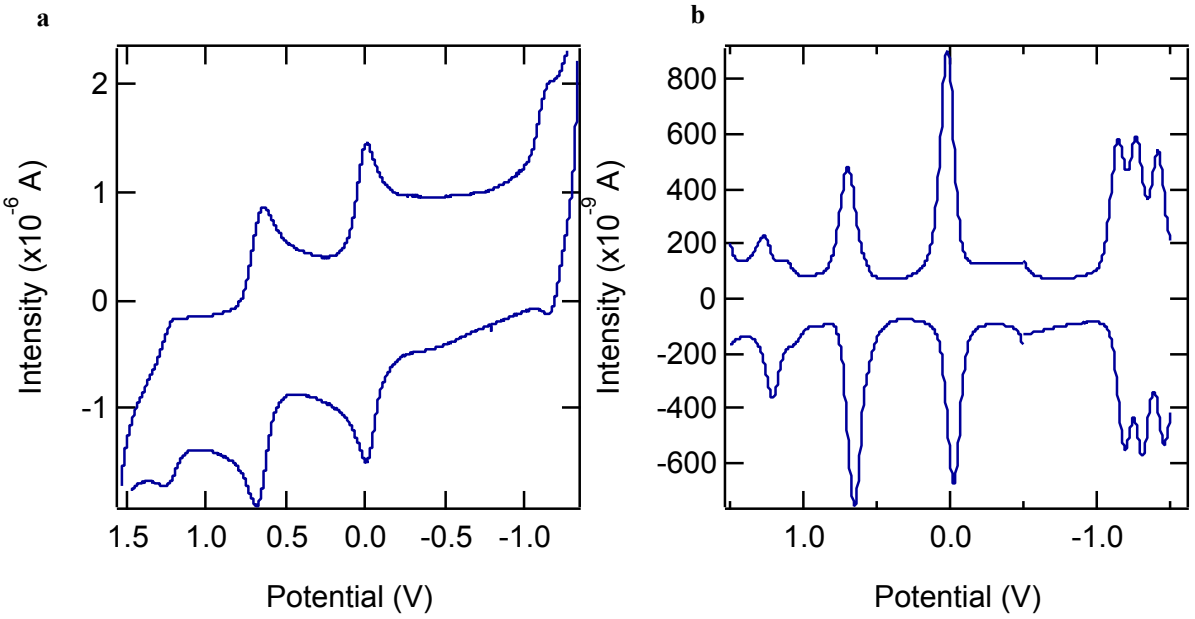

Figure 5.17. (a) Cyclic voltammogram and (b) differential pulse voltammogram of $[FeCu_2(L)](PF_6)_4$ in acetonitrile with 0.1 M $TBAPF_6$ and referenced internally to the Fc/Fc^+ couple.

Cyclic and differential pulse voltammograms of $[FeCu_2(L)]^{4+}$ (Figure 5.17) and $[ZnCu_2(L)]^{4+}$ (Figure 5.18) in acetonitrile were measured to further characterize the electronics of the two trinuclear complexes. Both copper-containing complexes have an oxidative feature between 600-700 mV versus Fc/Fc^+, which can thus be assigned to a $Cu^{I/II}$ oxidation. Only one of these features is observed for each complex, indicating that both Cu^{I} atoms in a given trinuclear complex are electronically equivalent. The 70 mV shift to more positive potentials for the $Cu^{I/II}$

oxidation in the $[FeCu_2(cage)]^{4+}$ versus its Zn(II) analogue reflects the decreased orbital overlap between Zn(II) and the ligand in comparison to Fe(II), as evidenced by the longer average Zn-N bond lengths (2.16 Å) than the average Fe-N bond length (1.98 Å). This effectively results in less electron donation from the ligand to Zn(II), allowing for a slight increase in electron density donation from the ligand to the Cu^I atoms, in comparison to the stabilization of Cu^I in $[FeCu_2(L)]^{4+}$.

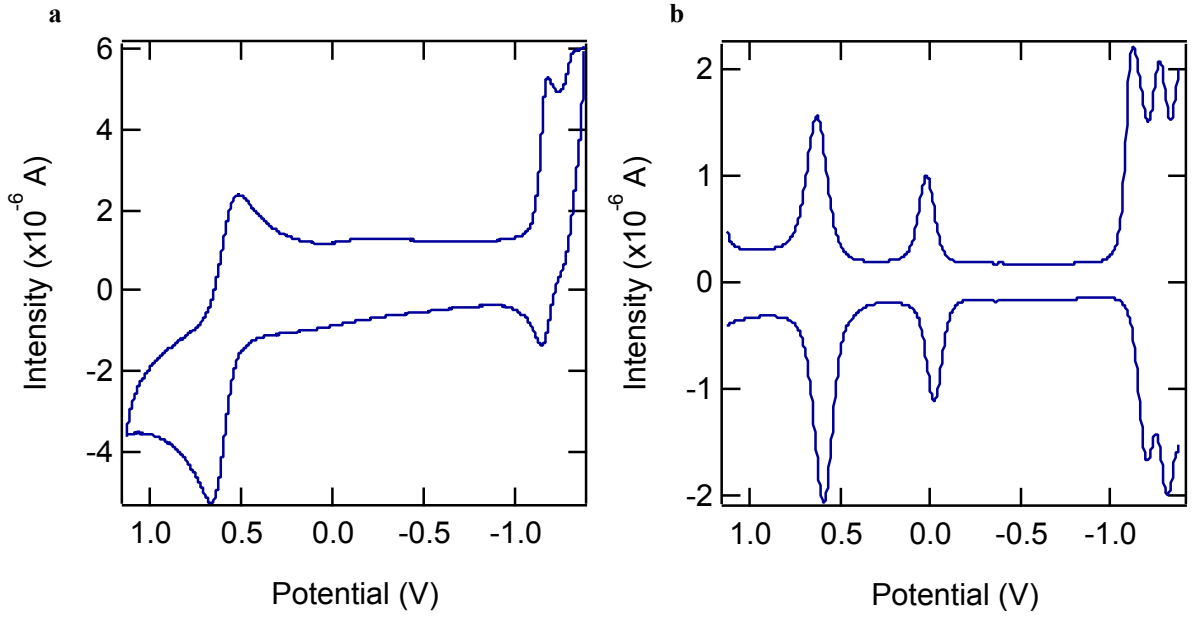

Figure 5.18. (a) Cyclic voltammogram (b) and differential pulse voltammograms of $[ZnCu_2(L)](PF_6)_4$ in acetonitrile with 0.1 M $TBAPF_6$ and referenced internally to the Fc/Fc^+ couple.

Likewise, the first reduction potential in $[FeCu_2(L)]^{4+}$ is 70 mV more positive in $[ZnCu_2(L)]^{4+}$. At more positive potentials, the $Fe^{II/III}$ oxidation wave is observed at 1.24 V in the cyclic voltammogram of $[FeCu_2(L)]^{4+}$. Because the $Cu^{I/II}$ oxidation occurs at less positive potentials than the $Fe^{II/III}$ oxidation, it is impossible to directly compare the potentials at which the

Table 5.4. Summary of the electrochemical potentials measured for the cage complexes in acetonitrile with 0.1 M $TBAPF_6$. All potentials are referenced to the Fc/Fc^+ couple.

Assignment	$[Fe(L)](PF_6)_2$	$[FeCu_2(L)](PF_6)_4$	$[ZnCu_2(L)](PF_6)_4$
$Fe^{II/III}$	0.90 V	1.24 V	–
$Cu^{I/III}$	–	0.68 V	0.61 V
L/L^-	-1.07 V	-1.17 V	-1.18 V

Fe^{II} center is oxidized in the $[Fe(L)]^{2+}$ and $[FeCu_2(L)]^{4+}$ complexes. The $Fe^{II/III}$ oxidation potential is also irreversible and appears to degrade the complex, further preventing a reliable comparison between iron-containing complexes.

5.3.9. Spectroelectrochemistry of trinuclear complexes

The addition of the non-photoredox-innocent Cu(I) to the Fe-containing cage complex has the potential to complicate interpretation of the photophysical data collected on $[FeCu_2(L)]^{4+}$. Although the ground-state absorption spectrum of the complex indicates that exclusive excitation into the Fe-based MLCT absorption features is possible (Figure 5.16), having clear spectral tags of photoinduced Cu(I) redox activity will enable the accurate elucidation of all forthcoming photophysical measurements on $[FeCu_2(L)]^{4+}$. The most feasible complication arising from Cu(I) is its potential ability to reductively quench the formally Fe^{3+} formed in the MLCT excited state. To model the differential absorption spectrum of this species, as well as the Fe-based MLCT spectrum in $[FeCu_2(L)](PF_6)_4$, spectroelectrochemistry of all three cage complexes was utilized (Figures 5.10 and 5.19).

First, oxidative and reductive spectroelectrochemistry was collected on both trinuclear complexes (Figure 5.19). The oxidative spectrum of $[ZnCu_2(L)]^{4+}$ (Figure 5.19a) shows that oxidation of Cu(I) results in the loss of the Cu-based MLCT, causing a ground-state bleach in the near-UV and only a very slight absorptive feature in the near-IR. A similar effect is observed in the oxidative spectrum of $[FeCu_2(L)]^{4+}$ (Figure 5.19c) with the additional loss of the Fe-based MLCT in the mid-visible, as it was not possible to isolate either the Fe^{II}-only or Cu^{I}-only oxidation in these experiments. Therefore, to look for any photo-induced Cu^{I} redox activity in the transient absorption of $[FeCu_2(L)]^{4+}$, probing at ~400 nm where the maximum of the GSB will be the most elucidating.

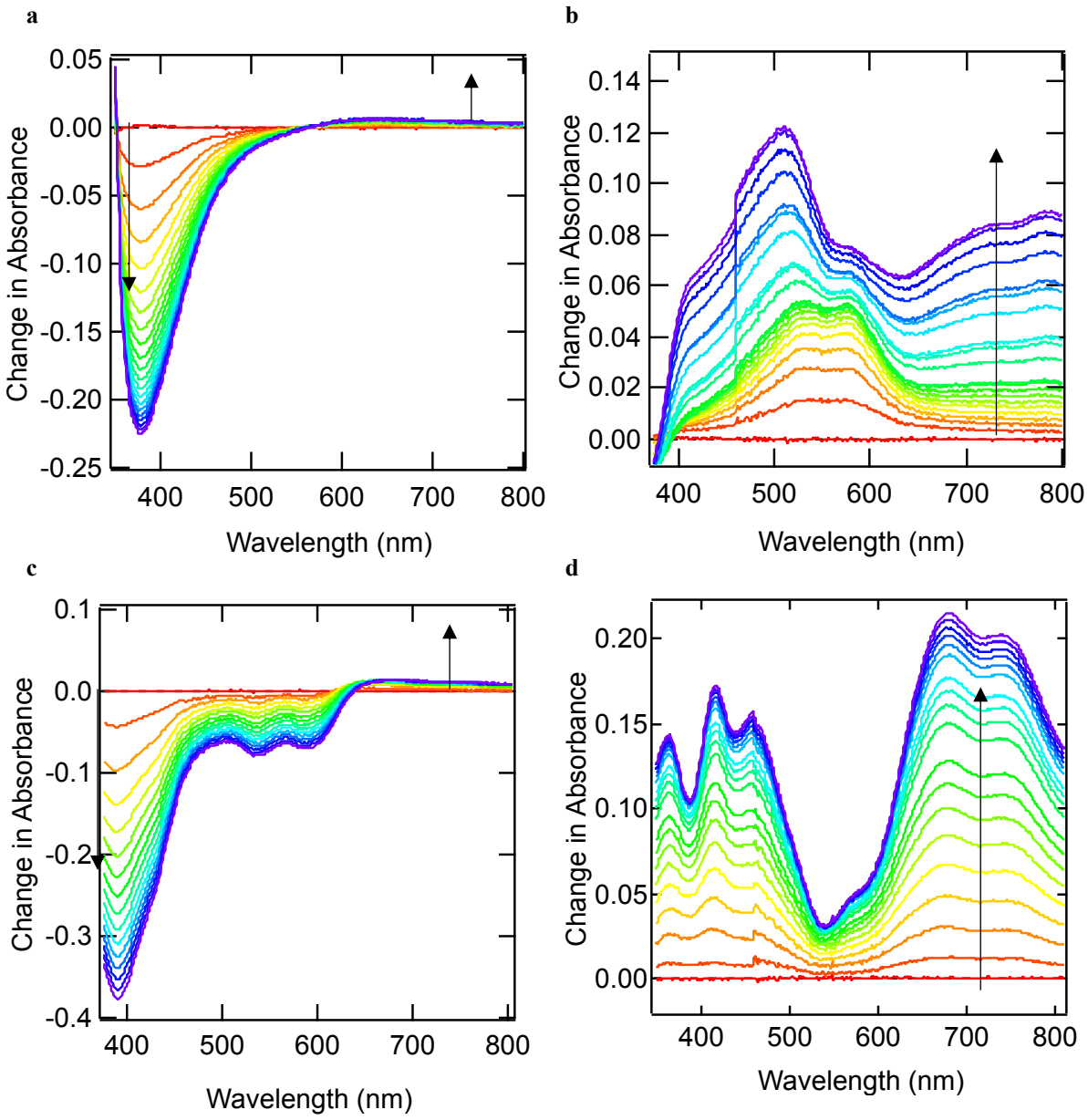

Figure 5.19. Change in absorbance monitored over time as a potential is applied. (a) Oxidative spectrum of $[ZnCu_2(L)](PF_6)_4$ with an applied potential of 0.7 V. (b) Reductive spectrum of $[ZnCu_2(L)](PF_6)_4$ with an applied potential of -1.3 V. (c) Oxidative spectrum of $[FeCu_2(L)](PF_6)_4$ with an applied potential of 1.35 V. (d) Reductive spectrum of $[FeCu_2(L)](PF_6)_4$ with an applied potential of -1.3 V. In all spectra, the red trace corresponds to the differential absorption spectrum with no applied potential (baseline), and the violet trace corresponds to the last spectrum collected with the applied potential. All spectra are collected in acetonitrile with 0.1 M $TBAPF_6$. All potentials are referenced to the Fc/Fc^+ redox couple.

To model the Fe-based MLCT difference spectrum of $[FeCu_2(L)]^{4+}$, two different approaches were taken. In the first method (Figure 5.20, blue trace), the oxidative spectrum of

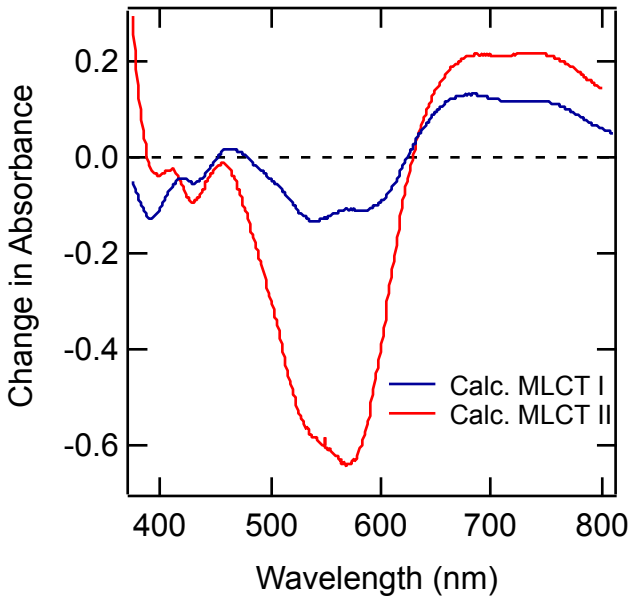

Figure 5.20. Calculated absorption spectrum of the MLCT excited state in $[FeCu_2(L)]^{4+}$.

$[ZnCu_2(L)]^{4+}$ was subtracted from the oxidative spectrum collected on $[FeCu_2(L)]^{4+}$. To this approximate "$[Fe^{III}Cu_2(L)]^{5+}$" spectrum, the differential absorptive trace obtained from the reduction of $[FeCu_2(L)]^{4+}$ (Figure 5.19d) was added. For the second model (Figure 5.20, red trace), the oxidative spectrum of $[Fe(L)]^{2+}$ (Figure 5.10, red trace) was added to the reductive spectrum of $[FeCu_2(L)]^{4+}$ (Figure 5.19d). Both of these two calculated Fe-based MLCT excited state spectra for $[FeCu_2(L)]^{4+}$ are qualitatively very similar (Figure 5.20), and indicate that the same probe wavelengths used to monitor the MLCT $\rightarrow {}^5T_2$ decay dynamics in $[Fe(L)]^{2+}$, i.e. $\lambda_{probe} > 600$ nm, should be sufficient.

5.3.10. Ground-state recovery of $[FeCu_2(L)]^{4+}$

To begin to address whether or not the coordination of the tren caps of L to Cu(I) atoms have affected the nuclear coordinate of Fe(II) excited state dynamics, the ground-state recovery dynamics of the trinuclear complex were investigated in acetonitrile and compared to those found for $[Fe(L)]^{2+}$. As with the mononuclear complex, exciting into the Fe(II)-based MLCT absorption of $[FeCu_2(L)]^{4+}$ results in a time-resolved differential spectrum characteristic of the ${}^5T_2$ ligand field

excited state (Figure 5.21a). In fact, the features observed in the full spectrum of $[FeCu_2(L)]^{4+}$ are essentially superimposable upon the full spectrum of $[Fe(L)]^{2+}$. No biphasic kinetics were observed when probing between 300-700 nm: thus, we can conclude that when exciting into the visible MLCT absorption, the dynamics on this time scale are solely attributable to Fe^{II}, without interference from the Cu^{I} atoms.

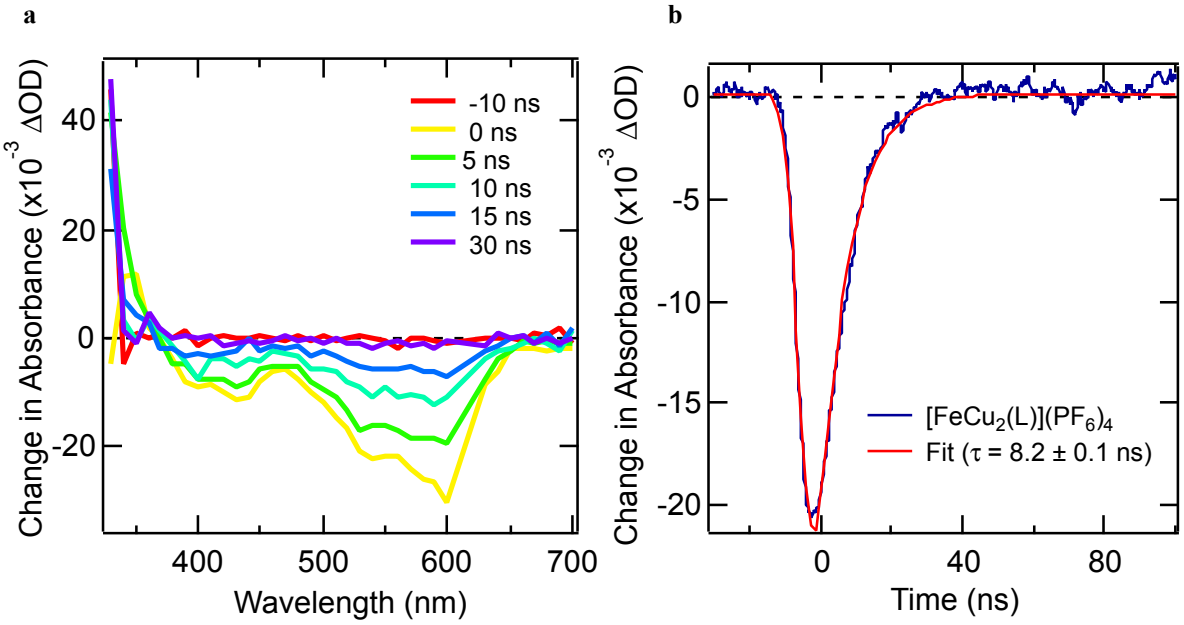

Figure 5.21. (a) Change in absorbance of $[FeCu_2(L)](PF_6)_4$ following excitation at λ_{pump} = 610 nm in acetonitrile. (b) Single wavelength kinetics of $[FeCu_2(L)](PF_6)_4$ monitored at λ_{probe} = 580 nm. Data were fit to an exponential modified Gaussian model to yield a time constant of τ = 8.2 ± 0.1 ns. All data collected at room temperature.

However, the time constant associated with the loss of the $^5T_2$ excited state of $[FeCu_2(L)]^{4+}$ is much shorter than that observed in the iron-only complex: only 7 ± 2 ns at 300 K, regardless of the pump/probe combination used. This reduction in excited-state lifetime by almost a factor three compared to $[Fe(L)]^{2+}$ indicates that the coordination of the Cu(I) atoms has disrupted either the energetics of the $^1A_1$ and $^5T_2$ states, their relative nuclear displacements, or a combination of these two factors, as the ground-state geometries of the Fe(II) coordination centers in complexes are identical (Figure 5.15c).

To probe the origin of the increased rate of GSR in $[FeCu_2(L)]^{4+}$ in comparison to $[Fe(L)]^{2+}$, variable-temperature transient absorption spectroscopy measurements were conducted on the complex in an acetonitrile solution. Surprisingly, the lifetime of the $^5T_2$ excited state only increases from 9 ± 2 ns at 295 K to only 17 ± 2 ns at 235 K, yielding an activation energy of 550 ± 80 cm^{-1} (Figure 5.22). Despite the large error associated with the Arrhenius parameters of $[FeCu_2(L)]^{4+}$, a result of the relatively short lifetimes,[xiii] the fact that the activation energy of $[FeCu_2(L)]^{4+}$ is almost half of that of the $[Fe(L)]^{2+}$ (Figure 5.8) is still significant.

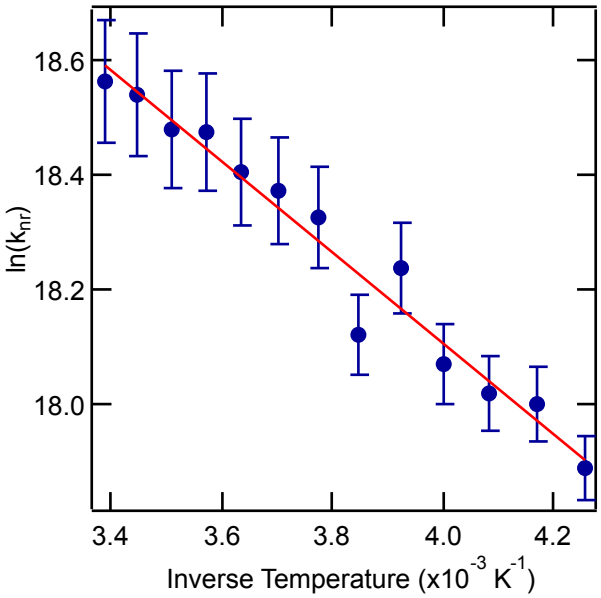

Figure 5.22. Arrhenius plot of the temperature dependence of the rate of nonradiative decay for the $^5T_2 \rightarrow {}^1A_1$ ground-state recovery of $[FeCu_2(L)](PF_6)_4$ in acetonitrile, monitoring at λ_{probe} = 570 nm and λ_{pump} = 600 nm. The red line represents a fit to the Arrhenius model, yielding E_a = 550 ± 80 cm^{-1} and A = (1.74 ± 0.8) × 10^9 s^{-1} (580 ps^{-1}).

Towards parsing out the electronic and nuclear components of the $^5T_2 \rightarrow {}^1A_1$ conversion in the two iron-containing compounds , we can approximate $\Delta G°$ electrochemically, as we have done for $[Fe(L)]^{2+}$ and other LS Fe(II) polypyridyl complexes.[28,32] However, the validity of this

[xiii] The instrument response function of the nanosecond transient absorption system used to collect these data is ~ 7 ns, establishing the lower limit of lifetimes that can be reliably resolved.

already debatable assumption[xiv] may be questioned even further in this case, as the presence of the Cu^{I} oxidation at more positive potentials that the $Fe^{II/III}$ couple most likely influences the measured Fe^{II} oxidation potential (Table 5.4). Keeping this in mind, $\Delta G°$ in $[FeCu_2(L)]^{4+}$ is -11800 ± 1180 cm^{-1}, technically outside of error of the value approximated for $[Fe(L)]^{2+}$ (-9200 ± 920 cm^{-1}, Table 5.2). Then, using this approximated value of $\Delta G°$, λ and be calculated from the activation energy (eq. 5.1) and was found to be 18100 ± 900 cm^{-1} for $[FeCu_2(L)]^{4+}$, within error of that found for $[Fe(L)]^{2+}$ in the same solvent (17700 ± 1770 cm^{-1}, Table 5.2). Unfortunately, making firm conclusions about the origin of the faster rate for GSR in $[FeCu_2(L)]^{4+}$ and its much lower $^5T_2 \rightarrow {}^1A_1$ barrier is impossible with so many approximations.

One piece of computational evidence suggests, however, that upon coordination of the two Cu(I) atoms into the cage ligand, the nuclear displacement ($\Delta Q_{LF/GS}$) between the $^5T_2$ and $^1A_1$ states decreases in comparison to the iron-only complex. A "linear reaction path" can describe the

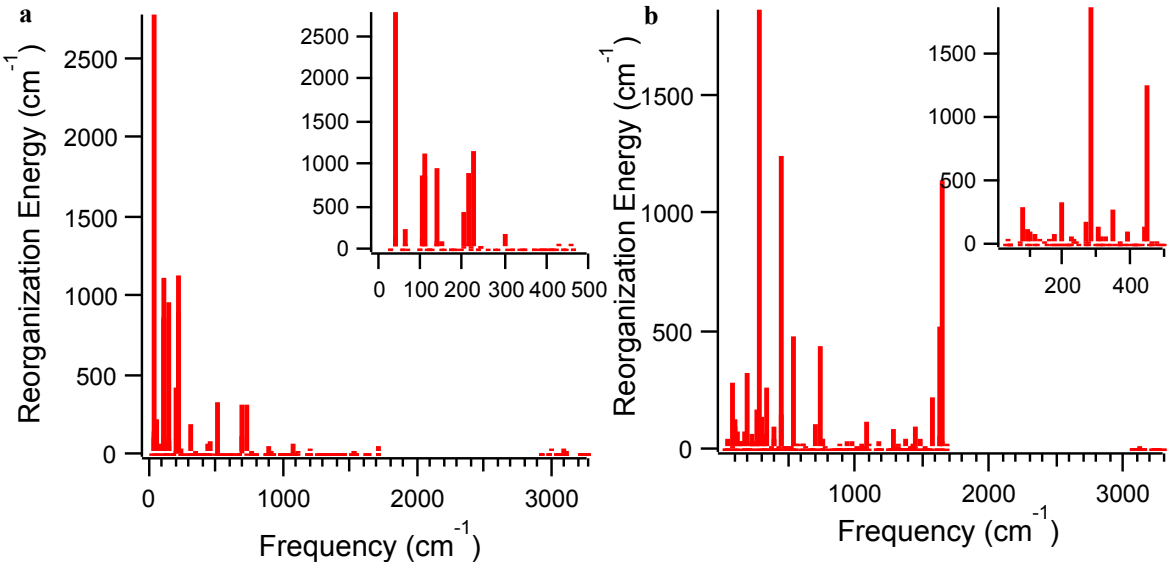

Figure 5.23. Decomposition of the total inner-sphere reorganization energy for the $^5T_2 \rightarrow {}^1A_1$ transition, as calculated from the Duschinsky method for a) $[Fe(L)]^{2+}$ and (b) $[FeCu_2(L)]^{4+}$. Reproduced from reference 20.

[xiv] See Chapter 2 of this dissertation for an explanation of the electrochemical approximation for $\Delta G°$ in LS Fe(II) polypyridyls.

straight-line, least motion geometric path[42] that accompanies an intersystem crossing event through linear interpolation and extrapolation, and has been used to describe nuclear reorganization during excited-state evolution in $Cr(acac)_3$.[43] From DFT geometry optimizations and frequency calculations on the $^1A_1$ and $^5T_2$ states of the two complexes conducted by Bryan Paulus,[20] a Duschinsky vector was constructed, which is the normal-mode representation of the Cartesian displacement vector between equilibrium geometries.[43] From these individual displacements (Figure 5.23), a total inner-sphere reorganization energy (λ_i) can be calculated. Bryan found that for $[Fe(L)]^{2+}$, $\lambda_i = 12100$ cm^{-1}, but for $[FeCu_2]^{4+}$, $\lambda_i = 9320$ cm^{-1}, suggesting that $\Delta Q_{LF/GS}$ is smaller in the trinuclear complex than in $[Fe(L)]^{2+}$. It should be noted that the values for λ_i calculated in this manner reflect the overall geometric distortions between the $^5T_2$ and $^1A_1$ states, not just those that are actually coupled to the ISC. In addition, these values ignore outer-sphere reorganization energy, which we know may be non-negligible for $[Fe(L)]^{2+}$. Nonetheless,

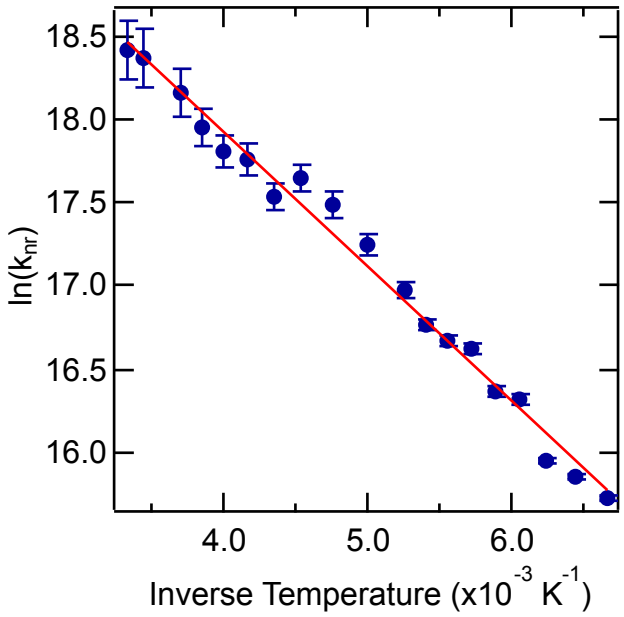

Figure 5.24. Arrhenius plot of the temperature dependence of the rate of nonradiative decay for the $^5T_2 \rightarrow {}^1A_1$ ground-state recovery of $[FeCu_2(L)](PF_6)_4$ in 9:1 methanol/ethanol, monitoring at $\lambda_{probe} = 580$ nm and $\lambda_{pump} = 610$ nm. The red line represents a fit to the Arrhenius model, yielding $E_a = 560 \pm 30$ cm^{-1} and $A = (1.52 \pm 0.4) \times 10^9$ s^{-1} (660 ps^{-1}).

these computational results, in addition to the VT-TA data on $[Fe(L)]^{2+}$ and $[FeCu_2(L)]^{4+}$, suggest that by rigidifying the macrocyclic cage ligand in $[Fe(L)]^{2+}$ through the coordination of two Cu(I) atoms, we may have impacted the nuclear coordinate defining GSR. These complexes would be excellent candidates to study with time-resolved x-ray techniques, such as EXAFS, to unequivocally determine which compound displays a higher degree of distortion in the $^5T_2$ state.

Finally, to access a wider range of temperatures for VT-TA with $[FeCu_2(L)]^{4+}$ and investigate the role of solute-solvent in GSR, the Arrhenius parameters for the $^5T_2 \rightarrow {}^1A_1$ were also collected in 9:1 methanol/ethanol (Figure 5.24). Unlike what was observed for $[Fe(L)]^{2+}$, the activation energy measured for GSR in the alcohol mixture is practically identical to that measured in acetonitrile, and the frequency factors measured in the two different solvent mixtures are within error of each other. The lack of solvent effects detected for $[FeCu_2(L)]^{4+}$ further increases the probability of an interaction occurring between the alcohol functional groups present in the 9:1 methanol/ethanol solvent mixture and uncoordinated imine caps in $[Fe(L)]^{2+}$.

5.3.11. MLCT excited-state deactivation in $[FeCu_2(L)]^{4+}$

The comparison between the GSR dynamics of $[Fe(L)]^{2+}$ and $[FeCu_2(L)]^{4+}$ have hinted at the possibility that we have affected the $^5T_2/{}^1A_1$ nuclear coordinate through synthetic modification, bringing up the question: will we also observe an impact of the rate of MLCT deactivation? Guided by spectroelectrochemistry on the three cage complexes (Figures 5.10 , 5.19, 5.20), Bryan C. Paulus collected and analyzed ultrafast time-resolved transient absorption spectroscopy on $[FeCu_2(L)]^{4+}$ in acetonitrile to measure the MLCT deactivation dynamics. Upon collecting full spectrum data following excitation into the Fe-based MLCT absorption (Figure 5.25), it became immediately apparent that the dynamics of the Cu-containing cage complex differed substantially from those of the Cu-free complex (Figure 5.11), and we can actually observe an excited-state

absorption red of 650 nm, which was virtually absent in $[Fe(L)]^{2+}$. The match between the data presented in Figure 5.25 and the predicted MLCT spectrum from spectroelectrochemistry (Figure 5.20) as well as the fact that they differ from the differential absorption data collected at longer timescales (Figure 5.21a) provided a strong indication of MLCT excited-state that persists longer than most LS Fe(II) polypyridyl complexes. Single wavelength kinetics[20,21] monitoring in the near-IR region revealed bi-phasic kinetics, with $\tau_1 = 440 \pm 50$ fs and $\tau_2 = 2.6 \pm 0.1$ ps. Most importantly, the 2.6 ps component is associated with the loss of the positive absorption feature in the near-IR, and therefore defines the decay of the ^{3}MLCT state. This 2.6 ps lifetime represents a >20-fold increase in the ^{3}MLCT excited-state lifetime compared to $[Fe(L)]^{2+}$, and is the longest-lived MLCT excited state to-date for a LS Fe(II) polypyridyl complex.

The origin of the 440 fs component is still unclear at this time, however based on previous work[44,45] on the ^{3}MLCT decay dynamics on $[Ru(bpy)_3]^{2+}$ as well as variable solvent studies[20,21] conducted on $[FeCu_2(L)]^{4+}$, both as the hexafluorophosphate and $^-BAr^F$ salt, seem to indicate that

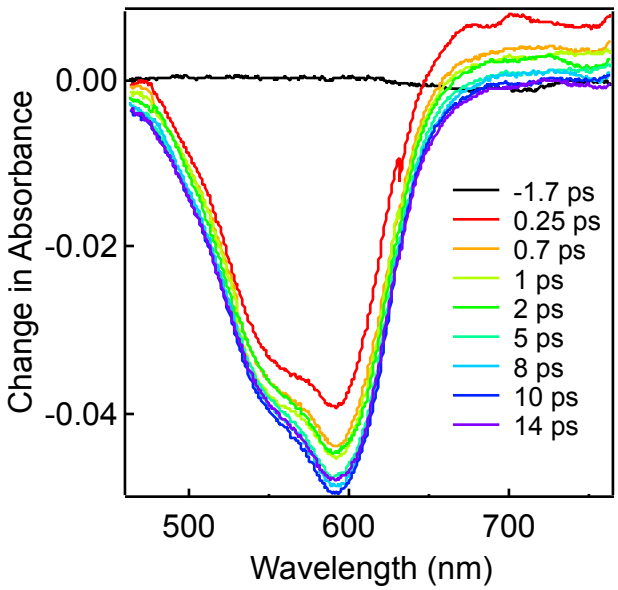

Figure 5.25. Full spectrum ultrafast time-resolved absorption spectrum of $[FeCu_2(L)](PF_6)_4$ in CH_3CN following excitation at 600 nm.

this time constant is due to librational motion of the solvent, which is induced by the redistribution of charge upon population of the MLCT excited state. To confirm that these dynamics associated with the 2.6 ps component are indeed due to the prolonged population of a Fe-based ^{3}MLCT excited state, and that the Cu^I atoms are not undergoing any change in oxidation state, ultrafast kinetics were collected while still exciting into the mid-visible absorption feature (600 nm) but probing at 396 nm.[20,21]This near-UV region is dominated by a Cu-based MLCT feature in the ground-state absorption spectrum of $[FeCu_2(L)]^{4+}$ (Figure 5.16) and is where the spectroelectrochemistry of the copper-containing trinuclear cage (Figure 5.19) indicates there should be a significant GSB upon oxidation of Cu^I. These studies revealed a small-amplitude bleach that decayed with a time constant of 2.6 ps, and the bleach did not exhibit a large-amplitude decay to even more negative values of ΔA. Obtaining the exact same time constant as when probing at 700 nm and the fact that large amplitude changes in ΔA were not observed indicate that Cu^I is not changing oxidation states upon photoexcitation of Fe^{II}.

These results all point to a longer-lived Fe-based MLCT excited state, which was achieved through synthetic modification of a closely-related compound. Because the ground-state geometries of the iron(II) center in $[Fe(L)]^{2+}$ and $[FeCu_2(L)]^{4+}$ are practically identical, and the MLCT energies are very similar in the two compounds, we know that the changes in the excited-state dynamics must be mainly attributable to changes in the lowest-energy excited state, the $^5T_2$. The exact nature of this change, however, is still unclear. Studies on the GSR of both compounds seem to indicate that both the $^5T_2/^1A_1$ energy gaps and reorganization energies are affected by the coordination of Cu^I atoms. This implies that the potential energy surface corresponding to the $^5T_2$ excited state in $[FeCu_2(L)]^{4+}$ is displaced both vertically and horizontally relative to that of $[Fe(L)]^{2+}$, which then of course would impact the dynamics of the $^3MLCT \rightarrow {}^5T_2$ conversion.

For more insight into the relative contributions of the energetic and nuclear perturbations to the $^5T_2$ excited state in the exciting dynamics of $[FeCu_2(L)]^{4+}$, we can consider cases in which very strong-field ligands have been employed to significantly destabilize the ligand field excited states of their respective LS Fe(II) complexes. What makes these complexes notable is that they deviate from the $^3MLCT \rightarrow {}^5T_2 \rightarrow {}^1A_1$ excited-state cascade[xv] that has been established for prototypical LS complexes, such as $[Fe(bpy)_3]^{2+}$, in one of two ways: 1) a ^3T ligand field state is the lowest-energy excited state (indicating that the ligand field strength has passed the $^3T/^5T_2$ crossing point on the d^6 Tanabe-Sugano diagram), resulting in a $^3MLCT \rightarrow {}^3T \rightarrow {}^1A_1$ photophysical pathway or 2) the ^{3}MLCT becomes the lowest energy excited-state, and GSR occurs from this state. For complexes belonging to the first class, the ^{3}MLCT excited state lifetimes range 0.8-9 ps and GSR from the ^3T ligand field state occurs in less than 20 ps.[46–48] For the other class of complexes, the reported ^{3}MLCT lifetimes (and therefore time constants for GSR) are between 0.02-2 ns.[49–52] However, in the unique example of $[FeCu_2(L)]^{4+}$, all experiments point towards the traditional photophysical cascade, but with the caveat of an unusually long-lived ^{3}MLCT excited state. Since this is unheard of in the realm of LS complexes with very strong-field ligands, we propose that the main mechanism behind prolonging the ^{3}MLCT excited state lifetime in $[FeCu_2(L)]^{4+}$ is actually the disruption of the $^3MLCT \rightarrow {}^5T_2$ nuclear coordinate, achieved by hindering the geometric changes coupled to the ISC event.

[xv] These are the excited-states that can be confirmed with transient absorption. Fluorescence up-conversion can capture the $^1MLCT \rightarrow {}^3$MLCT ISC event and femtosecond time-resolved x-ray fluorescence spectroscopy has shown evidence for a ^3T intermediate prior to $^5T_2$ population in $[Fe(bpy)_3]^{2+}$.

5.3.12. Attempts to synthesize other macrocyclic coordination compounds

Ideally, we would study the photophysics of an Fe-containing analog to $[FeCu_2(L)]^{4+}$ to test our hypothesis of the origin of the extended ^{3}MLCT excited-state lifetime and change in LF/GS barrier height. However, as detailed previously, Cu(I) seemed to be the "goldilocks" of cations for tetrahedral coordination into the tren caps of L. The most successful attempt towards the isolation of another iron-containing trinuclear cage complex was when $AgPF_6$ was added in the place of $[Cu(MeCN)_4](PF_6)_2$, followed by the addition of $Fe(BF_4)_2 \bullet 2H_2O$. Recrystallization via ether diffusion into acetonitrile solutions of the purple product yielded x-ray quality crystals, the structure of which is presented in Figure 5.26a and shows that the desired product, $[FeAg_2(L)]^{4+}$, was successfully synthesized, however $[FeAgH(L)]^{4+}$ was also formed and co-crystallized with the trinuclear complex. All further attempts to isolate the fully trinuclear complex $[FeAg_2(L)]^{4+}$ were unsuccessful, and the samples of the crude silver-contain products were photo-unstable, precluding any additional efforts. The ruthenium analogs to $[Fe(L)]^{2+}$ and $[FeCu_2(L)]^{4+}$ were also pursued, as they could provide an avenue to investigate the relative displacements of the ^{3}MLCT

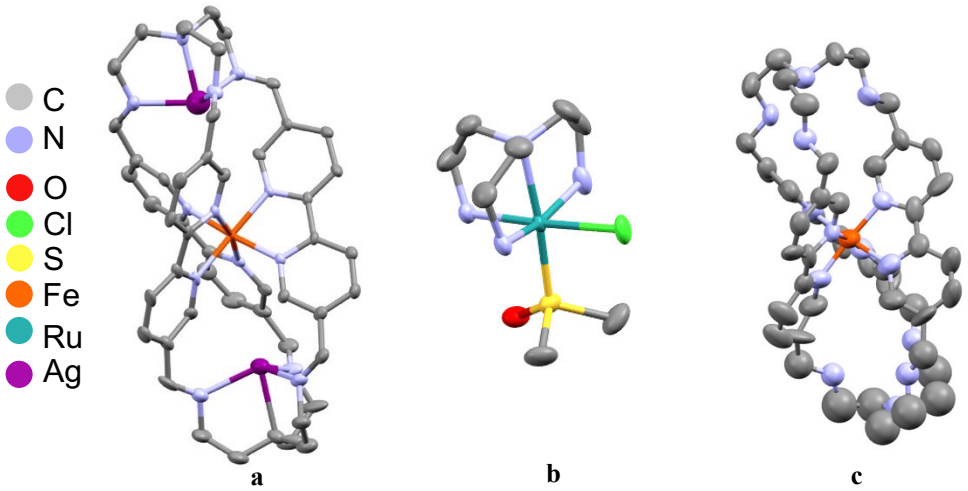

Figure 5.26. X-ray crystal structures of (a) $[FeAg_{1.5}H_{0.5}(L)]^{4+}$, (b) $[Ru(tren)(DMSO)Cl]^+$ (CCDC accession number: 1879066), and (c) $[Fe(LH)](PF_6)_2$. Hydrogen atoms, solvent molecules, and counteranions have been removed for clarity.

excited states via steady-state emission.[53] These attempts resulted either in no evidence of Ru(II) coordination to the tris-bpy core of the ligand or degradation of ligand (Figure 5.26b).

It could be worthwhile to investigate the effects of modulating the steric rigidity of the macrocyclic cage ligand through other means besides coordination of cations in the tren cap. One option for decreasing steric rigidity is to reduce the imines that compose the tren caps to secondary amines. Lehn reported that the imine reduction of L was successful with Pd/C and hydrogen gas in MeOH,[14] however no conversion of the imines to secondary amines under these conditions was observable in my hands. Instead, using conditions based off of those that Novotna *et al* developed for the reduction of imines in benzyl-based macrocycles,[54] the fully reduced version of L, "LH", was successfully synthesized using $NaBH_4$ in DCM/MeOH. This reaction was highly variable and difficult to optimize: it either yielded the desired product alone or in the presence of several impurities that could be separated in poor yields (~1 %) on a silica gel column. $[Fe(LH)]^{2+}$ was synthesized and the crystal structure indicated high levels of disorder in one of the tren caps (Figure

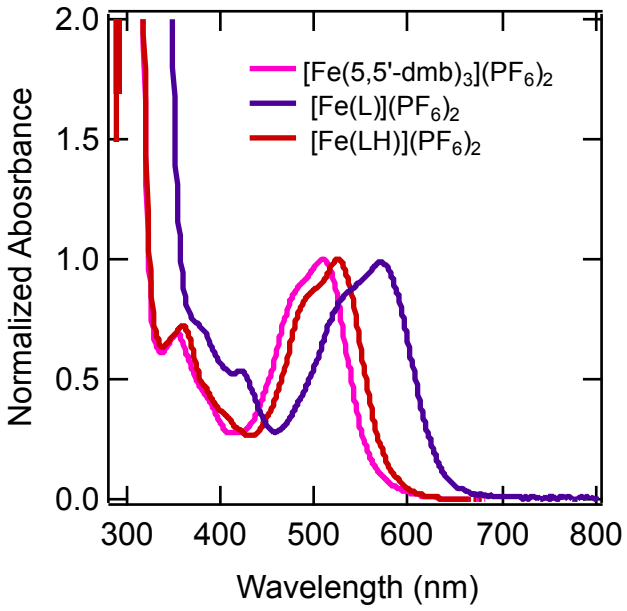

Figure 5.27. Normalized ground-state absorption spectra of $[Fe(5,5'\text{-dmb})_3](PF_6)_2$, $[Fe(L)](PF_6)_2$, and $[Fe(LH)](PF_6)_2$ in acetone at room temperature.

5.26c), most likely due to the increased flexibility of alkyl arms of tren. Due to the very small quantities of LH that were obtained, the photophysics of $[Fe(LH)]^{2+}$ have only just begun to be investigated, and the attempted synthesis of $[FeCu_2(L)]^{4+}$ was not optimized. In spite of the preliminary nature of work on complexes employing LH, it is still interesting to note that the absorption spectrum of the crude $[Fe(LH)]^{2+}$ complex much more closely resembles that of $[Fe(5,5'\text{-dmb})]^{2+}$ than $[Fe(L)]^{2+}$ (Figure 5.27), highlighting the significant impact of the imine moieties on the energetics of the MLCT manifold, in contrast to the long-held assumption that substitutions to the 5,5'-positions on bpy should have little to no impact on the energetics of the ligand-based π-system.

5.3.13. Possible synthetic modifications to the macrocyclic cage ligand L

Replacing the *tris*-bpy core of L with the more inflexible bidentate ligand 1,10-phenanthroline (phen) and subsequently comparing the excited-state properties of its Fe(II) and $[FeCu_2(X)]^{4+}$ complexes to their analogs reported in this chapter is another way in which the effects of increased rigidity on the excited-state dynamics of Fe(II) polypyridyls may be investigated. There are no published reports of a dual-tren capped phen-based macrocyclic. For that matter, of the synthesis of 3,8-diformyl-phen, which could form a phen-analog to L upon condensation with tris(2-aminoethyl)amine, has also not been reported. This diformyl building block should be synthetically accessible either from the direct oxidation of 3,8-dimethyl-phen with selenium dioxide, as is reported for the synthesis of 2,9- and 4,7-diformyl-phen,[55,56] or by following the same route used in this dissertation for 5,5'-diformyl-bpy, beginning with the Jones oxidation of a

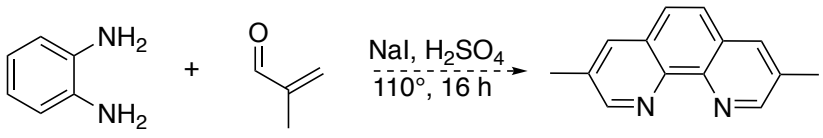

Figure 5.28. Synthesis of 3,8-dimethyl-1,10-phenanthroline.

dimethyl-phen starting material. Unlike 5,5'-dmb, 3,8-dimethyl-phen is not commercially available, and the only published procedure reports a <16% yield for its synthesis (Figure 5.28).[57]

In the opposite vein of a phen-based macrocycle, the flexibility of L could be increased by introducing an additional carbon to the bpy-imine linkage. This could be achieved by condensing 2,2'-([2,2'-bipyridine]-5,5'-diyl)diacetaldehyde, the synthesis of which is proposed in Figure 5.29 from the corresponding diol,[58] with tren. With these extended alkyl caps, the chances of coordinating cations with larger radii than Cu(I) would be improved, perhaps enabling the synthesis of other trinuclear complexes besides $[FeCu_2(X)]^{4+}$ and therefore extending the series of complexes with varying degrees of rigidity.

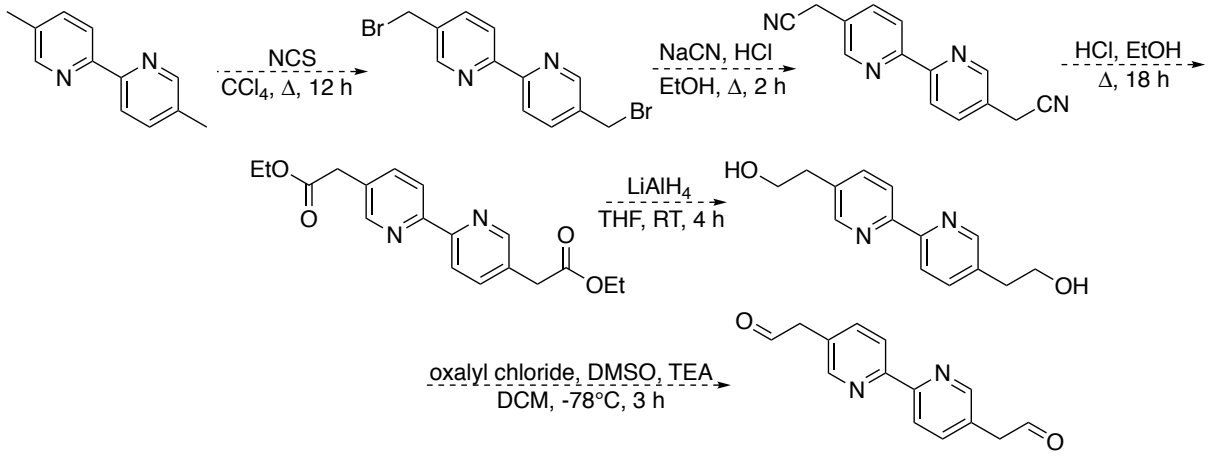

Figure 5.29. Proposed route to the diformyl precursor that would enable the synthesis of an extended bpy-imine linked cage ligand via a condensation with tris(2-aminoethyl)amine.

5.4. Concluding Remarks

In this chapter, we set out to disrupt the geometric distortions coupled to the MLCT → $^5T_2$ decay by employing a macrocyclic cage ligand. Following the synthesis of $[Fe(L)]^{2+}$, the Arrhenius parameters associated with the $^5T_2 \rightarrow {}^1A_1$ process were found using variable-temperature transient absorption spectroscopy. The high activation energy, as well as the large reorganization energy approximated from experimentally-derived parameters, indicated that this ligand may have impacted the GSR nuclear coordinate; however, the inability to precisely determine ΔG°, for this

complex and other LS Fe(II) complexes, has precluded a definitive conclusion. Ultrafast transient absorption spectroscopy was able to show that the MLCT → $^5T_2$ dynamics of $[Fe(L)]^{2+}$ were not significantly different than most other LS Fe(II) polypyridyls. However, these measurements also yielded vibronic coherences associated with the decay of the MLCT excited state. Visualization of the vibrational modes that give rise to these coherent features in ultrafast transient absorption kinetic traces with DFT frequency calculations showed that during the loss of the MLCT excited state Fe-N bond stretching and torsional motions were active. These vibrational modes were coupled to deformations of the uncoordinated peripheries of the ligand.

This observation prompted us to disrupt these motions through the coordination of a cation to the imine caps tethering together the bpy moieties of the ligand. The trinuclear complex $[FeCu_2(L)]^{4+}$ was successfully synthesized, and then a combination of experimental and theoretical analyses of the $^5T_2 \rightarrow {}^1A_1$ conversion indicated that in comparison to $[Fe(L)]^{2+}$, the relative nuclear displacements between the $^1A_1$ and $^5T_2$ states were affected by this synthetic modification. Most importantly, the MLCT excited state lifetime of $[FeCu_2(L)]^{4+}$ was found to be 2.6 ps, a 20× increase compared to $[Fe(L)]^{2+}$ and the longest reported MLCT lifetime for a LS Fe(II) polypyridyl complex. An investigation of the photophysics of $[Fe(L)]^{2+}$ and $[FeCu_2(L)]^{4+}$ with time-resolved x-ray absorption techniques would help elucidate the exact mechanism of prolongation of the MLCT excited state lifetime, as well as the role of solute-solvent interactions during excited state evolution. Even so, these highly collaborative results highlight not only the promise of utilizing nuclear coordinate information to inspire synthetic design to control excited-state dynamics, but also the possibility of obtaining this nuclear coordinate information from vibronic coherences observed in ultrafast transient absorption spectroscopy.

APPENDIX

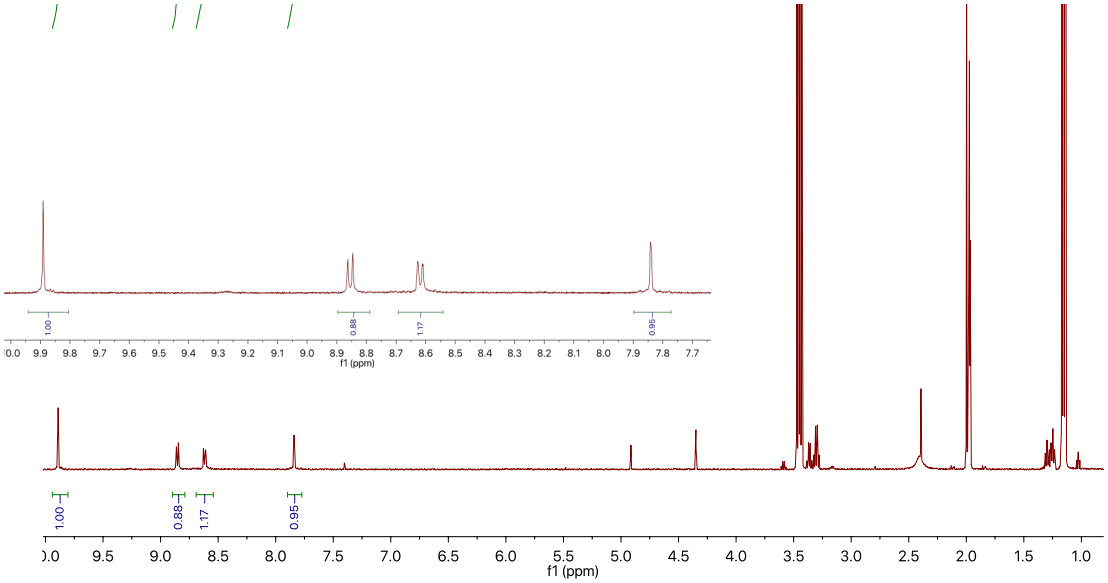

Figure 5.30. ^{1}H NMR of $[Fe(dfb)_3](PF_6)_2$ in CD_3CN. Inset shows an expansion of the aromatic region.

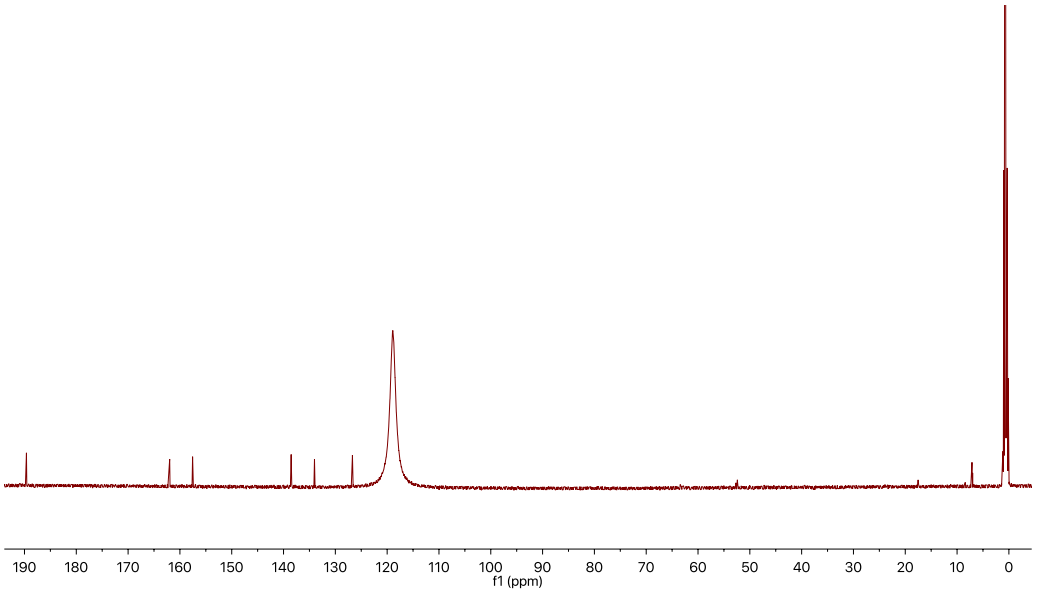

Figure 5.31. ^{13}C NMR of $[Fe(dfb)_3](PF_6)_2$ in CD_3CN.

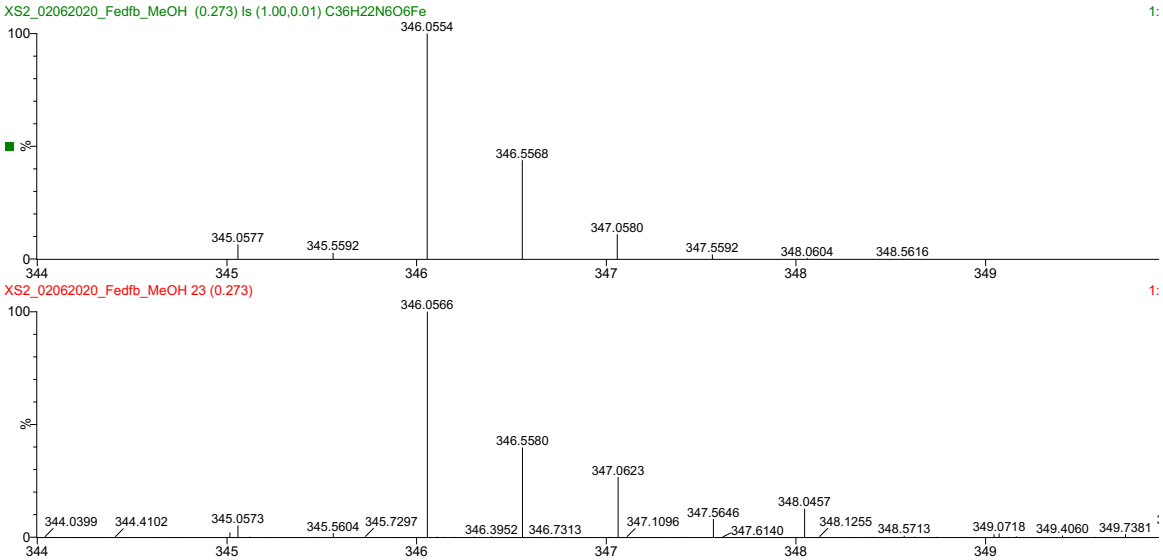

Figure 5.32. ESI-MS of $[Fe(dfb)_3](PF_6)_2$. Top: calculated isotope pattern for $[M\text{-}2(PF_6)]^{2+}$ ($C_{36}H_{24}N_6O_6Fe$). Bottom: experimental result.

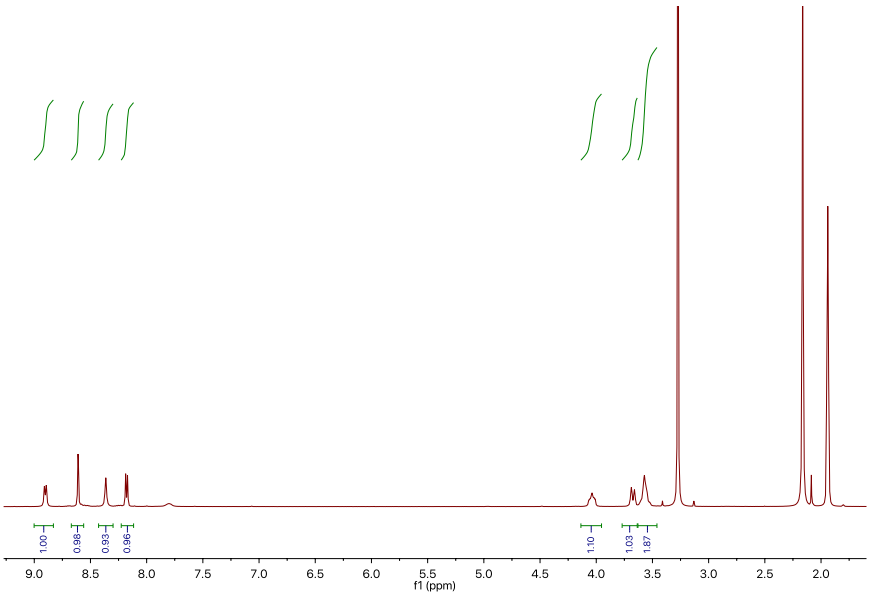

Figure 5.33. ^1H NMR of $[Fe(L)](PF_6)_2$ in CD_3CN.

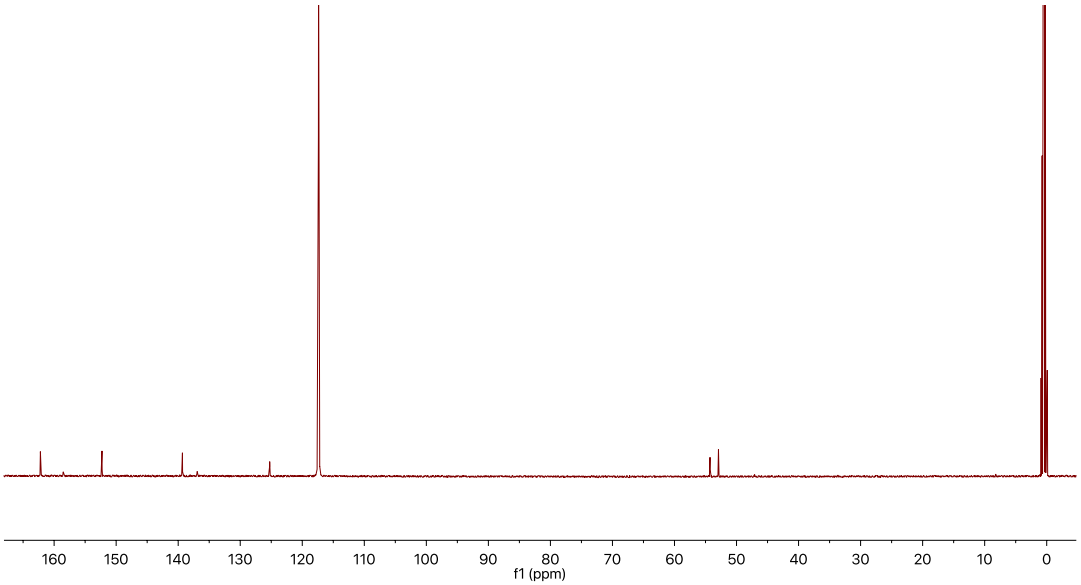

Figure 5.34. ^{13}C NMR of $[Fe(L)](PF_6)_2$ in CD_3CN.

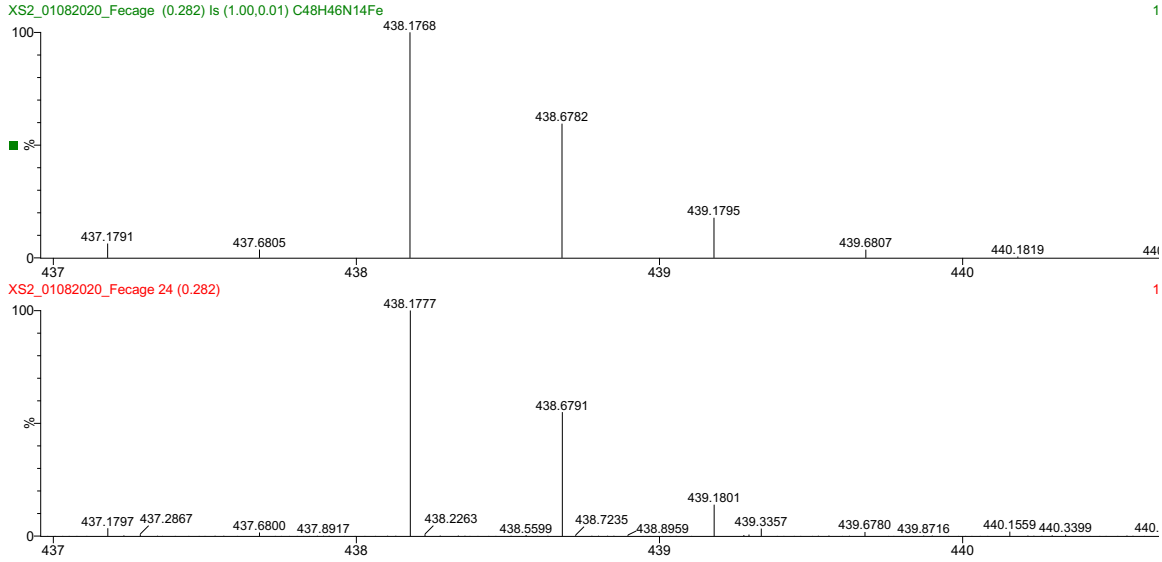

Figure 5.35. ESI-MS of $[Fe(L)](PF_6)_2$. Top: calculated isotope pattern for $[M\text{-}2(PF_6)]^{2+}$ ($C_{48}H_{48}N_{14}Fe$). Bottom: experimental result.

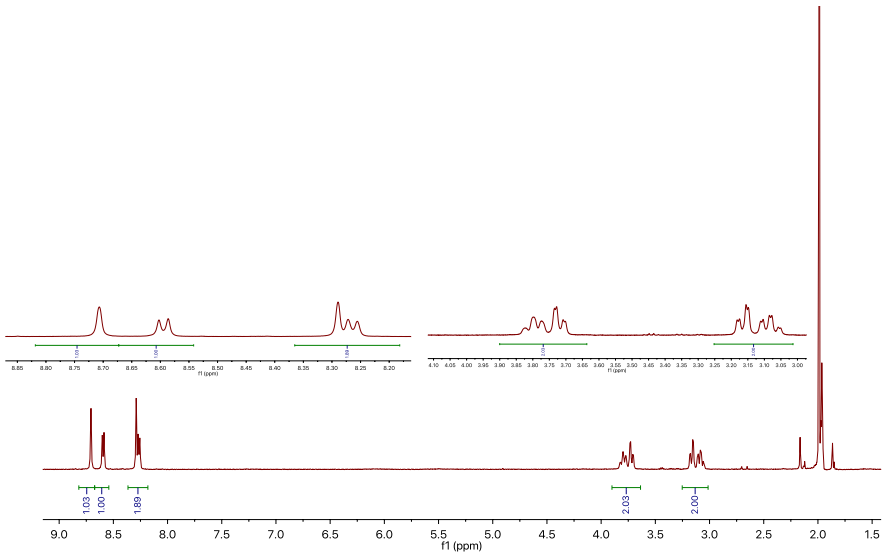

Figure 5.36. ^{1}H NMR of $[FeCu_2(L)](PF_6)_4$ in CD_3CN.

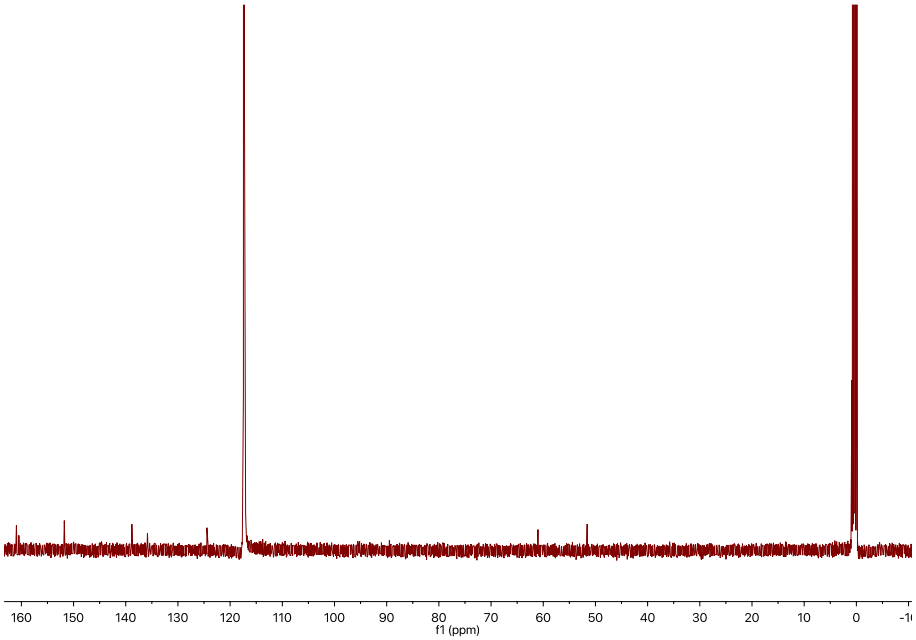

Figure 5.37. ^{13}C NMR of $[FeCu_2(L)](PF_6)_4$ in CD_3CN.

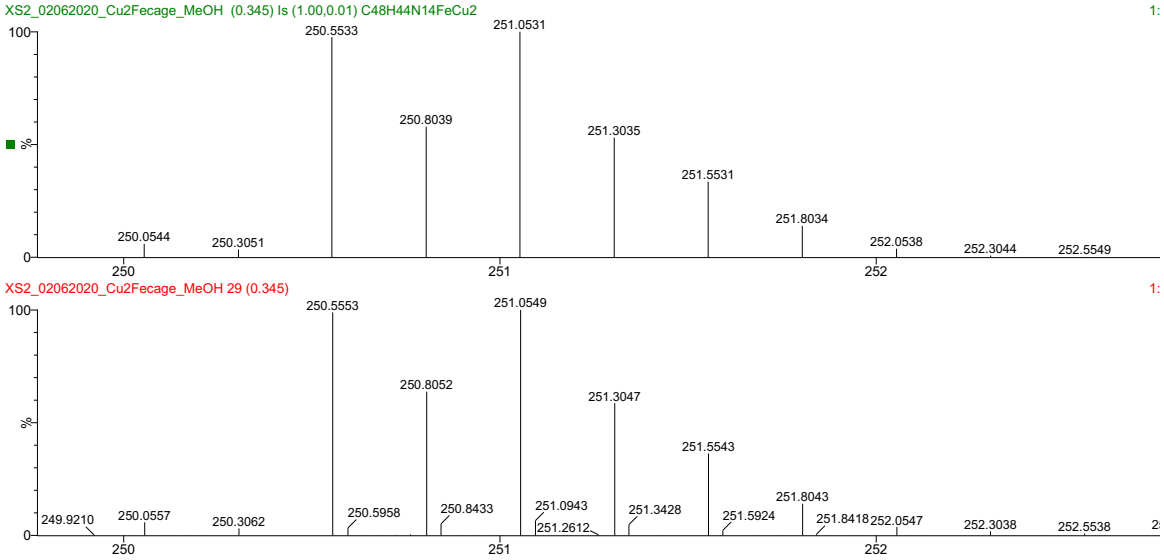

Figure 5.38. ESI-MS of $[FeCu_2(L)](PF_6)_2$. Top: calculated isotope pattern of $[M\text{-}4(PF_6)]^{4+}$ ($C_{48}H_{48}N_{14}FeCu_2$). Bottom: experimental result.

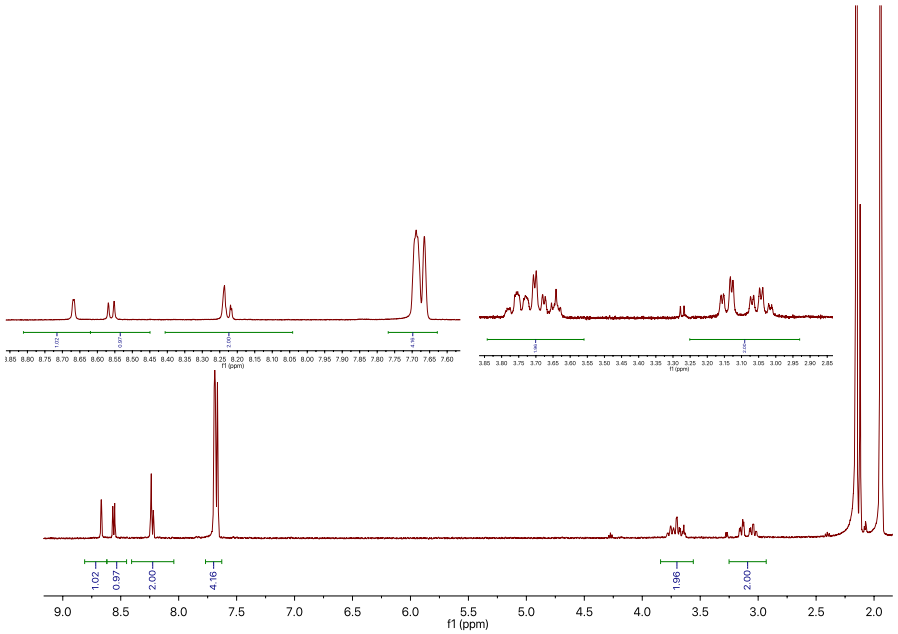

Figure 5.39. ^1H NMR of $[FeCu_2(L)](BAr^F)_4$ in CD_3CN.

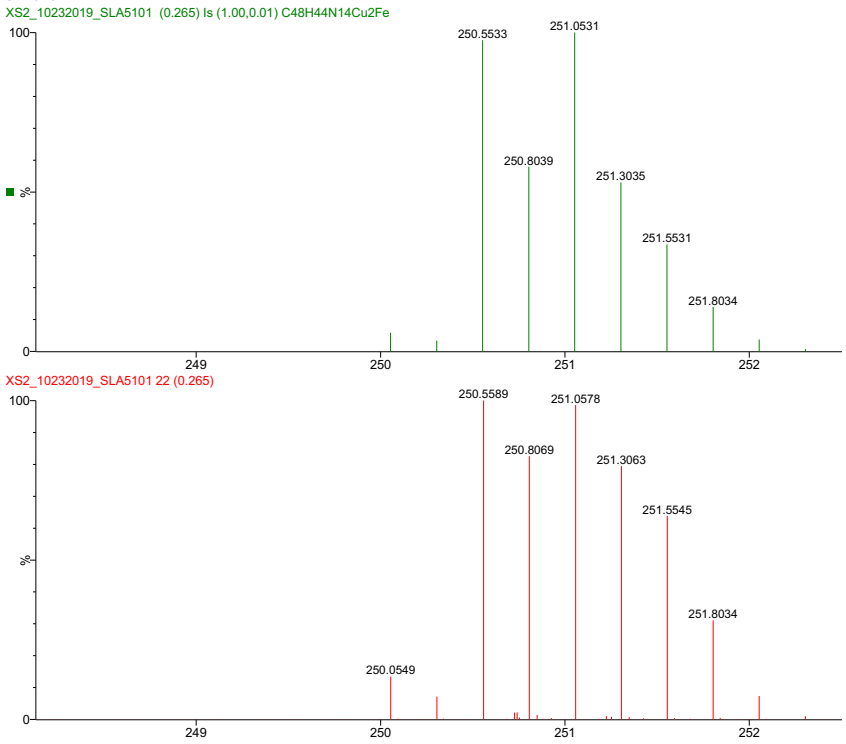

Figure 5.40. ESI-MS of $[FeCu_2(L)](BAr^F)_4$. Top: calculated isotope pattern for $[M\text{-}4(BAr^F)]^{4+}$ ($C_{48}H_{48}N_{14}FeCu_2$). Bottom: experimental result.

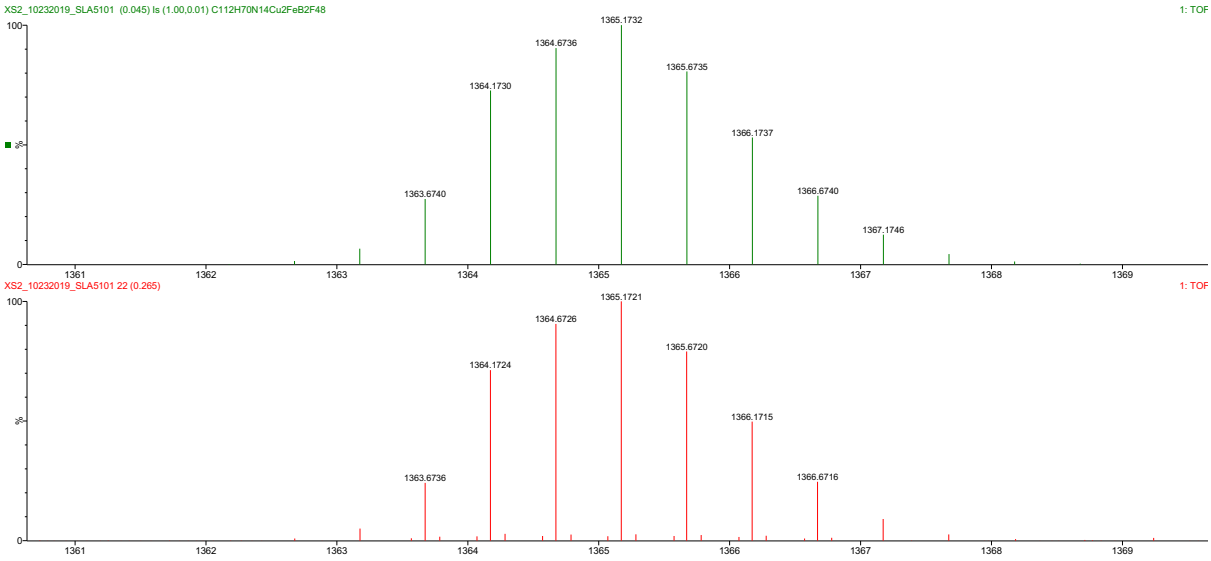

Figure 5.41. ESI-MS of $[FeCu_2(L)](BAr^F)_4$. Top: calculated isotope pattern for $[M\text{-}2(BAr^F)]^{2+}$ ($C_{112}H_{72}N_{14}FeCu_2B_2F_{48}$). Bottom: experimental result.

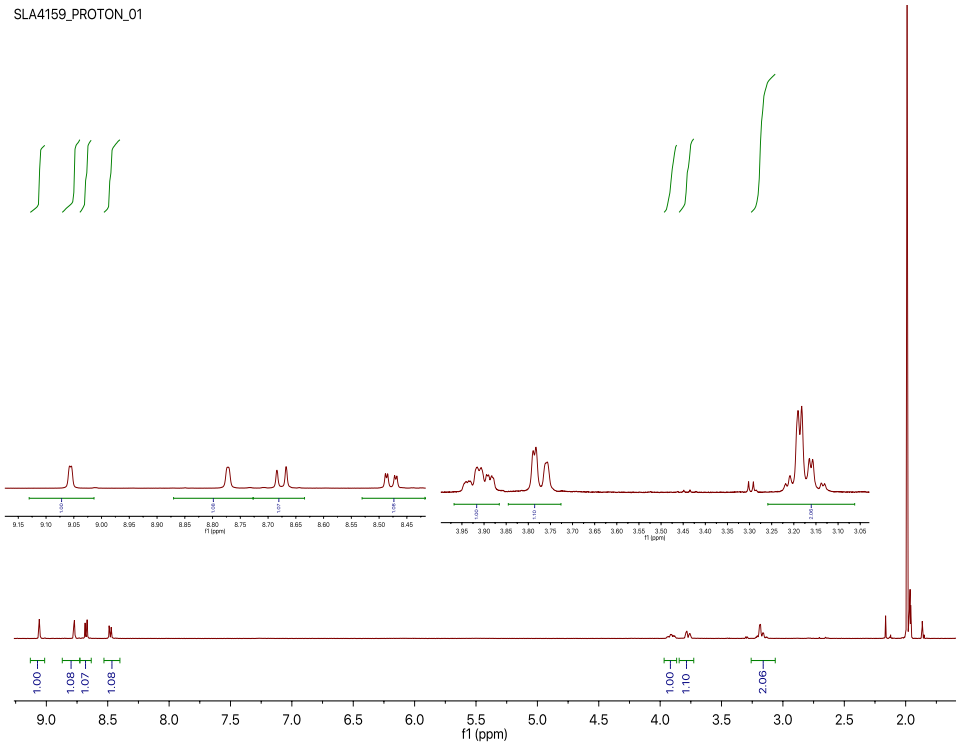

Figure 5.42 ^{1}H NMR of $[ZnCu_2(L)](PF_6)_4$ in CD_3CN.

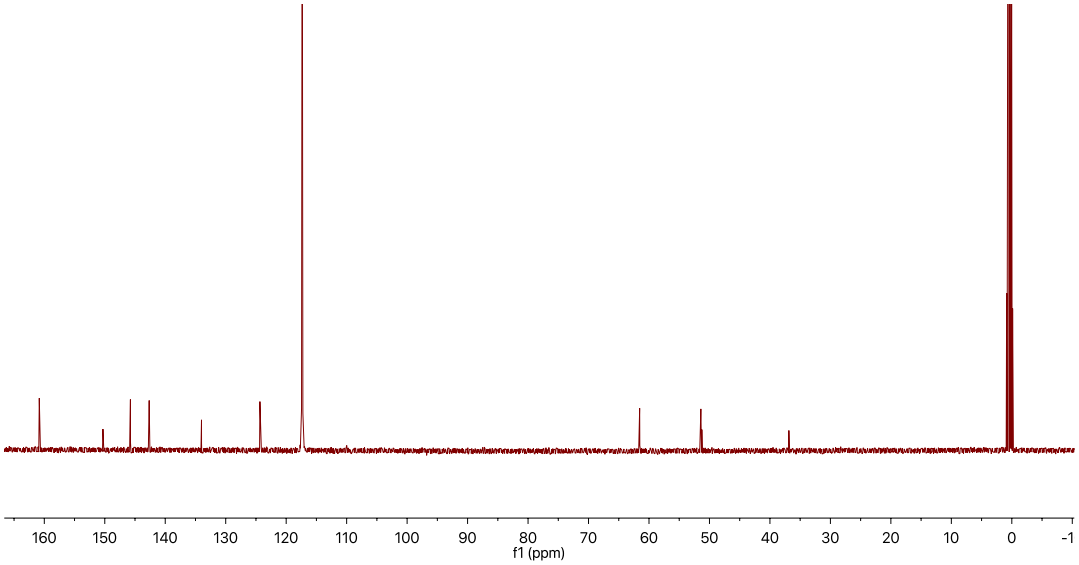

Figure 5.43. ^{13}C NMR of $[Cu_2Zn(L)](PF_6)_4$ in CD_3CN.

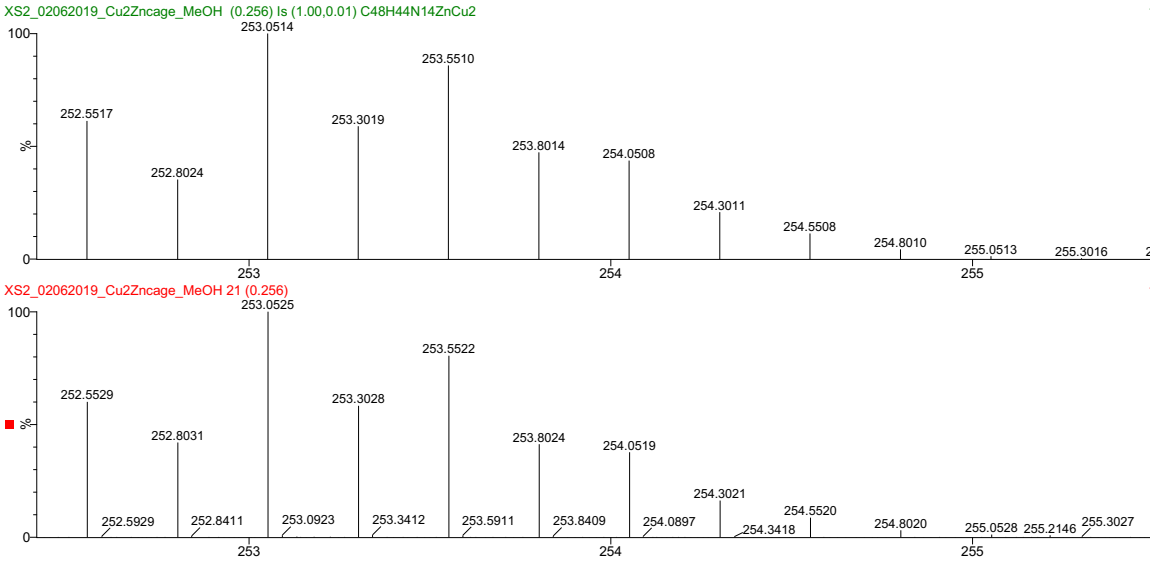

Figure 5.44. ESI-MS of $[ZnCu_2(L)](PF_6)_4$. Top: calculated isotope pattern for $[M\text{-}4(PF_6)]^{4+}$ ($C_{48}H_{48}N_{14}ZnCu_2$). Bottom: experimental result.

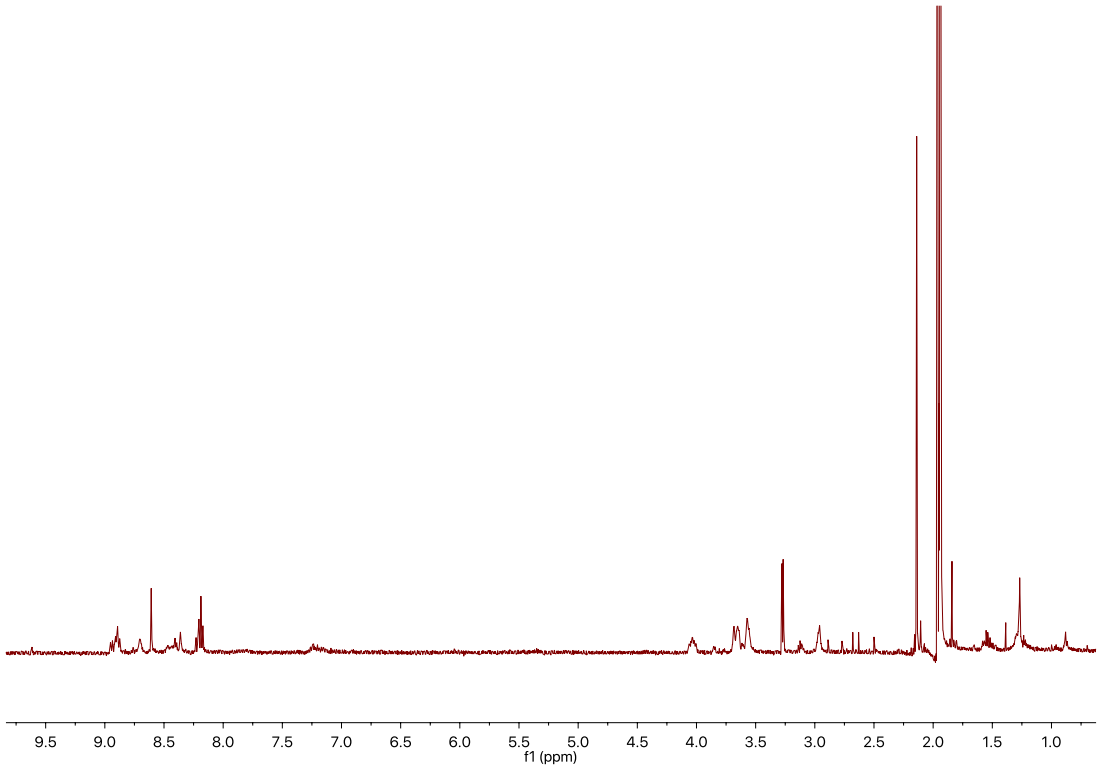

Figure 5.45. ^1H NMR in CD_3CN of the crude product from the reaction attempting to synthesize $[FeAg_2(L)](PF_6)_4$.

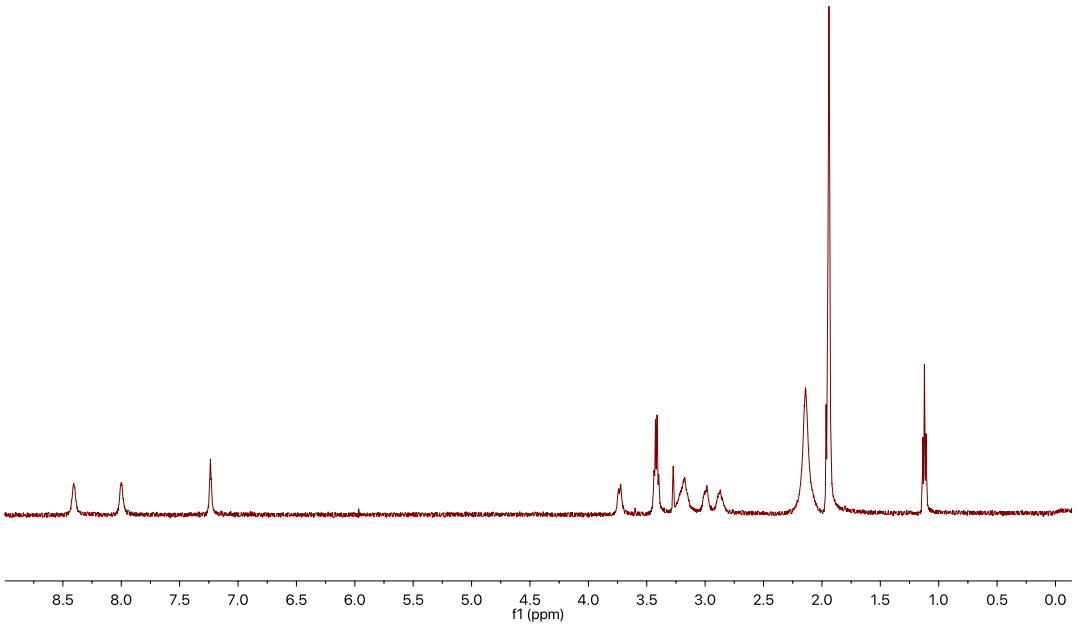

Figure 5.46. ^{1}H NMR of $[Fe(LH)](PF_6)_2$ in CD_3CN.

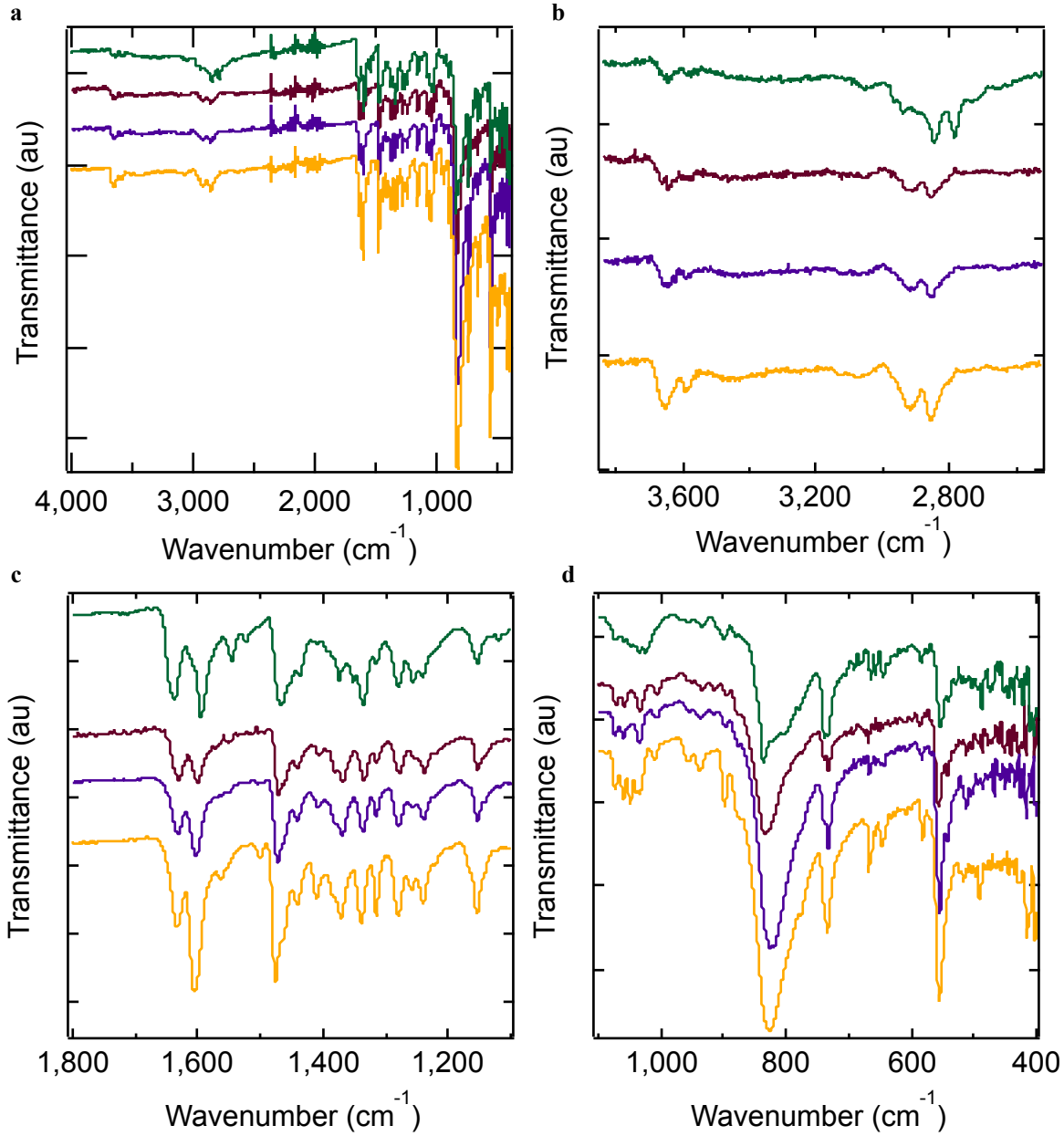

Figure 5.47. IR spectra of the cage ligand (green), $[Fe(L)](PF_6)_2$ (purple), $[FeCu_2(L)](PF_6)_4$ (maroon), and $[ZnCu_2(L)](PF_6)_4$ (yellow) (a) from 4000-400 cm^{-1}, (b) 3800-2500 cm^{-1}, (c) 1800-1100 cm^{-1}, (d) 1100-400 cm^{-1}.

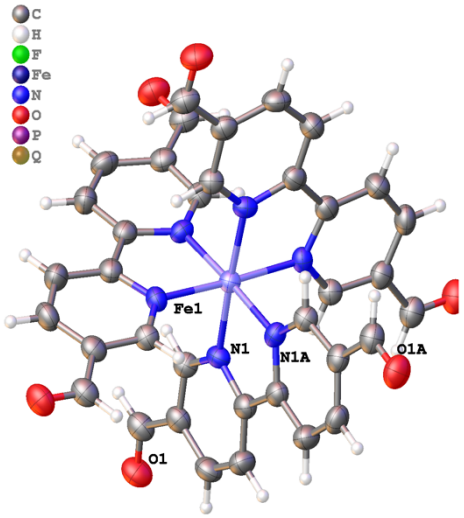

Figure 5.48. Thermal ellipsoid drawing of x-ray crystal structure of $[Fe(dfb)_3](PF_6)_2$ showing atom labels.

Table 5.5. Bond lengths from x-ray crystal structure of $[Fe(dfb)_3](PF_6)_2$.

Atom	Atom	Length/Å
Fe1	N1	1.961(4)
Fe1	N1[1]	1.961(4)
Fe1	N1[2]	1.961(4)
Fe1	N1[3]	1.961(4)
Fe1	N1[4]	1.961(4)
Fe1	N1[5]	1.961(4)
O1	C6	1.197(7)
N1	C1	1.364(6)
N1	C5	1.339(6)
C1	C1[2]	1.473(10)
C1	C2	1.381(7)
C2	C3	1.388(8)
C3	C4	1.402(8)
C4	C5	1.372(7)
C4	C6	1.472(8)
P1	F1[6]	1.601(6)
P1	F1[7]	1.601(6)
P1	F1	1.601(6)
P1	F2[6]	1.562(6)
P1	F2[7]	1.562(6)
P1	F2	1.562(6)

[1]-1/3+y,1/3+x,5/6-z; [2]2/3-x,1/3-x+y,5/6-z; [3]1-y,1+x-y,+z; [4]+y-x,1-x,+z; [5]2/3-y+x,4/3-y,5/6-z; [6]2-y,1+x-y,+z; [7]1+y-x,2-x,+z

Table 5.6. Bond angles from x-ray crystal structure of $[Fe(dfb)_3](PF_6)_2$.

Atom	Atom	Atom	Angle/°
N1	Fe1	N1[1]	96.08(14)
N1[1]	Fe1	N1[2]	81.9(2)
N1[1]	Fe1	N1[3]	86.0(2)
N1[2]	Fe1	N1[3]	96.08(14)
N1[4]	Fe1	N1[2]	86.0(2)
N1	Fe1	N1[3]	81.9(2)
N1	Fe1	N1[4]	96.08(14)
N1[4]	Fe1	N1[3]	177.3(3)
N1	Fe1	N1[5]	86.0(2)
N1[4]	Fe1	N1[5]	81.9(2)
N1[1]	Fe1	N1[4]	96.08(14)
N1[2]	Fe1	N1[5]	96.08(14)
N1[3]	Fe1	N1[5]	96.09(14)
N1	Fe1	N1[2]	177.3(3)
N1[1]	Fe1	N1[5]	177.3(3)
C1	N1	Fe1	115.3(3)
C5	N1	Fe1	126.8(3)
C5	N1	C1	117.8(4)
N1	C1	C1[3]	113.7(3)
N1	C1	C2	122.5(5)
C2	C1	C1[3]	123.8(3)
C1	C2	C3	118.4(5)
C2	C3	C4	119.5(5)
C3	C4	C6	120.1(5)
C5	C4	C3	118.1(5)
C5	C4	C6	121.9(5)
N1	C5	C4	123.6(5)
O1	C6	C4	124.0(6)
F1[6]	P1	F1	91.6(4)
F1[7]	P1	F1[6]	91.6(4)
F1[7]	P1	F1	91.6(4)
F2	P1	F1[7]	88.4(3)
F2[6]	P1	F1[7]	179.6(4)
F2[7]	P1	F1[6]	88.4(4)
F2[7]	P1	F1	179.6(4)
F2[6]	P1	F1[6]	88.9(4)
F2	P1	F1[6]	179.5(5)
F2	P1	F1	88.9(4)
F2[7]	P1	F1[7]	88.9(4)
F2[6]	P1	F1	88.4(4)
F2[6]	P1	F2	91.1(4)
F2[7]	P1	F2[6]	91.1(4)
F2[7]	P1	F2	91.1(4)

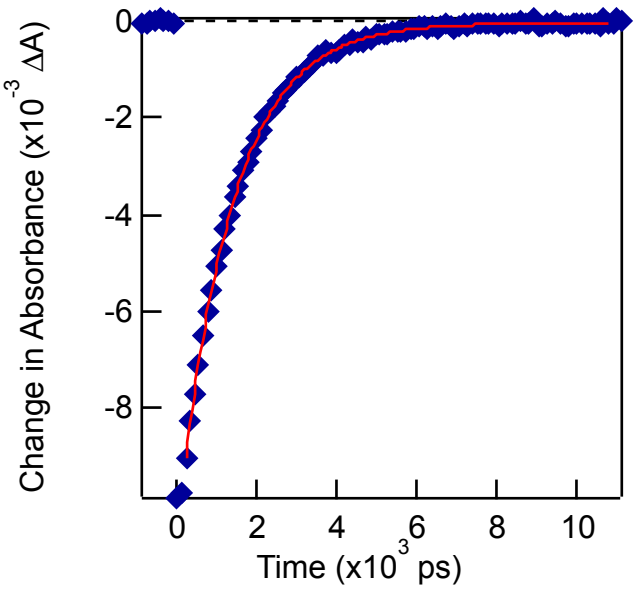

Figure 5.49. Ground-state recovery dynamics of $[Fe(dfb)_3](PF_6)_2$ in acetonitrile at room temperature following excitation at λ_{pump} = 530 nm and monitored at λ_{probe} = 600 nm. The blue line represents a fit to a single exponential function, yielding $\tau = 1.34 \pm 0.05$ ns. Data were collected by Hayden Biessel.

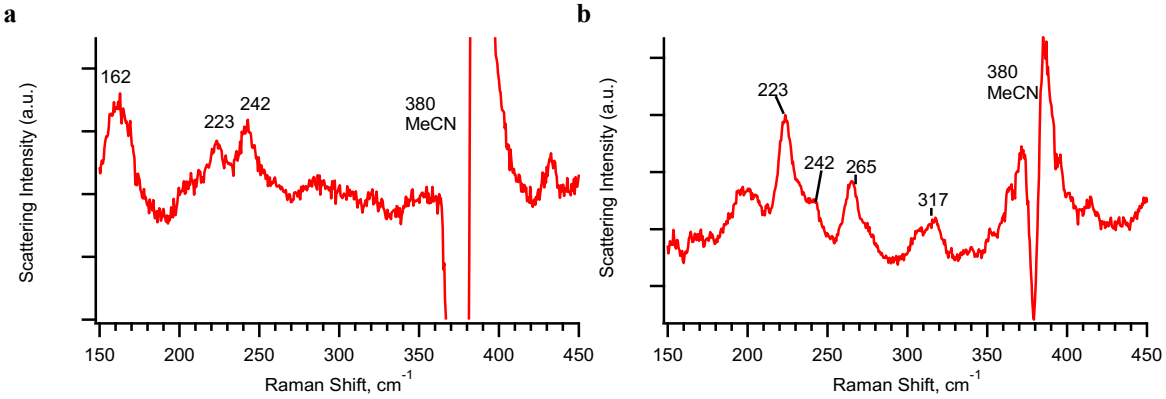

Figure 5.50. Resonance Raman spectra of (a) $[Fe(L)](PF_6)_2$ (**1**) and (b) $[FeCu_2(L)](PF_6)_2$ in acetonitrile solution with 488 nm excitation source collected in a spinning cell. The artifact around 380 nm is due to residual scattering from a CCN bending mode of the solvent. The data shown have had the solvent background subtracted and a 5th order polynomial baseline correction. Data were collected in the lab of Professor Denis Proshlyakov with the assistance of Allison Stettler. Bryan Paulus applied the baseline correction.

Table 5.7. Bond lengths in Å for $[FeAg(L)](BF_4)_{1.5}(PF_6)_{2.5}$.

Atom	Atom	Length/Å
Ag1	N3	2.232(6)
Ag1	N7	2.273(6)
Ag1	N11	2.256(6)
Ag1	N13	2.445(6)
Ag1B	N4	2.259(5)
Ag1B	N8	2.180(5)
Ag1B	N12	2.231(6)
Ag1B	N14	2.273(5)
Fe1	N1	1.980(4)
Fe1	N2	1.974(5)
Fe1	N5	1.983(5)
Fe1	N6	1.994(4)
Fe1	N9	1.977(5)
Fe1	N10	1.992(5)
N1	C1	1.348(7)
N1	C5	1.352(7)
N2	C6	1.360(7)
N2	C10	1.343(7)
N3	C11	1.278(9)
N3	C12	1.465(8)
N4	C14	1.269(8)
N4	C15	1.450(8)
N5	C17	1.335(7)
N5	C21	1.362(7)
N6	C22	1.362(8)
N6	C26	1.330(8)
N7	C27	1.254(10)
N7	C28	1.466(9)
N8	C30	1.268(8)
N8	C31	1.456(8)
N9	C33	1.336(8)
N9	C37	1.353(8)
N10	C38	1.357(8)
N10	C42	1.340(8)
N11	C43	1.250(10)
N11	C44	1.468(9)
N12	C01Z	1.251(9)
N12	C46	1.451(8)
N13	C13	1.463(11)
N13	C29	1.464(11)
N13	C45	1.487(10)
N14	C16	1.504(8)
N14	C32	1.495(8)
N14	C47	1.501(9)
C1	C2	1.389(8)
C01Z	C34	1.470(9)
C2	C3	1.387(9)
C2	C14	1.471(8)
C3	C4	1.379(8)
C4	C5	1.392(8)
C5	C6	1.472(8)
C6	C7	1.374(9)

Table 5.7. (cont'd)

Atom	Atom	Length/Å
C7	C8	1.381(8)
C8	C9	1.390(9)
C9	C10	1.387(9)
C9	C11	1.477(8)
C12	C13	1.545(10)
C15	C16	1.530(8)
C17	C18	1.388(8)
C18	C19	1.388(9)
C18	C30	1.474(9)
C19	C20	1.392(9)
C20	C21	1.391(8)
C21	C22	1.460(9)
C22	C23	1.391(8)
C23	C24	1.361(10)
C24	C25	1.402(10)
C25	C26	1.377(8)
C25	C27	1.486(9)
C28	C29	1.511(12)
C31	C32	1.528(10)
C33	C34	1.373(9)
C34	C35	1.382(9)
C35	C36	1.366(10)
C36	C37	1.391(9)
C37	C38	1.472(9)
C38	C39	1.397(9)
C39	C40	1.380(11)
C40	C41	1.367(11)
C41	C42	1.401(8)
C41	C43	1.494(10)
C44	C45	1.534(12)
C46	C47	1.536(9)
P1	F1	1.580(6)
P1	F2	1.579(5)
P1	F3	1.535(6)
P1	F4	1.592(5)
P1	F5	1.567(6)
P1	F6	1.545(6)
P2	F7	1.584(6)
P2	F8	1.588(5)
P2	F9	1.558(5)
P2	F10	1.591(5)
P2	F11	1.594(6)
P2	F12	1.563(5)
P3	F1P	1.545(12)
P3	F2P	1.675(16)
P3	F3P	1.508(9)
P3	F4P	1.10(2)
P3	F5P	1.558(12)
P3	F6P	1.517(18)
B2	F1B	1.4183
B2	F2B	1.4185
B2	F3B	1.4183
B2	F4B	1.4189
F13	B1	1.364(11)

Table 5.7. (cont'd)

Atom	Atom	Length/Å
F14	B1	1.390(12)
F15	B1	1.269(11)
F16	B1	1.409(10)
N1S	C1S	1.124(10)
C1S	C2S	1.467(12)
N2S	C3S	1.147(13)
C3S	C4S	1.432(16)

Table 5.8. Bond angles in degrees of $[FeAg(L)](BF_4)_{1.5}(PF_6)_{2.5}$.

Atom	Atom	Atom	Angle/°
N3	Ag1	N7	117.0(2)
N3	Ag1	N11	113.2(2)
N3	Ag1	N13	76.0(2)
N7	Ag1	N13	77.2(2)
N11	Ag1	N7	113.8(3)
N11	Ag1	N13	75.9(2)
N4	Ag1B	N14	77.74(18)
N8	Ag1B	N4	115.8(2)
N8	Ag1B	N12	116.3(2)
N8	Ag1B	N14	79.0(2)
N12	Ag1B	N4	116.3(2)
N12	Ag1B	N14	78.8(2)
N1	Fe1	N5	93.16(18)
N1	Fe1	N6	172.76(19)
N1	Fe1	N10	94.61(18)
N2	Fe1	N1	80.95(19)
N2	Fe1	N5	95.10(19)
N2	Fe1	N6	94.87(19)
N2	Fe1	N9	171.11(18)
N2	Fe1	N10	92.4(2)
N5	Fe1	N6	81.27(19)
N5	Fe1	N10	169.9(2)
N9	Fe1	N1	93.27(19)
N9	Fe1	N5	91.95(19)
N9	Fe1	N6	91.55(19)
N9	Fe1	N10	81.3(2)
N10	Fe1	N6	91.46(19)
C1	N1	Fe1	126.3(4)
C1	N1	C5	117.8(5)
C5	N1	Fe1	115.6(4)
C6	N2	Fe1	115.5(4)
C10	N2	Fe1	126.4(4)
C10	N2	C6	117.5(5)
C11	N3	Ag1	127.5(4)
C11	N3	C12	119.4(6)
C12	N3	Ag1	112.8(5)
C14	N4	Ag1B	122.3(4)
C14	N4	C15	119.3(5)
C15	N4	Ag1B	111.8(4)
C17	N5	Fe1	126.1(4)
C17	N5	C21	118.6(5)
C21	N5	Fe1	114.7(4)
C22	N6	Fe1	114.8(4)
C26	N6	Fe1	127.1(4)
C26	N6	C22	118.0(5)
C27	N7	Ag1	128.0(5)
C27	N7	C28	120.7(7)
C28	N7	Ag1	110.2(5)
C30	N8	Ag1B	127.1(4)
C30	N8	C31	119.2(5)
C31	N8	Ag1B	111.3(4)
C33	N9	Fe1	126.9(4)

Table 5.8. (cont'd)

Atom	Atom	Atom	Angle/°
C33	N9	C37	117.5(5)
C37	N9	Fe1	115.5(4)
C38	N10	Fe1	114.5(4)
C42	N10	Fe1	127.4(4)
C42	N10	C38	117.5(5)
C43	N11	Ag1	126.5(5)
C43	N11	C44	120.8(6)
C44	N11	Ag1	112.2(5)
C01Z	N12	Ag1B	126.1(5)
C01Z	N12	C46	120.2(6)
C46	N12	Ag1B	110.5(4)
C13	N13	Ag1	106.4(4)
C13	N13	C29	113.9(6)
C13	N13	C45	112.3(7)
C29	N13	Ag1	104.2(4)
C29	N13	C45	112.4(7)
C45	N13	Ag1	106.7(4)
C16	N14	Ag1B	108.6(4)
C32	N14	Ag1B	106.9(4)
C32	N14	C16	111.2(5)
C32	N14	C47	111.8(5)
C47	N14	Ag1B	107.2(4)
C47	N14	C16	110.9(5)
N1	C1	C2	123.3(6)
N12	C01Z	C34	120.2(6)
C1	C2	C14	119.4(5)
C3	C2	C1	118.2(5)
C3	C2	C14	122.3(5)
C4	C3	C2	118.9(5)
C3	C4	C5	119.9(6)
N1	C5	C4	121.6(5)
N1	C5	C6	113.9(5)
C4	C5	C6	124.4(5)
N2	C6	C5	113.6(5)
N2	C6	C7	122.4(5)
C7	C6	C5	124.0(5)
C6	C7	C8	119.9(6)
C7	C8	C9	118.4(6)
C8	C9	C11	121.5(6)
C10	C9	C8	118.9(5)
C10	C9	C11	119.3(6)
N2	C10	C9	122.9(5)
N3	C11	C9	118.7(6)
N3	C12	C13	109.3(6)
N13	C13	C12	113.0(6)
N4	C14	C2	121.0(5)
N4	C15	C16	109.5(5)
N14	C16	C15	112.0(5)
N5	C17	C18	123.0(5)
C17	C18	C19	118.7(6)
C17	C18	C30	119.4(5)
C19	C18	C30	121.8(5)
C18	C19	C20	118.6(5)
C21	C20	C19	119.7(5)

Table 5.8. (cont'd)

Atom	Atom	Atom	Angle/°
N5	C21	C20	121.1(5)
N5	C21	C22	114.9(5)
C20	C21	C22	123.9(5)
N6	C22	C21	114.1(5)
N6	C22	C23	121.1(6)
C26	C25	C27	119.3(6)
N6	C26	C25	123.6(6)
N7	C28	C29	111.3(7)
N13	C29	C28	115.1(6)
N8	C30	C18	118.8(5)
N8	C31	C32	109.1(5)
N14	C32	C31	110.7(5)
N9	C33	C34	124.0(6)
C33	C34	C01Z	119.8(6)
C33	C34	C35	118.0(6)
C35	C34	C01Z	122.0(6)
C36	C35	C34	119.3(6)
C35	C36	C37	119.6(6)
N9	C37	C36	121.5(6)
N9	C37	C38	114.0(6)
C36	C37	C38	124.5(6)
N10	C38	C37	114.4(5)
N10	C38	C39	122.2(6)
C39	C38	C37	123.4(6)
C40	C39	C38	119.1(7)
C41	C40	C39	119.2(6)
C40	C41	C42	119.0(6)
C40	C41	C43	121.8(6)
C42	C41	C43	119.0(7)
N10	C42	C41	122.9(6)
N11	C43	C41	118.5(6)
N11	C44	C45	110.4(7)
N13	C45	C44	111.8(7)
N12	C46	C47	109.1(5)
N14	C47	C46	111.0(6)
F1	P1	F4	90.1(4)
F2	P1	F1	88.7(3)
F2	P1	F4	177.2(3)
F3	P1	F1	179.0(5)
F3	P1	F2	91.8(4)
F3	P1	F4	89.4(4)
F3	P1	F5	89.6(6)
F3	P1	F6	92.5(6)
F5	P1	F1	89.6(5)
F5	P1	F2	89.5(3)
F5	P1	F4	88.1(3)
F6	P1	F1	88.3(5)
F6	P1	F2	90.3(3)
F6	P1	F4	92.1(3)
F6	P1	F5	177.9(6)
F7	P2	F8	89.8(3)
F7	P2	F10	88.4(4)
F7	P2	F11	89.7(4)

Table 5.8. (cont'd)

Atom	Atom	Atom	Angle/°
F7	P2	F11	89.7(4)
F8	P2	F10	90.3(3)
F8	P2	F11	89.9(3)
F9	P2	F7	178.8(4)
F9	P2	F8	89.1(3)
F9	P2	F10	92.0(3)
F9	P2	F11	89.9(4)
F9	P2	F12	92.0(3)
F10	P2	F11	178.1(4)
F12	P2	F7	89.2(3)
F12	P2	F8	178.8(3)
F12	P2	F10	90.4(3)
F12	P2	F11	89.4(3)
F1P	P3	F2P	75.9(8)
F1P	P3	F5P	90.5(9)
F3P	P3	F1P	156.5(10)
F3P	P3	F2P	85.5(8)
F3P	P3	F5P	99.4(8)
F4P	P3	F1P	96.7(10)
F4P	P3	F2P	167.3(15)
F4P	P3	F3P	98.8(10)
F4P	P3	F5P	113.3(13)
F4P	P3	F6P	95.2(15)
F5P	P3	F2P	77.4(9)
F6P	P3	F1P	76.0(12)
F6P	P3	F2P	73.2(10)
F6P	P3	F3P	85.0(9)
F6P	P3	F5P	149.8(13)
F1B	B2	F2B	109.5
F1B	B2	F3B	109.5
F1B	B2	F4B	109.4
F2B	B2	F4B	109.5
F3B	B2	F2B	109.5
F3B	B2	F4B	109.4
F13	B1	F14	104.2(8)
F13	B1	F16	111.3(8)
F14	B1	F16	103.9(7)
F15	B1	F13	111.6(8)
F15	B1	F14	113.9(11)
F15	B1	F16	111.5(9)
N1S	C1S	C2S	178.2(10)
N2S	C3S	C4S	178.4(12)

Table 5.9. Torsion angles in degrees of $[FeAg(L)](BF_4)_{1.5}(PF_6)_{2.5}$.

Atom	Atom	Atom	Atom	Angle/°
Ag1	N3	C11	C9	5.3(8)
Ag1	N3	C12	C13	44.3(7)
Ag1	N7	C27	C25	10.6(11)
Ag1	N7	C28	C29	41.7(8)
Ag1	N11	C43	C41	4.0(11)
Ag1	N11	C44	C45	44.2(9)
Ag1	N13	C13	C12	34.9(7)
Ag1	N13	C29	C28	36.8(8)
Ag1	N13	C45	C44	36.1(9)
Ag1B	N4	C14	C2	30.1(7)
Ag1B	N4	C15	C16	39.1(6)
Ag1B	N8	C30	C18	14.2(9)
Ag1B	N8	C31	C32	41.8(6)
Ag1B	N12	C01Z	C34	17.2(9)
Ag1B	N12	C46	C47	41.8(6)
Ag1B	N14	C16	C15	37.1(6)
Ag1B	N14	C32	C31	38.4(6)
Ag1B	N14	C47	C46	38.9(6)
Fe1	N1	C1	C2	172.0(4)
Fe1	N1	C5	C4	-177.1(4)
Fe1	N1	C5	C6	-0.6(5)
Fe1	N2	C6	C5	7.2(6)
Fe1	N2	C6	C7	-173.3(4)
Fe1	N2	C10	C9	168.7(4)
Fe1	N5	C17	C18	168.4(4)
Fe1	N5	C21	C20	-173.8(4)
Fe1	N5	C21	C22	3.2(6)
Fe1	N6	C22	C21	-2.5(6)
Fe1	N6	C22	C23	178.6(5)
Fe1	N6	C26	C25	175.9(5)
Fe1	N9	C33	C34	174.4(4)
Fe1	N9	C37	C36	-177.9(5)
Fe1	N9	C37	C38	0.4(6)
Fe1	N10	C38	C37	6.7(6)
Fe1	N10	C38	C39	-172.2(5)
Fe1	N10	C42	C41	168.8(4)
N1	C1	C2	C3	5.7(8)
N1	C1	C2	C14	-172.3(5)
N1	C5	C6	N2	-4.3(6)
N1	C5	C6	C7	176.2(5)
N2	C6	C7	C8	2.8(9)
N3	C12	C13	N13	-54.3(9)
N4	C15	C16	N14	-51.8(7)
N5	C17	C18	C19	6.2(9)
N5	C17	C18	C30	-169.4(5)
N5	C21	C22	N6	-0.4(7)
N5	C21	C22	C23	178.4(6)
N6	C22	C23	C24	3.3(10)
N7	C28	C29	N13	-55.9(10)
N8	C31	C32	N14	-54.6(7)
N9	C33	C34	C01Z	-171.3(6)
N9	C33	C34	C35	3.9(9)

Table 5.9. (cont'd)

Atom	Atom	Atom	Atom	Angle/°
N9	C37	C38	N10	-4.7(7)
N9	C37	C38	C39	174.2(6)
N10	C38	C39	C40	0.3(11)
N11	C44	C45	N13	-55.1(11)
N12	C01Z	C34	C33	28.1(10)
N12	C01Z	C34	C35	-147.0(7)
N12	C46	C47	N14	-55.4(7)
C1	N1	C5	C4	-2.7(7)
C1	N1	C5	C6	173.9(4)
C1	C2	C3	C4	-5.2(8)
C1	C2	C14	N4	17.7(8)
C01Z	N12	C46	C47	-119.3(7)
C01Z	C34	C35	C36	172.6(6)
C2	C3	C4	C5	1.1(9)
C3	C2	C14	N4	-160.2(6)
C3	C4	C5	N1	3.0(8)
C3	C4	C5	C6	-173.2(5)
C4	C5	C6	N2	172.1(5)
C4	C5	C6	C7	-7.4(8)
C5	N1	C1	C2	-1.8(7)
C5	C6	C7	C8	-177.8(5)
C6	N2	C10	C9	-1.9(8)
C6	C7	C8	C9	-0.3(9)
C7	C8	C9	C10	-3.1(9)
C7	C8	C9	C11	171.1(6)
C8	C9	C10	N2	4.3(9)
C8	C9	C11	N3	-134.0(7)
C10	N2	C6	C5	178.8(5)
C10	N2	C6	C7	-1.7(8)
C10	C9	C11	N3	40.2(8)
C11	N3	C12	C13	-129.8(7)
C11	C9	C10	N2	-170.0(5)
C12	N3	C11	C9	178.4(6)
C13	N13	C29	C28	152.4(7)
C13	N13	C45	C44	-80.1(9)
C14	N4	C15	C16	-112.9(6)
C14	C2	C3	C4	172.8(5)
C15	N4	C14	C2	179.1(5)
C16	N14	C32	C31	-80.0(6)
C16	N14	C47	C46	157.3(5)
C17	N5	C21	C20	-1.7(8)
C17	N5	C21	C22	175.3(5)
C17	C18	C19	C20	-5.1(9)
C17	C18	C30	N8	37.4(9)
C18	C19	C20	C21	1.0(9)
C19	C18	C30	N8	-138.1(6)
C19	C20	C21	N5	2.5(9)
C19	C20	C21	C22	-174.2(6)
C20	C21	C22	N6	176.5(5)
C20	C21	C22	C23	-4.7(10)
C21	N5	C17	C18	-2.7(8)
C21	C22	C23	C24	-175.4(6)
C22	N6	C26	C25	-0.7(9)

Table 5.9. (cont'd)

Atom	Atom	Atom	Atom	Angle/°
C22	C23	C24	C25	2.7(10)
C23	C24	C25	C26	-7.3(10)
C23	C24	C25	C27	168.6(7)
C24	C25	C26	N6	6.5(10)
C24	C25	C27	N7	-147.4(8)
C26	N6	C22	C21	174.5(5)
C26	N6	C22	C23	-4.4(9)
C26	C25	C27	N7	28.5(11)
C27	N7	C28	C29	-127.4(8)
C27	C25	C26	N6	-169.5(6)
C28	N7	C27	C25	177.5(7)
C29	N13	C13	C12	-79.4(8)
C29	N13	C45	C44	149.9(8)
C30	N8	C31	C32	-121.7(6)
C30	C18	C19	C20	170.4(6)
C31	N8	C30	C18	174.8(6)
C32	N14	C16	C15	154.5(5)
C32	N14	C47	C46	-78.0(7)
C33	N9	C37	C36	-0.9(8)
C33	N9	C37	C38	177.4(5)
C33	C34	C35	C36	-2.6(10)
C34	C35	C36	C37	-0.2(10)
C35	C36	C37	N9	2.1(10)
C35	C36	C37	C38	-176.0(6)
C36	C37	C38	N10	173.5(6)
C36	C37	C38	C39	-7.6(10)
C37	N9	C33	C34	-2.1(8)
C37	C38	C39	C40	-178.5(7)
C38	N10	C42	C41	-2.1(8)
C38	C39	C40	C41	1.7(11)
C39	C40	C41	C42	-3.8(11)
C39	C40	C41	C43	170.0(7)
C40	C41	C42	N10	4.1(10)
C40	C41	C43	N11	-131.7(9)
C42	N10	C38	C37	178.8(5)
C42	N10	C38	C39	-0.1(9)
C42	C41	C43	N11	42.1(10)
C43	N11	C44	C45	-128.5(9)
C43	C41	C42	N10	-169.9(6)
C44	N11	C43	C41	175.7(8)
C45	N13	C13	C12	151.3(6)
C45	N13	C29	C28	-78.4(9)
C46	N12	C01Z	C34	175.2(6)
C47	N14	C16	C15	-80.4(7)
C47	N14	C32	C31	155.4(5)

Table 5.10. Atomic occupancies for all atoms that are not fully occupied in $[FeAg(L)](BF_4)_{1.5}(PF_6)_{2.5}$.

Atom	Occupancy
Ag1	0.7549(9)
Ag1B	0.2451(9)
P3	0.5
F1P	0.5
F2P	0.5
F3P	0.5
F4P	0.5
F5P	0.5
F6P	0.5
B2	0.5
F1B	0.5
F2B	0.5
F3B	0.5
F4B	0.5

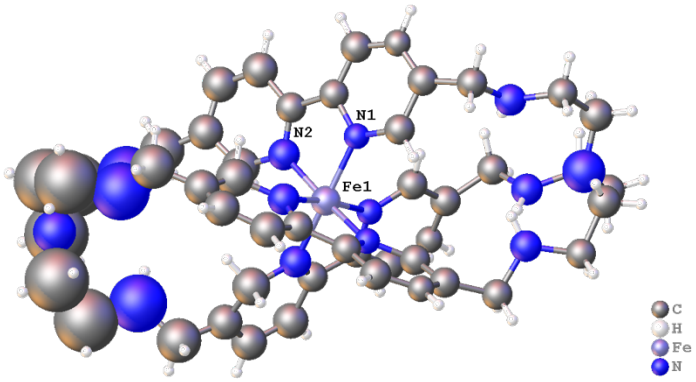

Figure 5.51. Numbering scheme in x-ray crystal structure of $[Fe(LH)](PF_6)_2$.

Table 5.11. Bond lengths for $[Fe(LH)](PF_6)_2$.

Atom	Atom	Length/Å	Atom	Atom	Length/Å
Fe1	N1[1]	1.976(14)	C3	C4	1.34(3)
Fe1	N1[2]	1.976(14)	C4	C5	1.47(2)
Fe1	N1	1.976(14)	C4	C6	1.51(3)
Fe1	N2	1.973(17)	C8	C9	1.52(3)
Fe1	N2[1]	1.973(17)	C10	C11	1.44(3)
Fe1	N2[2]	1.973(17)	C11	C12	1.29(3)
N1	C1	1.37(2)	C12	C13	1.41(4)
N1	C5	1.39(2)	C13	C14	1.40(3)
N2	C10	1.36(3)	C13	C15	1.50(4)
N2	C14	1.40(3)	C15	N5A	1.50(3)
N3	C6	1.48(2)	C16	C17	1.55(3)
N3	C8	1.52(3)	P2	F7	1.63(3)
N4	C9[1]	1.54(2)	P2	F7[3]	1.63(3)
N4	C9[2]	1.54(2)	P2	F8	1.63(2)
N4	C9	1.54(2)	P2	F8[3]	1.63(2)
N6A	C17[2]	1.62(10)	P2	F9	1.52(2)
N6A	C17[1]	1.62(10)	P2	F9[3]	1.52(2)
N6A	C17	1.62(10)	P1	F2	1.57(4)
N6A	C17A[1]	1.22(9)	P1	F1	1.48(5)
N6A	C17A	1.22(8)	P1	F3	1.76(4)
N6A	C17A[2]	1.22(8)	P1	F4	1.67(3)
N5	C15	1.47(3)	P1	F5	1.57(3)
N5	C16	1.50(3)	P1	F6	1.60(3)
C1	C2	1.42(3)	N5A	C16A	1.73(8)
C1	C10	1.41(3)	C16A	C17A	1.51(3)
C2	C3	1.40(3)			

Table 5.12. Bond angles for $[Fe(LH)](PF_6)_2$.

Atom	Atom	Atom	Angle/°	Atom	Atom	Atom	Angle/°
N1	Fe1	N1[1]	95.6(6)	N2	C10	C1	115.1(17)
N1[2]	Fe1	N1[1]	95.6(6)	N2	C10	C11	121(2)
N1	Fe1	N1[2]	95.6(6)	C1	C10	C11	124(2)
N2[2]	Fe1	N1[2]	81.2(7)	C12	C11	C10	120(2)
N2[2]	Fe1	N1[1]	173.3(6)	C11	C12	C13	122(2)
N2	Fe1	N1[2]	173.3(6)	C12	C13	C15	129(2)
N2	Fe1	N1	81.2(7)	C14	C13	C12	115(2)
N2[1]	Fe1	N1	173.3(6)	C14	C13	C15	116(3)
N2[1]	Fe1	N1[1]	81.2(7)	C13	C14	N2	123(2)
N2	Fe1	N1[1]	90.6(6)	N5	C15	C13	120(4)
N2[2]	Fe1	N1	90.6(6)	N5A	C15	C13	100(3)
N2[1]	Fe1	N1[2]	90.6(6)	N5	C16	C17	116(7)
N2[1]	Fe1	N2[2]	92.8(8)	C16	C17	N6A	94(6)
N2	Fe1	N2[2]	92.8(8)	F7	P2	F7[3]	163(2)
N2	Fe1	N2[1]	92.8(8)	F8[3]	P2	F7[3]	83.0(14)
C1	N1	Fe1	114.1(14)	F8	P2	F7	83.0(14)
C1	N1	C5	121.0(17)	F8	P2	F7[3]	84.8(17)
C5	N1	Fe1	124.5(13)	F8[3]	P2	F7	84.8(17)
C10	N2	Fe1	114.1(13)	F8	P2	F8[3]	89.0(15)
C10	N2	C14	116.1(19)	F9	P2	F7[3]	93.6(19)
C14	N2	Fe1	129.4(18)	F9	P2	F7	98.7(19)
C6	N3	C8	109.8(15)	F9[3]	P2	F7	93.6(19)
C9	N4	C9[2]	107.5(15)	F9[3]	P2	F7[3]	98.7(19)
C9	N4	C9[1]	107.5(15)	F9	P2	F8[3]	176.5(17)
C9[2]	N4	C9[1]	107.5(15)	F9[3]	P2	F8[3]	91.1(12)
C17[1]	N6A	C17[2]	119.1(12)	F9	P2	F8	91.1(12)
C17	N6A	C17[1]	119.1(12)	F9[3]	P2	F8	176.5(17)
C17	N6A	C17[2]	119.1(12)	F9[3]	P2	F9	89(2)
C17A[1]	N6A	C17[1]	45(5)	F2	P1	F3	83(2)
C17A	N6A	C17[1]	161(5)	F2	P1	F4	178.7(18)
C17A[2]	N6A	C17[1]	74(5)	F2	P1	F5	94.7(18)
C17A[2]	N6A	C17A[1]	118(2)	F2	P1	F6	85.0(16)
C17A	N6A	C17A[2]	118(2)	F1	P1	F2	88(2)
C17A	N6A	C17A[1]	118(2)	F1	P1	F3	171(2)
C15	N5	C16	126(5)	F1	P1	F4	93(2)
N1	C1	C2	119(2)	F1	P1	F5	84.9(16)
N1	C1	C10	114.7(19)	F1	P1	F6	91.3(16)
C2	C1	C10	125.9(18)	F4	P1	F3	96.1(18)
C3	C2	C1	119(2)	F5	P1	F3	96.7(15)
C4	C3	C2	123(2)	F5	P1	F4	86.5(17)
C3	C4	C5	117.0(19)	F5	P1	F6	176.2(17)

Table 5.12. (cont'd)

Atom	Atom	Atom	Angle/°	Atom	Atom	Atom	Angle/°
C3	C4	C6	128.7(18)	F6	P1	F3	87.0(16)
C5	C4	C6	114.3(17)	F6	P1	F4	93.9(16)
N1	C5	C4	120.0(19)	C15	N5A	C16A	106(4)
N3	C6	C4	104.3(16)	C17A	C16A	N5A	101(7)
N3	C8	C9	106.7(17)	N6A	C17A	C16A	136(9)
C8	C9	N4	110.0(18)				

Table 5.13. Torsion angles for $[Fe(LH)](PF_6)_2$.

A	B	C	D	Angle/°	A	B	C	D	Angle/°
Fe1	N1	C1	C2	-175.3(14)	C8	N3	C6	C4	170.3(16)
Fe1	N1	C1	C10	6(2)	$C9^1$	N4	C9	C8	165.4(19)
Fe1	N1	C5	C4	170.4(13)	$C9^2$	N4	C9	C8	-79(3)
Fe1	N2	C10	C1	9(2)	C10	N2	C14	C13	-6(4)
Fe1	N2	C10	C11	-175.3(17)	C10	C1	C2	C3	-179.3(18)
Fe1	N2	C14	C13	166(2)	C10	C11	C12	C13	12(5)
N1	C1	C2	C3	2(3)	C11	C12	C13	C14	-19(5)
N1	C1	C10	N2	-10(3)	C11	C12	C13	C15	167(3)
N1	C1	C10	C11	174.5(19)	C12	C13	C14	N2	16(5)
N2	C10	C11	C12	-1(4)	C12	C13	C15	N5	-133(4)
N3	C8	C9	N4	-58(2)	C12	C13	C15	N5A	-99(4)
N5	C16	C17	N6A	65(9)	C13	C15	N5A	C16A	166(5)
C1	N1	C5	C4	-2(3)	C14	N2	C10	C1	-177.8(19)
C1	C2	C3	C4	3(3)	C14	N2	C10	C11	-2(3)
C1	C10	C11	C12	175(2)	C14	C13	C15	N5	53(5)
C2	C1	C10	N2	171.6(19)	C14	C13	C15	N5A	87(4)
C2	C1	C10	C11	-4(3)	C15	N5	C16	C17	162(6)
C2	C3	C4	C5	-7(3)	C15	C13	C14	N2	-169(3)
C2	C3	C4	C6	172.7(18)	C15	N5A	C16A	C17A	127(6)
C3	C4	C5	N1	6(3)	C16	N5	C15	C13	170(6)
C3	C4	C6	N3	-99(2)	$C17^2$	N6A	C17	C16	33(11)
C5	N1	C1	C2	-2(3)	$C17^1$	N6A	C17	C16	-166(3)
C5	N1	C1	C10	178.8(16)	N5A	C16A	C17A	N6A	44(15)
C5	C4	C6	N3	80(2)	$C17A^1$	N6A	C17A	C16A	-157(7)
C6	N3	C8	C9	171.9(18)	$C17A^2$	N6A	C17A	C16A	48(21)

Table 5.14. Atomic occupancy for $[Fe(LH)](PF_6)_2$.

Atom	***Occupancy***	**Atom**	***Occupancy***	**Atom**	***Occupancy***
N5	0.3333	H5	0.3333	H15A	0.3333
H15B	0.3333	H15C	0.3333	H15D	0.3333
C16	0.5	H16A	0.5	H16B	0.5
C17	0.5	H17A	0.5	H17B	0.5
P1	0.5	F2	0.5	F1	0.5
F3	0.5	F4	0.5	F5	0.5
F6	0.5	N5A	0.3333	H5AA	0.3333
C16A	0.5	H16C	0.5	H16D	0.5
C17A	0.5	H17C	0.5	H17D	0.5

Table 5.15. Solvent mask information for $[Fe(LH)](PF_6)_2$

Number	X	Y	Z	Volume	Electron count	Content
1	-0.017	0.000	0.750	74.7	25.8	?
2	0.000	0.250	0.517	74.7	25.9	?
3	0.000	0.250	0.375	8.9	2.3	?
4	0.017	0.500	0.750	74.7	25.9	?
5	0.000	0.750	0.983	74.7	25.8	?
6	0.000	0.750	0.125	8.9	2.3	?
7	0.125	0.000	0.750	8.9	2.3	?
8	0.250	0.483	0.500	74.7	25.9	?
9	0.250	0.517	0.000	74.7	25.9	?
10	0.250	0.375	0.000	8.9	2.3	?
11	0.250	0.625	0.500	8.9	2.3	?
12	0.375	0.000	0.250	8.9	2.3	?
13	0.500	0.250	0.483	74.7	25.8	?
14	0.500	0.750	0.017	74.7	25.9	?
15	0.483	0.500	0.250	74.7	25.8	?
16	0.517	0.000	0.250	74.7	25.9	?
17	0.500	0.250	0.625	8.9	2.3	?
18	0.500	0.750	0.875	8.9	2.3	?
19	0.625	0.500	0.250	8.9	2.3	?
20	0.750	0.017	0.500	74.7	25.9	?
21	0.750	-0.017	1.000	74.7	25.9	?
22	0.750	0.125	0.000	8.9	2.3	?
23	0.750	0.875	0.500	8.9	2.3	?
24	0.875	0.500	0.750	8.9	2.3	?

REFERENCES

REFERENCES

1. Gawelda, W.; Pham, V. T.; Benfatto, M.; Zaushitsyn, Y.; Kaiser, M.; Grolimund, D.; Johnson, S. L.; Abela, R.; Hauser, A.; Bressler, C.; et al. Structural Determination of a Short-Lived Excited Iron(II) Complex by Picosecond X-Ray Absorption Spectroscopy. *Phys. Rev. Lett.* **2007**, *98*, 6–9. https://doi.org/10.1103/PhysRevLett.98.057401.

2. Smeigh, A. L.; Creelman, M.; Mathies, R. A.; McCusker, J. K. Femtosecond Time-Resolved Optical and Raman Spectroscopy of Photoinduced Spin Crossover: Temporal Resolution of Low-to-High Spin Optical Switching. *J. Am. Chem. Soc.* **2008**, *130*, 14105–14107. https://doi.org/10.1021/ja805949s.

3. Gütlich, P.; Goodwin, H. A. *Spin Crossover in Transition Metal Compounds I*; Springer-Verlag: Berlin, 2004.

4. Hauser, A. Light-Induced Spin Crossover and the High-Spin to Low-Spin Relaxation. In *Spin Crossover in Transition Metal Compounds II*; Gütlich, P.; Goodwin, H. A. Eds.; Springer-Verlag, 2004; pp 155–198.

5. Zhang, X.; Lawson Daku, M. L.; Zhang, J.; Suarez-Alcantara, K.; Jennings, G.; Kurtz, C. A.; Canton, S. E. Dynamic Jahn-Teller Effect in the Metastable High-Spin State of Solvated $[Fe(terpy)_2]^{2+}$. *J. Phys. Chem. C* **2015**, *119*, 3312–3321. https://doi.org/10.1021/jp5117068.

6. Vankó, G.; Bordage, A.; Pápai, M.; Haldrup, K.; Glatzel, P.; March, A. M.; Doumy, G.; Britz, A.; Galler, A.; Assefa, T.; et al. Detailed Characterization of a Nanosecond-Lived Excited State: X-Ray and Theoretical Investigation of the Quintet State in Photoexcited $[Fe(terpy)_2]^{2+}$. *J. Phys. Chem. C* **2015**, *119*, 5888–5902. https://doi.org/10.1021/acs.jpcc.5b00557.

7. Purcell, K. F. Pseudorotational Intersystem Crossing in d^6 Complexes. *J. Am. Chem. Soc.* **1979**, *101*, 5147–5152. https://doi.org/10.1021/ja00512a005.

8. McCusker, J. K.; Rheingold, A. L.; Hendrickson, D. N. Variable-Temperature Studies of Laser-Initiated $^5T_2 \rightarrow {}^1A_1$ Intersystem Crossing in Spin-Crossover Complexes: Empirical Correlations between Activation Parameters and Ligand Structure in a Series of Polypyridyl Ferrous Complexes. *Inorg. Chem.* **1996**, *35*, 2100–2112. https://doi.org/10.1021/ic9507880.

9. Collet, E.; Cammarata, M. Disentangling Ultrafast Electronic and Structural Dynamics with X-Ray Lasers. *Chem. Eur. J.* **2018**, *24*, 15696–15705. https://doi.org/10.1002/chem.201802105.

10. Ashley, D. C.; Jakubikova, E. Ray-Dutt and Bailar Twists in Fe(II)-Tris(2,2′-bipyridine): Spin States, Sterics, and Fe–N Bond Strengths. *Inorg. Chem*. **2018**, *57*, 5585–5596. https://doi.org/10.1021/acs.inorgchem.8b00560.

11. Lemke, H. T.; Kjær, K. S.; Hartsock, R.; van Driel, T. B.; Chollet, M.; Glownia, J. M.; Song, S.; Zhu, D.; Pace, E.; Matar, S. F.; et al. Coherent Structural Trapping through Wave Packet Dispersion during Photoinduced Spin State Switching. *Nat. Commun*. **2017**, 8, 15342.

12. Canton, S. E.; Zhang, X.; Lawson Daku, M. L.; Liu, Y.; Zhang, J.; Alvarez, S. Mapping the Ultrafast Changes of Continuous Shape Measures in Photoexcited Spin Crossover Complexes without Long-Range Order. *J. Phys. Chem. C* **2015**, *119*, 3322–3330. https://doi.org/10.1021/jp5117189.

13. Nance, J.; Bowman, D. N.; Mukherjee, S.; Kelley, C. T.; Jakubikova, E. Insights into the Spin-State Transitions in $[Fe(tpy)_2]^{2+}$: Importance of the Terpyridine Rocking Motion. *Inorg. Chem.* **2015**, *54*, 11259–11268. https://doi.org/10.1021/acs.inorgchem.5b01747.

14. de Mendoza, J.; Mesa, E.; Vogtle, F.; Rodriguz-Ubis, J. -C; Vaquez, P.; Windscheif, P.-M.; Rissanen, K.; Lehn, J.-M.; Lilianbaum, D.; Ziessel, R. A New Macrobicyclic Tris-Bipyridine Ligand and Its Cu(I) and Ag(I) Complexes. *Angew. Chem. Int. Ed. Engl.* **1991**, *30*, 1331–1333. https://doi.org/10.1002/anie.199113311.

15. Puodziukynaite, E.; Oberst, J. L.; Dyer, A. L.; Reynolds, J. R. Establishing Dual Electrogenerated Chemiluminescence and Multicolor Electrochromism in Functional Ionic Transition-Metal Complexes. *J. Am. Chem. Soc.* **2012**, *134*, 968–978. https://doi.org/10.1021/ja2065297.

16. Rivada-Wheelaghan, O.; Aristizábal, S. L.; López-Serrano, J.; Fayzullin, R. R.; Khusnutdinova, J. R. Controlled and Reversible Stepwise Growth of Linear Copper(I) Chains Enabled by Dynamic Ligand Scaffolds. *Angew. Chemie - Int. Ed*. **2017**, *56*, 16267–16271. https://doi.org/10.1002/anie.201709167.

17. Park, J. G.; Jeon, I. R.; Harris, T. D. Electronic Effects of Ligand Substitution on Spin Crossover in a Series of Diiminoquinonoid-Bridged Fe^{II}_2 Complexes. *Inorg. Chem*. **2015**, *54*, 359–369. https://doi.org/10.1021/ic5025586.

18. El-Ghayoury, A.; Ziessel, R. Facile Synthesis of Polypyridine Esters: A Route to Functionalized Aldehydes. *J. Org. Chem*. **2000**, *65*, 7757–7763. https://doi.org/10.1021/jo000635g.

19. Brown, A. M.; McCusker, C. E.; McCusker, J. K. Spectroelectrochemical Identification of Charge-Transfer Excited States in Transition Metal-Based Polypyridyl Complexes. *Dalton Trans.* **2014**, *43*, 17635–17646. https://doi.org/10.1039/c4dt02849j.

20. Paulus, B. C. Insights into the Photophysical Reaction Coordinate of First Fow Transition Metal Chromophores from Vibrational Coherences, PhD Dissertation, Michigan State University, East Lansing, MI 2020.

21. Paulus, B. C.; Adelman, S. L.; Jamula, L. L.; McCusker, J. K. Leveraging Excited-State Coherence for Synthetic Control of Ultrafast Dynamics. *Nature* **2020**, *Accepted*.

22. Jamula, L. L. Exploring Design Strategies to Tune the Electronic Structure and Ultrafast Dynamics of Iron(II) Polypyridyl Chromophores, PhD Dissertation, Michigan State University, East Lansing, MI, 2013.

23. Ciana, L. D.; Dressick, W. J.; Von Zelewsky, A. Synthesis of 4,4′-divinyl-2,2′-bipyridine. *J. Heterocycl. Chem*. **1990**, *27*, 163–165. https://doi.org/10.1002/jhet.5570270209.

24. Gouthaman, S.; Periyaraja, S.; Shanmugam, P. Bipyridine Carbaldehydes as Electrophiles in the Morita-Baylis-Hillman Reaction: Synthesis of Highly Functionalized Bipyridyl Ligands and a Macrocycle. *Tetrahedron Lett.* **2015**, *56*, 5920–5923. https://doi.org/10.1016/j.tetlet.2015.09.032.

25. Jamula, L. L.; Brown, A. M.; Guo, D.; McCusker, J. K. Synthesis and Characterization of a High-Symmetry Ferrous Polypyridyl Complex: Approaching the $^5T_2$/ $^3T_1$ Crossing Point for Fe^{II}. *Inorg. Chem.* **2014**, *53*, 15–17. https://doi.org/10.1021/ic402407k.

26. Hansch, C.; Leo, A.; Taft, R. W. A Survey of Hammett Substituent Constants and Resonance and Field Parameters. *Chem. Rev*. **1991**, *91*, 165–195. https://doi.org/10.1021/cr00002a004.

27. Dick, S. Experimental Crystal Structure Determination. *Zeitschrift fur Krist. - New Cryst. Struct*. **1998**, *213*, 356.

28. Carey, M. C.; Adelman, S. L.; McCusker, J. K. Insights into the Excited State Dynamics of Fe(II) Polypyridyl Complexes from Variable-Temperature Ultrafast Spectroscopy. *Chem. Sci.* **2019**, *10*, 134–144. https://doi.org/10.1039/C8SC04025G.

29. Monat, J. E.; McCusker, J. K. Femtosecond Excited-State Dynamics of an Iron(II) Polypyridyl Solar Cell Sensitizer Model. *J. Am. Chem. Soc*. **2000**, *122*, 4092–4097. https://doi.org/10.1021/ja992436o.

30. Brown, A. M. Excited-State Dynamics of Iron(II)-Based Charge Transfer Chromophores, PhD Dissertation, Michigan State University, East Lansing, MI, 2011.

31. *CRC Handbook of Chemistry and Physics*, 98th ed.

32. Carey, M. C. Achieving a Long-Lived Charge-Separated Fe(II) Chromophore: Insights into the Role of Reorganization Energy on the Ultrafast Photophysical Processes of d^6

Polypyridyl Complexes, PhD Dissertation, Michigan State University, East Lansing, MI, 2018.

33. Lawson Daku, L. M. Spin-State Dependence of the Structural and Vibrational Properties of Solvated Iron(II) Polypyridyl Complexes from AIMD Simulations: Aqueous $[Fe(bpy)_3]Cl_2$, a Case Study. *Phys. Chem. Chem. Phys*. **2018**, *20*, 6236–6253. https://doi.org/10.1039/c7cp07862e.

34. Haldrup, K.; Vankó, G.; Gawelda, W.; Galler, A.; Doumy, G.; March, A. M.; Kanter, E. P.; Bordage, A.; Dohn, A.; Van Driel, T. B.; et al. Guest-Host Interactions Investigated by Time-Resolved X-Ray Spectroscopies and Scattering at MHz Rates: Solvation Dynamics and Photoinduced Spin Transition in Aqueous $Fe(bipy)_3^{2+}$. *J. Phys. Chem. A* **2012**, *116*, 9878–9887. https://doi.org/10.1021/jp306917x.

35. Bressler, C.; Gawelda, W.; Galler, A.; Nielsen, M. M.; Sundström, V.; Doumy, G.; March, a. M.; Southworth, S. H.; Young, L.; Vankó, G. Solvation Dynamics Monitored by Combined X-Ray Spectroscopies and Scattering: Photoinduced Spin Transition in Aqueous $[Fe(bpy)_3]^{2+}$. *Faraday Discuss.* **2014**, *171*, 169–178. https://doi.org/10.1039/C4FD00097H.

36. Haldrup, K.; Gawelda, W.; Abela, R.; Alonso-Mori, R.; Bergmann, U.; Bordage, A.; Cammarata, M.; Canton, S. E.; Dohn, A. O.; Van Driel, T. B.; et al. Observing Solvation Dynamics with Simultaneous Femtosecond X-Ray Emission Spectroscopy and X-Ray Scattering. *J. Phys. Chem. B* **2016**, *120*, 1158–1168. https://doi.org/10.1021/acs.jpcb.5b12471.

37. Smeigh, A. L. Ultrafast Dynamics Associated with the Transition Metal-Based Sensitizers for Titanium Dioxide Based Solar Cells, PhD Dissertation, Michigan State University, East Lansing, MI, 2007.

38. Gawelda, W.; Cannizzo, A.; Pham, V.-T.; van Mourik, F.; Bressler, C.; Chergui, M.; Mourik, F. Van; Bressler, C.; Chergui, M. Ultrafast Nonadiabatic Dynamics of $[Fe^{II}(bpy)_3)]^{2+}$ in Solution. *J. Am. Chem. Soc.* **2007**, *129*, 8199–8206. https://doi.org/10.1021/ja070454x.

39. Bleiholder, C.; Börzel, H.; Comba, P.; Ferrari, R.; Heydt, M.; Kerscher, M.; Kuwata, S.; Laurenczy, G.; Lawrance, G. A.; Lienke, A.; et al. Coordination Chemistry of a New Rigid, Hexadentate Bispidine-Based Bis(amine)Tetrakis(pyridine) Ligand. *Inorg. Chem.* **2005**, *44*, 8145–8155. https://doi.org/10.1021/ic0513383.

40. Hensen, K. Synthesis and Structural Characterization of (1,4-Dihydropyrid-1-Yl)Aluminum Complexes. *Inorg. Chem.* **1999**, *38*, 4700–4704. https://doi.org/10.1021/ic9905695.

41. Akhuli, B.; Cera, L.; Jana, B.; Saha, S.; Schalley, C. A.; Ghosh, P. Formation and Transmetalation Mechanisms of Homo- and Heterometallic (Fe/Zn) Trinuclear Triple-

Stranded Side-by-Side Helicates. *Inorg. Chem*. **2015**, *54*, 4231–4242. https://doi.org/10.1021/ic502855g.

42. Miller, W. H.; Ruf, B. A.; Chang, Y. T. A Diabatic Reaction Path Hamiltonian. *J. Chem. Phys.* **1988**, *89*, 6298–6304. https://doi.org/10.1063/1.455395.

43. Ando, H.; Iuchi, S.; Sato, H. Theoretical Study on Ultrafast Intersystem Crossing of Chromium(III) Acetylacetonate. *Chem. Phys. Lett*. **2012**, *535*, 177–181. https://doi.org/10.1016/j.cplett.2012.03.043.

44. Damrauer, N.; Cerullo, G.; Yeh, A.; Boussie, T. R.; Shank, C. V; McCusker, J. K. Femtosecond Dynamics of Excited-State Evolution in $[Ru(Bpy)_3]^{2+}$. *Science* **1997**, *275*, 54–57. https://doi.org/10.1126/science.275.5296.54.

45. Yeh, A. T.; Shank, C. V; McCusker, J. K. Ultrafast Electron Localization Dynamics Following Photo-Induced Charge Transfer. *Science*, **2000**, *289*, 935–938. https://doi.org/10.1126/science.289.5481.935.

46. Liu, Y.; Harlang, T.; Canton, S. E.; Chabera, P.; Suarez-Alcantara, K.; Fleckhaus, A.; Vithanage, D. A.; Goransson, E.; Corani, A.; Lomoth, R.; et al. Towards Longer-Lived Metal-to-Ligand Charge Transfer States of Iron(II) Complexes: An N-Heterocyclic Carbene Approach. *Chem. Commun*. **2013**, *49*, 6412–6414. https://doi.org/10.1039/C3CC43833C.

47. Steube, J.; Burkhardt, L.; Päpcke, A.; Moll, J.; Zimmer, P.; Schoch, R.; Wölper, C.; Heinze, K.; Lochbrunner, S.; Bauer, M. Excited-State Kinetics of an Air-Stable Cyclometalated Iron(II) Complex. *Chem. Eur. J*. **2019**, 11826–11830. https://doi.org/10.1002/chem.201902488.

48. Paulus, B. C.; Nielson, K. C.; Tichnell, C. R.; Carey, M. C.; McCusker, M. C. Modular Approach to Controlling Excited State Properties of Iron(II) Polypyridyls.

49. Liu, L.; Duchanois, T.; Etienne, T.; Monari, A.; Beley, M.; Assfeld, X.; Haacke, S.; Gros, P. C. A New Record Excited State ^{3}MLCT Lifetime for Metalorganic Iron(II) Complexes. *Phys. Chem. Chem. Phys.* **2016**, *18*, 12550–12556. https://doi.org/10.1039/C6CP01418F.

50. Zhang, W.; Kjær, K. S.; Alonso-Mori, R.; Bergmann, U.; Chollet, M.; Fredin, L. A.; Hadt, R. G.; Hartsock, R. W.; Harlang, T.; Kroll, T.; et al. Manipulating Charge Transfer Excited State Relaxation and Spin Crossover in Iron Coordination Complexes with Ligand Substitution. *Chem. Sci*. **2016**, *8*, 515–523. https://doi.org/10.1039/C6SC03070J.

51. Chábera, P.; Kjaer, K. S.; Prakash, O.; Honarfar, A.; Liu, Y.; Fredin, L. A.; Harlang, T. C. B.; Lidin, S.; Uhlig, J.; Sundström, V.; et al. Fe^{II} Hexa N-Heterocyclic Carbene Complex with a 528 Ps Metal-To-Ligand Charge-Transfer Excited-State Lifetime. *J. Phys. Chem. Lett*. 2018, 9 (3), 459–463. https://doi.org/10.1021/acs.jpclett.7b02962.

52. Braun, J. D.; Lozada, I. B.; Kolodziej, C.; Burda, C.; Newman, K. M. E.; van Lierop, J.; Davis, R. L.; Herbert, D. E. Iron(II) Coordination Complexes with Panchromatic Absorption and Nanosecond Charge-Transfer Excited State Lifetimes. *Nat. Chem*. **2019**, *11*, 1144-1150. https://doi.org/10.1038/s41557-019-0357-z.

53. McCusker, C. E.; McCusker, J. K. Synthesis and Spectroscopic Characterization of CN-Substituted Bipyridyl Complexes of Ru(II). *Inorg. Chem*. **2011**, *50*, 1656–1669. https://doi.org/10.1021/ic102085b.

54. Novotna, J.; Laguerre, A.; Granzhan, A.; Pirrotta, M.; Teulade-Fichou, M. P.; Monchaud, D. Cationic Azacryptands as Selective Three-Way DNA Junction Binding Agents. *Org. Biomol. Chem*. **2015**, *13*, 215–222. https://doi.org/10.1039/c4ob01846j.

55. Selva Kumar, R.; Kumar, S. K. A.; Vijayakrishna, K.; Sivaramakrishna, A.; Brahmmananda Rao, C. V. S.; Sivaraman, N.; Sahoo, S. K. Development of the Smartphone-Assisted Colorimetric Detection of Thorium by Using New Schiff's Base and Its Applications to Real Time Samples. *Inorg. Chem*. **2018**, *57*, 15270–15279. https://doi.org/10.1021/acs.inorgchem.8b02564.

56. Khatua, S.; Samanta, D.; Bats, J. W.; Schmittel, M. Rapid and Highly Sensitive Dual-Channel Detection of Cyanide by Bis-Heteroleptic Ruthenium(II) Complexes. *Inorg. Chem*. **2012**, *51*, 7075–7086. https://doi.org/10.1021/ic2022853.

57. Thiele, S.; Malmgaard-Clausen, M.; Engel-Andreasen, J.; Steen, A.; Rummel, P. C.; Nielsen, M. C.; Gloriam, D. E.; Frimurer, T. M.; Ulven, T.; Rosenkilde, M. M. Modulation in Selectivity and Allosteric Properties of Small-Molecule Ligands for CC-Chemokine Receptors. *J. Med. Chem*. **2012**, *55*, 8164–8177. https://doi.org/10.1021/jm301121j.

58. Lindner, E.; Veigel, R.; Ortner, K.; Nachtigal, C.; Steimann, M. Preparation , Properties , and Reactions of Metal-Containing Heterocycles, Inclusion of Copper(I) into a Novel Bipyridine-Containing Tetraphosphadiplatinacyclophane. *Eur. J. Inorg. Chem*. **2000**, 959–969.

CHAPTER 6. FUTURE DIRECTIONS

6.1. Introduction

All of the research described in this dissertation has focused on identifying the vibrational modes coupled to the nuclear coordinate of excited-state evolution in Fe(II) polypyridyl complexes, with the ultimate goal of prolonging the lifetime of the MLCT excited state by disrupting the identified modes through targeted synthetic modification. The culmination of these efforts was the synthesis and characterization of a low-spin Fe(II) polypyridyl chromophore with a MLCT excited-state lifetime 20 times longer than that of a closely related Fe(II) complex, proving the validity of the proposed approach. In this final chapter, I will provide ideas for research to confirm and expand upon these results.

6.2. Experimental methods

6.2.1. Synthesis

General synthesis. Unless otherwise noted, all reactions were conducted either using standard Schlenk techniques or in an inert atmosphere glove box (nitrogen-filled, Vacuum Atmospheres). Zinc dust was activated by grinding commercially available zinc dust with a mortar and pestle, washing with 3% HCl, then water, EtOH, and finally Et_2O. The activated zinc dust was dried in a vacuum desiccator and used within 24 h. Anhydrous DMF, acetone, and chloroform were purchased from Acros Organics. NH_4OH refers to aqueous 30% ammonium hydroxide from Jade Scientific. 6,6'-dibromomethyl-2,2'-bipyridine (6,6'-dbmb),[1] 5,5'-dibromomethyl-2,2'-bipyridine (5,5'-dbmb),[2] *p*-toluenesulfonamide mono-sodium salt,[3] and 6,6'-bpy.bpy.bpy[4] were prepared according to the literature procedures. Hexamethylenetetramine (HMTA) was recrystallized from ethanol and thoroughly dried in a vacuum desiccator prior to use. All other chemicals were purchased from Sigma Aldrich, Acros, or Oakwood Chemical and used as received. Silica gel was

purchased from Silicycle (Silica Flash 60 Å porosity, 40-63μm/230-400 mesh). DCM for all optical measurements was dried over activated alumina under nitrogen and pumped into an inert atmosphere glovebox. Ground-state absorption measurements of [Fe(1,1'-biisoquinoline)$_3$](BF_4)$_2$ were collected on samples prepared in a nitrogen-filled glovebox in an air-free 1 cm quartz cuvette (FireFlySci).

1,1-biisoquinoline (biq). Prepared from the general procedure given in Tiecco *et al*.[5] A degassed solution of $NiCl_2$•$6H_2O$ (113 mg, 0.48 mmol) and PPh_3 (500 mg, 1.9 mmol) in DMF (5 mL) was stirred at 50°C under nitrogen. Activated Zn dust (31 mg, 0.47 mmol) was added to the deep aqua blue solution, instantly prompting a color change to yellowish green. This solution was stirred for 1 h, then 1-bromoisoquinoline (100 mg, 0.48 mmol) was added and stirred at 50°C until no more 1-bromoisoquionoline starting material was visible by TLC (Et_2O on silica), typically 3 h. The reaction mixture was poured into 1:1 H_2O/NH_4OH and extracted into $CHCl_3$ (3x10 mL). The organic fractions were combined, dried with Na_2SO_4, and the solvent was removed. Purification was performed by loading the crude product in acetone onto a flash silica gel column. Using Et_2O as the eluent, pure product was obtained as a white solid, 24% yield. X-ray quality crystals were obtained from slow evaporation of DCM/Et_2O from a solution of the purified product. ^{1}H NMR (500 MHz, $CDCl_3$) 8.71 (d, J = 5.7, 1 H), 7.95 (d, J = 8.3, 1 H), 7.82 (d, J = 5.7, 1 H), 7.76 (d, J = 8.6 Hz, 1 H), 7.71 (t, J = 7.1 Hz, 1 H), 7.49 (t, J = 7.2, 1 H). HRMS (ESI -TOF) m/z: $[M+H]^+$ calc'd for $[C_{18}H_{12}N_2]^{2+}$ 257.1079 obs. 257.1104.

***tris*-1,1-biisoquinoline iron(II) tetrafluoroborate [Fe(biq)$_3$](BF_4)$_2$.** In a nitrogen-filled glovebox, biq (58 mg, 0.23 mmol) was dissolved in 1:1 DCM/acetone (5 mL). Fe(BF_4)$_2$•$2H_2O$ (18 mg, 0.07 mmol) was dissolved in 1:1 DCM/acetone (2 mL) and added dropwise to the ligand with rapid stirring, instantly turning yellow, and after 5 min of stirring dark blue. The solution was

sealed in a pressure tube, taken out of the box, and stirred at 50°C for 12 h. After cooling to room temperature, the deep blue solution was pumped back into the box, and the solvent was removed. The blue solid was dissolved in the minimum amount of DCM and Et_2O was added until very cloudy. The blue precipitate was collected via filtration and washed with Et_2O. X-ray quality crystals were grown in the glovebox from Et_2O diffusion into DCM solutions of the product. Only free ligand could be detected by ESI-MS.

Attempted synthesis of [Fe(6,6'-bpy.bpy.bpy)](BF$_4$)$_2$. In a pressure tube in a nitrogen-filled glovebox, 6,6'-bpy.bpy.bpy (20 mg, 0.03 mmol) was dissolved in DCM (2 mL). A solution of $Fe(BF_4)_2 \bullet 2H_2O$ (8 mg, 0.03 mmol) in acetone (2 mL) was added dropwise to the ligand with rapid stirring, causing a color change from yellow to a pale red. The pressure tube was sealed and taken out of the box to heat at 40°C for 12 h. After pumping the reaction back into the glovebox, enough Et_2O was added to crash out an orange precipitate, which was collected by filtration. X-ray quality crystals were grown from ether diffusions into acetone/DCM solutions of the product. ^{1}H NMR spectrum in acetone-d^6 displayed broad signals that were difficult to assign.

5,5'-dimethylamino-2,2'-bipyridine dihydrobromide (dmab). A suspension of 5,5'-dbmb (100 mg, 0.292 mmol) in dry $CHCl_3$ (15 mL) was brought to reflux under N_2 and stirred until the dbmb fully dissolved. HMTA (88 mg, 0.63 mmol) was dissolved in dry $CHCl_3$ (10 mL) and added dropwise to the refluxing solution, leading to the formation of a white suspension. This suspension was kept at reflux for an additional 3 h and stirred overnight at room temperature. The fine off-white precipitate was collected via filtration, washed with $CHCl_3$, and dried in a vacuum desiccator for 12 h. This white powder was suspended in H_2O/EtOH/47% HBr (0.86 mL/3.5 mL/0.59 mL) and brought to 75°C under nitrogen, going into solution at 70°C, and stirred for 20 h. The solvent was removed and the yellow precipitate was suspended in EtOH (5 mL), filtered, washed with

EtOH, and dried in a vacuum desiccator, yielding 115 mg (83% yield assuming dihyrobromide salt) of yellow powder. ^{1}H NMR (500 MHz, D_2O) 8.84 (s, 1 H), 8.38 (d, J = 8.27, 1 H), 8.33 (dd, J_1 = 1.86, J_2 = 8.10, 1 H), 4.39 (s, 2 H). HRMS (ESI -TOF) m/z: $[M+H]^+$ calc'd for $[C_{12}H_{14}N_4]^+$ 215.1297 obs. 215.1301.

Attempted synthesis of 5,5'-bpy.bpy.bpy. 5,5'-damb (50 mg, 0.1 mmol) and 5,5'-dbmb (156 mg, 0.2 mmol) were suspended in MeCN (10 mL). Na_2CO_3 (156 mg, 1.5 mmol) was added, and the suspension was refluxed under nitrogen for 48 h. After cooling, the suspension was filtered and the solvent was removed from the filtrate, yielding impure 5,5'-bpy.bpy.bpy. HRMS (ESI -TOF) m/z: $[M+Na]^+$ calc'd for $[C_{36}H_{31}N_8Na]^+$ 599.2648 obs. 599.2651.

6.2.2. Physical characterization

X-ray crystal structure determination. Single crystal X-ray diffraction was collected on [Fe(6,6'-bpy.bpy.bpy)]$(BF_4)_2$ on a Bruker APEX-II CCD diffractometer with CuK_α radiation at 173 K at the Center for Crystallographic Research at Michigan State University. X-ray diffraction was collected by Dr. Richard Staples on single crystals of $[Fe(biq)_3](BF_4)_2$ were on a dectris-CrysAlisPro-abstract goniometer imported dectris images diffractometer at 293 K.

Variable-temperature magnetic susceptibility measurements. Evans method on $[Fe(biq)_3](BF_4)_2$ were performed in an analogous fashion as described in Chapter 2 of this dissertation. The only modifications are as follows: Samples were prepared in a nitrogen-filled glovebox and the solvent used was CD_2Cl_2.

Nanosecond time-resolved transient absorption spectroscopy. Measurements were conducted according to the procedures given in Chapter 2 on samples prepared in an Ar-filled glovebox in an air-free quartz cell (FireFlySci).

6.3. Results and Discussion

6.3.1. Defining the nuclear coordinate in other Fe(II) polypyriyl spin-crossover complexes

One of the most pressing questions raised by the results presented in Chapters 2 and 3 is how generalizable the results obtained on $[Fe(2\text{-}OMe\text{-}phen)_3](BF_4)_2$ and its Ru(II) analog are to other Fe(II) complexes. To begin to answer this question, it would be beneficial to investigate other polypyridyl Fe(II) SCO complexes, specifically at least one *tris*-bidentate complex with 2,2'-bipyridine-based ligands as well as *bis*-tridentate ligands. Although some strides have been made in predicting structural motifs that will lead to SCO complexes,[6] it is still unadvisable to attempt to design SCO complexes for the rather arduous investigations that are necessary to define the nuclear coordinate, as the synthetic effort may not pay off. Therefore, looking into the literature for Fe(II) SCO complexes with desirable coordination motifs is the most straight-forward route to identifying promising candidates that can expand the class of SCO complexes with defined nuclear coordinates. these results in our lab was problematic.

Onggo and Goodwin reported that the *tris*-Fe(II) complex with 1,1'-biisoquinoline (biq) exhibited temperature-dependent magnetic moments in acetone solution.[7] However, reproducing First, the synthetic preparation of biq given by Onggo and Goodwin, a homocoupling of isoquinoline using LDA and TMEDA, resulted in little to no product formation in my hands. Instead, the ligand was obtained from a Ni-catalyzed homocoupling of 1-bromoisoquinoline.[5] Once the ligand was in hand and the $[Fe(biq)_3](BF_4)_2$ complex was synthesized, however, it became obvious that there was a bigger issue: the complex rapidly dissociated in an acetone solution, as characterized by the almost instant color change from dark blue to yellow upon exposure to acetone in air, the conditions under which the reported magnetic behavior were collected, calling into question whether or not the reported temperature-dependent magnetic data

are actually a result of complex degradation. Luckily, the complex is stable in dichloromethane solutions with the rigorous exclusion of air and water.

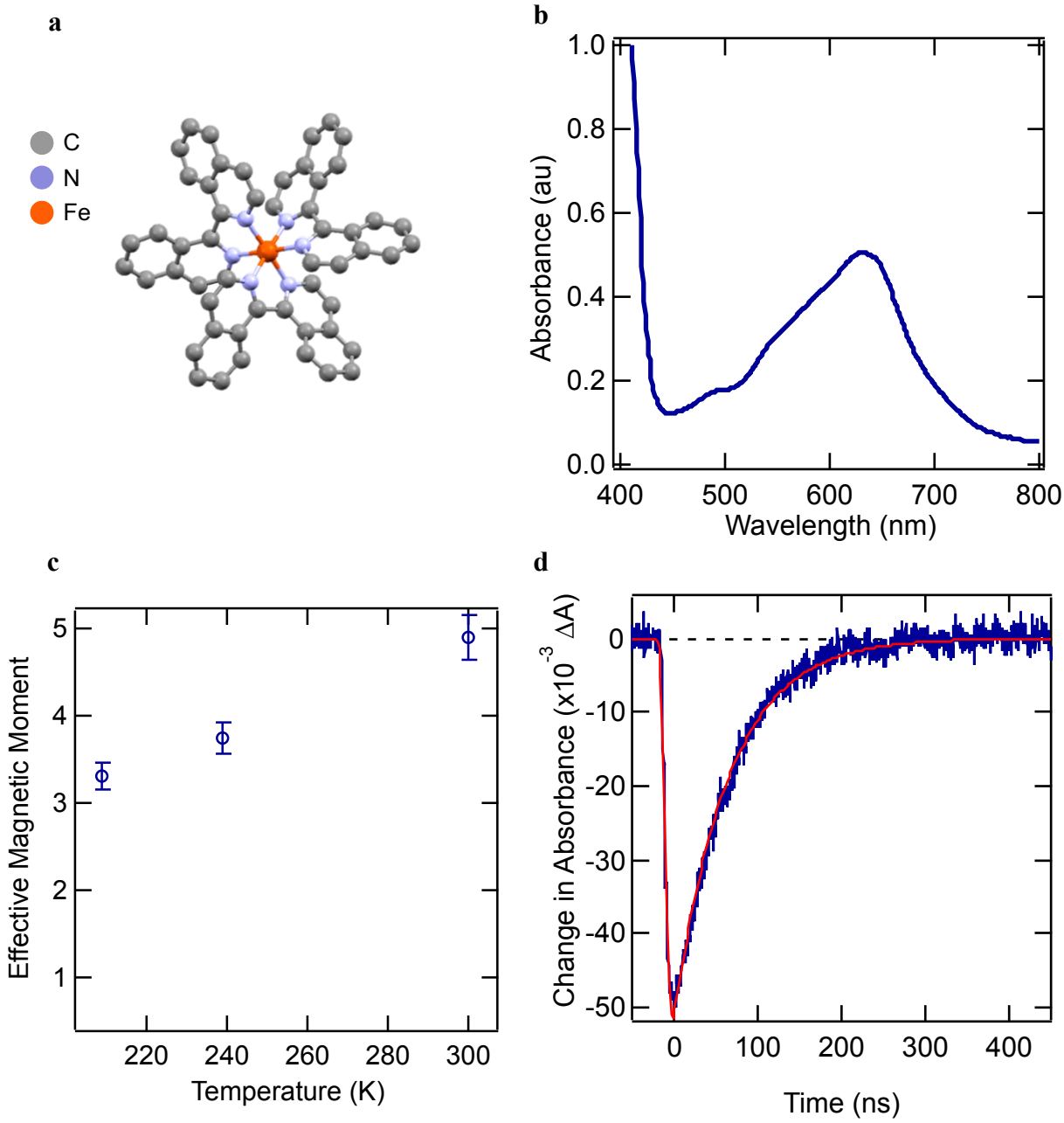

Figure 6.1. X-ray crystal structure of $[Fe(biq)_3](BF_4)_2$. Hydrogen atoms, solvent molecules, and counteranions have been excluded for clarity. (b) Ground-state absorption spectrum of $[Fe(biq)_3](BF_4)_2$ in DCM at room temperature. (c) Variable-temperature magnetic moment of $[Fe(biq)_3](BF_4)_2$ in DCM, as measured by Evans method. (d) Nanosecond transient absorption single-wavelength kinetics of $[Fe(biq)_3](BF_4)_2$ in DCM at room temperature, monitoring at λ_{probe} = 630 nm following excitation at λ_{pump} = 660 nm. Red trace is a monoexponential fit, yielding τ = 65 ns.

Despite the unpleasant surprises from $[Fe(biq)_3](BF_4)_2$, there were some interesting ones as well. The single-crystal structure of $[Fe(biq)_3](BF_4)_2$ reveals that the geometry of the complex is closest to an ideal octahedron that has been measured by our group (Figure 6.1a), with all Fe- N bond distances equal at 1.975 Å, all *trans*-N-Fe-N bond angles equal at 177.86°, and an average *cis*-N-Fe-N bond angle of 90.01°. In addition, the presumed $^1A_1 \rightarrow {}^{1,3}$MLCT feature in the ground-state absorption spectrum of $[Fe(biq)_3]^{2+}$ is very low in energy, with λ_{max} at 635 nm (Figure 6.1b). Preliminary magnetic measurements (Figure 6.1c) indicated that $[Fe(biq)_3](BF_4)_2$ is in fact a spin-crossover complex in solution, with μ_{eff} dropping from 4.89 at 300 K to 3.31 at 210 K. Additionally, the ground-state recovery dynamics measured in $[Fe(biq)_3]^{2+}$, as probed by monitoring the ground-state bleach at 630 nm following excitation into the MLCT absorption manifold to yield an excited-state lifetime of 65 ns (Figure 6.1d), are consistent with those expected for an Fe(II) spin-crossover complex. So, if absolute care is taken to exclude oxygen and water during variable-temperature magnetic measurements and transient absorption spectroscopy, this complex could not only provide nuclear coordinate information on another *tris*-bidentate Fe(II) system, but deliver insight into another complex our group has studied intensely: $[Fe(dcpp)_2]^{2+}$ (dcpp = 2,6-di(2-carboxypyridyl)pyridine).

$[Fe(dcpp)_2]^{2+}$ was first synthesized with the hopes that obtaining a nearly perfect octahedral Fe(II) complex would lower the density of ligand field states available to deactivate the MLCT excited-state manifold and thus increase the lifetime of the MLCT. Further investigations revealed that although $[Fe(dcpp)_2]^{2+}$ is quite symmetric and had a surprisingly low-energy MLCT (λ_{max} of the absorption feature is 610 nm), no extension in MLCT lifetime was observed.[8–10] However variable-temperature transient absorption spectroscopy on ground-state recovery of $[Fe(dcpp)_2]^{2+}$ found that the process was essentially barrierless, a phenomenon that has not been conclusively

observed before in a transition metal chromophore.[11] Therefore, having a spin-crossover complex like $[Fe(biq)_3]^{2+}$ with a very red-shifted MLCT and symmetric coordination environment, echoing traits observed in $[Fe(dcpp)_2]^{2+}$, could help further characterize the interesting electronic and structural factors at play in both the ground-state recovery and MLCT deactivation dynamics in $[Fe(dcpp)_2]^{2+}$.

In terms of tridentate ligands that upon *bis*-coordination lead to Fe(II) spin-crossover complexes, there are three promising candidates (Figure 6.2). All three $[Fe(L)_2]^{2+}$ complexes have

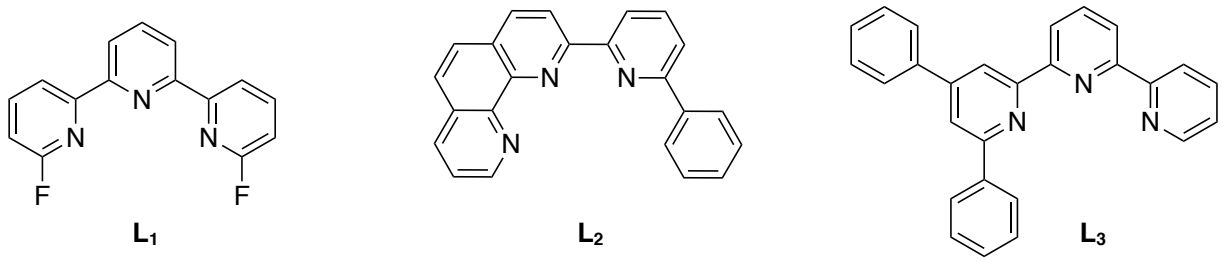

Figure 6.2. Three potential ligands to use to study the nuclear coordinate of tridentate polypyridyl spin-crossover complexes.

been reported in the literature, and characterized spectroscopically and magnetically to varying degrees. $[Fe(L_1)_2]^{2+}$ is the most well-characterized of the proposed complexes, with both variable-temperature (VT) solution-phase magnetic data and VT-transient absorption spectroscopy with a subsequent Arrhenius analysis carried out by the Damrauer group.[12] Next, Petzold and coworkers analyzed the linewidths of ^{1}H NMR resonances in solution to describe the spin-crossover equilibrium in $[Fe(L_2)_2]^{2+}$, however no transient absorption measurements are reported.[13] Finally, only VT ground-state absorption measurements were used to identify $[Fe(L_3)_2]^{2+}$ as a SCO complex,[14] providing plenty of opportunity to collect new data. Following the synthesis of these spin-crossover complexes as well as their Ru(II) analogs, they may be subjected to the same analysis presented in Chapter 3 to identify the geometric distortions that are coupled to two segments of the nuclear coordinate of excited-state evolution. With a collection of Fe(II) SCO

complexes with defined nuclear coordinates in hand, relationships may become clear between changes in denticity and which types of geometric motions are kinetically relevant. Furthermore, increasing the sample size of Fe(II) SCO complexes studied in this manner will aid the computational work necessary to codify the identity of the ^{3}MLCT → $^5T_2$ nuclear coordinate.

6.3.2. Sterically hindered cryptand ligands

The results presented in Chapter 5 on the photophysics of Fe(II) cage complexes suggest that the while the ligand employed did perturb the nuclear coordinate for ground-state recovery, it was not sterically hindering enough to impact MLCT excited-state lifetimes. That ligand could be synthetically tuned via coordination of Cu(I) atoms into the imine caps flanking the *tris*-bpy core

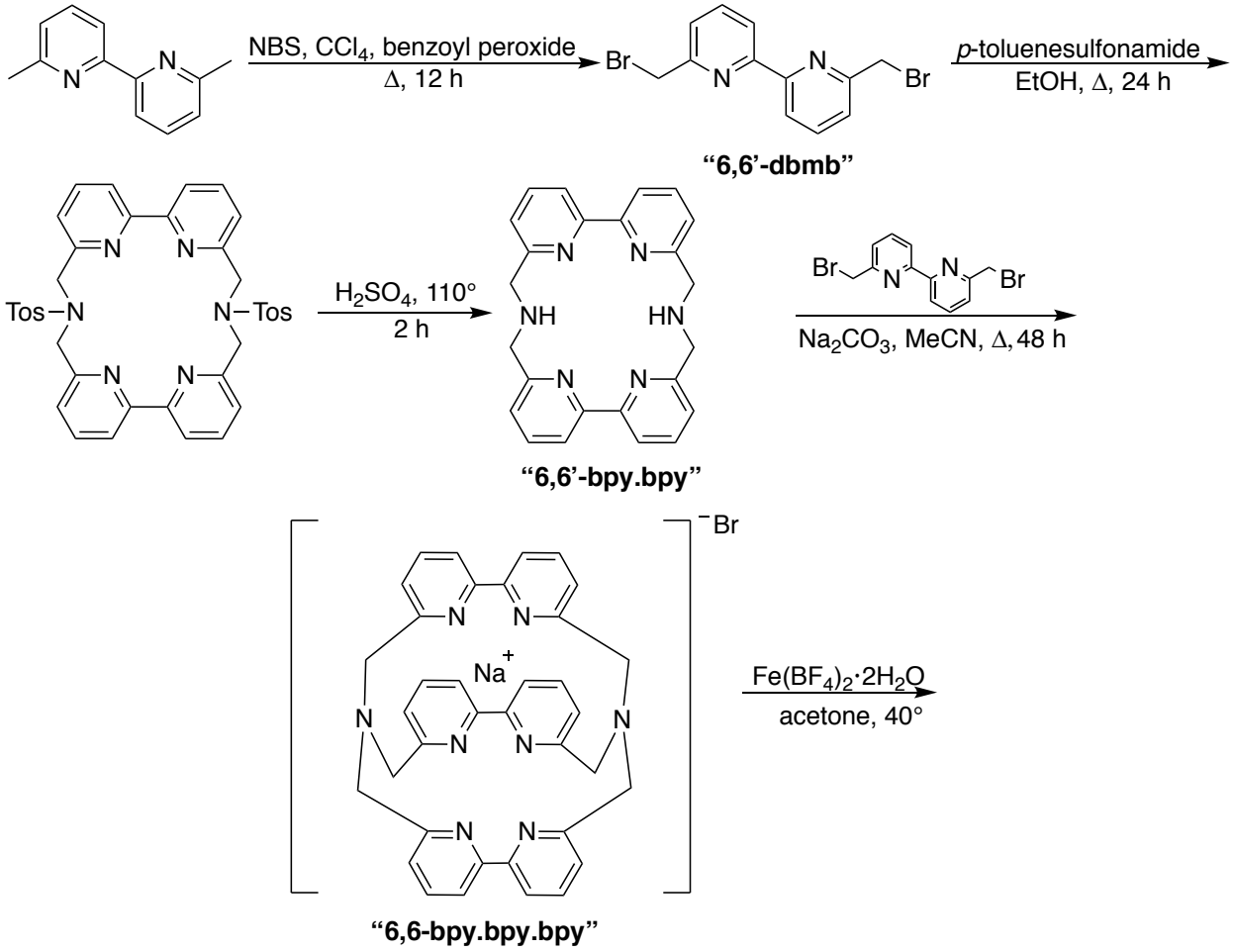

Figure 6.3. Synthetic route to 6,6'-bpy.bpy.bpy. ligand and attempted Fe(II) complexation.

of the ligand, however it would be ideal to not be reliant on the coordination of another metal to disrupt the geometric motions coupled to the MLCT → $^5T_2$ transition. Therefore, an alternative ligand system was explored to investigate whether or not a long-lived MLCT excited state could be observed in another sterically hindered Fe(II) polypyridyl complex. 6,6'-bpy.bpy.bpy (Figure 6.3) is another macrocyclic ligand developed by Lehn,[15] but instead of floppy imine caps to link together three bipyridine units, they are tethered together with methylene bridged tertiary amines.

The one potential issue with 6,6'-bpy.bpy.bpy is the linkage through the 6,6'-positions of the bpy moieties, which could be too sterically imposing to form a low-spin Fe(II) complex, as even methyl substituents in these positions have been shown to prohibit formation of *tris*-Fe(II) complexes, instead favoring *bis*-products.[7] To investigate if 6,6'-bpy.bpy.bpy is able to strike the balance of being flexible enough to stabilize a low-spin Fe(II) complex but sufficiently rigid to disrupt motion associated with excited-state evolution, the 6,6'-bpy.bpy.bpy ligand was synthesized according to the general procedure given by Lehn and coworkers with the modifications given by Setiz and coworkers (Figure 6.3).[4] The reaction time for the bromination of 6,6'-dimethyl-2,2'-bipyridine was increased from the 2 h reported by Lehn to 12 h[1] to modestly increase the yield to 18% and no attempts were made to isolate the bromination side products. For the final S_N2 reaction to prepare the ligand, Lehn reports a dropwise addition of the bicyclic 6,6'-bpy.bpy precursor to a refluxing solution of 6,6'-dbmb. However, 6,6'-bpy.bpy is quite insoluble in acetonitrile and hence it was impractical to follow Lehn's instructions. Instead, following the procedure given by Seitz and coworkers for the preparation of a deuterated 6,6'-bpy.bpy.bpy,[4] all reagents were simply suspended in acetonitrile and brought to reflux for 48 h.

Once the ligand was isolated as the sodium bromide salt, complexation with Fe(II) was attempted. This reaction resulted in a pale yellow product with a paramagnetic ^1H NMR spectrum,

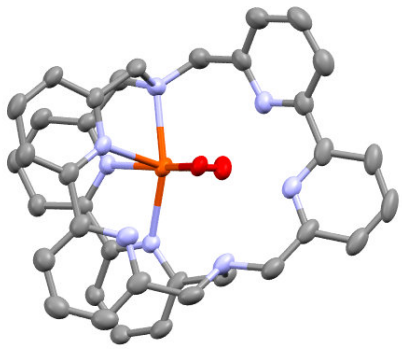

Figure 6.4. X-ray crystal structure of the product from complexation of 6,6'-bpy.bpy.bpy with Fe(II). Counteranions and hydrogen atoms have been removed for clarity.

suggesting a high-spin Fe(II) complex. Indeed, from the crystal structure obtained on a single crystal of the product (Figure 6.4), the coordination environment of [Fe(6,6'-bpy.bpy.bpy)]$(BF_4)_2$ is not conducive to a low-spin complex, as Fe(II) is coordinated to one of the tertiary amines of the ligand and two water molecules, despite the elevated reaction temperature used for its formation. An anhydrous Fe(II) starting material could be used to avoid coordinating water molecules, however the main issue with 6,6'-bpy.bpy.bpy is that it appears to be too rigid to coordinate an octahedral Fe(II) in a *tris*-bipyridine manner, and a less hindered ligand should be explored.

Therefore, the synthesis of the 5,5'-analog of 6,6'-bpy.bpy.bpy was pursued, as linking the bpy units together through their *meta*-positions should provide a more flexible ligand. However, the synthesis of 5,5'-bpy.bpy.bpy was not as straightforward as following the route given in Figure 5.3 but starting with 5,5'-dimethyl-2,2'-bipyridine (5,5'-dmb) in place of 6,6'-dmb. The problems arose when attempting to couple together two equivalents of 5,5'-dbmb to form the bicyclic product 5,5'-bpy.bpy using *p*-toluenesulfonamide. The origin of the issue is unclear, but both ^{1}H NMR and mass spectrometry show no sign of the desired product using this synthetic method. As this reaction proved difficult to optimize, an alternate approach was investigated (Figure 5.5a),

where the macrotricyclic ligand is synthesized from one equivalent of 5,5'-di-aminomethyl-2,2'-bipyridine (damb) and two equivalents of 5,5'-dbmb.

The only published instance of 5,5'-damb reports that the molecule could be made following the reduction of the corresponding azide using H_2 gas and Pd/C.[16] In my hands, this reaction was highly variable and resulted in the formation of several inseparable side products. So

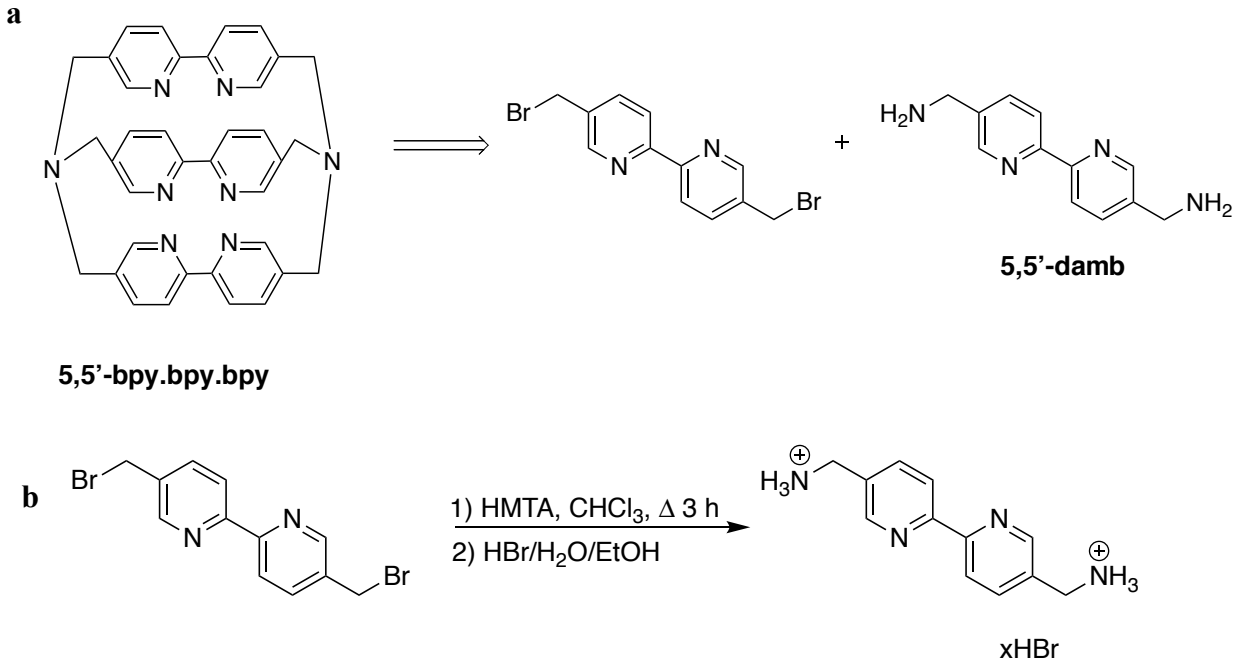

Figure 6.5. (a) Proposed synthesis of 5,5'-bpy.bpy.bpy. (b) Synthetic route to prepare 5,5'-damb. HMTA = hexamethylenetetramine.

instead, I opted for a Delèpine reaction from 5,5'-dbmb using hexamethylenetetramine (HMTA), followed by hydrolysis of the quaternary ammonium salt with hydrobromic acid (Figure 6.5b), similar to reactions described for the synthesis of 5-aminomethyl-2,2'-bipyridine[17] and 6,6'-damb.[4] Under these conditions, 5,5'-damb could be cleanly isolated in 83% yield. The final step for the synthesis of 5,5'-bpy.bpy.bpy has not been optimized, however refluxing a suspension of one equivalent of 5,5'-damb and two equivalents of 5,5'-dbmb with sodium carbonate in acetonitrile has led to formation of the desired product, as confirmed by mass spectrometry.

In these initial reactions, there remains a large excess of unreacted 5,5'-dbmb, even after refluxing for 48 h. Other unidentified side products have so far stymied the isolation of pure 5,5'-bpy.bpy.bpy. Despite the obvious need for adjustment of reaction and purification conditions, the synthetic route in Figure 6.5 has been proven successful for the synthesis of 5,5'-bpy.bpy.bpy. Complexation of the isolated ligand should be attempted using an Fe(II) starting material with noncoordinating anions, such as anhydrous $[Fe(BF_4)_2]$ or $[Fe(MeCN)_6](BAr^F)_2$,[18] in a similarly noncoordinating solvent like acetone or dichloromethane. If $[Fe(5,5'\text{-bpy.bpy.bpy})]^{2+}$ can be synthesized to obtain a low-spin *tris*-bpy like complex, other closely related ligands could be prepared to create a series of Fe(II) complexes with systematically decreasing steric hinderance (Figure 6.6), similar to the series of ligands proposed for 6,6'-substituted bpy.[19] These complexes could be characterized using the full suite of methods discussed in Chapter 5 and have the potential to better test the limits of the ability of sterically hindered ligands to produce low-spin Fe(II) complexes with long-lived MLCT excited-state lifetimes.

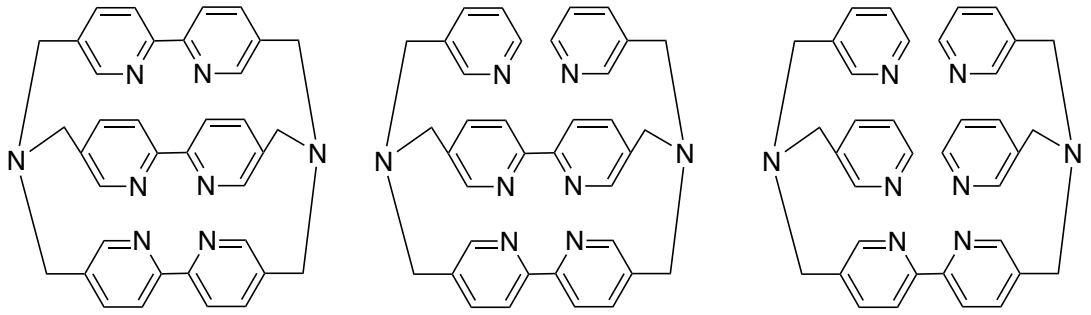

Figure 6.6. Proposed series of ligands based off of 5,5'-bpy.bpy.bpy.

6.4.Closing remarks

In the past six years there have been several successes in prolonging the lifetime of the metal-to-ligand charge transfer excited states in iron-based chromophores. These triumphs may have changed the narrative of the field: instead of investigating whether or not the MLCT lifetime can be extended, we are now faced with the challenge of how to best exploit the light-induced redox activity garnered by the longer-lived MLCT excited state in these earth abundant

chromophores. Regardless of their application, be it in dye-sensitized solar cells or photoredox catalysis, there will undoubtedly be a need to identify, define, and control the factors that determine the photophysical properties of iron(II) chromophores to tailor and improve their performance. In this dissertation, I hope to have underscored the importance of not overlooking the utility of identifying kinetically relevant geometric distortions associated with excited-state evolution in iron(II) polypyridyl chromophores, as their definition can inspire targeted synthetic design to manipulate excited-state dynamics.

APPENDIX

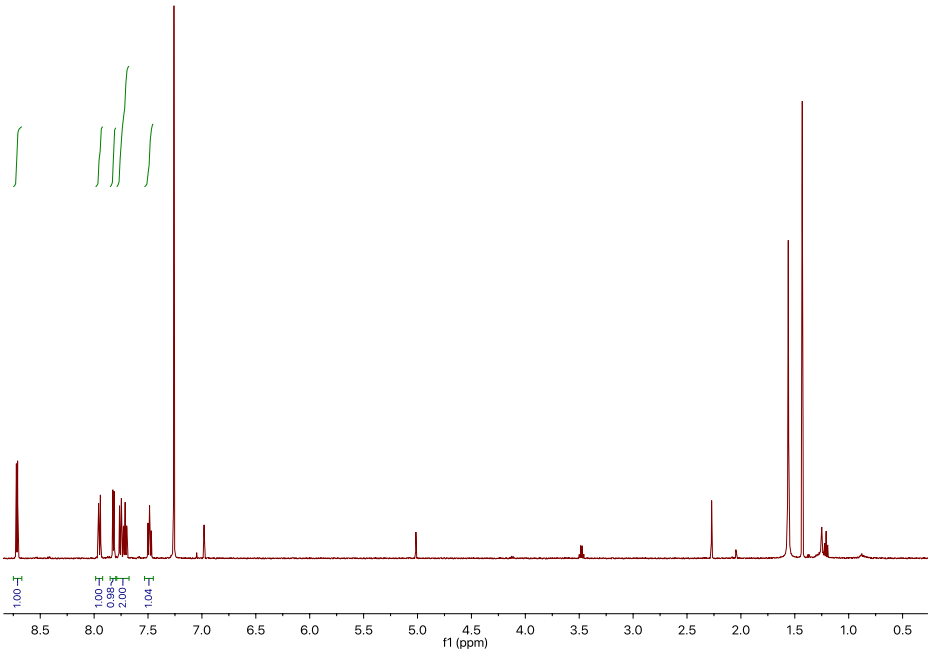

Figure 6.7.[1]H NMR of 1,1'-biisoquinoline in $CDCl_3$.

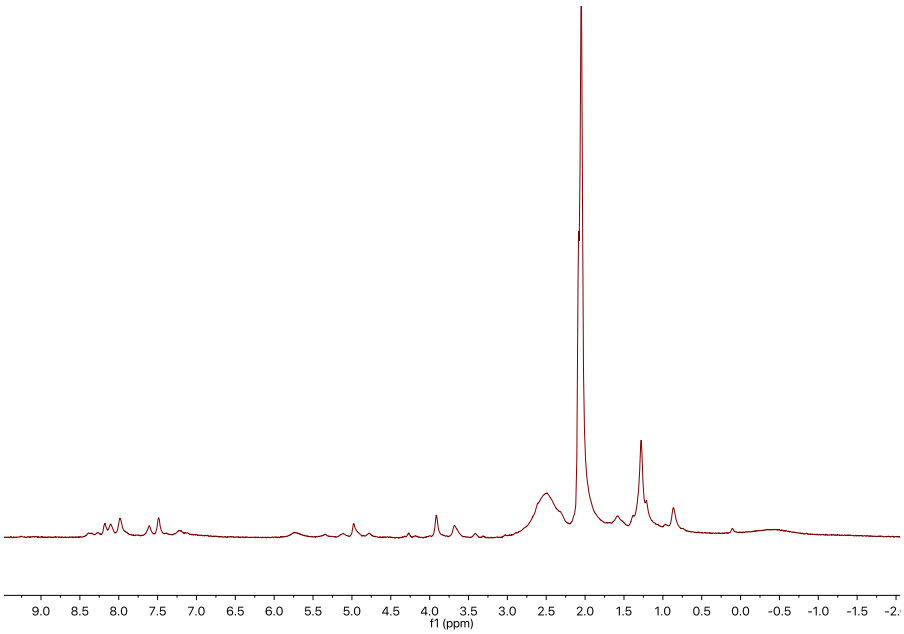

Figure 6.8. [1]H NMR of crude [Fe(6,6'-bpy.bpy.bpy)]$(BF_4)_2$ in acetone-d_6.

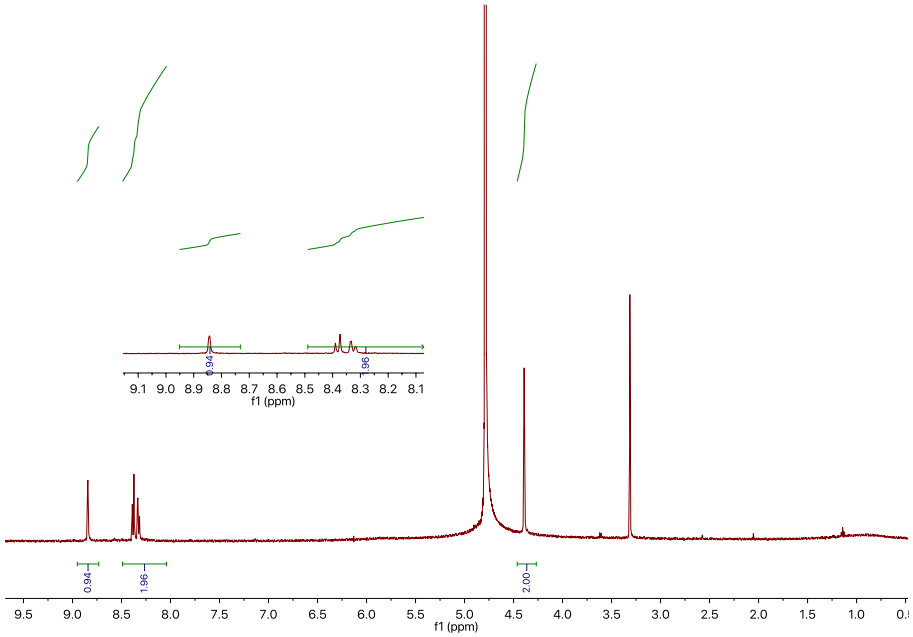

Figure 6.9. ^{1}H NMR of 5,5'-damb in D_2O.

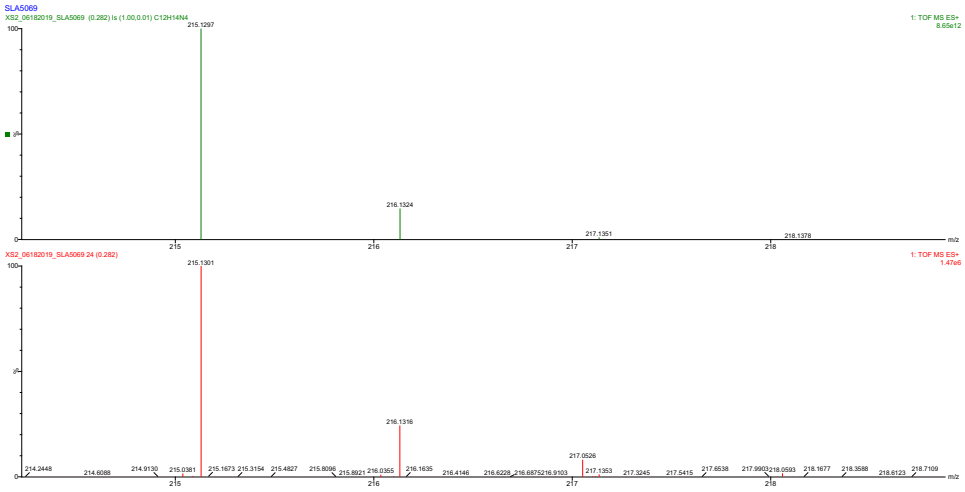

Figure 6.10. ESI-MS of 5,5'-damb. Top: predicted isotope pattern for $[M+H]^+$ ($C_{12}H_{14}N_4$). Bottom: experimental result.

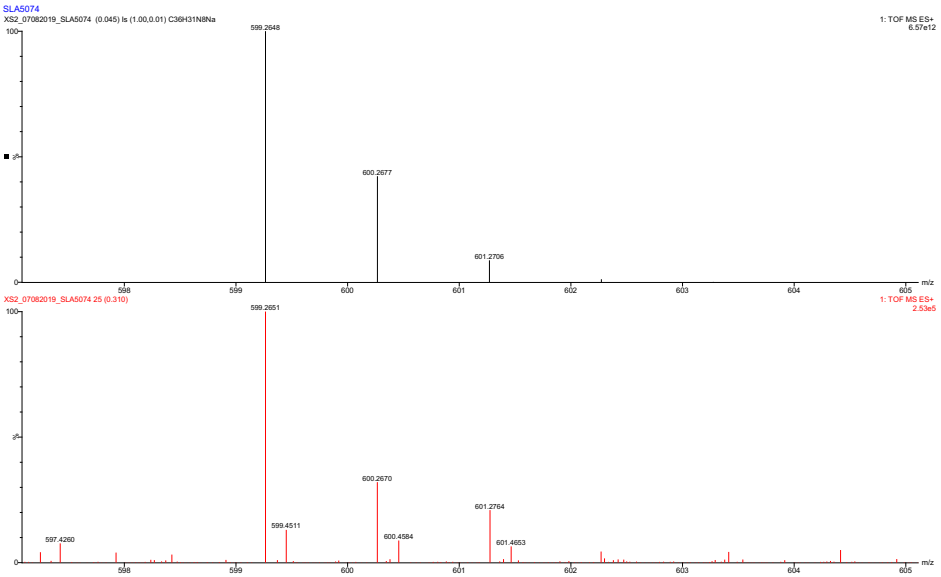

Figure 6.11. ESI-MS of crude 5,5'-bpy.bpy.bpy. Top: predicted isotope pattern for $[M+Na]^+$ ($C_{36}H_{31}N_8Na$). Bottom: experimental result.

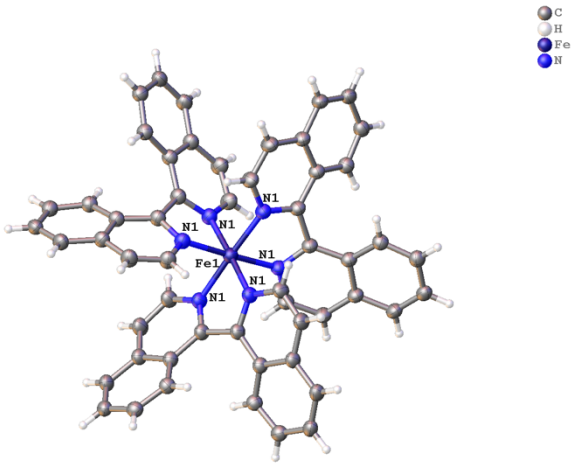

Figure 6.12. Atom labels of $[Fe(biq)_3](BF_4)_2$.

Table 6.1. Bond lengths for $[Fe(biq)_3](BF_4)_2$.

Atom	Atom	Length/Å	Atom	Atom	Length/Å
Fe1	N1[1]	1.975(4)	C8	C9	1.365(5)
Fe1	N1[2]	1.975(4)	C6	C7	1.425(4)
Fe1	N1	1.975(4)	C6	C5	1.362(5)
Fe1	N1[3]	1.975(4)	C1	C1[2]	1.480(6)
Fe1	N1[4]	1.975(4)	C1	C2	1.426(4)
Fe1	N1[5]	1.975(4)	C2	C7	1.420(4)
N1	C1	1.349(5)	F00D	B00F	1.360(11)
N1	C9	1.365(5)	F00E	B00F	1.406(12)
C3	C4	1.366(4)	B00F	F00D[6]	1.360(11)
C3	C2	1.425(4)	B00F	F00E[6]	1.406(12)
C4	C5	1.422(5)	C1AA	C0AA	1.60(4)
C8	C7	1.414(5)	C0AA	C1AA[7]	1.60(4)

Table 6.2. Bond angles for $[Fe(biq)_3](BF_4)_2$

Atom	Atom	Atom	Angle/°	Atom	Atom	Atom	Angle/°
$N1^1$	Fe1	$N1^2$	81.43(19)	C9	C8	C7	120.0(3)
$N1^3$	Fe1	$N1^4$	81.43(19)	C5	C6	C7	120.3(3)
$N1^1$	Fe1	$N1^4$	84.69(16)	N1	C1	$C1^5$	112.0(2)
$N1^5$	Fe1	$N1^4$	177.84(16)	N1	C1	C2	122.7(3)
$N1^5$	Fe1	N1	81.44(19)	C2	C1	$C1^5$	124.9(2)
$N1^3$	Fe1	N1	84.68(16)	C3	C2	C1	123.8(3)
$N1^1$	Fe1	$N1^3$	96.96(13)	C7	C2	C3	118.4(3)
$N1^1$	Fe1	$N1^5$	96.96(13)	C7	C2	C1	117.4(3)
$N1^2$	Fe1	$N1^3$	177.84(16)	C8	C7	C6	122.4(3)
$N1^1$	Fe1	N1	177.85(16)	C8	C7	C2	117.8(3)
$N1^5$	Fe1	$N1^3$	96.96(13)	C2	C7	C6	119.7(3)
$N1^2$	Fe1	$N1^5$	84.69(16)	C6	C5	C4	120.1(3)
$N1^2$	Fe1	N1	96.96(13)	C8	C9	N1	123.1(3)
$N1^2$	Fe1	$N1^4$	96.96(13)	$F00D^6$	B00F	F00D	110.9(13)
$N1^4$	Fe1	N1	96.95(13)	F00D	B00F	F00E	114.3(4)
C1	N1	Fe1	113.6(3)	F00D	B00F	$F00E^6$	108.8(4)
C9	N1	Fe1	125.9(3)	$F00D^6$	$F00D^6$	B00F	108.8(4)
C4	C3	C2	120.4(3)	F00E	F00E	B00F	99.5(11)
C3	C4	C5	120.9(3)	$C1AA^7$	$C1AA^7$	C0AA	180(3)

Table 6.3. Torsion angles for $[Fe(biq)_3](BF_4)_2$.

A	B	C	D	Angle/°	A	B	C	D	Angle/°
Fe1	N1	C1	C1[1]	23.4(4)	C1[1]	C1	C2	C7	176.5(3)
Fe1	N1	C1	C2	-149.7(3)	C1	C2	C7	C8	1.5(4)
Fe1	N1	C9	C8	156.3(3)	C1	C2	C7	C6	178.1(3)
N1	C1	C2	C3	161.8(3)	C2	C3	C4	C5	-2.3(5)
N1	C1	C2	C7	-11.4(5)	C7	C8	C9	N1	-6.5(5)
C3	C4	C5	C6	3.3(5)	C7	C6	C5	C4	-0.3(5)
C3	C2	C7	C8	-172.0(3)	C5	C6	C7	C8	172.8(3)
C3	C2	C7	C6	4.6(5)	C5	C6	C7	C2	-3.6(5)
C4	C3	C2	C1	-174.7(3)	C9	N1	C1	C1[1]	-174.9(3)
C4	C3	C2	C7	-1.7(5)	C9	N1	C1	C2	12.1(5)
C1	N1	C9	C8	-2.9(5)	C9	C8	C7	C6	-169.5(3)
C1[1]	C1	C2	C3	-10.4(6)	C9	C8	C7	C2	6.9(5)

REFERENCES

REFERENCES

1. Maheswari, P. U.; Lappalainen, K.; Sfregola, M.; Barends, S.; Gamez, P.; Turpeinen, U.; Mutikainen, I.; Van Wezel, G. P.; Reedijk, J. Structure and DNA Cleavage Properties of Two Copper(II) Complexes of the Pyridine-Pyrazole-Containing Ligands Mbpzbpy and Hmpzbpya. *Dalton Trans*. **2007**, *33*, 3676–3683. https://doi.org/10.1039/b704390b.

2. Yu, T.; Tsang, D. P. K.; Au, V. K. M.; Lam, W. H.; Chan, M. Y.; Yam, V. W. W. Deep Red to Near-Infrared Emitting Rhenium(I) Complexes: Synthesis, Characterization, Electrochemistry, Photophysics, and Electroluminescence Studies. *Chem. Eur. J*. **2013**, *19*, 13418–13427. https://doi.org/10.1002/chem.201301841.

3. Wessel, A. J.; Schultz, J. W.; Tang, F.; Duan, H.; Mirica, L. M. Improved Synthesis of Symmetrically & Asymmetrically: N-Substituted Pyridinophane Derivatives. *Org. Biomol. Chem.* **2017**, *15*, 9923–9931. https://doi.org/10.1039/c7ob02508d.

4. Bischof, C.; Wahsner, J.; Scholten, J.; Trosien, S.; Seitz, M. Quantification of C-H Quenching in near-IR Luminescent Ytterbium and Neodymium Cryptates. *J. Am. Chem. Soc.* **2010**, *2*, 14334–14335.

5. Tiecco, M.; Testaferri, L.; Tingoli, M.; Chianelli, D.; Montanucci, M. A Convenient Synthesis of Bipyridines by Nickel-Phosphine Complex-Mediated Homo Coupling of Halopyridines. *Synthesis* **1984**, *9*, 736–738.

6. Kepp, K. P. Theoretical Study of Spin Crossover in 30 Iron Complexes. *Inorg. Chem*. **2016**, *55*, 2717–2727. https://doi.org/10.1021/acs.inorgchem.5b02371.

7. Onggo, D.; Goodwin, H. A. Steric Effects of the Spin State of Iron(II) in Complexes of Substituted Bipyridine Derivatives. *Aust. J. Chem*. **1991**, *44*, 1539–1551. https://doi.org/10.1071/CH9911539.

8. Jamula, L. L. Exploring Design Strategies to Tune the Electronic Structure and Ultrafast Dynamics of Iron(II) Polypyridyl Chromophores, PhD Dissertation, Michigan State University, East Lansing, MI, 2013.

9. Brown, A. M. Excited-State Dynamics of Iron(II)-Based Charge Transfer Chromophores, PhD Dissertation, Michigan State University, East Lansing, MI, 2011.

10. Jamula, L. L.; Brown, A. M.; Guo, D.; McCusker, J. K. Synthesis and Characterization of a High-Symmetry Ferrous Polypyridyl Complex: Approaching the $^5T_2/^3T_1$ Crossing Point for Fe^{II}. *Inorg. Chem*. **2014**, *53*, 15–17. https://doi.org/10.1021/ic402407k.

11. Carey, M. C. Achieving a Long-Lived Charge-Separated Fe(II) Chromophore: Insights into the Role of Reorganization Energy on the Ultrafast Photophysical Processes of d^6

Polypyridyl Complexes, PhD Dissertation, Michigan State University, East Lansing, MI 2018.

12. Fatur, S. M.; Shepard, S. G.; Higgins, R. F.; Shores, M. P.; Damrauer, N. H. A Synthetically Tunable System to Control MLCT Excited-State Lifetimes and Spin States in Iron(II) Polypyridines. *J. Am. Chem. Soc.* **2017**, *139*, 4493–4505. https://doi.org/10.1021/jacs.7b00700.

13. Petzold, H.; Djomgoue, P.; Hörner, G.; Lochenie, C.; Weber, B.; Rüffer, T. Bis-Meridional Fe^{2+} Spincrossover Complexes of Phenyl and Pyridyl Substituted 2-(pyridin-2-yl)-1,10-phenanthrolines. *Dalton Trans.* **2018**, *47*, 491–506. https://doi.org/10.1039/c7dt02320k.

14. Constable, E. C.; Baum, G.; Bill, E.; Dyson, R.; Eldik, V.; Fenske, D.; Kaderli, S.; Morris, D.; Neubrand, A.; Neuburger, M.; et al. Control of Iron(II) Spin States in 2,2':6',2'-Terpyridine Complexes through Ligand Substitution. *Chem. Eur. J.* **1999**, *5*, 498–508.

15. Rodriguz-Ubis, J. -C; Alpha, B.; Plancherel, D.; Lehn, J. M. Synthesis of the Sodium Cryptates of Macrobicyclic Ligands Containing Bipyridine and Phenanthroline Groups. *Helv. Chim. Acta* **1984,** *67*, 2264–2269. https://doi.org/10.1002/hlca.19840670833.

16. Xing, B.; Yu, C. W.; Ho, P. L.; Chow, K. H.; Cheung, T.; Gu, H.; Cai, Z.; Xu, B. Multivalent Antibiotics via Metal Complexes: Potent Divalent Vancomycins Against Vancomycin-Resistant *Enterococci*. *J. Med. Chem*. **2003**, *46*, 4904–4909. https://doi.org/10.1021/jm030417q.

17. Panetta, C. A.; Kumpaty, H. J.; Heimer, N. E.; Leavy, M. C.; Hussey, C. L. Disulfide-Functionalized 3-, 4-, 5-, and 6-Substituted 2,2'-Bipyridines and Their Ruthenium Complexes. *J. Org. Chem*. **1999**, *64*, 1015–1021. https://doi.org/10.1021/jo9814795.

18. Park, J. G.; Jeon, I. R.; Harris, T. D. Electronic Effects of Ligand Substitution on Spin Crossover in a Series of Diiminoquinonoid-Bridged Fe^{II}_2 Complexes. *Inorg. Chem*. **2015**, *54*, 359–369. https://doi.org/10.1021/ic5025586.

19. Dürr, H.; Zengerle, K.; Trierweiler, H.; Chemie, O.; Saarlandes, U.; Saarbrücken, D.-. Podanden, Coronanden, Und Kryptanden Als Neue Komplex-Liganden Fur Photoelektronentransfer-Reaktionen Synthese Und Erste Photophysikalische Studien. *Z. Naturforsch.* **1988**, *43b*, 361–367.